System Identification of Civil Engineering Structures through Wireless Structural Monitoring and Subspace System Identification Methods

by

Junhee Kim

A dissertation submitted in partial fulfillment
of the requirements for the degree of
Doctor of Philosophy
(Civil Engineering)
in The University of Michigan
2011

Doctoral Committee:

Associate Professor Jerome P. Lynch, Chair
Professor Victor C. Li
Professor Radoslaw Michalowski
Associate Professor Mingyan Liu
Professor Kincho H. Law, Stanford University

DEDICATIONS

I dedicate this thesis to my father and mother
who have missed their son while praying for his achievement.

I dedicate this thesis to my wife, Seon-Yeong,
who has missed her man while taking care of his family.

I dedicate this thesis to my daughter, Min-Chae,
who has missed her dad while being curious about his absence.

ACKNOWLEDGEMENTS

The work presented herein was financially supported by the National Science Foundation under Grant CMMI-0726812 (PI: Prof. Jerome P. Lynch) and Grant CMMI-0724022 (PI: Prof. Radoslaw Michalowski), NIST Technology Innovation Program under Contract 70NANB9H9008 (PI: Prof. Jerome P. Lynch), and the Office of Naval Research under Contracts N00014-09-1-0567 (PI: Prof. Jerome P. Lynch). I deeply appreciate the opportunities provided by these funding agencies.

I have completed the doctoral program at the University of Michigan with tremendous assistance from numerous people. First of all, I would like to express my deepest gratitude to my advisor, Prof. Jerome P. Lynch, for the academic and personal guidance he provided through my entire Ph.D. study. He provided me with the technological blueprints that guided me in concentrating on, and eventually solving, relevant problems which had seemed impossible to me at the outset. He also introduced to me a land unexplored by traditional civil engineers; amazingly, there were many keys which unlocked many civil engineering problems. All achievements in the thesis are possible due to his guidance. In addition to professional advising, I am very grateful for his warm care over the years.

I appreciate the support of my committee members: Prof. Kincho H. Law (Structures, Civil and Environmental Engineering, Stanford University) gave me the invaluable opportunity to study a Bayesian probabilistic approach for damage detection; Prof. Radoslaw Michalowski (Geotechnical Engineering, Civil and Environmental Engineering, University of Michigan) opened my mind to soil mechanics; and Prof. Victor C. Li (Material Engineering, Civil and Environmental Engineering, University of Michigan) exposed me to the world of cementitious material as well as fracture mechanics. Prof. Mingyan Liu (Electrical Engineering, University of

Michigan) guided me on signal processing techniques. I am honored to have them as my doctoral committee.

All experiments presented in the thesis were successfully conducted thanks to the development of *Narada* wireless sensor by former lab members, Dr. Andrew Swartz (Assistant Professor, Civil and Environmental Engineering, Michigan Technological University) and Dr. Andrew Zimmerman (Civionics, LLC), with whom I have enjoyed an intellectual journey into a new world. I cannot emphasize enough the importance of the experimental testbeds used to validate the theories of this thesis. I value Prof. Chin-Hsiung Loh (Civil Engineering, National Taiwan University, Taiwan) for his close collaboration with our laboratory. I dare to say that the six-story building structure experiments revealed many secrets about structural dynamics to me. I appreciate Prof. Chung-Bang Yun (Civil and Environmental Engineering, KAIST, Korea), Dr. Chang-Geun Lee (Korea Expressway Corp., Korea), and Dr. Jong-Jae Lee (Civil and Environmental Engineering, Sejong University, Korea) for their support and encouragement through numerous experiments on the Korean test road. Especially, I am indebted to Prof. Chung-Bang Yun who laid the foundation of structural dynamics during my M.S. degree, which gave me the passion to pursue system theory, a more attractive mathematical approach to experiments of dynamic systems.

I thank the brilliant members in my research team of the Laboratory for Intelligent Structural Technology (LIST), particularly Mr. Sean O'Connor, Mr. Mike Kane, and Mr. Sukhoon Pyo for their assistance during experimentation. In addition to research life, my close fellowship with the labmates made my life in Ann Arbor highly enjoyable. I also have many pleasant memories of Dr. Kenneth Loh (Assistant Professor, Civil and Environmental Engineering, UC Davis) with whom I started my research journey four and half years ago. I will never forget the exciting voyage I have made with the passionate crew of the vessel "LIST" under the direction of "Captain Lynch".

PROLOGUE

Structures, Electronics, and Mathematics

I really wanted to talk to structures physically.
… So, I borrowed electronics and mathematics
‘cause structures cannot say.

TABLE OF CONTENTS

LIST OF FIGURES

LIST OF TABLES

ABSTRACT

System Identification of Civil Engineering Structures through Wireless Structural Monitoring and Subspace System Identification Methods

by

Junhee Kim

Chair: Dr. Jerome P. Lynch

Recent dramatic catastrophic failures of civil engineering infrastructure systems, such as the I-35 Bridge collapse (Minneapolis, MN, 2007) and the PG&E gas pipeline explosion (San Bruno, CA, 2010), have called attention to the need to better manage these complex engineered systems to ensure safe usage by society. Structural health monitoring (SHM) has emerged over the past decade as an active, interdisciplinary research field dealing with the development and implementation of sensing technologies and data processing methods aimed to perform condition assessment and damage detection of structural systems (*e.g.*, civil infrastructure, aircraft, ships, machines, among others). While many advances have been made over that period, some technological hurdles still remain. For example, high costs and laborious installations of monitoring systems hinder their widespread adoption. Furthermore, there exists a lack of generalized data processing algorithms (*e.g.*, black-box system identification algorithms) that extract information from sensed data. This thesis addresses these fundamental bottlenecks. At the core of the dissertation is the advancement of wireless sensors for cost-effective structural monitoring. Wireless sensors have the potential to reduce the cost of monitoring systems while offering onboard data processing capabilities for sensor-based data interrogation. A wireless

sensor node designed explicitly for monitoring civil infrastructures is introduced and deployed on operational bridge structures. Numerous advantages inherent to wireless sensors are illustrated including their role in reconfigurable monitoring system installations, their use for mobile sensing, and their ability for in-network computing.

To process the large tracts of structural response data created by wireless monitoring systems, data-driven subspace system identification techniques, recently developed in the field of control theory, are explored for application to SHM. While subspace system identification enjoys exclusive superiority over other black-box system identification methods, a physical interpretation of the estimated black-box model remains an unresolved issue. This thesis proposes a new methodology for the extraction of physical parameters from the black-box models. By explicitly linking physical system parameters with subspace-derived black-box models, a grey-box system identification method is created for the detection (*e.g.*, location and severity) of damage in monitored structures. Having established subspace identification as a powerful data processing tool, embedment of these methods within the wireless sensors is proposed for autonomous in-network execution.

Traditionally, the civil engineering community has exclusively focused on output-only data interrogation methods due to the difficulties associated with directly monitoring loads on a civil engineering structure. By leveraging the mobility of wireless sensors, a novel approach to monitoring the dynamic loading of bridges is proposed. Specifically, wireless sensors installed in vehicles are combined with a permanently deployed wireless bridge monitoring system to collect data associated with the bridge loading. The input-output data set collected can be used to better understand vehicle-bridge interaction. The dissertation offers a data processing algorithm for the identification of the bridge system under a position-changing input (*i.e.*, truck) so that vehicle-bridge interaction can be studied. The thesis cohesively integrates interdependent research threads to offer a powerful, new paradigm for model-based structural health monitoring using wireless sensing technology.

CHAPTER 1

INTRODUCTION

1.1 Civil Infrastructure Systems and the Need for Structural Monitoring

Civil infrastructure systems (*e.g.*, bridges, buildings, dams, pipelines) are large, spatially distributed engineered systems that will gradually deteriorate with time if they are not properly managed and maintained. Considering their invaluable societal functionality, the long-term health management of civil infrastructure systems is just as important as their design and construction. For example, if the onset of structural damage goes undetected, future repair will likely be more expensive. Furthermore, undetected damage can pose as a very serious safety issue because undetected damage can weaken the structure to a point where partial or global collapse is possible.

To ensure public safety, almost all civil infrastructure systems are managed through vigilant monitoring. Traditionally, monitoring has been performed by trained inspectors who use visual inspections to assess the condition of the structure. However, schedule-based visual inspection has proven inefficient (Inaudi and Deblois 2009). Specifically, manual visual inspections are subjective (*e.g.*, more qualitative than quantitative in nature) and often fail to detect the onset of structural damages (especially those hidden below the surface or those placed in locations difficult to reach by inspectors). In addition, visual inspections are time-consuming and expensive to carry out.

To acquire more quantitative evidence of structural performance, structural monitoring systems can be installed to measure structural responses to loadings and environmental factors. A structural monitoring system entails the use of sensors (*e.g.*, accelerometers, strain gages, *etc.*) to measure structural responses. Analog sensor voltages are communicated (typically using coaxial wires) to a centralized data acquisition system where the analog sensor outputs are digitized and stored. Structural monitoring systems are fairly mature technologies that have been in use for more than three decades. For example, permanent structural monitoring systems have been

successfully installed on many long-span bridges worldwide. In California, more than 900 sensor channels (*e.g.*, accelerometers, anemometers, thermometers, *etc.*) have been permanently instrumented on many of the state's long-span bridges including the Golden Gate Bridge and Vincent Thomas Suspension Bridge (Hipley 2001). In Asia, sensors have also been instrumented on many cable-supported bridges such as the Seohae Bridge and Gwangan Bridges in Korea (Koh *et al.* 2003), the Ting Kau Bridge in China (Ko 2003), and the Akashi Kaikyo Bridge and Tatara Bridges in Japan (Tamura 2001).

There is a pronounced gap between the motivations that led to the adoption of current monitoring systems deployed on operational structures and the need for structural health monitoring. For example, the motivation to install the aforementioned monitoring systems was to record the behavior of bridges during extreme loading, such as earthquakes or strong winds (Celebi 2006). Recorded data has been used to analyze actual structural responses to these extreme loads so as to create better design codes for future structures. Unfortunately, instrumentation is rarely used for health monitoring purposes; in fact, almost all of the U.S. bridges with permanent monitoring systems are still required to undergo annual or bi-annual visual inspections. This is a rather unfortunate situation when considering the costs associated with installing these monitoring systems. For example, cable-based monitoring systems for civil structures are widely cited to cost thousands of dollars per channel (Celebi 2002). If the same monitoring systems can also be used for automated health monitoring, then this added functional feature can help infrastructure owners justify the high cost associated with their installations.

1.2 Emergence of Structural Health Monitoring

While structural monitoring has historically focused on trigger-based monitoring systems for monitoring structural behavior under extreme events, a recent shift of emphasis has been placed on long-term structural health monitoring (SHM). Public demand for SHM has grown out of recent catastrophic structural failures (*e.g.*, I-35 Bridge collapse, Minneapolis, MN, 2007). The ubiquitous sensing and communication technologies (*e.g.*, cell phones, smart phones, tablet computers, RFID tags, *etc.*) that are beneficially impacting many facets of everyday life, have raised the public's expectation that these technologies are also used to protect them during their use of critical infrastructure systems. Toward this end, many federal agencies including the National Science Foundation (NSF), the Federal Highway Administration (FHWA), and the National Institute of Standards and Technology (NIST) have collectively invested hundreds of millions of dollars in the development of SHM technologies over the past decade.

Structural health monitoring (SHM) is an active multidisciplinary research area dealing with the development and implementation of sensing technologies and data processing tools for structural condition assessment and damage detection. Even though SHM shares many functional elements (*i.e.*, data collection and processing) with classical structural monitoring approaches, SHM distinguished itself by attempting to autonomously process collected data for the assessment of structural condition (*e.g.*, undamaged versus damaged). SHM would offer a more effective and reliable approach to interpreting structural performance and be used to supplement subjective and qualitative visual inspections in current use (Brownjohn 2007). Generally, SHM is a long-term process that tracks structural functionality over long-periods of time such as decades (Aktan *et al.* 2000; Ko and Ni 2005; Farrar and Worden 2007; Frangopol *et al.* 2008). A short-term condition assessment of operational structures using a temporally installed monitoring system can be considered as a sub-discipline of the SHM field (Brownjohn 2007). Such short-term vibration-based damage detection (Doebling *et al.* 1998) is born out of the field of experimental structural dynamics and modal analysis (Salawu and Williams 1995; Cunha and Caetano 2006). The goal of a SHM can be broadly outlined as follows:

Cost-effective assessment of structural performance: The overarching objective of SHM is to provide an objective basis for more accurately assessing structural performance and health (Brownjohn 2007). In addition, such systems must be low-cost to ensure they are applicable not only to large-scale critical structures (*e.g.*, long-span bridge), but also to ordinary small- to medium-scale structures (*e.g.*, short-span highway bridges). Cable-based monitoring systems are currently expensive often costing thousands of dollars per channel (Celebi 2002). Thus, new technologies for sensing and data collection that inherently lower cost are being developed by the SHM research community. Data-processing methodologies for reliable evaluation of structural performance are also being explored by researchers in the field (Sohn and Farrar 2001). Additional benefits of SHM include verification of design specifications and real-time stability tracking of structures under construction (Inaudi and Deblois 2009).

Load estimation: Many infrastructure systems are exposed to large loads that can lead to long-term deterioration. A goal of SHM is to monitor the loads imposed on structures. In the case of SHM of bridges, direct measurement of structural loads (*e.g.*, vehicles) would allow engineers to assess unsafe overloading conditions and to improve their understanding of long-term degradation introduced by traffic. Traffic loads on bridges lead to a complex dynamic

phenomena known as vehicle-bridge interactions (VBI). Unfortunately, the observation of vehicle-bridge interaction is very challenging due mobility of the vehicle introducing the bridge vibrations. With most monitoring systems being wired, it is nearly impossible to include vehicle-based sensors within the same data acquisition architecture as the bridge monitoring system. Thus, new sensing methods are needed to directly monitor vehicle loading and more generally, vehicle-bridge interaction.

Detection and location of damage: Damage is generally defined as a change to the material or geometric properties of a structure that adversely affect structural performance and safety (Farrar and Worden 2007). In general, damage is a local phenomenon that typically occurs at a highly localized area of a structure. Depending on its stage of development, damage can be categorized into one of two stages: damage initiation (*e.g.*, material-level defects or flaws) and system-level damage evolution where a structure is not operating as it was designed (Farrar and Worden 2007). Once initiated, damage can continue to grow and intensify, leading to degradation of the performance of the global system or an eradication of the safety margin that is included during design. Once the capacity of the structures is reduced (*i.e.*, due to damage) to a point below the structure's demand, structural failure occurs (Frangopol *et al.* 2008). Once damage initiates, SHM is intended to provide an early warning of the structural system's degradation. This early warning can potentially lead to lower-cost repairs and, generally speaking, safer structures.

Structural prognosis: Thus far, the research community has focused on the development of data processing algorithms for health diagnosis. However, SHM does not end at diagnosis; rather SHM concludes with prognosis. Prognosis entails the analysis of what detected damage means for the structural owner. Critical questions, such as "how much remaining life is there in the structure" and "what cost-effective actions must be taken to ensure the structure remains safe" are answered during prognosis. Hence, the goal of SHM is to use its diagnosis and prognosis capabilities to aid the structural owner with his/her decision making process.

1.3 Limitations and Opportunities for SHM

Despite the aforementioned objectives of SHM, meaningful SHM systems have yet to be deployed on operational structures. Rather, the majority of SHM systems have been limited to

only small-scale and well-conditioned laboratory studies (Brownjohn 2007). Two factors are at the root of this issue. First, there are many hardware-oriented problems associated with current SHM systems. Despite recent advances in sensing hardware, wired data acquisition is still too expensive for most structures. In addition, the measurement of structural loads remains challenging, especially for moving traffic loads on bridges. Second, generalized data-processing algorithms that can be applied as an autonomous black-box SHM tool have yet to be developed. Without autonomous data-processing algorithms that can be generically applied to a broad class of structures, it is difficult for the structural owner to justify the cost of an expensive monitoring system when the benefits of such systems have yet to be proven.

In response to the high cost associated with tethered monitoring system hardware, the SHM community has begun to utilize wireless sensing technologies after the seminal study of Straser and Kimidjian (1998) established that wireless radios could be reliably used for communicating data in a structural monitoring system. By eliminating the coaxial wires that are used in conventional cable-based monitoring systems, wireless sensing technologies reduce the cost and the complexity of the system installation (Lynch and Loh 2006). The cost-effectiveness of wireless sensing also encourages the installation of high sensor densities within a fixed budget. Successful field deployments in bridges over the past five years have demonstrated the feasibility and value of the technology: Alamosa Canyon Bridge, New Mexico (Lynch *et al.* 2004a), Geumdang Bridge, Korea (Lynch *et al.* 2006), Gi-Lu Bridge, Taiwan (Lu *et al.* 2006), Golden Gate Bridge, California (Pakzad *et al.* 2008) Wright Bridge, New York (Whelan and Janoyan 2009), Jindo Bridge, Korea (Cho *et al.* 2010; Jang *et al.* 2010), just to name a few.

In addition to being cost-effective, wireless sensing technology also offers: 1) on-board computational capabilities and 2) mobility. Processing raw sensor data locally followed by transmitting only processed results drastically reduces the amount of data to be transmitted. Reduced demand for communication saves communication bandwidth and scarce on-board energy (*e.g.*, battery energy). When emphasizing their embedded data processing capabilities, wireless sensors are often labeled as "smart" sensors (Spencer *et al.* 2004). On-board data processing has been leveraged by many researches with numerous system identification and damage detection algorithms implemented and tested in operational structures (Lynch *et al.* 2004b; Sim *et al.* 2008; Zimmerman *et al.* 2008). The fact that wireless sensors are not physically tied to the data acquisition system allows them to be used to monitor moving objects. This mobility has recently been proposed for monitoring the behavior of vehicles as they travel over a bridge (Kim and Lynch 2010; Kim *et al.* 2010b; Kim *et al.* 2010a). Monitoring both vehicles and

the bridge over which they cross can be instrumental for better understanding vehicle-bridge interaction.

To date, the most successful data-processing algorithms used to process structural monitoring data are mainly system identification algorithms. Identified system properties can be used to directly identify damage, or serve in the updating of analytical models that are used to identify damage-induced changes in structural performance. Nowadays, output-only system identification based on measured ambient vibrations (*i.e.*, without knowledge of the excitation source) is popular, especially in civil engineering where it is difficult to excite large-scale civil structures in a controlled manner. Output-only system identification is considered as operational evaluation and is enhanced by recently proposed statistical pattern recognition (Farrar *et al.* 2001; Sohn and Farrar 2001). Another approach to system identification blends classical modal parameter estimation with eigensystem realization algorithm (ERA) methodologies (Juang and Pappa 1984). Based on estimated modal parameters, various methodologies for the indication of damage have been proposed (Bernal 2002). More recently, researchers (Weng 2010) have started to pay attention to the recently developed subspace identification methods (Van Overschee and De Moor 1994; Verhaegen 1994) that have emerged in the control theory community.

1.4 Research Objectives and Strategies

There are four major research objectives associated with this dissertation. These objectives are aimed to address the aforementioned limitations of the state-of-practice in SHM. However, the individual objectives and the proposed strategies for achieving these objectives share a common prime target: application of *wireless sensor technologies* to solve the problem of accurate *system identification* of operational civil engineering structures for SHM. The four objectives are: 1) field validation of wireless sensors in operational bridge structures; 2) physical interpretation of black-box system identification methods; 3) implementation of subspace identification algorithms in a wireless sensor network; and 4) monitoring and identification of vehicle-bridge interaction.

1.4.1 Field Validation of Extended-Range Wireless Sensors

The monitoring of civil structures within their natural operational environment is a key prerequisite for model updating, system identification, and structural health management. While

wired monitoring systems exist, they suffer from high costs and laborious installations as previously discussed. Hence, wireless sensors can be leveraged to more cost-effectively monitor large-scale civil engineering structures. In addition, the mobility of wireless sensors can be exploited to monitor the vibratory behavior of heavy trucks that impose a dynamic load on a bridge. This thesis explores the use of a low-cost wireless sensor platform (termed *Narada*) for low-cost monitoring of bridges and trucks. Power amplified telemetry is used to increase the communication range of the *Narada* wireless sensor. The *Narada* wireless sensing node (Swartz *et al.* 2005) and its extended-range radio are used during a series of dynamic load tests on bridges in Korea.

1.4.2 Physical Interpretation on Identified System Models

Recently developed data-driven subspace system identification techniques from the control theory field provide a rich set of analytical tools for system identification in the structural dynamics field. However, the physical interpretation of these black-box system identification techniques remains a major hurdle in their application to civil engineering problems such as SHM. Physical interpretation of black-box system identification models is direly needed to extract a physical description (*i.e.*, discretized finite element formulation) of the target structural system using measurement data. Through the physical system description, baselining and damage detection problems in SHM can be effectively solved.

1.4.3 Decentralized System Identification for In-network Execution

As wireless monitoring systems emerge as viable alternatives to traditional wired data acquisition systems (DAQs), scalable approaches to autonomously processing measurement data in-network are necessary. Embedded data processing has the benefit of improving system scalability, reducing wireless communication and reducing power consumption. When using embedded data processing for system identification, the global system must be decomposed into sub-systems that are easier to analyze on a single wireless sensor. Towards this end, decentralized Markov parameter identification (MPID) is an ideal approach to system identification. In this thesis, two different decentralized MPID methods are embedded in *Narada* for the in-network execution: 1) deterministic MPID using input-output data; 2) stochastic MPID using output-only data.

1.4.4 Monitoring and Identification of Vehicle-Bridge Interaction

Highway bridges undergo a complex dynamic phenomenon when loaded by vehicles (*i.e.*, vehicle-bridge interaction). It has been revealed that repeated vehicles, especially heavy trucks, lead to an acceleration of bridge deterioration through repeated dynamic loading to the bridge. However, due to the numerous challenges inherent to observing the behavior of a moving vehicle (*e.g.*, limitations of traditional cable-based monitoring), vehicle-bridge interaction is difficult to observe in the field setting. The potential of wireless sensors as a mobile sensing platform is leveraged to monitor the dynamics of both a heavy truck vehicle and bridge as the vehicles crosses the bridge. This thesis is one of the first efforts aimed at using wireless sensors to observe vehicle-bridge interaction using heavy truck loading highway bridges instrumented with wireless monitoring systems. Integration of mobile vehicle-based wireless sensor nodes with a static bridge-based wireless monitoring system can provide time-synchronized vehicle-bridge dynamic data which represents a complete set of input-output experimental data for system identifications. However, identification of vehicle-bridge interaction from experimental input-output data is very challenging due to the time-varying loading and complex coupled dynamics between the vehicle and the bridge.

1.5 Organization of the Thesis

The thesis can be delineated into two major parts. The first half of the thesis is focused on wireless sensing technology including field validation of the technology and exploration on its use for monitoring moving loads (*i.e.*, heavy trucks). The second half of the thesis addresses the need for data processing algorithms for system identification. Specifically, subspace system identification methods for black-box state-space model estimation are explored including their physical interpretation. Furthermore, a data processing algorithm for the identification of a structural system under position-changing input is explored to analyze vehicle-bridge interaction experimentally observed in the field. The organization of this thesis is depicted in Fig. 1.1; a brief descriptions of each chapter is introduced as follows:

- Chapter 2 presents an introduction to the wireless sensor platform, *Narada*, which will be used as the primary data collection tool in this thesis. A detailed description of *Narada* is

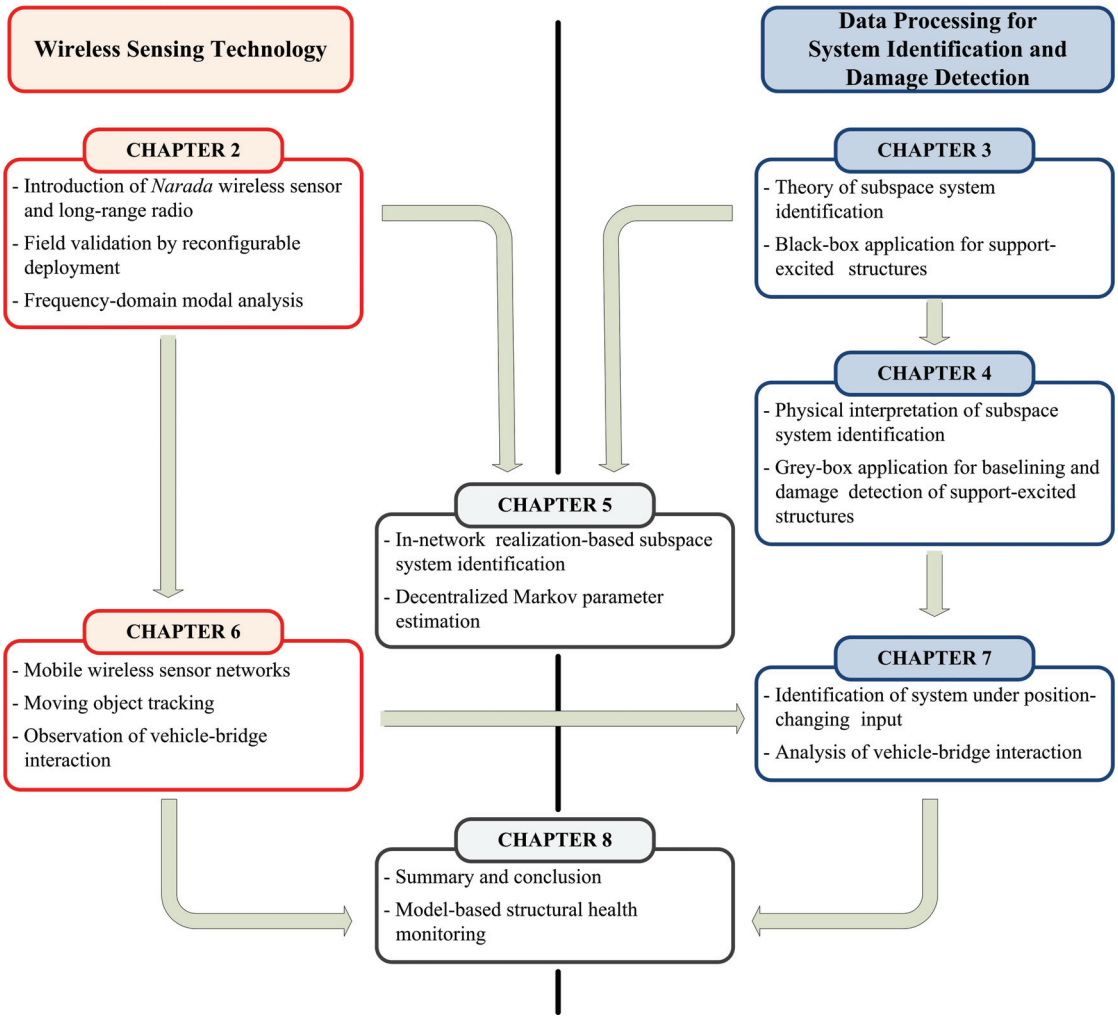

Figure 1.1 Outline of the thesis.

provided, including details about its extended-range radio as well as its embedded software design. Field validation of *Narada* is conducted on a 180-meter long steel-box girder bridge (Yeondae Bridge, Korea) with the monitoring system reconfigured during its use. The truck-induced bridge vibration data collected during testing is used to estimate the modal parameters of the bridge. The modal properties identified will serve as a basis for the study of vehicle-bridge interaction presented in Chapter 7.

● Chapters 3 and 4 discuss the use of subspace system identification. A detailed explanation of the subspace system identification method is reviewed in Chapter 3 with a particular focus on the physical meaning (based on traditional structural dynamics) that can be extracted from

the subspace mathematical procedures. Without considering the physical interpretation of the estimated data-driven system model (*i.e.*, a black-box model), examples of input-output and output-only system identification of support-excited (*i.e.*, seismically excited) structures are presented. Chapter 4 completes the theory of subspace system identification by developing a methodology for physical interpretation of the black-box model to yield a grey-box model of the structural system. The mathematical theory introduced in Chapter 4 allows structural parameters estimated from measured dynamic data to be used to baseline the target structure and to detect damage quantitatively when damage is induced. A six-story steel frame shear structure is used to validate the grey-box model's use for damage diagnosis.

● In Chapter 5, a system identification strategy is presented for in-network execution by a wireless monitoring system. The method aims to balance the accuracy of subspace system identification (Chapter 3) with the scalability of a wireless sensor network (Chapter 2). Decentralized Markov parameter identification in a wireless sensor network is adopted as a sensor-level local data processing algorithm. Through communication of a limited number of estimated Markov parameters, global system identification is conducted by realization-based subspace system identification (*i.e.*, eigensystem realization algorithm). The proposed strategy is evaluated using input-output and output-only data recorded during dynamic testing of a balcony in a historic theater structure.

● In Chapters 6 and 7, vehicle-bridge interaction is explored as the last major topic of the thesis. Chapter 6 presents the experimental observation vehicle-bridge interaction by exploiting the mobility of wireless sensors. The strategy of a single wireless sensing network architecture is discussed for unification of vehicle-based mobile wireless sensors with a static bridge wireless monitoring system. Kalman filtering combined with fixed-interval smoothing is proposed for mobile vehicle tracking. Chapter 7 presents a strategy for system identification for a bridge when the vehicle is a position-changing sprung mass. System identification of the bridge is conducted in two stages: free vibration analysis followed by forced vibration analysis. Furthermore, a combined algorithm of subspace system identification (Chapter 3) and modified prediction error method (Ljung 1999) is utilized and experimentally verified.

● Chapter 8 serves as the conclusion of the thesis, highlighting achievements and key contributions of the thesis. A discussion on future extensions of the research is offered. Lastly, the framework of model-based structural health monitoring is introduced.

CHAPTER 2

MODULAR WIRELESS MONITORING SYSTEM FOR BRIDGES USING AN EXTENDED-RANGE WIRELESS SENSOR

In this chapter, a wireless sensor platform (termed *Narada*) is introduced. To enhance the communication range of the platform an extended-range radio is developed. Since the *Narada* serves as the main data acquisition system throughout the thesis, a detailed explanation of the *Narada* design is given including information about its hardware and software design. Key functional attributes such as time-synchronization accuracy, power consumption, and communication-range are quantified. Field performance of *Narada* is verified during a full-scale dynamic testing of the Yeondae Bridge (Korea). A wireless monitoring system assembled from *Narada* units is deployed to measure the global response of the bridge to controlled truck loading. To obtain acceleration measurements at a large number of locations along the bridge length, the wireless monitoring system is installed three times with each installation concentrating sensors in one localized area of the bridge. The modular installation and reconfiguration of the wireless monitoring system is proven feasible for short-term monitoring of operational highway bridges. Analysis of measurement data after the installation of three monitoring system configurations leads to reliable estimation of the bridge modal properties, including mode shapes.

2.1 Introduction

The monitoring of civil structures is an important step in improving the civil engineering field's understanding of structural behavior under normal and extreme loads (*e.g.,* earthquakes). Monitoring can also provide empirical evidence of the degradation mechanisms that naturally occur in aging infrastructure systems. Currently, structural monitoring is reserved for special

structures (*e.g.,* long-span bridges, hospitals) located in zones of high seismic risk or where strong wind conditions prevail. Even fewer monitoring systems have been deployed for monitoring the health of structures; such systems would be termed structural health monitoring (SHM) systems. Market penetration for structural monitoring remains largely limited by the cost and by the complexity of installing wired monitoring systems in large structures. Wireless sensors have been proposed to alleviate the expense and effort required to install a monitoring system. Since the seminal study of wireless structural monitoring by Straser and Kiremidjian (1998), the state-of-art in wireless sensing has rapidly evolved with many viable wireless sensing solutions available for reliable structural monitoring (Spencer *et al.* 2004; Lynch and Loh 2006). In addition, many academic groups have showcased the potential role that wireless sensors can play in future structural monitoring systems through field implementations in actual operational bridges. A non-exhaustive set of recent field deployments include wireless monitoring of the Alamosa Canyon Bridge, New Mexico (Lynch *et al.* 2004a), Geumdang Bridge, Korea (Lynch *et al.* 2006), Gi-Lu Bridge, Taiwan (Lu *et al.* 2006), Golden Gate Bridge, California (Pakzad *et al.* 2008), Wright Bridge, New York (Whelan and Janoyan 2009), and Jindo Bridge, Korea (Cho *et al.* 2010; Jang *et al.* 2010).

Historically, structural monitoring systems have been viewed as static systems that once installed in a structure are rarely changed or modified. This perspective finds it origin in the fact that wired monitoring systems are challenging to install and modify. However, wireless sensors eliminate the need for wiring and are therefore easier to install than their wired counterparts. Rapid installation renders wireless monitoring systems very attractive for short-term deployments where response data from operational structures is desired over short periods of time (*e.g.*, hours, days, or weeks). For example, short-term monitoring can offer sufficient data from which a rapid condition assessment can be made of an operational bridge (Salawu and Williams 1995). Furthermore, the modularity of the wireless sensors within the monitoring system architecture allows for reconfiguration and modification of the monitoring system topology. Using a small number of wireless sensor nodes, a large number of sensor measurements can be made at many locations in the structure.

In this chapter, a rapid-to-deploy wireless monitoring system is proposed for short-term monitoring of highway bridges. The wireless monitoring system is assembled using a low-cost, low-power wireless sensor node previously developed for monitoring civil engineering structures. The wireless sensor node features a high-resolution sensing interface, a powerful microcontroller core, and a wireless communication interface. To allow the wireless sensor node to achieve adequate communication ranges appropriately scaled to the dimensions of large civil engineering

structures, a modified version of a standard IEEE 802.15.4 wireless transceiver is fabricated for long-range wireless communications. Specifically, a power amplification circuit is coupled with the transceiver to increase the radio output signal by 10 dB. To highlight the utility of a reconfigurable wireless monitoring system, a network of 20 *Narada* wireless sensors are deployed on the Yeondae Bridge (Icheon, Korea). The monitoring system is installed and reconfigured twice in order to achieve three different sensor topologies in the structure. The vertical acceleration response of this 180 m steel box girder bridge is monitored during controlled truck loading for each configuration of the wireless monitoring system. With intentional overlapping of the three topologies, the mode shapes of the Yeondae Bridge are obtained during off-line analysis of the wirelessly acquired acceleration response data. The chapter is structured as follows: first, the *Narada* wireless sensor node is introduced; second, a modified wireless transceiver for extended-range telemetry is integrated with *Narada* and analyzed during range testing; third, a short-term measurement campaign on the Yeondae Bridge using the proposed wireless monitoring system is presented along with measurement results; finally, the chapter concludes with a detailed modal analysis of the bridge conducted off-line using the wireless response data collected.

2.2 Extended-Range Wireless Sensor, *Narada*

The *Narada* wireless sensor (Fig. 2.1) was designed at the University of Michigan for use in smart structure applications including monitoring and feedback control of large-scale civil structures (Swartz *et al.* 2005). Unlike other application areas, the use of wireless sensors in civil structures requires a low-power hardware design that allows a node to survive for long periods of time (*e.g.*, years) on battery or energy harvesting power sources. The large spatial dimensions of civil structures require large communication distances in the hundreds of meters range. In addition, many civil structures exhibit low amplitude vibrations; high-resolution digitization is therefore necessary to ensure sensor outputs characterized by low voltage signals remain well above the quantization error inherent to the analog-to-digital conversion process. Finally, the overall cost of the wireless sensor design should be minimized to ensure that the technology is attractive for commercial adoption. *Narada* has been designed using commercial off-the-shelf embedded system components to achieve a low-power, high-resolution wireless sensing node capable of long-range communication. In comparison to other commercial wireless sensor nodes (*e.g.,* Crossbow Motes, Crossbow iMote, and Moteiv Telos), the *Narada* wireless sensor platform offers true, 16-bit analog-to-digital conversion for the digitalization of sensor data, as well as a modular radio design that supports the use of a power amplified IEEE 802.15.4 radio capable of

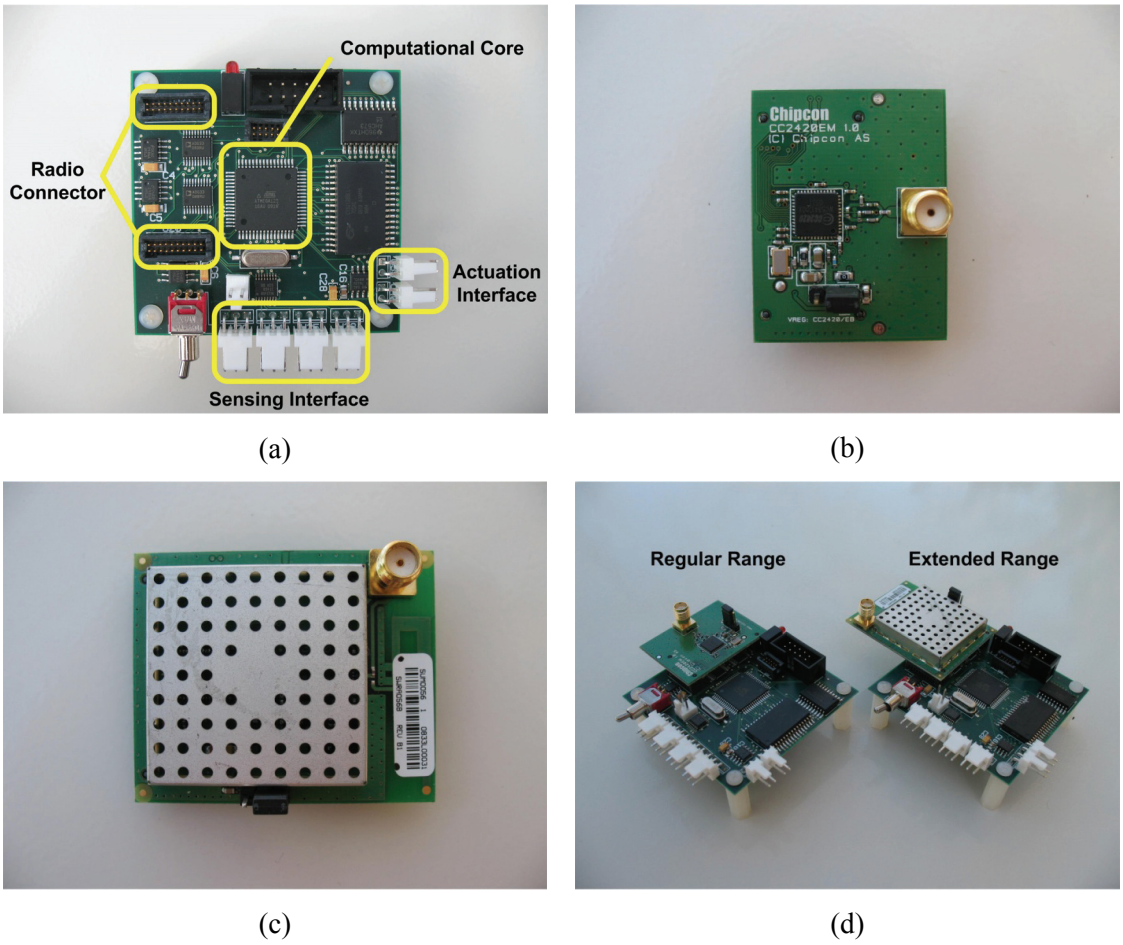

Figure 2.1 *Narada* wireless sensor for structural monitoring: (a) main printed circuit board with four functional blocks specified; (b) standard commercial CC2420 transceiver daughter board; (c) power amplified CC2420 daughter board; (d) fully assembled unit for regular- and extended-range telemetry.

communication ranges in excess of 600 m. Another distinguishing feature of the *Narada* wireless sensor node that is beyond the scope of this chapter is the inclusion of an actuation interface for high speed feedback control of actuators.

2.2.1 Narada Hardware Design

The hardware design of *Narada* encapsulates the aforementioned functionality necessary for effective operation in structural monitoring applications. In particular, the hardware design of the low-power node is decomposed into four functional blocks that support the node's capabilities to sense, communicate, compute, and actuate (Swartz *et al.* 2005). The first two capabilities (*i.e.*, sensing and communication) replicate the functionality of sensors in the traditional monitoring paradigm. However, the inclusion of computing into the wireless sensor node represents a

significant departure from that paradigm since it empowers the wireless sensor node to interrogate raw sensor data individually or collectively with other wireless sensors in a network. In-network data processing (in lieu of communicating high-bandwidth raw data streams) has proven effective in enhancing the reliability of the wireless communication channel while preserving power in battery operated devices (Lynch *et al.* 2004b; Nagayama and Spencer 2007; Rice *et al.* 2008; Zimmerman *et al.* 2008; Jones and Pei 2009; Kijewski-Correa and Su 2009).

For data collection, *Narada*'s sensing interface is designed around the Texas Instruments ADS8341 analog-to-digital converter (ADC). This ADC supports high data rate collection (maximum 100 kHz) simultaneously on four independent sensing channels (Texas Instruments Inc. 2003). The ADS8341 was chosen for the *Narada* design for two reasons. First, it has a high 16-bit digital resolution that is suitable for ambient structural vibration measurements. Second, the ADC can be programmed to collect four channels of single-ended inputs or two channels of differential inputs. While a large fraction of sensors used for structural monitoring are single-ended, some sensors recently proposed for structural monitoring (*e.g.*, the Silicon Designs SD2012 accelerometer) offer superior performance when utilized in differential output mode (Silicon Designs Inc. 2009). After data is collected by the sensing interface, it is passed to the computational core consisting of an embedded microcontroller (Atmel ATmega128) and memory. The ATmega128 is a low-power, 8-bit microcontroller with 128 kB of flash memory (for the storage of programs), 4 kB of electrically erasable programmable read-only memory (for the storage of program constants) and 4kB of static random access memory (for the storage of sensor data). To enlarge the amount of memory available for the storage of sensor data, an additional 128 kB of external static random access memory (SRAM) is included in the sensor design. The physical circuit corresponding to the computational core and sensing interface are combined on the same 4-layer printed circuit board (PCB) (Fig. 2.1-a). While beyond the scope of this work, a 2-channel, 12-bit digital-to-analog converter (Texas Instruments DAC7612) is also included in the *Narada* circuit board to serve as an actuation interface. The *Narada* actuation interface has been previously utilized during wireless structural control studies (Swartz and Lynch 2009). The PCB has been carefully designed to ensure digital circuitry (*e.g.*, microcontroller and memory) and its associated noise does not contaminate the performance of the ADC (*i.e.,* reduce the effective resolution). The PCB design preserves almost the full 16-bit ADC resolution with the quantization error measured to be slightly greater than one bit (*i.e.,* ADC's resolution is estimated to be about 15-bits which corresponds to a quantization error of 0.15 mV relative to the 0 to 5V input voltage range of the ADC).

2.2.2 Modular Radio Boards for Short- and Extended-Range Telemetry

The performance of the wireless structural monitoring system is directly correlated to the performance of the wireless transceivers utilized for communication in the system. While a plethora of transceivers have been previously integrated with various commercial and academic prototypes (Lynch and Loh 2006), the field appears to be converging on transceivers that comply with the IEEE 802.15.4 radio standard. This standard defines a physical (PHY) and medium access control (MAC) protocol layer for low-power, short-range wireless personal area networks (WPAN) such as sensor networks (IEEE 2006). In the design of *Narada*, the popular Texas Instruments CC2420 IEEE 802.15.4 transceiver is selected (Texas Instruments Inc. 2008). The CC2420 operates on the 2.4 GHz band at 250 kbps using direct sequence spread spectrum (DSSS) radio frequency modulation techniques. The transceiver is obtained from the vendor on its own printed circuit board; this daughter board (Fig. 2.1-b) can be easily connected to the main *Narada* circuit board through a standard connector (Fig. 2.1-d).

A particularly useful feature of the CC2420 transceiver is that the output wireless signal can be easily varied from weak to strong; signal strength is set by writing to an internal hardware register on the CC2420. Allowing the user to set the wireless signal strength is a powerful feature of the CC2420. In effect, an end-user can balance communication range and power consumption of the radio. For example, eight discrete levels of radio strength can be selected ranging from 0 to -25 dB. The power consumption of the radio when using a signal strength of 0 dB (long-range) is 57.4 mW. In contrast, when configured to use a signal strength of -25 dB (short-range), the radio only consumes 28 mW. The discrete levels of radio strength and their corresponding power consumption characteristics during transmission are plotted in Fig. 2.2 (Kim *et al.* 2010c). It is difficult to prescribe a precise range to each of these output signal strengths since communication range is a function of the output power, antenna type, antenna location, as well as many other environmental parameters (Bensky 2004). However, under favorable conditions, an output power of -25 dB would offer short communication ranges (10's of meters) while a 0 dB power level could achieve ranges in excess of 100 m.

In civil engineering applications, the size of the instrumented structure often necessitates that data be transmitted distances in the hundreds of meters. Therefore, the short communication range offered by the standard CC2420 transceiver could require the deployment of a multi-hop wireless sensor network in which data is "hopped" from node-to-node until it reaches its intended recipient. However, the redundant data transmission in multi-hop networks consumes precious communication bandwidth thereby limiting the effective throughput of the network as a whole (Raghavendra *et al.* 2004). Where data throughput is critical, bandwidth may be recovered by

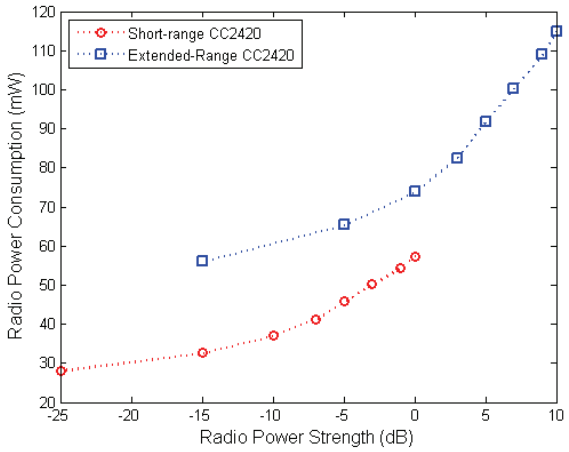

Figure 2.2 CC2420 power consumption during transmission for discrete levels of radio signal strength.

increasing the transmission range of individual units. Increased range can be achieved by increasing the transmitted signal strength. One means of increasing signal strength is to adopt specialized antennas such as high-gain, directional antennas where the signal is concentrated in a radio frequency (RF) beam oriented in a specific direction. Another approach is to amplify the signal output.

In this study, a power-amplified CC2420 transceiver circuit (Fig. 2.1-c) fabricated to fit the *Narada* radio interface is adopted (Grini 2006). This extended-range transceiver amplifies the CC2420 output signal by 10 dB using a power amplifier circuit between the CC2420 chip and the antenna connector. In the United States, the power amplified CC2420 still operates below the Federal Communications Commission (FCC) permissible power level of 1 W. To achieve the 10 dB gain in signal strength, the power-amplified circuit consumes twice the current of the standard CC2420 transceiver board when transmitting. The radio strength of the extended-range radio and its corresponding power consumption characteristics when transmitting are plotted in Fig. 2.2. When the extended range radio is idle, the power amplification circuit only draws 6 mW of power. The short-range and extended-range radios are modular components that can be swapped using the same underlying *Narada* circuit board as shown in Fig. 2.1-d. This design approach allows the end-user to select the CC2420 transceiver board that best meets their range requirements and energy budgets (in the case of battery operated devices).

2.2.3 Embedded Software Design

An embedded operating system has been custom written for the *Narada* wireless sensor node. The role of the operating system is to simplify the operation of the wireless sensor for end-users and to provide an intermediate software layer between hardware and software written for data interrogation purposes. Data acquisition (DAQ) modules have been written for the embedded operating system to provide *Narada* with the capability of two types of data collection: 1) real-time continuous data streaming or 2) buffer-burst data transfer. For each type of collection method, the DAQ package included in the embedded operating system is written to collect data from the node ADC and to wirelessly transmit the data to a desired location including to a laptop personal computer (PC) serving as a remote data repository. In this study, a centralized PC will be utilized to coordinate the activities of the wireless monitoring system and to serve as a single repository of measurement data. A text file containing DAQ parameters is created by the user, processed by an executable server program running on the PC, and wirelessly transmitted to the network over a CC2420 development board connected to the PC serial port. This text file includes parameters such as the desired system mode of operation (*e.g.*, continuous data streaming versus buffer-burst data transfer), identification numbers of the *Narada* nodes to use, *Narada* ADC sensor channels to use, sampling frequency (up to 10 kHz), sampling time (dependent on the sampling frequency), and number of samples to buffer locally before transmitting in the buffer-burst mode of operation (up to 30,000 samples).

Real-time continuous data collection is designed to allow for indefinite data collection by the network of wireless sensors with nodes regularly sending their data to the repository. There are practical limitations on the total number of sensing channels that may be included in a network designated to run in the continuous data streaming mode. In effect, the wireless sensor network is limited by the available bandwidth on a specific channel of the IEEE 802.15.4 radio spectrum (2.4 GHz). Access to the shared wireless channel is controlled by a time-division multiple access (TDMA) scheme in which each sensor is queried by the server at a specified time for data locally stored in its memory bank. Once data is successfully transmitted, it can be overwritten by the node. However, this method is only reliable if the server has sufficient time to collect locally buffered measurement data before the memory bank fills to capacity. Given the number of sensor channels in the monitoring system and the sampling rate, the server can determine before data collection if the network has enough time to collect data from each node before the local buffer must be overwritten. If the server determines *a priori* that there is a risk of losing data (due to too many channels collecting data at too fast of a sampling rate), it will stop the data collection process and alert the end user. For example, the system sampling at 100 Hz will only be able to collect data from 15 sensor channels before data transmission between the wireless sensors and

the PC would require more time than the time it takes to completely fill the local memory at the sensor nodes. To increase the total number of sensor channels in the monitoring system, one approach is to divide the network of *Narada* nodes into separate channels in the 2.4 GHz spectrum (16 channels are available); each channel can then be concurrently serviced by the PC using separate receivers (Swartz and Lynch 2009).

If a user wishes to collect data from more nodes than can be accommodated in continuous data collection mode, buffer-burst mode can be adopted. This model will only collect data for a short period and waits for data to be collected by the system modes before communicating data to the repository. In buffer-burst mode, the PC commands the network of wireless sensors to collect a fixed number of data points, store the data in memory (up to 60,000 data points), and stop data collection. The PC server then would query each sensor, one at a time, to retrieve the measurement data that is locally stored after data collection has ceased. In this approach, there is no theoretical limit on the number of channels that can be collected at one time by the monitoring system.

Another challenge inherent to wireless sensing is time synchronization of individual nodes operating in the wireless network (Raghavendra *et al.* 2004). Unlike in traditional wired monitoring systems where a single ADC is used in a multiplexed fashion to sample multiple sensor channels, a wireless sensor network is composed of multiple ADCs each being timed by a local clock. Precise time synchronization of the independent clocks must take place using the communication media and will be dependent upon the propagation and processing of synchronization messages broadcast between wirelessly networked nodes. Errors in synchronization between data streams lead to corruption of the phase information contained in the data signals. This can adversely affect the accuracy of some processing algorithms commonly associated with modal analysis (Ginsberg 2001), input-output or multiple-output modeling (Lei *et al.* 2005), or feedback control (Lian *et al.* 2005). This task is made more difficult in wireless networks where signal propagation times are stochastic and direct communication between all units in the network may not be possible (Raghavendra *et al.* 2004). Only recently have elegant strategies for accurate time synchronization have been reported (Nagayama and Spencer 2007; Yan *et al.* 2009).

In the embedded operating system of *Narada*, time synchronization is achieved through the use of beacon signals. Prior to data collection, the *Narada* wireless sensors in the monitoring system are notified of a pending data collection request. Upon receipt of this notification, each node goes into standby mode waiting to receive a beacon packet from the PC. Assuming the receipt of the beacon packet occurs at the same time in all of the nodes, a start time is established,

and the data collection process initiated. However, small synchronization errors can result from beaconing due to different signal propagation and packet processing times. The differential signal propagation times are stochastic, but are limited by the signal propagation range of the system. For example, if a node is 1 km from the PC server, the time for the beacon to travel (based on the speed of light) is as large as 3.3 μs (a rather negligible number when considering the fact that sampling frequencies in structural monitoring systems are generally less than 1 kHz). More significant is the differential processing time. The synchronization error from differential processing can be minimized by limiting the actions of the wireless sensors prior to the start of a data collection run. In *Narada*, the node is placed in a wait state (composed of a "while" loop) that repeats the execution of four assembly instructions. The wait state is terminated when the PC server beacon packet is received by the node. This practice limits the differential processing time to at most, four clock cycles on the ATmega128 microcontroller plus any delays in wireless transceiver processing in the CC2420 transceiver.

Since the time synchronization error is stochastic, it must be experimentally quantified. The synchronization error due to the differential processing time has been characterized experimentally by use of multiple, collocated sensing nodes programmed to raise a digital logic line when the first data point is ready upon reception of the system start beacon. The differential processing time is then measured on a digital oscilloscope (Agilent 54621D) during repeated measurements. The average differential processing time synchronization error on *Narada* is found to be a Poisson distribution with a mean of 7.4 μs and peak observed value of 30 μs. The distribution of these errors is depicted in Fig. 2.3. Considering 200 Hz as a typical sampling frequency for civil engineering applications, these results indicate a maximum synchronization error of less than 1 % of a typical time step on the *Narada* system.

2.3 Performance Assessment of the Extended-Range Wireless Transceiver

The performance of the extended-range IEEE 802.15.4 wireless transceiver is quantified by conducting range testing in an outdoor paved lot. Special embedded software is written for the *Narada* wireless sensor node where one wireless sensor transmits data packets that are then received by a PC server. The strength of the *Narada* radio signal is recorded using the radio signal strength indicator (RSSI) that is appended to each packet header received by the transceiver. To understand how the performance of the radio varies as a function of range, the test is repeated with the wireless sensor placed at varying distances away from the PC server. A total of four tests are conducted using a *Narada* wireless sensor node placed 50 cm above the surface of the ground:

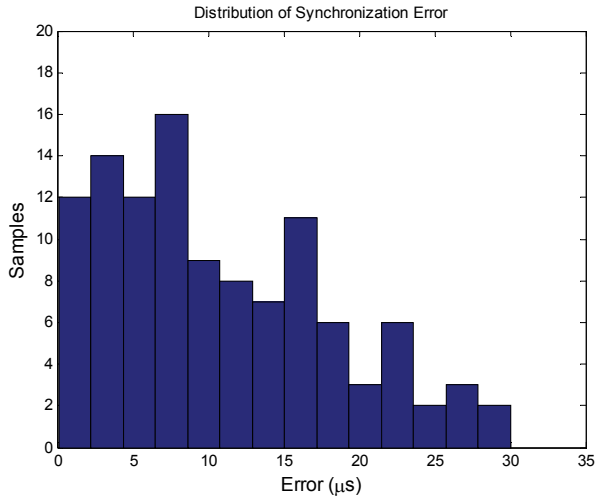

Figure 2.3 Histogram of the measured differential beacon time synchronization errors experimentally obtained in a *Narada* wireless sensor network (a total of 111 samples collected).

i. A *Narada* wireless sensor node with a standard-range IEEE 802.15.5 transceiver integrated is used during range testing. An omni-directional swivel antenna (Antenova Titanis) is used as the radio's primary antenna.

ii. A *Narada* wireless sensor node with an extended-range IEEE 802.15.5 transceiver integrated is used during range testing. An omni-directional swivel antenna (Antenova Titanis) is used as the radio's primary antenna.

iii. A *Narada* wireless sensor node with a standard-range IEEE 802.15.5 transceiver integrated is used during range testing. A directional antenna (D-Link DWL-M60AT) is used as the radio's primary antenna.

iv. A *Narada* wireless sensor node with an extended-range IEEE 802.15.5 transceiver integrated is used during range testing. A directional antenna (D-Link DWL-M60AT) is used as the radio's primary antenna.

First, the omni-directional antenna is used with the standard- and extended-range IEEE 802.15.4 transceivers. The omni-directional antenna radiates radio frequency (RF) energy in all directions from the *Narada* wireless sensor node. The test results are plotted in Fig. 2.4-a; the signal strength of the standard-range radio drops quickly at around 200 m with communication failures experienced. However, the extended-range radio operates at 300 m due to its enhanced signal strength. Next, the directional antenna is used with *Narada* nodes with the standard- and extended-range radios integrated. The directional antenna concentrates the RF energy into a

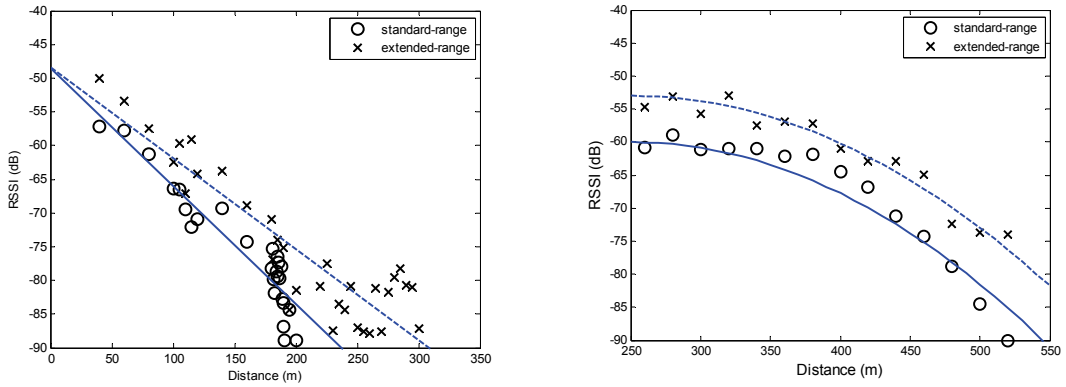

Figure 2.4 Range testing of the *Narada* wireless sensor: (a) RSSI of the standard- and extended-range radios using an omni-directional antenna; (b) RSSI of the standard- and extended-range radios using a directional antenna.

specific beam direction; the concentration of RF energy in a single direction should result in higher RSSI measurements and with greater communication ranges. Fig. 2.4-b shows the results focusing on ranges greater than 250 m. The signal strength of the extended-range radio is roughly 10 dB greater than that of the standard-range radio. It can be concluded that the communication range of the standard-range radio is around 500 m. However, performance range of the extended-range radios is expected to be more than 600 m.

In general, the 10 dB gain achieved by the extended-range radio results in at least 100 m of additional range for the case of both antennas (omni-directional and directional). However, it should be noted that this added range does come at the cost of increased power consumption by the radio. When maximum communication range is necessary, the range tests reveal that the best antenna to use with *Narada* is a directional antenna. While impressive communication ranges are achieved with a directional antenna, the wireless sensor node is only capable of communication in one direction. While acceptable in a hub-spoke network architecture, directional communication is less attractive in multi-hop mesh network architectures.

2.4 Validation of the Reconfigurable Wireless Monitoring System on the Yeondae Bridge

To validate the performance of a reconfigurable wireless monitoring system designed from *Narada* wireless sensors, full-scale dynamic testing is conducted on an operational highway bridge. The Yeondae Bridge, located in Icheon, Korea along the Korea Expressway Corporation

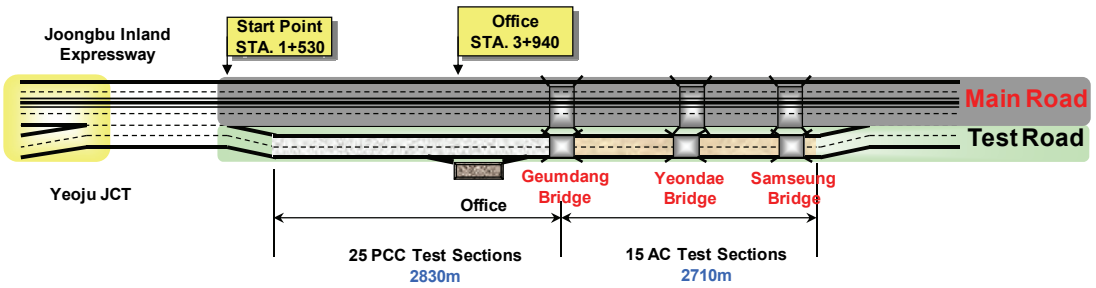

(a)

(b) (c) (d)

Figure 2.5 Korea Expressway Corporation (KEX) test road: (a) layout of the test road; (b) Yeondae Bridge (180 m); (c) Geumdang Bridge (273 m); (d) Samseung Bridge (40 m).

(KEX) test road is selected. The monitoring system is installed and reconfigured multiple times during forced vibration testing of the bridge using a heavy truck.

2.4.1 Yeondae Bridge in the Korea Expressway Corporation Test Road

The Korea Expressway Corporation (KEX) has constructed a 7.7 km test road (Fig. 2.5) along the Jungbu Inland Highway in the vicinity of Icheon, Korea (Kim *et al.* 2009). The test road is a redundant section of the two lane southbound Jungbu Inland Highway that can be opened and closed to highway traffic. The test road was constructed to develop a mechanistic-based design guide for pavement systems in Korea by monitoring the performance of two types of pavement systems (*i.e.*, Portland cement concrete (PCC) and asphalt concrete (AC)) under normal truck loads (Lee *et al.* 2004). To monitor the behavior of pavement systems under traffic and varying environmental conditions, a combination of strain gages, soil pressure sensors, thermocouples, and crack displacement gages are installed along the length of the test road; in total, 1897 sensors are installed within the test road. Along the length of the test road are two medium-span highway bridges (*i.e.*, Geumdang and Yeondae Bridges) and one short-span highway bridge (*i.e.*, Samseung Bridge). Despite the existence of the pavement monitoring system along the test road, the bridges are not instrumented with sensors. Rather, the KEX has

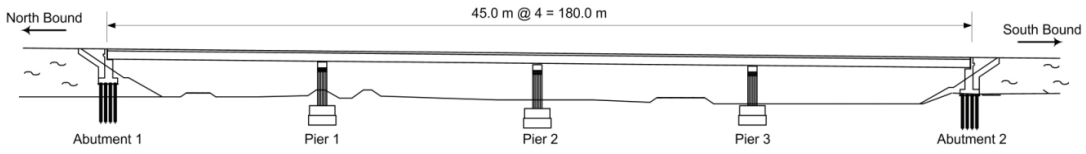

(a)

(b)

(c)

Figure 2.6 Yeondae Bridge: (a) profile schematic of the bridge; (b) perspective view at the northern abutment (the curved plan is evident); (c) view at the top road surface.

partnered with the Smart Infrastructures Technology Center (SISTeC) to install new structural health monitoring (SHM) technologies on the test road bridges. A large number of studies focused on the installation of sensors on the three highway bridges have been reported in the literature (Lee *et al.* 2004; Lynch *et al.* 2006; Lee *et al.* 2007; Koo *et al.* 2008).

Of the three bridges available, the Yeondae Bridge (Fig. 2.6) is selected for validation of the reconfigurable wireless structural monitoring system. The bridge is 180 m long and is slightly curved at one end (with a radius of curvature of 1718 m). Along the length of the bridge are three concrete piers that divide the bridge into four identical spans each 45 m long. To safely accommodate vehicles driving along the curved sections of the bridge, the road has a varying cross-sectional slope from 2.75 % to 4 %. The bridge also has a large skew angle of 40º at both ends.

The cross section of the bridge consists of two partially-closed trapezoidal steel box girders. The boxes are 2.2 m tall with top and bottom widths of 3.1 m and 2.1 m, respectively. The concrete deck is 27 cm thick and is designed to act in composite action with the steel box girders. The design of the top flange of the steel box girder varies depending on the flexural moment imposed on the section. At the middle of each span (where positive bending moment occurs), the steel box girders are open at their tops, a detail that forces the concrete deck to take the full

compressive stress of the bridge section. In contrast, the steel box girders are closed on the supports in order to impose the tensile stress to the top flange of the girder rather than in the concrete deck. The Yeondae Bridge is the first example of a partially-open steel box girder bridge in Korea. Due to the unique geometric and structural design features of the Yeondae Bridge, it is anticipated that the bridge will exhibit unique modal properties. To accurately identify these modal properties, a dense instrumentation of vibration sensors will be required during monitoring of the bridge. Later in this thesis, the Yeondae Bridge will be again used to study vehicle-bridge interaction. The modal analysis conducted in this chapter will play a critical role in the modeling of vehicle-bridge interaction as presented in Chapter 7.

2.4.2 MEMS Accelerometers and Signal Conditioning

To measure the vertical acceleration of the bridge, two different types of microelectromechanical system (MEMS) accelerometers are adopted for integration with the *Narada* wireless sensor nodes: 14 Crossbow CXL02 accelerometers and 6 PCB Piezotronics 3801D1FB3G accelerometers. Both accelerometers are capacitive-type MEMS accelerometers and are commercially fabricated using standard micromachining methods in a clean-room environment. Compared to other accelerometer types (*e.g.*, piezoelectric or force-balanced), these capacitive MEMS accelerometers are relatively inexpensive, costing $300 or less. The CXL02 accelerometer has an acceleration range of ±2 g, noise floor of 0.5 mg, and sensitivity of 1 V/g. The 3801D1FB3G is a ±3 g accelerometer with a 0.15 mg noise floor and 0.7 V/g sensitivity. Both accelerometers are powered by 5 V and output an analog voltage signal between 0 and 5 V (with 2.5 V corresponding to 0 g).

The low noise floors associated with both MEMS accelerometers are determined to be slightly below the quantization error inherent to the 16-bit ADC (with an effective resolution of 15-bits). Hence, amplification of the accelerometer outputs can drastically improve the signal-to-noise ratio of the digitized acceleration signals. In order to overcome the reduced resolution of the 16-bit ADC, the outputs of the MEMS accelerometers were amplified by a factor of 20 using a custom-designed amplification board (Lynch *et al.* 2006; Wang *et al.* 2007). The signal conditioning board also includes a band-pass filter with a pass-band of 0.014 to 25 Hz. The band-pass filter rejects high frequency electrical noise and serves as an anti-aliasing filter for the acceleration signals.

2.4.3 Deployment of the Wireless Monitoring System

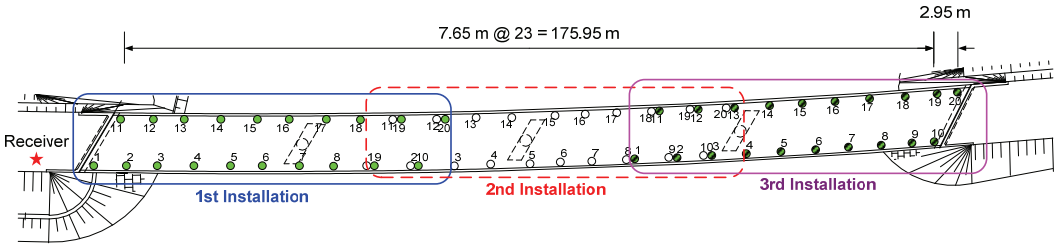

(a)

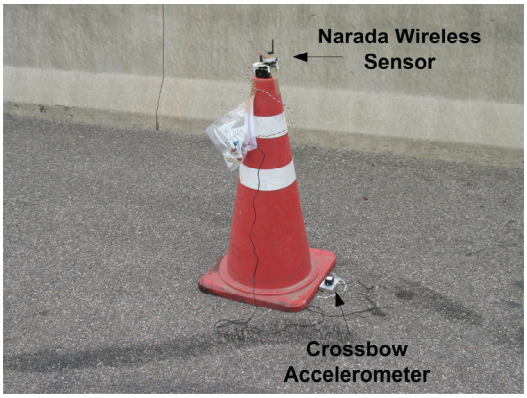

(b)

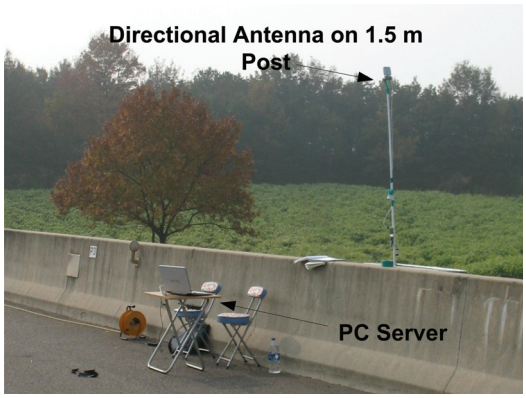

(c)

Figure 2.7 Wireless monitoring system installed on the Yeondae Bridge: (a) installation of 20 *Narada* wireless sensors in three separate topologies on the bridge; (b) *Narada* wireless sensor with omni-directional antenna installed upon a traffic cone; (c) receiver station with directional antenna installed on a 1.5 m tall post for improved communication performance.

In this study, 20 *Narada* wireless sensor nodes are utilized with one single-axis accelerometer (Crossbow CXL02 or PCB 3801D1FB3G) interfaced to each node. Each accelerometer is mounted directly to the surface of the bridge deck to measure the vertical deck acceleration (see Fig. 2.7-b). In order to realize a very dense sensor network along the 180 m long bridge, a reconfiguring strategy was adopted with the system modified twice after the initial deployment. Instead of installing all 20 wireless sensors across the entire length of the bridge, the system is first deployed with a dense instrumentation of sensors (7.65 m separation between each sensor) concentrated along the northern one-third of the bridge span with 10 units on each side of the bridge (Fig. 2.7-a). To improve the performance of wireless communications, each wireless sensor node was placed on top of a 56 cm tall rubber traffic cone with the accelerometer (which is bonded to the road surface) connected to each node via a short shielded wire (Fig. 2.7-b).

One of the main advantages of wireless sensors is their mobility; in this study, this mobility is exploited to facilitate reconfiguration of the monitoring system. After dynamic testing with the

first installation, the 20 wireless sensor-accelerometer pairs are relocated to the center sections of the bridge, as shown in Fig. 2.7-a. Since modal analysis will be conducted using the response data collected, four sensor locations are kept the same between the first and second system configurations. This intentional overlap between the two separate installations will allow the bridge response to be compared between separate excitation events and to permit the stitching together of global mode shapes. After data is collected by the second installation, the system is again reconfigured to form a third installation that records the response of the southern-most portion of the Yeondae Bridge (Fig. 2.7-a). Due to the absence of cabling work, each sensor installation takes less than one hour to complete. By the end of this test, this reconfiguring strategy results in a dense nodal configuration with wireless sensors installed in 50 different locations along the bridge length.

A receiver (using a directional antenna) is attached to a PC server so that the server can operate the network and collect data from individual wireless sensor nodes deployed along the deck of the bridge. The PC server consists of a laptop computer with a Chipcon CC2420 transceiver attached to its serial port. The PC server is positioned in a fixed location near the northern abutment of the bridge (Fig. 2.7-c). This location commands a line-of-sight view of every wireless node on the bridge deck. Reliable communication is anticipated between the receiver and the furthest deployed *Narada* node (which is using a directional antenna and extended-range radio) during the 3rd installation because the maximum communication distance between them is less than 180 m. During the 1st system installation, sensors closest to the receiver (nodes S1 through S5 and S11 through S14) utilize omni-directional antennas attached to the extended-range radio. For the other sensor locations along the bridge deck, directional antennas are attached to the *Narada* extended-range radio.

2.4.4 Forced Vibration Bridge Testing

During the time of testing, the KEX closes the test road to regular traffic so that forced vibration testing of the Yeondae Bridge can be conducted using controlled truck loading. Forced vibration tests are conducted using a 3-axle truck (Fig. 2.8) with a total weight of 25 tons (measured at a local weigh station prior to arrival at the bridge site). Considering the fact that the truck speed is a key factor in the excitation of bridges (Cantieni 1983), this study explores different truck speeds varied from 30 to 70 km/hr in increments of 10 km/hr (*i.e.,* 30, 40, 50, 60, and 70 km/hr).

For each installation of the wireless monitoring system, the truck is driven over the bridge at each of the five truck speeds. Each time the truck is driven over the bridge, the wireless

Figure 2.8 Vibrations introduced into the Yeondae Bridge using a heavy 3-axle truck driving at constant speeds over the bridge.

monitoring system records the vertical acceleration response of the deck at a sample rate of 100 Hz in a buffer-burst data collection mode. Prior to the truck's entry onto the bridge, the PC server in the wireless monitoring system time synchronizes the nodes and initiates the data collection process by broadcasting a beacon signal. A total of 90 seconds of acceleration data is collected by the wireless monitoring system during each bridge crossing by the truck. The 90 sec acceleration time history record collected at each wireless sensor is stored in memory prior to communication to the PC server. With each measurement point collected as a 16-bit digital number, the 90 sec time history record occupies 18 kB of memory which is only 14 % of the random access memory available on the *Narada* node. Once the data collection task is completed, the central PC server queries each wireless sensor one-by-one for measurement data.

In total, 15 separate dynamic tests are conducted during the measurement campaign on the Yeondae Bridge. Specifically, the truck is driven across the bridge at five different speeds for each configuration of the wireless monitoring system. Fig. 2.9 presents a typical measured response of the bridge for sensor location S1 through S10 (Fig. 2.7-a) for the first sensor network installation. Fig. 2.9-a corresponds to the response of the bridge (at S1 through S10) resulting from the truck crossing the bridge at 30 km/hr, while Fig. 2.9-b corresponds to the truck crossing at 70 km/hr. The wireless monitoring system collects data for 90 seconds which is sufficient to completely capture the response of the bridge regardless of the truck speed. During data collection, no data loss is encountered revealing the robustness of the wireless communications in

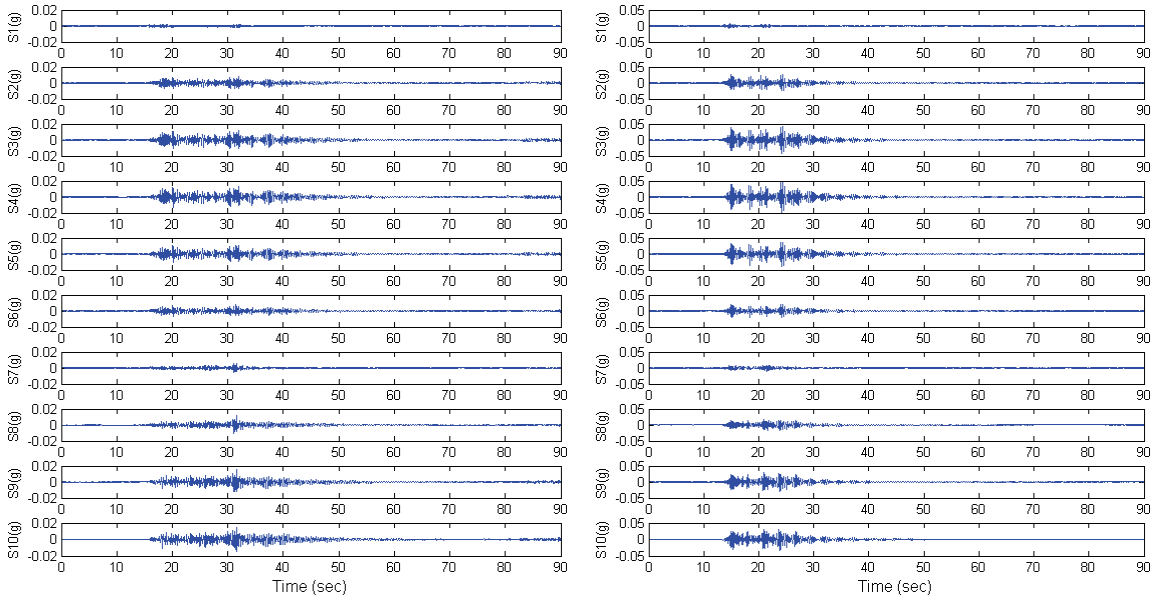

(a) (b)

Figure 2.9 Acceleration response of the Yeondae Bridge measured at the first sensor installation: (a) 30 km/hr truck speed and (b) 70 km/hr truck speed. Sensor number (S1 through S10) corresponds to the number presented in Fig. 2.7-a.

the *Narada* wireless sensor network. As can be observed in the time history plots, the acceleration response for each truck crossing is time synchronized with the initiation of bridge response occurring at the same time. As expected, larger levels of acceleration are observed when the truck is driven over the bridge at higher speeds.

2.5 Modal Analysis by Frequency Domain Decomposition

Modal analysis is conducted on the bridge response data to derive mode shapes. The extraction of mode shapes represents one form of system identification of the Yeondae Bridge. These system properties will play a more vital role later in this thesis when the interaction between the vehicle and bridge will be analyzed in Chapter 7. Hence, the frequency domain decomposition (FDD) method is used for mode shape estimation, because it is an output-only modal analysis method. While some information is known about the bridge loading (*e.g.,* the weight and speed of the truck), only measurements of the bridge response (*i.e.*, system output) are available for analysis.

2.5.1 Frequency Domain Decomposition

FDD is an output-only version of the complex mode indication function (CMIF) method (Peeters and Ventura 2003) which is a sophisticated frequency domain modal identification method that is capable of accurately identifying the real and imaginary components of closely spaced modes. Output-only system identification is theoretically valid under the assumption of a broadband, white noise input. Broadband inputs excite every vibrational mode of the system with identical intensity due to their infinite frequency bandwidth and constant spectra. Therefore, system identification can still be conducted using broadband excitations despite ignorance of the specific input time history record. Since the early 1980's, the decomposition of output spectra using singular value decomposition (SVD) has been studied (Shih *et al.* 1988; Peeters and Ventura 2003) to decompose system frequency response functions (FRF) identifing complex-valued modes using input-output data sets. Later, Brinker *et al.* (2001) reformulated their approach by using the power spectral density (PSD) functions of the system output; the approach was named frequency domain decomposition or FDD. The approach offers a robust method of extracting mode shapes of a structure when excited by a broad-band excitation source.

The power relationship between the system input, $u(t)$, and the measured output, $y(t)$, can be expressed in the frequency domain as follows:

$$G_{yy}(j\omega) = H(j\omega)\, G_{uu}(j\omega)\, H^{H}(j\omega) \tag{2.1}$$

where $G_{uu}(j\omega)$ is the power spectral density (PSD) matrix of the input, $G_{yy}(j\omega)$ is the PSD matrix of the output, $H(j\omega)$ is the FRF matrix of the structural system, and $H^{H}(j\omega)$ is the complex transpose conjugate of $H(j\omega)$. If the input $u(t)$ is ideal white noise, then $G_{uu}(j\omega)$ can be considered constant in an infinite frequency range; hence, the output PSD, $G_{yy}(j\omega)$ directly reflects the product of FRFs, $H(j\omega)H^{H}(j\omega)$ (*i.e.*, the system power characteristics). By using SVD, the output PSD matrix can be decomposed into singular vectors and singular values. It is singular vectors corresponding to large singular values (modal frequencies) that are strongly correlated to the mode shapes of the structure.

2.5.2 Data Partitioning prior to the Application of FDD

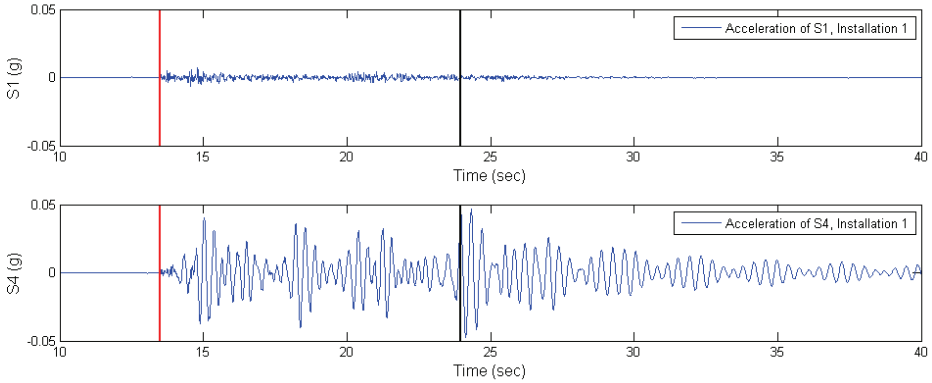

Figure 2.10 Acceleration response of the Yeondae Bridge for the 70 km/hr truck at sensor locations S1 (top) and S4 (bottom) in the 1st installation of the monitoring system. The two vertical lines correspond to the estimated time when the truck enters and exits the bridge.

Some challenges associated with the application of the FDD method are first identified prior to its use for identification of the Yeondae Bridge mode shapes. Specifically, the FDD method is based on the estimated output PSD function which is only valid for a stationary stochastic process. Unfortunately, dynamic bridge testing using a single moving truck does not represent a stationary stochastic process since the truck is moving, thereby experiencing a time-varying coupling with the bridge widely known as vehicle-bridge interaction. However, the free vibration response of the bridge after the truck has left the bridge can be considered a stationary stochastic process. Thus, in this study the free vibration response of the bridge is used exclusively during modal analysis.

The full time history response collected by the monitoring system is delineated into two portions (*i.e.*, forced and free vibrations). Forced vibration corresponds to the portion of the acceleration time history record when the truck is on the bridge. After the truck has exited the bridge, the bridge continues to vibrate due to its free vibration behavior. Fig. 2.10 shows the acceleration time history response of the Yeondae Bridge corresponding to the 70 km/hr truck excitation measured at sensor locations S1 and S4 in the first sensor network installation. In Fig. 2.10, two vertical lines are superimposed on the two time history plots to denote the arrival and exit times of the truck on the bridge. Given the location of sensor S1 (it is only 0.55 m away from the expansion joint between the bridge deck and the northern bridge approach), it can be used as a trigger sensor from which the time of the truck first entering the bridge can be identified. It should be noted that because the Yeondae Bridge is supported on elastomeric pads (which act mechanically like low-pass filters isolating vibration from the span surroundings), determination

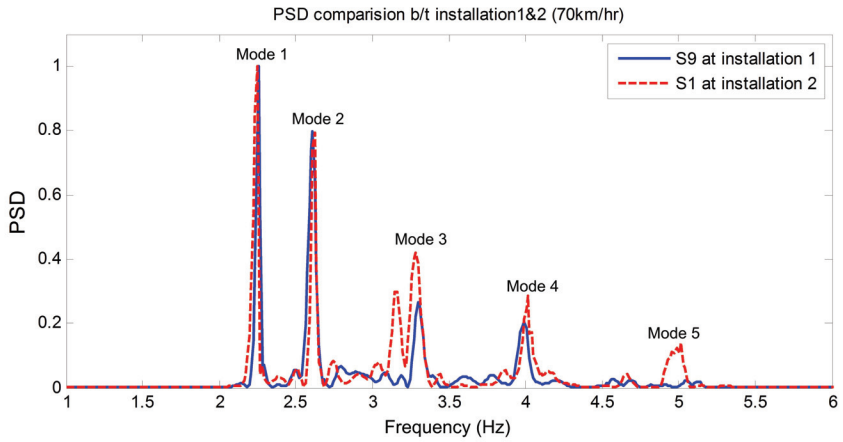

Figure 2.11 Power spectral density function at sensor location S9 (1st installation) and S1 (2nd installation) for the free vibration response of the Yeondae Bridge. It should be noted that the two sensor locations are collocated.

of truck arrival times based on threshold detection should be fairly accurate. The exiting time calculated from the known bridge length and established truck speed is recognized to only be a rough approximation of the exit time of the truck. To proceed with modal analysis, the free vibration response of the bridge well after the estimated exit time of the truck is used for modal analysis by the FDD method. This approach to partitioning the measured bridge response is executed on the entire data set (*i.e.*, on every data record collected during the 15 separate dynamic tests).

2.5.3 Application of the FDD Method

In this study, the free vibration response of the bridge is used for extraction of the bridge modal frequencies and mode shapes. Before mode shapes can be estimated, the modal frequencies of the bridge must be identified. A peak picking approach for estimation of modal frequencies is adopted. As shown in Fig. 2.11, power spectral density functions obtained from the free vibration response of two collocated sensors at location S9 (1st installation) and S1 (2nd installation) are plotted. The PSD function calculated for each sensor location was improved by using a Hanning window on the time-history data prior to the use of the fast Fourier transform (FFT) algorithm. In addition, repeated Fourier spectra calculated from time-history records with 50% time-domain overlap are averaged. This approach to improving the PSD spectra provides a good trade-off between the reduction of noise and the distinctive qualities of the modal peaks (Oppenhiem and Schafer 1999). Based on the PSD plots, the first five modal frequencies of the bridge are identified at 2.25, 2.64, 3.34, 4.00, and 4.88 Hz.

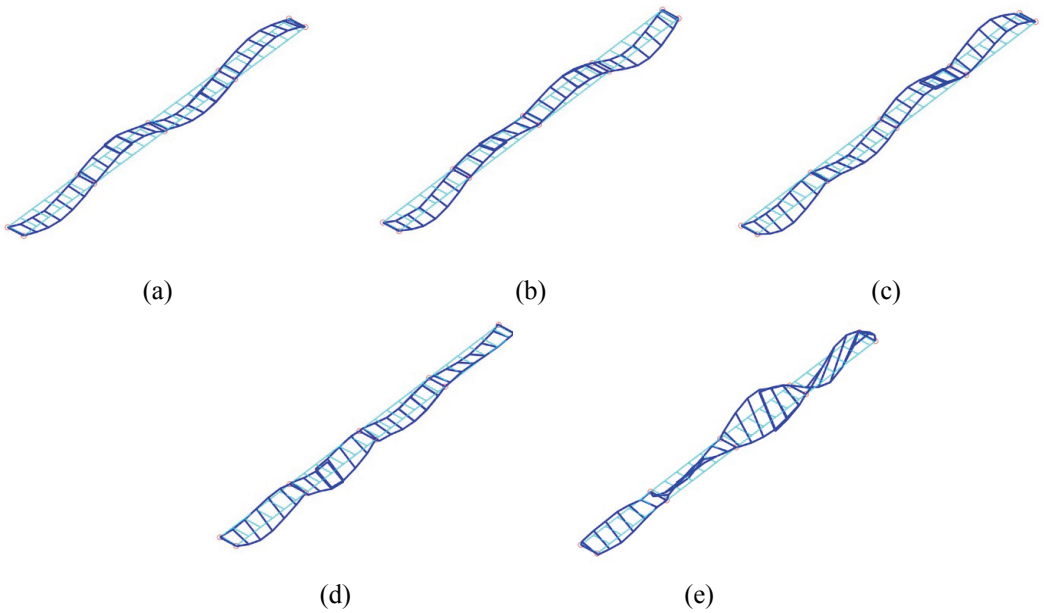

Figure 2.12 Five estimated mode shapes of the Yeondae Bridge: (a) 2.25 Hz, (b) 2.64 Hz, (c) 3.34 Hz, (d) 4.00 Hz, and (e) 4.88 Hz.

Using the estimated PSD functions, the mode shapes of the Yeondae Bridge are estimated by the FDD method for each network configuration. Then, the mode shapes calculated for the three separate network installations are stitched together. Specifically, the local mode shape corresponding to one system installation is scaled (by a scalar constant) relative to the local mode shape of the next installation such that the sum of the differences between the mode shape values at the overlapping nodes is minimized. Fig. 2.12 depicts the first five modes identified (2.25, 2.64, 3.34, 4.00, and 4.88 Hz). Of the five modes extracted, the first three modes are pure flexure modes (2.25, 2.64, and 3.34 Hz) and the last mode (4.88 Hz) is a pure torsion mode. The fourth mode (4.00 Hz) appears to be a combined flexure and torsion mode. The first three mode shapes are flexural bending modes that also correspond to modes calculated off-line using a finite element model of the bridge (Kim *et al.* 2009). The fifth mode is a torsional mode that is also in strong agreement with the finite element model. These results, including strong agreement to the modes estimated by finite element analysis, prove the quality of the data collected by the wireless monitoring system and the accuracy of the off-line modal analysis by FDD.

2.6 Chapter Summary and Conclusions

In this chapter, an extended-range *Narada* wireless sensor is proposed for structural monitoring applications. Power amplification of the output of an IEEE 802.15.4 transceiver (*i.e.,* Texas Instruments CC2420) led to a 10 dB gain in the radio signal strength resulting in improved wireless communications in large-scale structures, such as medium-span highway bridges. Twenty extended-range *Narada* wireless sensors are deployed for short periods of time on the Yeondae Bridge to measure the bridge acceleration response to truck loading. The mobility of the wireless sensors is leveraged to reconfigure the wireless monitoring system to attain three network configurations that capture the complete response of the bridge at 50 different measurement locations. For each of the three network configurations, a 3-axle truck weighing 25 tons is driven across the bridge at speeds ranging from 30 to 70 km/hr. Rapid installation and reconfiguration of the wireless monitoring system is proven feasible for short-term monitoring of operational highway bridges. The installation and reconfiguration of the monitoring system took about 1 hour to complete. The performance of the extended-range radio integrated with each *Narada* node proves robust with nearly 100% data delivery rates during three consecutive days of testing. In addition, time synchronization using a beacon approach proves to be reliable and accurate. Using the high fidelity acceleration data collected by the wireless monitoring system, off-line modal analysis is conducted including peak picking to identify modal frequencies and the use of the frequency domain decomposition method to identify mode shapes. Reasonable modal frequencies and mode shapes are attained. This chapter lays the foundation for research aimed at monitoring vehicle-bridge interaction by a mobile *Narada* wireless sensor network (Chapter 6) and the analysis/identification of the system dynamics for vehicle-bridge interaction (Chapter 7).

CHAPTER 3

SUBSPACE SYSTEM IDENTICATION: THEORY AND APPLICATION TO SUPPORT-EXCITED STRUCTURES

In this chapter, subspace system identification is introduced as a powerful black-box system identification tool for civil structures. In particular, the application of the method to support-excited structures is emphasized. The black-box state-space models derived from subspace system identification are used to estimate the modal properties (*i.e.*, modal frequency, modal damping, and mode shapes) of the structures. To showcase the merits of subspace system identification, a six-story partial-scale steel frame structure is used. Mounted to a six degree-of-freedom shake table, the structure is excited by support motion while its response is measured. While support-excited structures are emphasized, it should be noted that the methods presented in this chapter can be easily generalized for a broader set of excitations commonly found in civil engineering applications.

3.1 Introduction

Output-only system identification using ambient vibrations is a popular practice in the civil engineering community. The use of ambient excitations is convenient because of the technical difficulties associated with exciting large-scale civil engineering structures in a controlled manner (Abdelghani *et al.* 1998; Hermans and Van Der Auweraer 1999; Peeters and Roeck 1999; Brownjohn 2003; Capecchi *et al.* 2004; Yi and Yun 2004; Weng *et al.* 2008). While output-only identification is popular, numerous limitations have been pointed out. For example, one of the critical drawbacks of the practice is that a mathematical evaluation of the accuracy of the

estimated system model is absent due in large part to the absence of a measured input. Thus, output-only system identification is treated as operational modal analysis being different from experimental modal analysis. Considering the definition of system identification (*i.e.*, the processes of building a mathematical model of a physical system from experimental data (Ljung 1999)) and the engineering goal of system identifications (*i.e.*, a prediction of the physical quantities of the system taken from the estimated model of the system), system identification by output-only methods might be insufficient to completely fulfill the general definition and goal of system identification. As a result of these technical challenges, input-output system identification is favored over output-only methods, if the excitation (*i.e.*, input) to the system can be adequately observed and measured.

The vibration of foundations is one of the most widely studied problems in the civil engineering field (Richart *et al.* 1970). Foundation excitations originating from earthquakes, rotating machines (Svinkin 2008), vehicle traffic (Katoua *et al.* 2008), and construction equipment (Wiss 1981) may harmfully affect surrounding structures. Paradoxically, the vibration of structures from support motion can also be viewed as a valuable opportunity to examine the performance of the excited structure (Chaudhary *et al.* 2000). Structural characteristics extracted from vibration measurements can be correlated to the real state or integrity of the structure. For example, the dynamic characteristics of a structure during or after strong ground motions (*e.g.*, earthquakes) can be used to assess structural health by comparing characteristics to a set of characteristics before the application of ground motion. Support-excited structures have a distinctive feature that is leveraged in this study: the input (*i.e.*, ground motion) excites the boundary of the structure, which is different from applying force to the degrees-of-freedom of the structure like in other structural excitation scenarios. The input motion (*i.e.*, the vibration) of the foundation is typically easy to measure just like a system output. This makes it feasible to apply input-output system identification methods to support-excited structures.

Since the introduction of data-driven stochastic subspace identification (SSI) to the civil and mechanical engineering communities by Peeters and Roeck (1999), SSI has become one of the most popular system identification methods in the literature among the numerous time- and frequency-domain output-only methods. The SSI algorithm is a special member of the broader subspace state-space system identification (4SID) family (Viberg 1995; Van Overschee and De Moor 1996), which is widely recognized as a significant achievement of the system identification and control theory communities (Gevers 2003). Since 4SID was introduced to the civil engineering community as a set of output-only system identification methods, a mathematically

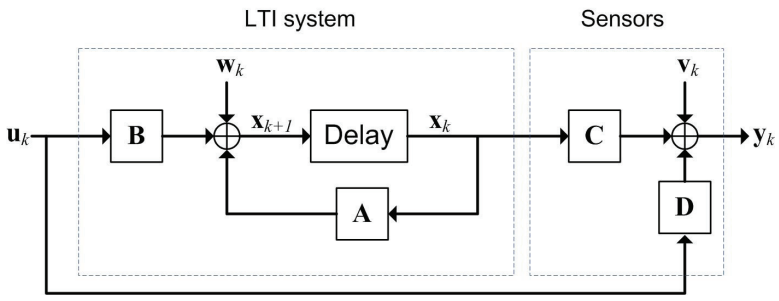

Figure 3.1 A black-box state-space model for system identification.

rigorous manner of relating state-space model parameters to physical parameters has yet been undiscovered. The lack of a mapping between the state-space model by 4SID and physical parameters of the system renders 4SID as a black-box tool. While the tool offers impressive predictive capabilities, its use for structural health monitoring is severely limited.

This chapter has three major objectives. First, a detailed explanation of the subspace system identification method is reviewed. In addition to presenting the mathematical procedures of subspace system identification, its physical meaning is introduced. Second, this chapter is intended to serve as a theoretical foundation for Chapter 4 where the subspace system identification methods are utilized to realize a physically meaningful model derived from experiments. Third, the uncertainty associated with output-only system identifications of support-excited structures is verified experimentally. By leveraging the fully identified and evaluated system model from an input-output system identification, modal parameters extracted from the input-output model and the output-only model are compared. This comparison complements the analytical study of the uncertainty bounds of covariance-based output-only identification models (Reynders *et al.* 2008).

3.2 Theory of Subspace System Identification

3.2.1 Problem Statements of System Identification with State-Space Models

Consider a combined deterministic-stochastic discrete-time state-space model (Fig. 3.1) as:

$$\mathbf{x}_{k+1} = \mathbf{A}\,\mathbf{x}_k + \mathbf{B}\,\mathbf{u}_k + \mathbf{w}_k \tag{3.1}$$

$$\mathbf{y}_k = \mathbf{C}\,\mathbf{x}_k + \mathbf{D}\,\mathbf{u}_k + \mathbf{v}_k \tag{3.2}$$

where $\mathbf{u}_k \in \Re^m$ is a vector of m measured inputs at time step k, $\mathbf{y}_k \in \Re^l$ is a vector of l measured outputs at time step k, and $\mathbf{x}_k \in \Re^n$ is n-dimensional unknown discrete state vector. The model considers two additional stochastic processes: process noise $\mathbf{w}_k \in \Re^n$ which represents an uncertain process noise and measurement noise $\mathbf{v}_k \in \Re^l$ which represents a measurement noise. Assuming $\mathbf{w}_k$ and $\mathbf{v}_k$ are uncorrelated and the processes are Gaussian zero-mean white noise sequences, their (cross) covariance matrices are defined simply as:

$$E\left[\begin{pmatrix}\mathbf{w}_k\\ \mathbf{v}_k\end{pmatrix}\begin{pmatrix}\mathbf{w}_l^T & \mathbf{v}_l^T\end{pmatrix}\right] := \begin{bmatrix}\mathbf{Q} & \mathbf{S}\\ \mathbf{S}^T & \mathbf{R}\end{bmatrix}\delta_{kl} \tag{3.3}$$

where $\mathbf{Q} \in \Re^{n\times n}$, $\mathbf{S} \in \Re^{n\times m}$, and $\mathbf{R} \in \Re^{n\times l}$. Assuming a linear system, the states and outputs in the model (Eqs (3.1) and (3.2)) are split into deterministic and stochastic components as follows:

$$\mathbf{x}_k = \mathbf{x}_k^d + \mathbf{x}_k^s; \quad \mathbf{y}_k = \mathbf{y}_k^d + \mathbf{y}_k^s \tag{3.4}$$

By considering Eqs (3.1), (3.2) and (3.3), the deterministic subsystem is formulated as:

$$\mathbf{x}_{k+1}^d = \mathbf{A}\mathbf{x}_k^d + \mathbf{B}\mathbf{u}_k; \quad \mathbf{y}_k^d = \mathbf{C}\mathbf{x}_k^d + \mathbf{D}\mathbf{u}_k \tag{3.5}$$

Similarly, the stochastic subsystem is written as:

$$\mathbf{x}_{k+1}^s = \mathbf{A}\mathbf{x}_k^s + \mathbf{w}_k; \quad \mathbf{y}_k^s = \mathbf{C}\mathbf{x}_k^s + \mathbf{v}_k \tag{3.6}$$

If the stochastic process $\mathbf{x}_k^s$ is zero-mean stationary then the state covariance matrix can be defined as:

$$\mathbf{\Sigma} := E\left[\mathbf{x}_k^s\left(\mathbf{x}_k^s\right)^T\right] = \mathbf{A}\mathbf{\Sigma}\mathbf{A}^T + \mathbf{Q} \in \Re^{n\times n} \tag{3.7}$$

Now, the problem statement for the system identification of a linear time-invariant (LTI) system can be stated as the estimation of $\mathbf{A}, \mathbf{B}, \mathbf{C}, \mathbf{D}, \mathbf{Q}, \mathbf{R}, \mathbf{S}$ given the measured input sequence (*i.e.* $\mathbf{u}_0, \mathbf{u}_1, \cdots, \mathbf{u}_{N-1}$) and output sequence (*i.e.*, $\mathbf{y}_0, \mathbf{y}_1, \cdots, \mathbf{y}_{N-1}$) as $N \to \infty$ (Van Overschee and De Moor 1994; Verhaegen 1994).

3.2.2 Subspace State-Space System Identification (4SID) Family

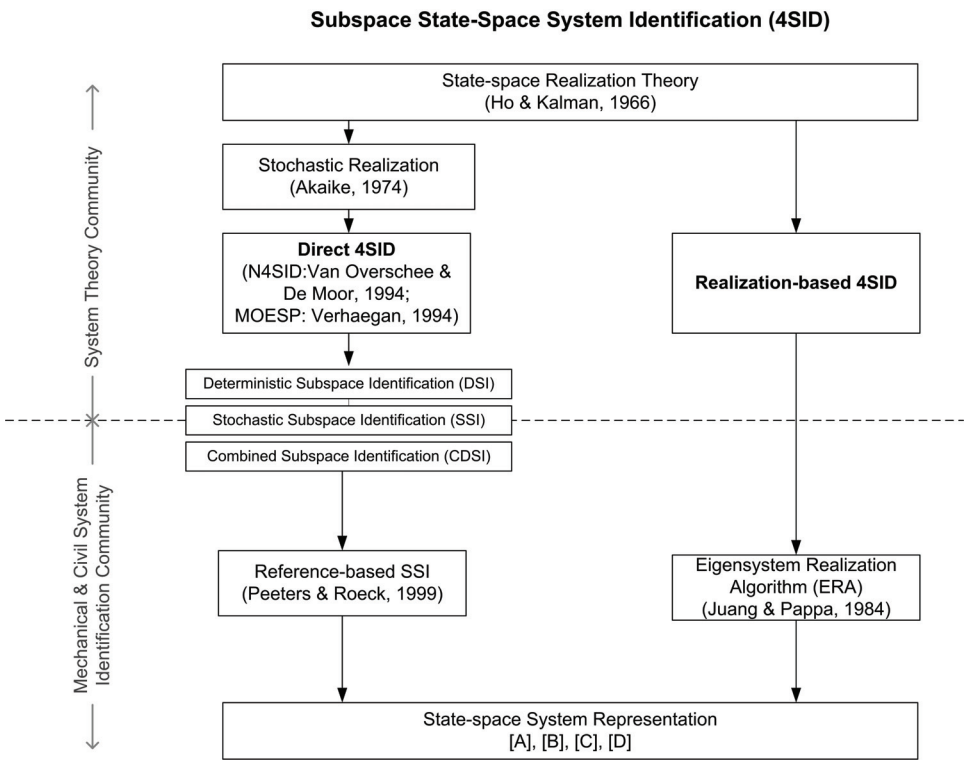

Figure 3.2 Overview of the family of 4SID methods.

The methods associated with subspace state-space system identification (4SID) are generally categorized into two groups (Fig. 3.2): realization-based and direct 4SID methods (Viberg 1995). Realization-based 4SID methods find their origins in the seminal work of Ho and Kalman (Ho and Kalman 1965) and offer a means of extracting state-space models from the extended observability matrix. At the core of the realization-based 4SID methods is the need for a reliable estimate of system impulse responses, often termed the system Markov parameters (MP); the extended observability matrix is estimated from these MPs. Realization-based 4SID methods and estimation of the MPs will be intensively discussed later in Chapter 5. In contrast, direct 4SID methods, also referred to as data-driven subspace identification in the civil engineering community (Peeters and Ventura 2003), strive to estimate a state-space model directly from an arbitrary input and output sequences (*i.e.*, without requiring the estimation of impulse responses). Through the dedication of numerous researchers in the 1970's and 1980's (*e.g.*, stochastic realization (Akaike 1974)), direct 4SID methods were established as numerical algorithms, such as the multivariable output-error state-space (MOESP) (Verhaegen 1994) and the numerical algorithms for subspace state-space system identification (N4SID) (Van Overschee and De Moor

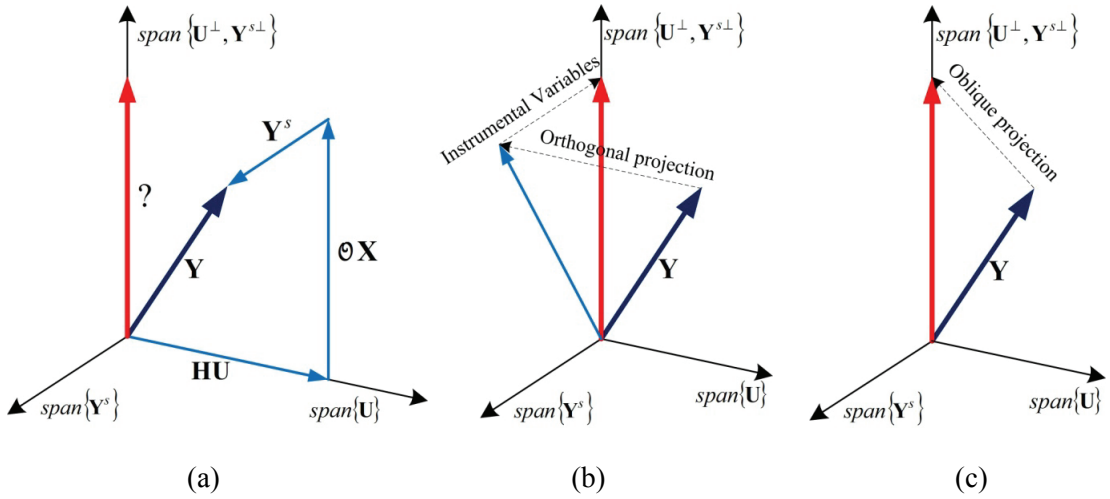

Figure 3.3 Geometric interpretation of subspace system identification: (a) definitions of three subspaces by measurements; (b) subspace operations in MOESP; (c) subspace operations in N4SID.

1994). Generally, direct 4SID methods are referred to simply as subspace methods or subspace system identifications.

Fig. 3.3-a illustrates a geometric concept of the direct 4SID methods from which the name "subspace methods" is derived. Given measurements of the system input $\mathbf{U}$ and output $\mathbf{Y}$, two subspaces spanned by the input $\mathbf{U}$ and the colored noise $\mathbf{Y}^s$ and one subspace spanned by the joint null space of the input and the colored noise $\left\{\mathbf{U}^\perp, \mathbf{Y}^{s\perp}\right\}$ are defined. The output $\mathbf{Y}$ positions at a specific location in the space. The colored noise $\mathbf{Y}^s$ is the system output from unmeasured colored noise input as will be discussed in the following sections. Based on structural dynamics, the measured response of the dynamic system consists of forced vibration, free vibration, and noise. In this context, $\mathbf{Y}$ can be divided into three orthogonal matrices $\mathbf{HU}, \Theta\mathbf{X}$, and $\mathbf{Y}^s$, each parallel to the spans of $\{\mathbf{U}\}$, $\left\{\mathbf{Y}^s\right\}$, and $\left\{\mathbf{U}^\perp, \mathbf{Y}^{s\perp}\right\}$, respectively. Since free vibration reflects the system's dynamic properties, the 4SID strives to estimate the term of $\Theta\mathbf{X}$ (*i.e.*, the product of the extended observability matrix and the state sequence) along the span of $\left\{\mathbf{U}^\perp, \mathbf{Y}^{s\perp}\right\}$ (as denoted with a question mark in Fig 3.3-a) and then to extract system matrices $\{\mathbf{A}, \mathbf{B}, \mathbf{C}, \mathbf{D}\}$. The estimation algorithm is purely a mathematical procedure that seeks to find the best fit black-box model for the measured input-output data by subspace operations followed by least square solutions. However, it should be noted that the term "black-box" model in the 4SID is different from nonlinear black-box models defined in heuristic algorithms (*e.g.* neural networks

(Haykin 1999)), since it is directly connected to the structural dynamics as will be covered in Chapter 4.

Subspace operations that estimate the term $\mathcal{O}\mathbf{X}$ from the measured output are illustrated in Figs 3.3-b and -c for the MOESP and N4SID algorithms, respectively. In the MOESP method (Fig. 3.3-b), the orthogonal projection of $\mathbf{Y}$ onto the null space of input is conducted first in order to remove the input dependency. Then, the coloredness of the output is eliminated by adopting instrumental variables. In contrast, the two-step MOESP operation is combined to a one step oblique projection in the N4SID method (Fig. 3.3-c). Essentially, the two estimation processes are identical (*i.e.*, MOESP and N4SID) except for weightings used as will be explained later. Thus, the product of the extended observability matrix and the state sequence ($\mathcal{O}\mathbf{X}$) are similarly obtained in both methods. Now, the estimated product of $\mathcal{O}$ and $\mathbf{X}$ can be further simplified to extract a state-space model of the system. Specifically, singular value decomposition (SVD) of the estimated $\mathcal{O}\mathbf{X}$ is conducted to determine system order and to truncate the extended observability matrix. The main difference between the MOESP and N4SID is the numerical procedure used for the estimation of system matrices $\{\mathbf{A},\mathbf{B},\mathbf{C},\mathbf{D}\}$. In the MOESP method, system matrices $\{\mathbf{A},\mathbf{C}\}$ are calculated from the estimated observability matrix. Then, the input system matrices $\{\mathbf{B},\mathbf{D}\}$ are calculated by linear regression from estimated $\{\mathbf{A},\mathbf{C}\}$ and measured input-output data. However, the N4SID method adopts a one-step estimation of the system matrices $\{\mathbf{A},\mathbf{B},\mathbf{C},\mathbf{D}\}$ by solving a least square problem. In order to compose an over-determined linear regression, the system state sequence needs to be estimated. Van Overschee and De Moor argue the intermediate state sequence as the state sequence of the Kalman filter (Van Overschee and De Moor 1996). Even though the two methods in the 4SID family are posed differently, the accuracy of both methods are reported to be similar in the literature (Viberg *et al.* 1993).

During the development of the aforementioned N4SID method, the stochastic identification problem (in Fig. 3.4) which was presented by Akaike as stochastic realization (Akaike 1974) played an important role, since it established the concept of the Kalman filter state sequence and a least square solution for the determination of system matrices (Van Overschee and De Moor 1993). The stochastic identification problem can be stated as the estimation of $\mathbf{A},\mathbf{C},\mathbf{Q},\mathbf{R},\mathbf{S}$ given the measured output sequence (*i.e.*, $\mathbf{y}_0,\mathbf{y}_1,\cdots,\mathbf{y}_{N-1}$) as $N\to\infty$. Since the stochastic system identification problem can also be interpreted as an output-only system identification method under the assumption of an unmeasured white noise input, it has been widely applied to the identification of civil engineering structures excited by ambient vibrations. (Peeters and Roeck

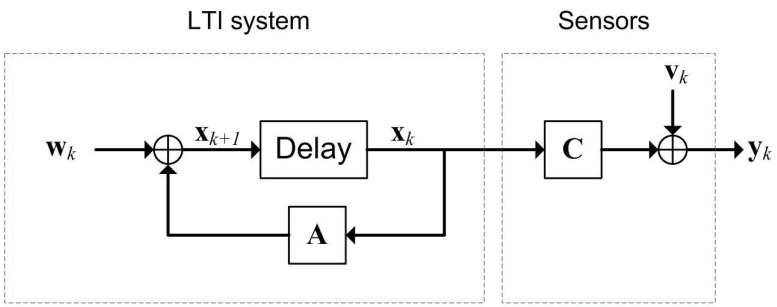

Figure 3.4 A black-box state-space model for stochastic system identification.

1999). After Peeters and Roeck's introduction of data-driven stochastic subspace identification (SSI) to the civil engineering community, numerous researchers have adopted SSI for output-only modal analysis of structural system, thereby attaining greater accuracy compared to classical frequency domain methods (Arici and Mosalam 2005; Yan and Golinval 2006; Weng *et al.* 2008). In this chapter, the N4SID method will be exclusively focused on system identification of support-excited structures.

3.3 Numerical Algorithms for Subspace State-Space System Identification (N4SID)

The application of N4SID is considered for input-output system identification (*i.e.*, combined deterministic-stochastic subspace identification) (Van Overschee and De Moor 1996) in this chapter. This general case can be further specialized for output-only system identification by ignoring input system matrices $\{\mathbf{B},\mathbf{D}\}$ which represent the deterministic subsystem. A convenience of using N4SID is the availability of a MATLAB toolbox function (*i.e.*, "n4sid") that executes the method (Ljung 2009). This section will delineate N4SID for input-output system identification by summarizing the formulation detailed by Van Overschee and De Moor (1994 and 1996); interested readers are referred to this seminal work for a more rigorous mathematical proof.

3.3.1 Deterministic Subsystem

Assume the dimension of the state of the system is *n*, the extended observability matrix, Θ_i, is defined as (where the subscript *i* denotes the number of block rows and is assumed greater than *n*):

$$\mathfrak{O}_i := \begin{bmatrix} \mathbf{C}^T & (\mathbf{CA})^T & \left(\mathbf{CA}^2\right)^T & \cdots & \left(\mathbf{CA}^{i-1}\right)^T \end{bmatrix}^T \tag{3.8}$$

The reversed extended controllability matrix associated with the deterministic input, $\mathbf{\Delta}_i^d$, and the lower block triangular Toeplitz matrix composed of deterministic Markov parameters, $\mathbf{H}_i^d$, are respectively defined as:

$$\mathbf{\Delta}_i^d := \begin{bmatrix} \mathbf{A}^{i-1}\mathbf{B} & \cdots & \mathbf{AB} & \mathbf{B} \end{bmatrix} \tag{3.9}$$

$$\mathbf{H}_i^d := \begin{bmatrix} \mathbf{D} & \mathbf{0} & \mathbf{0} & \cdots & \mathbf{0} \\ \mathbf{CB} & \mathbf{D} & \mathbf{0} & \cdots & \mathbf{0} \\ \mathbf{CAB} & \mathbf{CB} & \mathbf{D} & \cdots & \mathbf{0} \\ \vdots & \vdots & \vdots & \ddots & \vdots \\ \mathbf{CA}^{i-2}\mathbf{B} & \mathbf{CA}^{i-3}\mathbf{B} & \mathbf{CA}^{i-4}\mathbf{B} & \cdots & \mathbf{D} \end{bmatrix} \tag{3.10}$$

3.3.2 Stochastic Subsystem

The reversed extended stochastic controllability matrix, $\mathbf{\Delta}_i^s$, is also defined as:

$$\mathbf{\Delta}_i^s := \begin{bmatrix} \mathbf{A}^{i-1}\mathbf{G} & \cdots & \mathbf{AG} & \mathbf{G} \end{bmatrix} \tag{3.11}$$

where $\mathbf{G}$ is the stochastic state and output covariance matrix:

$$\mathbf{G} := E\left[\mathbf{x}_k^s \left(\mathbf{y}_k^s\right)^T \right] \in \Re^{n \times l} \tag{3.12}$$

The block Toeplitz covariance matrix composed of stochastic Markov parameters, $\mathbf{H}_i^s$, is expressed as:

$$\mathbf{H}_i^s := \begin{bmatrix} \mathbf{\Lambda}_i & \mathbf{\Lambda}_{i-1} & \cdots & \mathbf{\Lambda}_1 \\ \mathbf{\Lambda}_{i+1} & \mathbf{\Lambda}_i & \cdots & \mathbf{\Lambda}_2 \\ \vdots & \vdots & \ddots & \vdots \\ \mathbf{\Lambda}_{2i-1} & \mathbf{\Lambda}_{2i-2} & \cdots & \mathbf{\Lambda}_i \end{bmatrix} \tag{3.13}$$

where the stochastic output covariance matrix $\mathbf{\Lambda}_i := E\left[\mathbf{y}_k^s \left(\mathbf{y}_k^s\right)^T \right] \in \Re^{l \times l}$ has the values:

$$\mathbf{\Lambda}_i = \begin{cases} \mathbf{C}\mathbf{A}^{i-1}\mathbf{G} & i > 0 \\ \mathbf{C}\mathbf{\Sigma}\mathbf{C}^T + \mathbf{R} & i = 0 \\ \mathbf{G}^T(\mathbf{A}^T)^{-i-1}\mathbf{C}^T & i < 0 \end{cases} \tag{3.14}$$

3.3.3 Input-output Data Equations

The input and output block Hankel matrices are defined as:

$$\mathbf{U}_{0|i-1} \coloneqq \begin{bmatrix} \mathbf{u}_0 & \mathbf{u}_1 & \cdots & \mathbf{u}_{j-1} \\ \mathbf{u}_1 & \mathbf{u}_2 & \cdots & \mathbf{u}_j \\ \vdots & \vdots & \ddots & \vdots \\ \mathbf{u}_{i-1} & \mathbf{u}_i & \cdots & \mathbf{u}_{i+j-2} \end{bmatrix} \tag{3.15}$$

$$\mathbf{Y}_{0|i-1} \coloneqq \begin{bmatrix} \mathbf{y}_0 & \mathbf{y}_1 & \cdots & \mathbf{y}_{j-1} \\ \mathbf{y}_1 & \mathbf{y}_2 & \cdots & \mathbf{y}_j \\ \vdots & \vdots & \ddots & \vdots \\ \mathbf{y}_{i-1} & \mathbf{y}_i & \cdots & \mathbf{y}_{i+j-2} \end{bmatrix} \tag{3.16}$$

where j is the sample size (and should be selected as $j >> i$ since it will be assumed as infinity in the Kalman filter state sequence as discussed later). The input and output block Hankel matrices can be partitioned into "past" $\mathbf{U}_p$ and $\mathbf{Y}_p$, respectively and "future" $\mathbf{U}_f$ and $\mathbf{Y}_f$, respectively parts as follows:

$$\mathbf{U}_{0|2i-1} = \begin{bmatrix} \mathbf{U}_{0|i-1} \\ \hline \mathbf{U}_{i|2i-1} \end{bmatrix} \coloneqq \begin{bmatrix} \mathbf{U}_p \\ \hline \mathbf{U}_f \end{bmatrix} \tag{3.17}$$

$$\mathbf{Y}_{0|2i-1} = \begin{bmatrix} \mathbf{Y}_{0|i-1} \\ \hline \mathbf{Y}_{i|2i-1} \end{bmatrix} \coloneqq \begin{bmatrix} \mathbf{Y}_p \\ \hline \mathbf{Y}_f \end{bmatrix} \tag{3.18}$$

The deterministic and stochastic state sequence matrices are defined respectively as:

$$\mathbf{X}_i^d \coloneqq \begin{bmatrix} \mathbf{x}_i^d & \mathbf{x}_{i+1}^d & \mathbf{x}_{i+2}^d & \cdots & \mathbf{x}_{i+j-1}^d \end{bmatrix} \tag{3.19}$$

$$\mathbf{X}_i^s \coloneqq \begin{bmatrix} \mathbf{x}_i^s & \mathbf{x}_{i+1}^s & \mathbf{x}_{i+2}^s & \cdots & \mathbf{x}_{i+j-1}^s \end{bmatrix} \tag{3.20}$$

Analogous to the previous definition of partitioned input and output block Hankel matrices, past and future deterministic state sequence matrices are defined as:

$$\mathbf{X}_p^d := \mathbf{X}_0^d \tag{3.21}$$

$$\mathbf{X}_f^d := \mathbf{X}_i^d \tag{3.22}$$

Finally, the input-output data equations are established with the predefined matrices and Eqs (3.1) and (3.2) as:

$$\mathbf{Y}_p = \mathfrak{O}_i \mathbf{X}_p^d + \mathbf{H}_i^d \mathbf{U}_p + \mathbf{Y}_p^s \tag{3.23}$$

$$\mathbf{Y}_f = \mathfrak{O}_i \mathbf{X}_f^d + \mathbf{H}_i^d \mathbf{U}_f + \mathbf{Y}_f^s \tag{3.24}$$

$$\mathbf{X}_f^d = \mathbf{A}^i \mathbf{X}_p^d + \mathbf{\Delta}_i^d \mathbf{U}_p \tag{3.25}$$

The geometric interpretation of Eqs (3.23) or (3.24) was already presented in Fig. 3.3-a. State evolution (Eq. (3.25)) bridges the past and future deterministic state sequence matrices.

3.2.4 Oblique Projection by LQ Decomposition

The oblique projection (Fig. 3.3-c) can be numerically implemented using LQ decomposition. Householder transformations are preferred among the numerous LQ decomposition algorithms (Golub and Van Loan 1996). The LQ decomposition of the system input, **U**, and output, **Y**, is:

$$\left[\begin{array}{c}\mathbf{U}_{0|2i-1}\\ \hline \mathbf{Y}_{0|2i-1}\end{array}\right] = \left[\begin{array}{c}\mathbf{U}_p\\ \hline \mathbf{U}_f\\ \hline \mathbf{Y}_p\\ \hline \mathbf{Y}_f\end{array}\right] = \left[\begin{array}{c}\mathbf{U}_{0|i-1}\\ \hline \mathbf{U}_{i|i}\\ \hline \mathbf{U}_{i+1|2i-1}\\ \hline \mathbf{Y}_{0|i-1}\\ \hline \mathbf{Y}_{i|i}\\ \hline \mathbf{Y}_{i+1|2i-1}\end{array}\right] = \left[\begin{array}{c|cccccc} \mathbf{L}_{11} & \mathbf{0} & \mathbf{0} & \mathbf{0} & \mathbf{0} & \mathbf{0} \\ \hline \mathbf{L}_{21} & \mathbf{L}_{22} & \mathbf{0} & \mathbf{0} & \mathbf{0} & \mathbf{0} \\ \mathbf{L}_{31} & \mathbf{L}_{32} & \mathbf{L}_{33} & \mathbf{0} & \mathbf{0} & \mathbf{0} \\ \hline \mathbf{L}_{41} & \mathbf{L}_{42} & \mathbf{L}_{43} & \mathbf{L}_{44} & \mathbf{0} & \mathbf{0} \\ \hline \mathbf{L}_{51} & \mathbf{L}_{52} & \mathbf{L}_{53} & \mathbf{L}_{54} & \mathbf{L}_{55} & \mathbf{0} \\ \mathbf{L}_{61} & \mathbf{L}_{62} & \mathbf{L}_{63} & \mathbf{L}_{64} & \mathbf{L}_{65} & \mathbf{L}_{66} \end{array}\right] \left[\begin{array}{c}\mathbf{Q}_1^T\\ \hline \mathbf{Q}_2^T\\ \mathbf{Q}_3^T\\ \hline \mathbf{Q}_4^T\\ \hline \mathbf{Q}_5^T\\ \mathbf{Q}_6^T\end{array}\right] \tag{3.26}$$

where $\mathbf{L}_{11}, \cdots, \mathbf{L}_{66}$ are lower triangular matrices and $\mathbf{Q}_1, \cdots, \mathbf{Q}_6$ are orthogonal matrices. Since the null space of colored noise output $\mathbf{Y}^{s\perp}$ can be determined from the joint space of "past" input and output $\left\{\mathbf{U}_p, \mathbf{Y}_p\right\}$ (this is also related with the concept of instrumental variables), the oblique projection of **Y** onto the span of joint null space $\left\{\mathbf{U}^{\perp}, \mathbf{Y}^{s\perp}\right\}$ is defined as a projection of the future output $\mathbf{Y}_f$ onto the span of the "past" input and output $\left\{\mathbf{U}_p, \mathbf{Y}_p\right\}$ and the null space of future input $\mathbf{U}_f^{\perp}$ is denoted by $\mathbf{P}_i$ and can be calculated as:

$$\mathbf{P}_i := \mathbf{Y}_f /_{\mathbf{U}_f^{\perp}} \begin{pmatrix} \mathbf{U}_p \\ \mathbf{Y}_p \end{pmatrix} = \mathbf{L}_{\mathbf{U}_p} \mathbf{L}_{11} \mathbf{Q}_1^T + \mathbf{L}_{\mathbf{Y}_p} \begin{bmatrix} \mathbf{L}_{41} & \mathbf{L}_{42} & \mathbf{L}_{43} & \mathbf{L}_{44} \end{bmatrix} \begin{bmatrix} \mathbf{Q}_1 & \mathbf{Q}_2 & \mathbf{Q}_3 & \mathbf{Q}_4 \end{bmatrix}^T \quad (3.27)$$

where $\mathbf{L}_{\mathbf{U}_p}$ and $\mathbf{L}_{\mathbf{Y}_p}$ are subspace weighting matrices corresponding to past input and past output, respectively, and determined by:

$$\begin{bmatrix} \mathbf{L}_{\mathbf{U}_p} & \mathbf{L}_{\mathbf{U}_f} & \mathbf{L}_{\mathbf{Y}_p} \end{bmatrix} = \left[\begin{array}{c|cc|c} \mathbf{L}_{51} & \mathbf{L}_{52} & \mathbf{L}_{53} & \mathbf{L}_{54} \\ \mathbf{L}_{61} & \mathbf{L}_{62} & \mathbf{L}_{63} & \mathbf{L}_{64} \end{array}\right] \left[\begin{array}{c|ccc} \mathbf{L}_{11} & \mathbf{0} & \mathbf{0} & \mathbf{0} \\ \hline \mathbf{L}_{21} & \mathbf{L}_{22} & \mathbf{0} & \mathbf{0} \\ \mathbf{L}_{31} & \mathbf{L}_{32} & \mathbf{L}_{33} & \mathbf{0} \\ \hline \mathbf{L}_{41} & \mathbf{L}_{42} & \mathbf{L}_{43} & \mathbf{L}_{44} \end{array}\right]^{-1} \quad (3.28)$$

Another oblique projection $\mathbf{P}_{i-1}$ can be defined similarly as:

$$\mathbf{P}_{i-1} := \mathbf{Y}_f^- /_{(\mathbf{U}_f^-)^{\perp}} \begin{pmatrix} \mathbf{U}_p^+ \\ \mathbf{Y}_p^+ \end{pmatrix} \quad (3.29)$$

where one block row added (superscript +) or deleted (superscript -) input and output matrices are defined respectively as:

$$\left[\begin{array}{c} \mathbf{U}_p^+ \\ \hline \mathbf{U}_f^- \end{array}\right] := \left[\begin{array}{c} \mathbf{U}_{0|i} \\ \hline \mathbf{U}_{i+1|2i-1} \end{array}\right] \quad (3.30)$$

$$\left[\begin{array}{c} \mathbf{Y}_p^+ \\ \hline \mathbf{Y}_f^- \end{array}\right] := \left[\begin{array}{c} \mathbf{Y}_{0|i} \\ \hline \mathbf{Y}_{i+1|2i-1} \end{array}\right] \quad (3.31)$$

Thus, the oblique projection can be calculated as:

$$\mathbf{P}_{i-1} = \mathbf{L}_{\mathbf{U}_p^+} \begin{bmatrix} \mathbf{L}_{11} & \mathbf{0} \\ \mathbf{L}_{21} & \mathbf{L}_{22} \end{bmatrix} \begin{bmatrix} \mathbf{Q}_1^T \\ \mathbf{Q}_2^T \end{bmatrix} + \mathbf{L}_{\mathbf{Y}_p^+} \begin{bmatrix} \mathbf{L}_{41} & \mathbf{L}_{42} & \mathbf{L}_{43} & \mathbf{L}_{44} & \mathbf{0} \\ \mathbf{L}_{51} & \mathbf{L}_{52} & \mathbf{L}_{53} & \mathbf{L}_{54} & \mathbf{L}_{55} \end{bmatrix} \begin{bmatrix} \mathbf{Q}_1 & \mathbf{Q}_2 & \mathbf{Q}_3 & \mathbf{Q}_4 & \mathbf{Q}_5 \end{bmatrix}^T \quad (3.32)$$

where both subspace weighting matrices are calculated as:

$$\begin{bmatrix} \mathbf{L}_{\mathbf{U}_p^+} & \mathbf{L}_{\mathbf{U}_f^-} & \mathbf{L}_{\mathbf{Y}_p^+} \end{bmatrix} = \begin{bmatrix} \mathbf{L}_{61} & \mathbf{L}_{62} \mid \mathbf{L}_{63} \mid \mathbf{L}_{64} & \mathbf{L}_{65} \end{bmatrix} \left[\begin{array}{ccc|c|c} \mathbf{L}_{11} & \mathbf{0} & \mathbf{0} & \mathbf{0} & \mathbf{0} \\ \mathbf{L}_{21} & \mathbf{L}_{22} & \mathbf{0} & \mathbf{0} & \mathbf{0} \\ \hline \mathbf{L}_{31} & \mathbf{L}_{32} & \mathbf{L}_{33} & \mathbf{0} & \mathbf{0} \\ \hline \mathbf{L}_{41} & \mathbf{L}_{42} & \mathbf{L}_{43} & \mathbf{L}_{44} & \mathbf{0} \\ \mathbf{L}_{51} & \mathbf{L}_{52} & \mathbf{L}_{53} & \mathbf{L}_{54} & \mathbf{L}_{55} \end{array}\right]^{-1} \tag{3.33}$$

3.3.5 Kalman Filter State Sequence

Before exploring the oblique projection, P_i and P_{i-1}, presented in Section 3.3.4, the non-steady state Kalman filter state estimate (*i.e.*, the optimal state estimate based on the measured input and output data) is first reviewed herein (Kalman 1960). Given the initial state estimate, $\hat{\mathbf{x}}_0$, initial state covariance, $\mathbf{\Sigma}_0$, noise covariances, $\mathbf{Q}, \mathbf{R}, \mathbf{S}$, input sequence, $\mathbf{u}_0, \mathbf{u}_1, \cdots, \mathbf{u}_{k-1}$, and output sequence, $\mathbf{y}_0, \mathbf{y}_1, \cdots, \mathbf{y}_{k-1}$, along with a model of a linear time-invariant system, $\mathbf{A}, \mathbf{B}, \mathbf{C}, \mathbf{D}$, then the non-steady state Kalman filter state estimate at time step *k*, $\hat{\mathbf{x}}_k$, is defined in a recursive form with the Kalman gain, $\mathbf{K}_{k-1}$, and algebraic Riccati equation for state covariance, $\mathbf{\Sigma}_k$, defined as:

$$\hat{\mathbf{x}}_k = \mathbf{A}\hat{\mathbf{x}}_{k-1} + \mathbf{B}\mathbf{u}_{k-1} + \mathbf{K}_{k-1}\left(\mathbf{y}_{k-1} - \mathbf{C}\hat{\mathbf{x}}_{k-1} - \mathbf{D}\mathbf{u}_{k-1}\right) \tag{3.34}$$

$$\mathbf{K}_{k-1} = \left(\mathbf{A}\mathbf{\Sigma}_{k-1}\mathbf{C}^T + \mathbf{G}\right)\left(\mathbf{\Lambda}_0 + \mathbf{C}\mathbf{\Sigma}_{k-1}\mathbf{C}^T\right)^{-1} \tag{3.35}$$

$$\mathbf{\Sigma}_k = \mathbf{A}\mathbf{\Sigma}_{k-1}\mathbf{A}^T + \left(\mathbf{A}\mathbf{\Sigma}_{k-1}\mathbf{C}^T + \mathbf{G}\right)\left(\mathbf{\Lambda}_0 + \mathbf{C}\mathbf{\Sigma}_{k-1}\mathbf{C}^T\right)^{-1}\left(\mathbf{A}\mathbf{\Sigma}_{k-1}\mathbf{C}^T + \mathbf{G}\right)^T \tag{3.36}$$

The Kalman filter state estimate, $\hat{\mathbf{x}}_k$, of Eq. (3.34) can be also written in the matrix form as:

$$\hat{\mathbf{x}}_k = \left[\mathbf{A} - \mathbf{K}_{k-1}\mathbf{C} \mid \mathbf{B} - \mathbf{K}_{k-1}\mathbf{D} \mid \mathbf{K}_{k-1}\right]\left[\hat{\mathbf{x}}_{k-1}^T \mid \mathbf{u}_{k-1}^T \mid \mathbf{y}_{k-1}^T\right]^T \tag{3.37}$$

The recursive form of Eq. (3.37) is written from the initial time to the time step *k* as:

$$\hat{\mathbf{x}}_k = \left[\mathbf{A}^k - \mathbf{\Omega}_k\mathbf{\Theta}_k \mid \mathbf{\Delta}_k^d - \mathbf{\Omega}_k\mathbf{H}_k^d \mid \mathbf{\Omega}_k\right]\left[\hat{\mathbf{x}}_0^T \mid \mathbf{u}_0^T \quad \cdots \quad \mathbf{u}_{k-1}^T \mid \mathbf{y}_0^T \quad \cdots \quad \mathbf{y}_{k-1}^T\right]^T \tag{3.38}$$

where the modified Kalman gain, $\mathbf{\Omega}_k$, is:

$$\mathbf{\Omega}_k := \left(\mathbf{\Delta}_k^s + \mathbf{A}^k\mathbf{\Sigma}_0\mathbf{\Theta}_k^T\right)\left(L_k^s + \mathbf{\Theta}_k\mathbf{\Sigma}_0\mathbf{\Theta}_k^T\right)^{-1} \tag{3.39}$$

and $L_k^s := \lim_{j\to\infty} 1/j\, \mathbf{Y}_p^s \left(\mathbf{Y}_p^s\right)^T$ is the limit for the past stochastic output, which can be defined under the assumption of an infinite sample size. A bank of Kalman filter state estimates can be expressed as:

$$\hat{\mathbf{X}}_i := \begin{bmatrix} \hat{\mathbf{x}}_i & \hat{\mathbf{x}}_{i+1} & \hat{\mathbf{x}}_{i+2} & \cdots & \hat{\mathbf{x}}_{i+j-1} \end{bmatrix} \tag{3.40}$$

Substituting Eq. (3.38) into Eq. (3.40) leads to the following expression for the Kalman filter state estimate bank:

$$\hat{\mathbf{X}}_i = \left[\mathbf{A}^i - \mathbf{\Omega}_i \Theta_i \mid \Delta_i^d - \mathbf{\Omega}_i \mathbf{H}_i^d \mid \mathbf{\Omega}_i\right] \begin{bmatrix} \hat{\mathbf{X}}_0 \\ \hline \mathbf{U}_{0|i-1} \\ \hline \mathbf{Y}_{0|i-1} \end{bmatrix} = \left[\mathbf{A}^i - \mathbf{\Omega}_i \Theta_i \mid \Delta_i^d - \mathbf{\Omega}_i \mathbf{H}_i^d \mid \mathbf{\Omega}_i\right] \begin{bmatrix} \hat{\mathbf{X}}_0 \\ \hline \begin{pmatrix} \mathbf{U}_p \\ \mathbf{Y}_p \end{pmatrix} \end{bmatrix} \tag{3.41}$$

This expression for the Kalman filter state estimate bank is significant. It implies that the Kalman filter state estimate sequence, $\hat{\mathbf{X}}_i$, is simply a linear combination of the initial state estimate sequence, $\hat{\mathbf{X}}_0$, and the "past" input and output sequences, $\left\{\mathbf{U}_p, \mathbf{Y}_p\right\}$; it is located in the joint space of the past input and output. Thus, considering the equation of orthogonal decomposition of the future output (Eq. (3.24)), the oblique projection P_i (*i.e.*, projection of the future output $\mathbf{Y}_f$ onto the span of the past input and output $\left\{\mathbf{U}_p, \mathbf{Y}_p\right\}$ and the null space of future input $\mathbf{U}_f^{\perp}$) is equal to the product of the extended observability matrix, Θ_i, and Kalman filter state estimate sequence, $\mathbf{X}_i$, as:

$$\mathrm{P}_i = \Theta_i \hat{\mathbf{X}}_i \tag{3.42}$$

Similarly, the oblique projection P_{i-1} is equal to:

$$\mathrm{P}_{i-1} = \Theta_{i-1} \hat{\mathbf{X}}_{i+1} \tag{3.43}$$

3.3.6 Extraction of the Observability Matrix by SVD

Singular value decomposition (SVD) of the oblique projection P_i, (*i.e.*, Eq. (3.27)) is calculated as:

$$\begin{aligned}\mathrm{P}_i &= \left[\mathbf{L}_{\mathbf{U}_p}\begin{bmatrix}\mathbf{L}_{11} & \mathbf{0} & \mathbf{0} & \mathbf{0}\end{bmatrix} + \mathbf{L}_{\mathbf{Y}_p}\begin{bmatrix}\mathbf{L}_{41} & \mathbf{L}_{42} & \mathbf{L}_{43} & \mathbf{L}_{44}\end{bmatrix}\right]\begin{bmatrix}\mathbf{Q}_1 & \mathbf{Q}_2 & \mathbf{Q}_3 & \mathbf{Q}_4\end{bmatrix}^T \\ &\cong \begin{bmatrix}\mathbf{U}_1 & \mathbf{U}_2\end{bmatrix}\begin{bmatrix}\mathbf{S}_1 & \mathbf{0} \\ \mathbf{0} & \mathbf{0}\end{bmatrix}\begin{bmatrix}\mathbf{V}_1^T \\ \mathbf{V}_2^T\end{bmatrix}\begin{bmatrix}\mathbf{Q}_1 & \mathbf{Q}_2 & \mathbf{Q}_3 & \mathbf{Q}_4\end{bmatrix}^T = \mathbf{U}_1\mathbf{S}_1\mathbf{V}_1^T\begin{bmatrix}\mathbf{Q}_1 & \mathbf{Q}_2 & \mathbf{Q}_3 & \mathbf{Q}_4\end{bmatrix}^T\end{aligned} \tag{3.44}$$

where the significant singular value diagonal matrix is $\mathbf{S}_1 \in \Re^{n\times n}$. This means the system order is determined by checking the singular values extracted. Taking the left singular vectors and the half of the singular values leads to the observability matrix:

$$\mathcal{O}_i = \mathbf{U}_1\mathbf{S}_1^{1/2} \tag{3.45}$$

As seen in Eq. (3.44), SVD is only applied to the part of the lower triangular matrix of the LQ decomposition of Eq. (3.26).

3.3.7 Least Square Problems for System Matrices Estimates

The Kalman filter state estimate sequence can also be calculated from Eq. (3.44) as:

$$\hat{\mathbf{X}}_i = \mathbf{S}_1^{1/2}\mathbf{V}_1^T\begin{bmatrix}\mathbf{Q}_1 & \mathbf{Q}_2 & \mathbf{Q}_3 & \mathbf{Q}_4\end{bmatrix}^T \tag{3.46}$$

By using Eqs (3.43) and (3.45), the one-step shifted Kalman filter state estimate can be calculated as:

$$\hat{\mathbf{X}}_{i+1} = \mathcal{O}_{i-1}^{\dagger}\mathrm{P}_{i-1} \tag{3.47}$$

where $\mathcal{O}_{i-1}$ is the notation of $\mathcal{O}_i$ without the last one block row. A space-state equation is composed of state estimates and measured inputs and outputs as follows:

$$\begin{bmatrix}\hat{\mathbf{X}}_{i+1} \\ \mathbf{Y}_{i|i}\end{bmatrix} = \begin{bmatrix}\hat{\mathbf{A}} \\ \hat{\mathbf{C}}\end{bmatrix}\hat{\mathbf{X}}_i + \begin{bmatrix}\hat{\mathbf{B}} \\ \hat{\mathbf{D}}\end{bmatrix}\mathbf{U}_{i|i} + \begin{bmatrix}\boldsymbol{\rho}_{\mathbf{W}} \\ \boldsymbol{\rho}_{\mathbf{v}}\end{bmatrix} = \begin{bmatrix}\hat{\mathbf{A}} & \hat{\mathbf{B}} \\ \hat{\mathbf{C}} & \hat{\mathbf{D}}\end{bmatrix}\begin{bmatrix}\hat{\mathbf{X}}_i \\ \mathbf{U}_{i|i}\end{bmatrix} + \begin{bmatrix}\boldsymbol{\rho}_{\mathbf{W}} \\ \boldsymbol{\rho}_{\mathbf{v}}\end{bmatrix} \tag{3.48}$$

where $\boldsymbol{\rho}_{\mathbf{W}}$ and $\boldsymbol{\rho}_{\mathbf{v}}$ are residual matrices due to white noise related with process and measurement, respectively. Hence, the least square solution of the system matrices can be calculated as:

$$\begin{bmatrix}\hat{\mathbf{A}} & \hat{\mathbf{B}} \\ \hat{\mathbf{C}} & \hat{\mathbf{D}}\end{bmatrix} = \begin{bmatrix}\hat{\mathbf{X}}_{i+1} \\ \mathbf{Y}_{i|i}\end{bmatrix}\begin{bmatrix}\hat{\mathbf{X}}_i \\ \mathbf{U}_{i|i}\end{bmatrix}^{\dagger} \tag{3.49}$$

Finally, the noise covariance matrices are estimate by the residual matrices from Eq. (3.48):

$$\begin{bmatrix} \hat{\mathbf{Q}} & \hat{\mathbf{S}} \\ \hat{\mathbf{S}}^T & \hat{\mathbf{R}} \end{bmatrix} = \frac{1}{j} \begin{bmatrix} \boldsymbol{\rho}_{\mathbf{W}} \\ \boldsymbol{\rho}_{\mathbf{v}} \end{bmatrix} \begin{bmatrix} \boldsymbol{\rho}_{\mathbf{W}}^T & \boldsymbol{\rho}_{\mathbf{v}}^T \end{bmatrix} \tag{3.50}$$

The estimated system matrices in Eq. (3.49) represent a black-box state-space model for the system by input-output identification.

3.4 System Identification of Support-Excited Structures

Section 3.3 (Numerical Algorithms for Subspace State-Space System Identification) has laid a theoretical foundation for the system identification algorithm. This section will build on the N4SID algorithm for the estimation of black-box state-space models of support-excited (*i.e.*, seismically excited) structures. A six-story steel frame structure that is base-excited by a laboratory shake table is used to validate the proposed subspace system identification strategy.

3.4.1 Testbed Structure and Support-Exciting Testing

A single-bay steel frame structure (Fig. 3.5) constructed on a shaking table at the National Center for Research in Earthquake Engineering (NCREE) at National Taiwan University (NTU) is selected as a testbed structure in this study. The structure is a partial scale six-story single-bay steel building where the inter-story height is 1 m (hence, the total structure height is 6 m). Four steel columns support steel diaphragms (1 m by 1.5 m) at each story. Since system identification of the structure focuses on estimation of a black-box state-space model, more detailed description of the structure is not necessary. Due to the rectangular cross section of the columns, the structure has two orthogonal axes: a flexurally weak axis (termed the x-axis) and a flexurally strong axis (termed the y-axis). For the precise study of the dynamic behavior of the structure, two-dimensional lateral excitation by the shaking table is adopted in the experimental phase of the study. In total, 20 accelerometers are installed as seen in Fig. 3.5-b. Each floor is instrumented with three accelerometers (two oriented in the x-axis (denoted as xa and xb) and one oriented in the y-axis (denoted as y)). Additionally, two accelerometers are installed in two orthogonal directions at the ground level to measure the two dimensional support motion.

Two moderate excitation inputs are applied to both axes of the shake table. First, the 40 sec-long scaled El Centro earthquake motion is applied to the two different axes. The peak ground accelerations of each direction is 0.053 g (x-direction) and 0.044 g (y-direction). Second, a 120 sec-long white noise motion recorded as 0.061 g and 0.0745 g at each axis was applied also. During the tests, acceleration signals are measured with a 100 Hz sampling rate.

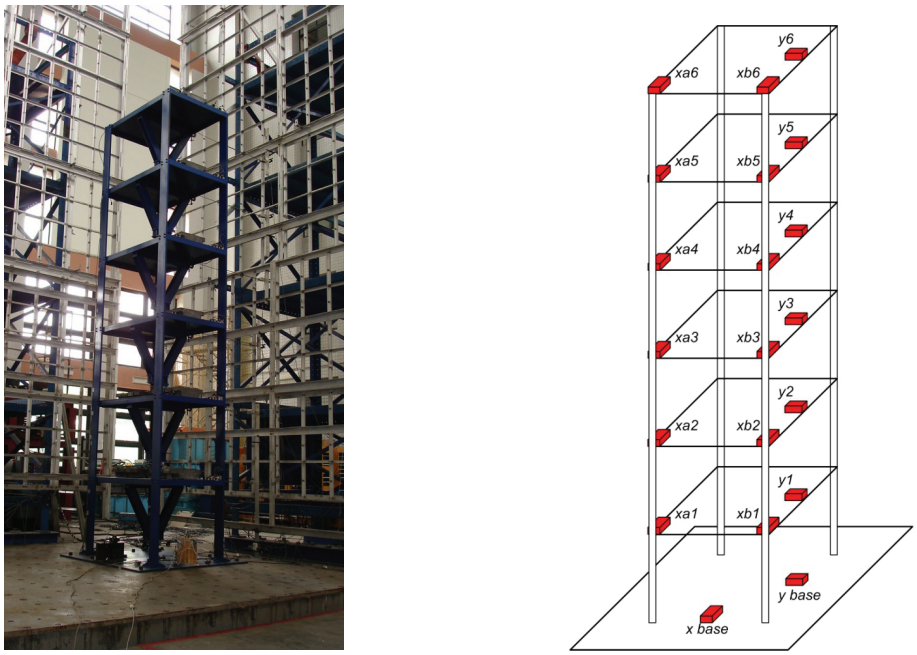

(a) (b)

Figure 3.5 Large-scale six-story steel frame building structure: (a) perspective view of test structure on NCREE shake table; (b) schematic of the sensor installation (20 accelerometers).

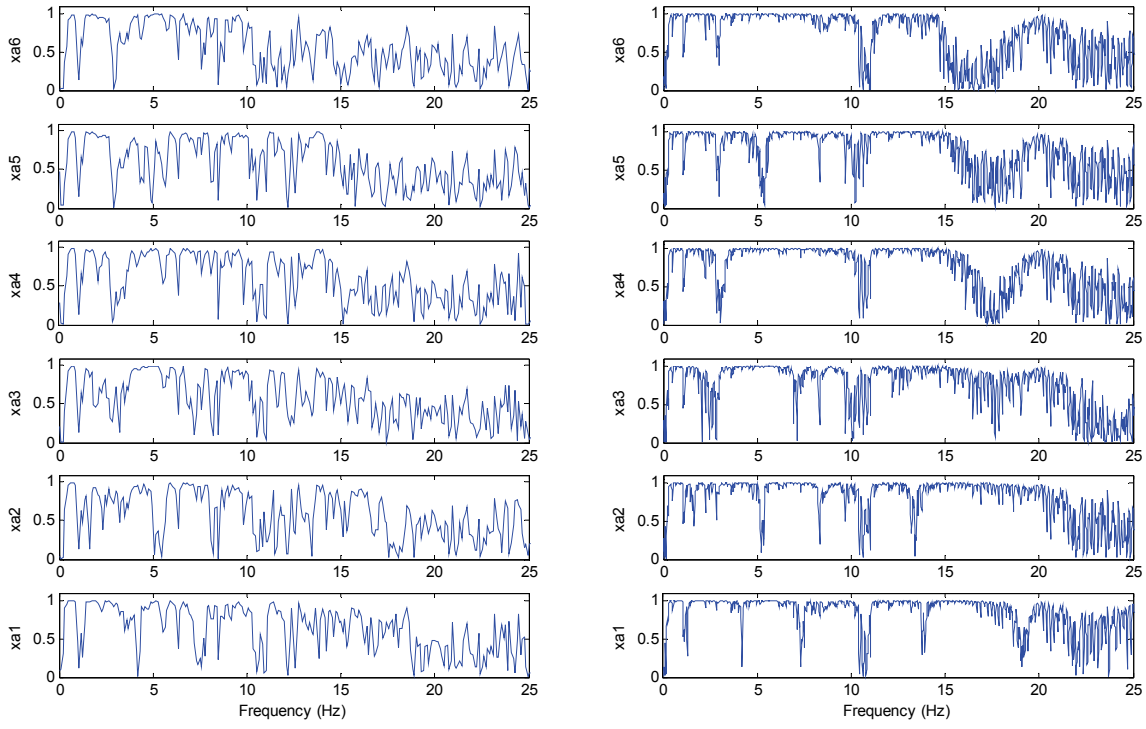

(a) (b)

Figure 3.6 Coherence of input-output PSD of the support-excited steel frame structure in the x-direction: (a) El Centro test; (b) white noise test.

3.4.2 Black-Box Input-Output Model Estimation and Evaluation

Through the aforementioned testing, two sets of input-output data were collected: 1) the El Centro test and 2) white noise test. Since the N4SID algorithm is only applicable to linear systems, linearity of recorded input-output data must first be checked prior to use in off-line system identification. Towards this end, the coherence of the power spectral density (PSD) of the input and output was studied as displayed in Fig. 3.6. The white noise test (Fig. 3.6-b) shows stronger linearity than the El Cento test (Fig. 3.6-a). However, considering the small level of intensity of the input motion of the El Centro test (Fig. 3.7) as compared to that of the white noise test, it seems that the noise contamination of the measured data also strongly affects the results. Regardless, strong linearity is confirmed for both tests and system identification by N4SID is valid using the input-output data collected.

Subspace system identification by the N4SID is conducted off-line using 30 sec long input and output segments from both tests. Since structurally meaningful responses last for less than 30 sec in the El Centro test, an identical length of data is also utilized during system identification using the white noise test data. To validate the estimated black-box model, the model's ability to reproduce the output signal of the system for a given input signal is checked. Fig. 3.7 displays the predicted system output (*i.e.*, floor accelerations) compared to that measured. Before making a comparison between measured and predicted signals, the interaction between the table and structural response should be noted. Specifically, due to the dynamic feedback of the structural motion to the shaking table, the input motions are slightly different from the El Centro earthquake and white noise input records. Regardless, a very close match is discovered in both tests: intuitively, the deterministic predicted output signal strongly agrees with the measured signal. The small differences encountered between the predicted and actual measured signals seems to be random along the time axis and is considered as an innovation process or a random residual of the prediction. To confirm this belief, stochastic signal analysis is conducted on the prediction residuals.

Ideally, the residual is an asymptotically Gaussian process with zero mean and independent from the input record. This ideal condition can be checked using the autocorrelation function of the residual and the cross-correlation between the residual and the input. Fig. 3.8 plots the autocorrelation and the cross-correlation functions for the El Centro test. In the case of the autocorrelation function (Fig. 3.8-a), a high peak at time lag 0 implies strong whiteness of the residual time series. After time lag 0, a small-value bounded signal implies a little coloredness to the residual with a certain uncertainty. Furthermore, a small arbitrary signal along the time lag

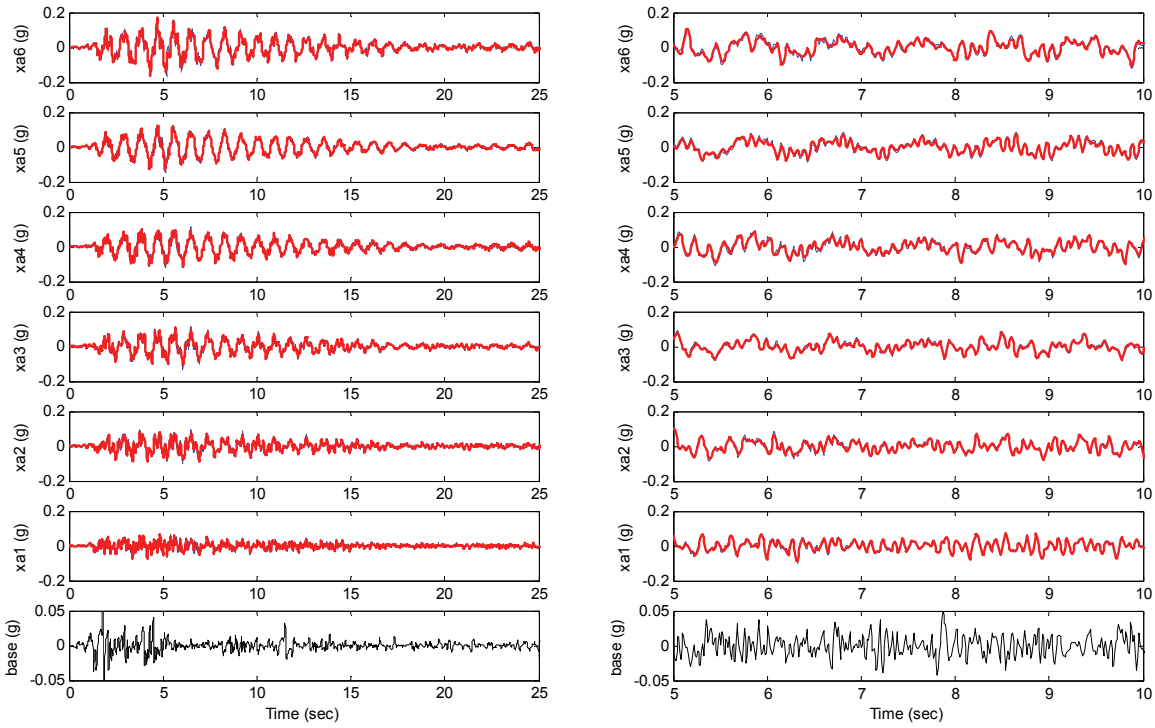

Figure 3.7 Comparison plots of the measured (thin) versus predicted in the x-direction (thick): (a) El Centro test; (b) white noise test. The base excitation is also shown for each test.

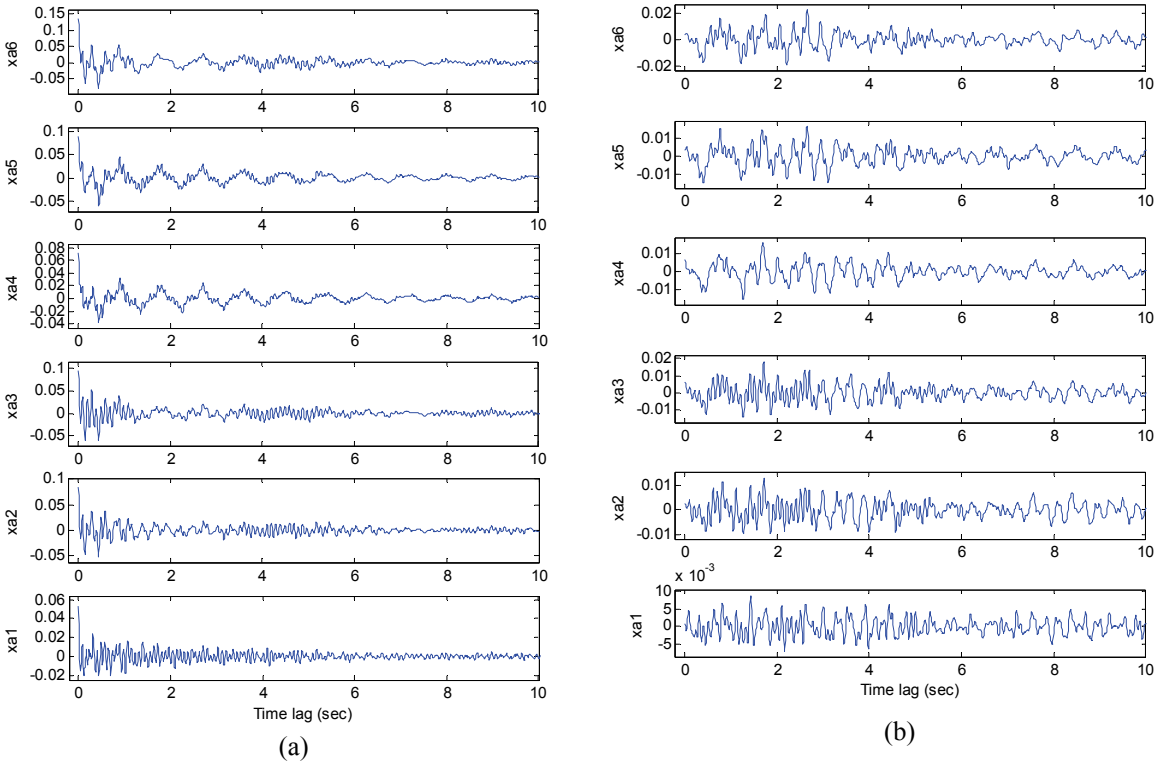

Figure 3.8 Stochastic residual analysis for the El Centro test: (a) autocorrelations of model residuals; (b) cross-correlations of residuals and the applied base signal.

axis is found in the cross-correlation function (Fig. 3.8-b), which implies the residual is not related to the input signal. Based on the excellent results of the model's ability to reproduce the deterministic output signal of the system (Fig. 3.7), the whiteness of the residual (Fig. 3.8-a), and model's independence to the system input (Fig. 3.8-b), the performance of the N4SID analysis is validated and the accuracy of the estimated black-box model is also confirmed for both tests.

3.4.3 Black-Box Output-Only Model Estimation

The deterministic subsystem (*i.e.*, Eq. (3.5)) is ignored to conduct stochastic subspace system identification of the support-excited structure. The model $\{\mathbf{A}, \mathbf{C}\}$ is estimated by:

$$\begin{bmatrix} \hat{\mathbf{A}} \\ \hat{\mathbf{C}} \end{bmatrix} = \begin{bmatrix} \hat{\mathbf{X}}_{i+1} \\ \mathbf{Y}_{i|i} \end{bmatrix} \hat{\mathbf{X}}_i^{\dagger} \tag{3.51}$$

In Eq. (3.51) only output data is used and no knowledge of the system input is needed.

3.5 Comparison of Input-Output and Output-Only Black-Box Models

A validation of the black-box model estimated by input-output identification was presented in the previous section. However, a black-box model by output-only identification (*i.e.*, stochastic subspace system identification) is difficult to be verified by prediction (since no determinist input is measured). Hence, the conventional approach to validate black-box models derived from output-only identification is to compare modal parameters.

3.5.1 Modal Parameter Estimation

Modal parameters (*e.g.*, mode shapes, natural frequencies, and damping ratio) can be estimated from both input-output and output-only black-box models. Modal parameters are extracted from the estimated system matrices, $\hat{\mathbf{A}}$ and $\hat{\mathbf{C}}$. The estimated system matrix $\hat{\mathbf{A}}$ can be decomposed by eigen-decomposition as:

$$\hat{\mathbf{A}} = \boldsymbol{\Psi}\boldsymbol{\Lambda}\boldsymbol{\Psi}^{-1} \tag{3.52}$$

where the diagonal matrix $\mathbf{\Lambda} = \text{diag}(\lambda_{di}) \in \mathbb{C}^{2n \times 2n}$, ($i = 1, \cdots, 2n$) consists of the discrete-time complex eigenvalues, λ_{di} , (*i.e.*, system poles in the *z*-plane). $\mathbf{\Psi} \in \mathbb{C}^{2n \times 2n}$ contains the complex-valued eigenvectors in each column. By using the discrete time interval, Δt , the continuous-time complex eigenvalues (*i.e.*, system poles in the *s*-plane) can be calculated as:

$$\lambda_{ci} = \frac{\ln(\lambda_{di})}{\Delta t} \tag{3.53}$$

The real and imaginary components of the conjugate pairs of eigenvalues can be written as:

$$\lambda_{ci}, \lambda_{ci}^{*} = -\varsigma_i \omega_{ni} \pm j\omega_{ni}\sqrt{1-\varsigma_i^2} \tag{3.54}$$

where ς_i is the damping ratio of *i*-th mode and ω_{ni} is the natural frequency of *i*-th mode. The mode shape vectors for *i*-th mode $\Phi_i \in \mathbb{C}^n$, can be calculated as:

$$\mathbf{\Phi} := \begin{bmatrix} \Phi_1 & \cdots & \Phi_i & \cdots & \Phi_n \end{bmatrix} = \hat{\mathbf{C}}\,\mathbf{\Psi} \tag{3.55}$$

3.5.2 Output-Only Black-Box Model Validation by Modal Parameter Comparison

Modal parameter comparison between the output-only model and the previously evaluated input-output model (in Section 3.4.2) is conducted in order to evaluate the output-only model. A comparison of the modal parameters is tabulated in Table 3.1 and Table 3.2, respectively for the El Centro and white noise tests, respectively. Mode shapes for the El Centro test (both, input-output and output-only models) are depicted in Fig. 3.9. In total, 12 modes are identified in both the El Centro models and the white noise models. Mode 1, 4, 5, 7, 9, and 10 are clearly flexural modes in the x-direction, while modes 2, 6, and 11 are flexural modes in the y-direction. Mode 3, 8 and 12 are pure torsional modes.

Output-only subspace system identification is supposed to generate some estimation outliers, since it is based on stochastic analysis. In this study, anomalous outliers are identified when comparing the natural frequencies, damping ratios, and mode shapes (or modal assurance criteria, also termed MAC) of the output-only models to those from the input-output models. Namely, modal parameters deemed as big or small are highlighted in Tables 3.1 and 3.2 using a grey shading. The output-only identification of the system using the white noise test data shows much closer agreement with that of the input-output identification with fewer outliers found. In contrast,

Table 3.1 Comparisons of estimated modal parameters for the El Centro test from input-output identification and output-only identification with 30 sec long data.*

Mode number	Natural frequencies (Hz)			Damping ratio			MAC value
	Input-Output	Output-only	Error (%)	Input-Output	Output-only	Error (%)	
Mode 1	1.115	1.125	0.880	0.013	0.006	57.477	0.999
Mode 2	2.206	2.192	0.643	0.019	0.008	57.384	0.037
Mode 3	3.056	3.198	4.650	0.062	0.051	16.855	0.927
Mode 4	3.626	3.630	0.123	0.010	0.010	0.558	0.990
Mode 5	6.324	6.310	0.227	0.009	0.017	85.510	0.998
Mode 6	8.454	8.333	1.432	0.015	0.026	70.177	0.996
Mode 7	9.225	9.254	0.323	0.009	0.011	19.914	0.989
Mode 8	10.270	10.240	0.286	0.011	0.015	30.130	0.997
Mode 9	12.122	12.055	0.556	0.004	0.009	152.256	0.861
Mode 10	14.329	14.337	0.052	0.004	0.004	3.457	0.963
Mode 11	19.544	19.583	0.202	0.010	0.023	121.802	0.832
Mode 12	21.870	21.812	0.262	0.016	0.016	3.332	0.971
Mean			0.803	0.015	0.016	51.571	0.880

* Note: Grey shaded numbers indicate anomalous results.

Table 3.2 Comparisons of estimated modal parameters for the white noise test from input-output identification and output-only identification with 30 sec long data.*

Mode number	Natural frequencies (Hz)			Damping ratio			MAC value
	Input-Output	Output-only	Error (%)	Input-Output	Output-only	Error (%)	
Mode 1	1.123	1.121	0.011	0.011	0.005	52.094	1.000
Mode 2	2.243	2.232	0.018	0.018	0.030	67.774	0.999
Mode 3	2.937	2.931	0.013	0.013	0.013	3.464	0.228
Mode 4	3.627	3.639	0.009	0.009	0.009	0.894	1.000
Mode 5	6.327	6.352	0.008	0.008	0.010	23.874	1.000
Mode 6	8.535	8.525	0.013	0.013	0.015	9.703	0.999
Mode 7	9.208	9.169	0.007	0.007	0.011	50.648	0.998
Mode 8	10.452	10.421	0.009	0.009	0.012	27.985	0.981
Mode 9	12.090	12.092	0.005	0.005	0.004	14.979	0.954
Mode 10	14.335	14.343	0.003	0.003	0.006	69.438	0.990
Mode 11	19.758	19.701	0.009	0.009	0.015	60.688	0.999
Mode 12	21.975	21.987	0.006	0.006	0.007	13.804	0.996
Mean			0.009	0.009	0.011	32.946	0.929

* Note: Grey shaded numbers indicate anomalous results.

the output-only models derived from the El Centro test data set appear to have more anomalous results. This discovery is not surprising due to the narrow band colored attributes of the El Centro excitation. If it is assumed that the input-output model estimated from the white noise test data is the most accurate model, it can then serve as the baseline model to which all the other models can be compared. Therefore, assuming the accuracy of the identified model from the input-output

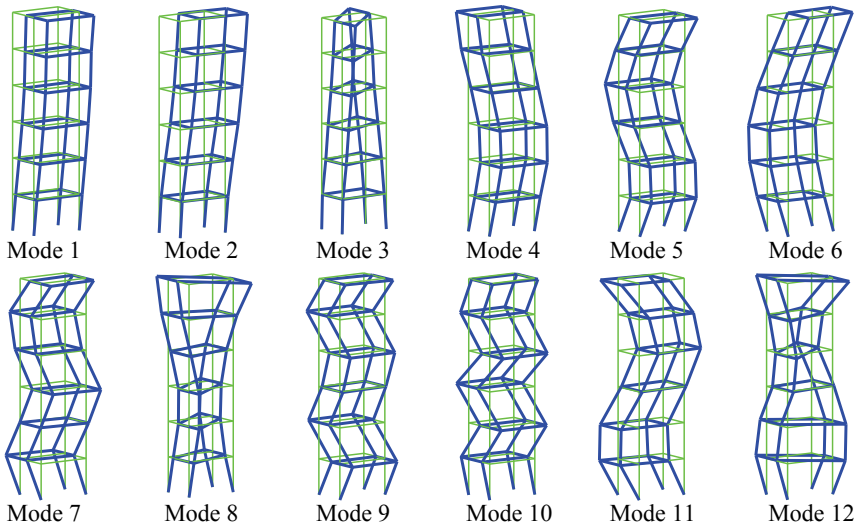

(a)

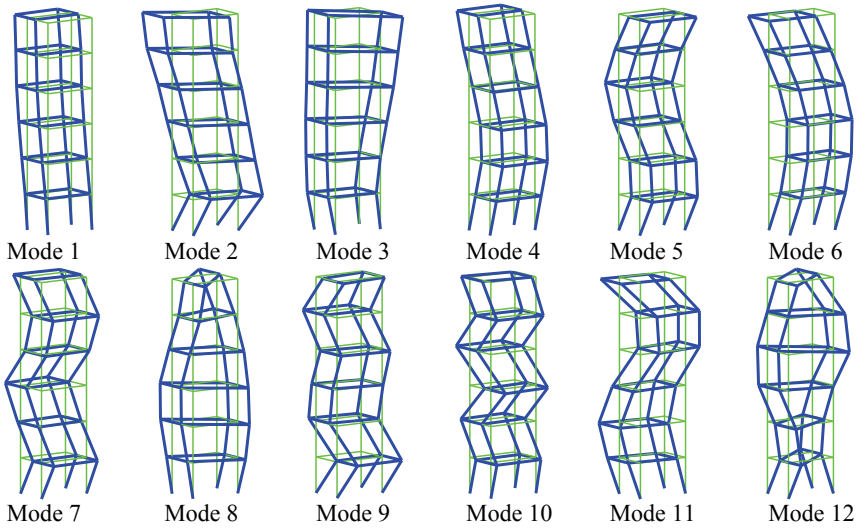

(b)

Figure 3.9 Mode shapes extracted from the system matrices $\{\mathbf{A},\mathbf{C}\}$ estimated from the El Centro test data: (a) input-output analysis; (b) output-only analysis.

data of the white noise test is of the highest order, it can then be concluded that the accuracies of the output-only models depend on the input quality (*i.e.*, coloredness), since the fundamental assumption of output-only identification is that the excitation is ideally white noise. In other words, the output-only model estimated from the white noise test data is nearly perfect while the output-only model extracted from the El Centro test data set is not as accurate. However, even for

this colored narrow-band excitation, the output-only model is still an excellent model that is still quite close to the input-output model estimated from the white noise test data.

In Reynders *et al.* (2008), there is an analytical formula that describes the uncertainty bound of covariance-based output-only system identifications. Covariance-based output-only identification is directly based on Ho and Kalman's realization using the estimated output covariance sequence; this is different from the N4SID where projection operations replace the need to compute covariance. Reynders derives an equation which relates the perturbation of the output covariance to the perturbation of modal parameters. Based on their equation, the uncertainty bound (with a 95 % reliability) on the modal parameters from the covariance-based output-only identification can be calculated under the assumption of an ideal white noise input. Even though direct comparison between the uncertainty bound and the results of this study (Table 3.2) is difficult, a similar conclusion can be drawn from Table 3.2: estimation of natural frequency and mode shape from output-only identification is accurate for white noise inputs but the estimation of modal damping remains very challenging.

3.6 Chapter Summary and Conclusions

This chapter provided a detailed explanation of the subspace system identification algorithm (*i.e.*, N4SID); N4SID is a powerful estimation tool for formulating black-box state-space models. One of the most difficult concepts in the N4SID (*i.e.*, estimation of the non-stationary state Kalman filter state sequence without knowledge of system matrices) was geometrically explained. In addition to the theoretical exploration of the N4SID, the application of the method to classical identification problems in the structural engineering (*i.e.*, system identification of support-excited structures) was also introduced. A partial scale six-story steel frame structure mounted on a shaking table (NCREE, National Taiwan University, Taiwan) was identified under two base excitations (*i.e.*, scaled El Centro earthquake and white noise). The accuracy of the estimated model using input-output data was evaluated deterministically (*i.e.*, comparison of the estimated model's prediction and the measured response) and stochastically (*i.e.*, correlation analysis of the residual error of the prediction). Based on confirmation of the accuracy of the estimated model by input-output system identification, the accuracy of the output-only model was checked by comparing modal parameters of the input-output model and the output-only model. It was confirmed that the estimated model by output-only identification using white noise test data provided that the most accurate output-only model. The modal parameters of these models were in excellent agreement with those of the input-output model.

CHAPTER 4

GREY-BOX INTERPRETATIONS OF SUBSPACE SYSTEM IDENTIFICATION MODELS FOR DAMAGE DETECTION OF SUPPORT-EXCITED STRUCTURES

In the previous chapter (Chapter 3), input-output and output-only state-space models were estimated for support-excited structures based on subspace system identification. As previously discussed, such models are black-box models; mathematically, they provide the best possible model to fit the data but are not based on any physical interpretations of the system. In contrast, this chapter offers a theoretical framework that allows physical parameters of the structure to be estimated by considering two state-space models: a physics-based model and a data-driven mathematical model derived from subspace identification. For support-excited structures, the two state-space models are derived physics-based and subspace system identification followed by canonical form conversion. Canonical form conversion allows the data-driven mathematical model to be explicitly linked to the physics-based model; through this linking, physical parameters can be estimated from the data-driven mathematical model (mentioned as the grey-box model). The estimated physical parameters are then utilized to capture any structural change that may have occurred in the structure. As a result, this grey-box approach to system identification can serve as a powerful tool in assessing the health of a monitored structure with that goal in mind. The proposed system identification methodology is experimentally verified using the six-story steel frame structure introduced in Chapter 3. Specifically, intentional damage is introduced to the structure to determine if the grey-box system identification method is sufficiently accurate to capture the damage location and severity.

4.1 Introduction

System identification is the art and science of building a mathematical model of a dynamic system using experimental data (Ljung 1999). System identification has been under development in a number of different engineering communities since the 1960's. The goal of system identification largely depends on the requirements of the applications: In the control community, system identification has been studied extensively, since the establishment of the prediction error method (PEM) by Ljung and his colleagues in the 1980's (Gevers 2003). Prediction by an estimated mathematical model of the system plays a vital role in the design of a feedback control system because the estimated model provides an efficient means of describing the system dynamics without requiring a deep understanding of the system's physical principles. In the structural engineering community, the prediction of the response of the structural system is also an important application of system identification. With the emergence of structural health monitoring (SHM), system identification has historically played a significant role since an estimated mathematical model reflecting the system dynamics can be used for damage detection (Betti 2008). For example, a model of the system estimated before and after damage will likely have notable differences. The PEM requires canonical parameterization when applied to state-space model estimation. Furthermore, it requires nonlinear search to solve an optimization problem; this can lead to poor convergence, especially for multi-input multi-output (MIMO) systems. An early application of PEM to the identification of structures is reported by Hjelmstad *et al.* (Hjelmstad *et al.* 1993). Their study utilized the finite-element formulation as a canonical parameterization under the assumption that the geometry of the structure is known. As part of their approach, a nonlinear search is conducted along the time axis to estimate system parameters.

A new approach to system identification emerged in the control community in the 1990's, which has been named as subspace system identification (Larimore 1990; Van Overschee and De Moor 1994; Verhaegen 1994). The most notable characteristic of subspace system identification is to eliminate the need to specify a canonical parameterization of the mathematical model of the system. Rather, subspace system identification allows to estimate a mathematical model of the system directly from data skipping a consideration of the underlying physics of the system. Furthermore, subspace system identification does not involve a nonlinear search. The approach has gained popularity in the control community; Ljung (2009) proposed the use of subspace system identification as an initial model for PEM in 2000. While very powerful, structural engineers have not paid much attention to subspace system identification due to the absence of a

physical explanation of the method and the complex mathematical derivation. Only recently subspace system identification has made major inroads in the structural engineering community.

In the literature, there are countless studies on system identification methods applied to SHM. These studies are divided into global vibration-based damage detection methods (Doebling *et al.* 1998) and local active sensing damage detection methods (Park *et al.* 2000). The methods applied to global vibration-based damage detection methods using linear time-invariant (LTI) state-space models are most relevant to this thesis. Such methods have been used to estimate the spatial distribution of a structure's physical parameters, such as mass, stiffness, and damping. By monitoring changes in these physical parameters, the condition of the structure can be estimated. Betti (2008) provided an overview of the area and presented methodologies that he and colleagues have developed (Lus *et al.* 2003; Franco *et al.* 2006; Betti 2008). Their methodologies consist of two major steps: 1) estimation of a state-space model from input-output data; 2) estimation of physical parameters from the state-space model via normalized complex eigen-properties under the assumption of a proportionally damped system (Ibrahim 1983; Balmes 1997). The physical parameters are spatial distributions of the structure's mass, stiffness, and damping in the form of finite element discretization. The first step, which is referred to as minimal realization, is the identification of the system's impulse response function by the observer Kalman filter identification (OKID) method followed by the eigensystem realization algorithm (ERA) (Juang and Pappa 1984; Juang *et al.* 1991). The OKID and ERA are based on the Kalman filter (Kalman 1960) and the Ho and Kalman realization algorithm (Ho and Kalman 1965), respectively. Application of these methodologies to damage detection in structures was studied for the case of: 1) a full set installation of sensors and actuators to degree-of-freedom (DOF) (De Angelis *et al.* 2002); 2) a sparse set of sensors and actuators (Lus *et al.* 2003) applied to DOF; 3) an undamped shear-type structure (Franco *et al.* 2006). Xiao *et al.* (2001) also proposed a unique methodology directly extracting matrices of system physical parameters from a minimal realization with *a priori* information of the structure's mass distribution (Xiao *et al.* 2001). They also defined the problem of a sparse set of sensors and actuators as an optimization problem that can be solved by an iterative algorithm. The aforementioned damage detection algorithms by Betti *et al.* and Xiao *et al.* were demonstrated using numerical simulation of various structure types.

This chapter tries to offer a bridge between the two different (*i.e.*, control and structural engineering) system identification communities balancing the heritages from both communities to solve the damage detection problems in civil structures. On one hand, the physics-based models

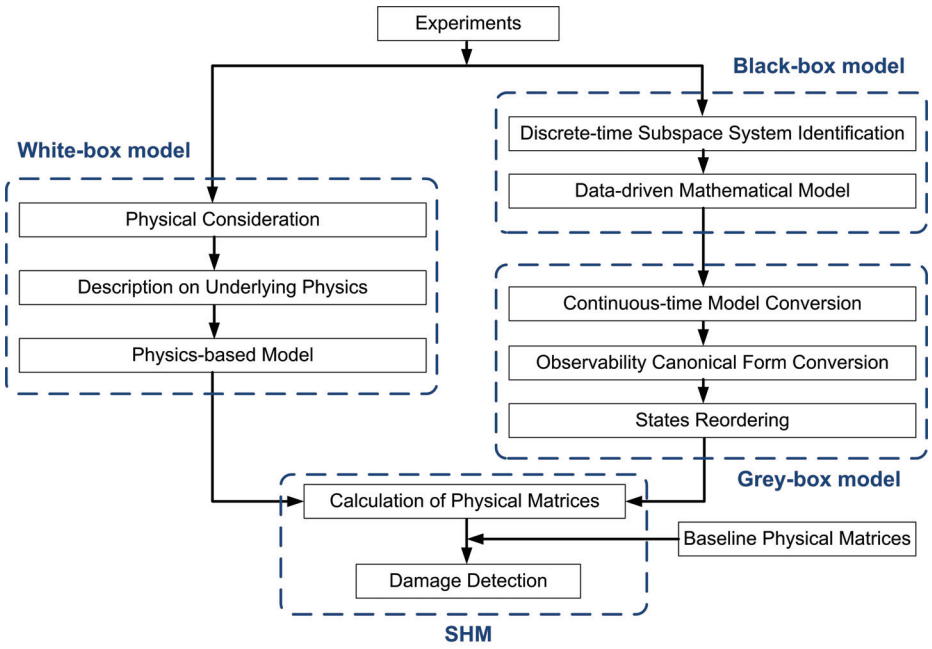

Figure 4.1 Algorithmic flow of the proposed estimation of physical parameters.

are derived for support-excited structures. On the other hand, the underlying physics of the system is ignored and a data-driven mathematical model is identified from experimental data by means of subspace system identification. What might appear to be two different representations of the system can be equated through the use of the mature linear system theories (Kailath 1980; Chen 1984) available in the control system community. Specifically, the mathematical model of the system can be manipulated through canonical form conversion. Next, the physics-based model and the data-driven mathematical model are linked together in order to extract the physical parameters of the system. The black-box model derived by data-driven subspace system identification is effectively converted to a grey-box model; this grey-box model, with its physical meaning, may serve as a valuable tool for SHM. The proposed strategy is summarized in Fig. 4.1. For validation, a series of experimental vibration tests were conducted on the same six-story steel frame structure built on the shaking table at the National Center for Research in Earthquake Engineering (NCREE) presented in Chapter 3. This structure is excited with different damage cases introduced. Physical parameter estimations, followed by system identification, were conducted off-line using input-output data and output-only data sets. Quantitative evaluation of the system parameter allow the location and severity of damage to be identified using the proposed strategy.

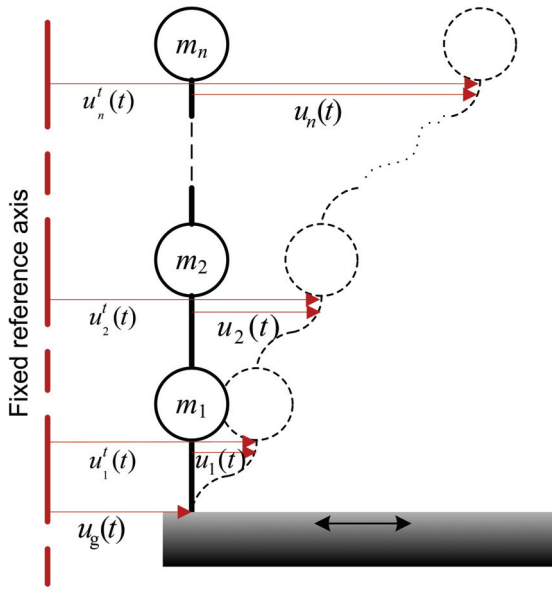

Figure 4.2 Lumped mass, shear structure deformed under a base motion excitation.

4.2 State-Space Model Formulation from Underlying Physics

The equation of motion of a discrete-time finite degree-of-freedom (DOF) structural system with n lumped masses and excited by base motion (Fig. 4.2) can be formulated as:

$$\mathbf{M}\ddot{\mathbf{u}}^t(t) + \mathbf{F}_{nc}(\dot{\mathbf{u}}(t), \mathbf{u}(t)) + \mathbf{K}\mathbf{u}(t) = \{\mathbf{0}\} \tag{4.1}$$

where $\mathbf{M} = \sum_e^n \mathbf{M}^e \in \Re^{n\times n}$, $\mathbf{K} = \sum_e^n \mathbf{K}^e \in \Re^{n\times n}$, and $\mathbf{F}_{nc} = \sum_e^n \mathbf{F}_{nc}{}^e \in \mathbb{C}^{n\times n}$ are the system's mass, stiffness, and non-conservative force matrices, respectively. In addition, $\mathbf{u}^t \in \Re^n$ and $\mathbf{u} \in \Re^n$ are the total and relative (with respect to the support) displacement vectors, respectively.

The first term in Eq. (4.1) represents the inertia force which is the rate of change of momentum of any mass node. The third term represents the spring force which is a linear-elastic approximation of the structure based on Hooke's law. The second term represents non-conservative forces. Generally, non-conservative forces are related to dissipation of energy and are typically considered as damping forces. Numerous damping forces have been formulated in the field of structural dynamics. Viscous damping, which is damping that is proportional to velocity, has been popular because it can be modeled as dashpots that allows the differential equation of the system (*i.e.*, Eq. (4.1)) to be linear using real numbered coefficients. Hysterestic

damping (or structural damping) can also be used which is proportional to the out-of-phase displacement of the system's mass nodes. Hysterestic damping accurately captures the energy dissipation in civil structures, but results in a linearization with complex numbers in Eq. (4.1). Coulomb damping can be also considered, which represents energy dissipation from friction. Coulomb damping has a nonlinear formulation because the friction force acts in the opposite direction of the motion of the mass node. In this study, equivalent viscous damping is adopted to ensure compatibility with subspace system identification which deals with real numbered matrix operations for linear time-invariant (LTI) systems.

Using equivalent viscous damping, the equation of motion can be written:

$$\mathbf{M}\ddot{\mathbf{u}}^{t}(t) + \mathbf{C}\dot{\mathbf{u}}(t) + \mathbf{K}\mathbf{u}(t) = \{\mathbf{0}\} \tag{4.2}$$

where $\mathbf{C} = \sum_{e}^{n} \mathbf{C}^{e} \in \Re^{n \times n}$ is the system damping matrix. Assuming the structure is modeled as a shear-structure, the deformation of the system is concentrated in the columns as shown in Fig. 4.2. The total displacement in Eq. (4.2) can be expressed as the sum of support motion (absolute displacement) $u_g(t) \in \Re$ and relative displacement. Since the relative displacement is parallel to the absolute displacement, the total displacement of the shear structure is given by:

$$\mathbf{u}^{t}(t) = \mathbf{u}(t) + \{\mathbf{1}\}u_g(t) \tag{4.3}$$

where $\{\mathbf{1}\} \in \Re^{n}$ is a unitary vector. By substituting Eq. (4.3) in Eq. (4.2), the equation of motion with respect to the ground motion is formulated as:

$$\mathbf{M}\ddot{\mathbf{u}}(t) + \mathbf{C}\dot{\mathbf{u}}(t) + \mathbf{K}\mathbf{u}(t) = -\mathbf{M}\{\mathbf{1}\}\ddot{u}_g(t) \tag{4.4}$$

The equation of motion will now be converted to a form compatible with the data-driven mathematical model to be formulated later. The differential operator is applied twice to both sides of Eq. (4.4):

$$\mathbf{M}\overset{\cdots\cdot}{\mathbf{u}}(t) + \mathbf{C}\ddot{\mathbf{u}}(t) + \mathbf{K}\ddot{\mathbf{u}}(t) = -\mathbf{M}\{\mathbf{1}\}\overset{\cdots\cdot}{u}_g(t) \tag{4.5}$$

Assuming the mass matrix is square and invertible, both sides of Eq. (4.5) can be pre-multiplied by $\mathbf{M}^{-1}$ and arranged as follows:

$$\dddot{\mathbf{u}}(t) = -\mathbf{M}^{-1}\mathbf{K}\,\ddot{\mathbf{u}}(t) - \mathbf{M}^{-1}\mathbf{C}\,\ddot{\mathbf{u}}(t) - \{\mathbf{1}\}\dddot{u}_g(t) \tag{4.6}$$

Now, a state-space model will be created from Eq. (4.6). By defining the state with acceleration and its differential $\left(\mathbf{x}(t) \coloneqq \left[\ddot{\mathbf{u}}(t)^T \quad \dddot{\mathbf{u}}(t)^T\right]^T\right)$, the continuous-time state-space equation is formulated as:

$$\dot{\mathbf{x}}(t) = \mathbf{A}_\mathbf{c}\mathbf{x}(t) + \overline{\mathbf{B}}_\mathbf{c}\dddot{u}_g(t) \tag{4.7}$$

where

$$\mathbf{A}_\mathbf{c} = \begin{bmatrix} \mathbf{0} & \mathbf{I} \\ -\mathbf{M}^{-1}\mathbf{K} & -\mathbf{M}^{-1}\mathbf{C} \end{bmatrix} \in \Re^{2n\times 2n} \tag{4.8}$$

$$\overline{\mathbf{B}}_\mathbf{c} = \begin{bmatrix} \{\mathbf{0}\} \\ -\{\mathbf{1}\} \end{bmatrix} \in \Re^{2n} \tag{4.9}$$

If it is assumed that an accelerometer is installed on every lumped mass, then the observation equation can be formed. Absolute acceleration, $\ddot{\mathbf{u}}^t(t)$, is calculated by applying the differential operator twice to Eq. (4.3) as:

$$\ddot{\mathbf{u}}^t(t) = \ddot{\mathbf{u}}(t) + \{\mathbf{1}\}\ddot{u}_g(t) \tag{4.10}$$

Accelerometers are electromechanical systems which have very fast dynamics compared to structural system dynamics. Thus, the fundamental dynamics of the sensor can be ignored. Hence, the observation equation does not involve a differential equation. By the predefined state vector, the observation equation is formulated as:

$$\mathbf{y}(t) = \mathbf{C}_\mathbf{c}\,\mathbf{x}(t) + \mathbf{D}_\mathbf{c}\ddot{u}_g(t) \tag{4.11}$$

where $\mathbf{C}_\mathbf{c} = \begin{bmatrix}\mathbf{I} & \mathbf{0}\end{bmatrix} \in \Re^{n\times 2n}$ and $\mathbf{D}_\mathbf{c} = \{\mathbf{1}\} \in \Re^{n}$. The continuous-time state-space model (*i.e.*, Eqs (4.7) and (4.11)) derived from the underlying physics of the system is referred to as the "white-box model" in this study and is depicted in Fig. 4.3-a.

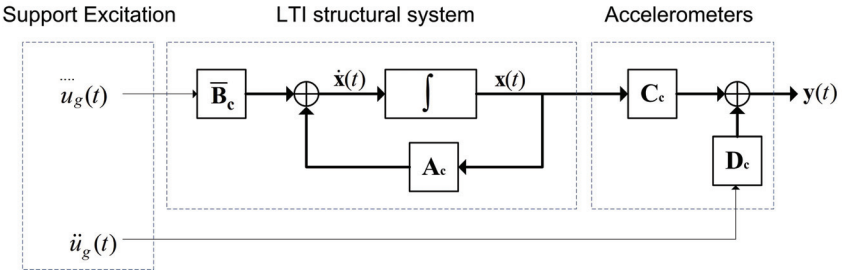

(a)

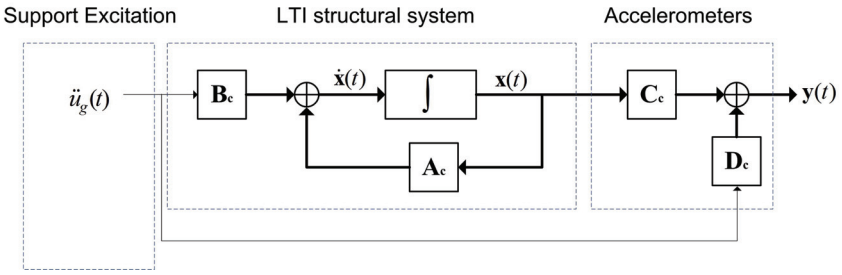

(b)

Figure 4.3 Continuous-time state-space model for support-excited structures with acceleration measurements: (a) physics-based model; (b) data-driven mathematical model.

4.3 State-Space Model Estimation from Experiments

A state-space model is created using the input-output data set of a support-excited structure. using subspace system identification. Let us assume the discrete-time system matrices, $\mathbf{A_d} \in \Re^{2n \times 2n}$, $\mathbf{B_d} \in \Re^{2n}$, $\mathbf{C_d} \in \Re^{n \times 2n}$, and $\mathbf{D_d} \in \Re^{n}$ are identified up to similarity transformation by the N4SID algorithm (Chapter 3) using the measured ground acceleration (*i.e.*, input) and the accelerations of the structure masses (*i.e.*, output). Since the identified data-driven model is a "black-box model", the states are arbitrary and unknown. There are mathematical procedures that allow the black-box model to be physically interpreted. In effect, the conversion renders the model into a "grey-box model". The physics-based model previously developed is defined in the continuous-time domain. Hence, the discrete-time state-space model must be converted to the continuous-time domain as follows:

$$\mathbf{A_c} = \frac{1}{\Delta t} \ln(\mathbf{A_d}) \tag{4.12}$$

$$\mathbf{B_c} = \left(\int_0^{\Delta t} \exp(\mathbf{A_c}\, \tau) d\tau \right)^{-1} \mathbf{B_d} \tag{4.13}$$

$$\mathbf{C_c} = \mathbf{C_d}\,;\ \mathbf{D_c} = \mathbf{D_d} \tag{4.14}$$

where Δt is the sampling time. Continuous-time state-space equations are given with the identified matrices as:

$$\dot{\mathbf{x}}(t) = \mathbf{A_c}\mathbf{x}(t) + \mathbf{B_c}\ddot{u}_g(t) \tag{4.15}$$

$$\mathbf{y}(t) = \mathbf{C_c}\,\mathbf{x}(t) + \mathbf{D_c}\ddot{u}_g(t) \tag{4.16}$$

The continuous-time state-space mathematical model is depicted in Fig. 4.3-b. The model relates the system input, $\ddot{u}_g(t)$, with the system output, $\mathbf{y}(t)$, using an internal intermediate state, $\mathbf{x}(t)$. The output is the absolute acceleration measured by accelerometers. By applying specific coordinate transformations to the intermediate state, it is possible to let the state become a specific physical quantity, *i.e.*, acceleration, which is identical to the sensor output. In this state-space model, the sensor system matrix, $\mathbf{C_c}$, would be the identity matrix for the measured states. This is a key concept of the observability canonical form of the state-space model realization (Kailath 1980).

If $\{\mathbf{A_c}, \mathbf{B_c}, \mathbf{C_c}, \mathbf{D_c}\}$ is any minimal realization of a true system, then $\{\mathbf{A_c}, \mathbf{B_c}, \mathbf{C_c}, \mathbf{D_c}\}$ and $\{\mathbf{A'_c}, \mathbf{B'_c}, \mathbf{C'_c}, \mathbf{D'_c}\}$ can be related by the similarity transformation, *i.e.*, there exists a nonsingular transformation matrix, $\mathbf{T}$, such that:

$$\mathbf{A'_c} = \mathbf{T}\mathbf{A_c}\mathbf{T}^{-1}; \quad \mathbf{B'_c} = \mathbf{T}\mathbf{B_c}; \quad \mathbf{C'_c} = \mathbf{C_c}\mathbf{T}^{-1}; \quad \mathbf{D'_c} = \mathbf{D_c} \tag{4.17}$$

The observability canonical form can be constructed by taking the transformation matrix, $\mathbf{T}$, to be the observability matrix, $\mathcal{O}$ (*i.e.*, $\mathbf{T} = \mathcal{O}$). The observation matrix $\mathbf{C_c}$ (in Eq. (4.14)) can be expressed with the n rows as:

$$\mathbf{C_c} = \begin{bmatrix} \mathbf{c}_1 \\ \vdots \\ \mathbf{c}_n \end{bmatrix} \tag{4.18}$$

where $\mathbf{c}_1, \cdots, \mathbf{c}_n \in \Re^{1\times 2n}$ are n row vectors. By using row-wise expression of $\mathbf{C_c}$, the observability matrix can be composed as:

$$\mathcal{O} = \left[\mathbf{c}_1^T \quad \cdots \quad \left(\mathbf{c}_1\mathbf{A}_\mathbf{c}^{\gamma_1-1}\right)^T \quad \mathbf{c}_2^T \quad \cdots \quad \left(\mathbf{c}_2\mathbf{A}_\mathbf{c}^{\gamma_2-1}\right)^T \quad \cdots \quad \mathbf{c}_n^T \quad \cdots \quad \left(\mathbf{c}_n\mathbf{A}_\mathbf{c}^{\gamma_n-1}\right)^T \right]^T \tag{4.19}$$

where γ_i $(i = 1,2,\cdots,n)$ are observability indices. Since a minimal state-space realization is completely observable, the rank of the observability matrix is 2*n*. Thus, all observability indices, γ_i, are 2. By Eq. (4.17), the transformed system matrices have the following structure:

$$\mathbf{A_c} = \left[\begin{array}{cc|cc|ccc|cc} 0 & 1 & 0 & 0 & \cdots & \cdots & & 0 & 0 \\ * & * & * & * & \cdots & \cdots & & * & * \\ \hline 0 & 0 & 0 & 1 & \cdots & \cdots & & 0 & 0 \\ * & * & * & * & \cdots & \cdots & & * & * \\ \hline \vdots & \vdots & \vdots & \vdots & \ddots & & & \vdots & \vdots \\ \vdots & \vdots & \vdots & \vdots & & \ddots & & \vdots & \vdots \\ \hline 0 & 0 & 0 & 0 & \cdots & \cdots & & 0 & 1 \\ * & * & * & * & \cdots & \cdots & & * & * \end{array}\right] \tag{4.20}$$

$$\mathbf{C_c} = \left[\begin{array}{cc|cc|ccc|cc} 1 & 0 & 0 & 0 & \cdots & \cdots & & 0 & 0 \\ \hline 0 & 0 & 1 & 0 & \cdots & \cdots & & 0 & 0 \\ \hline \vdots & \vdots & \vdots & \vdots & \ddots & & & \vdots & \vdots \\ \vdots & \vdots & \vdots & \vdots & & \ddots & & \vdots & \vdots \\ \hline 0 & 0 & 0 & 0 & \cdots & \cdots & & 0 & 0 \\ \hline 0 & 0 & 0 & 0 & \cdots & \cdots & & 1 & 0 \end{array}\right] \tag{4.21}$$

where * stands for a non-zero entity. The order of the states in the experimentally identified model is different from that of the predefined states in the physics-based model. By reordering the states as $\mathbf{x}(t) = \left[\ddot{u}_1(t) \quad \cdots \quad \ddot{u}_n(t) \quad \dddot{u}_1(t) \quad \cdots \quad \dddot{u}_n(t)\right]^T$, the identified system matrices $\{\mathbf{A_c}, \mathbf{B_c}, \mathbf{C_c}, \mathbf{D_c}\}$ have the following structure:

$$\mathbf{A_c} = \begin{bmatrix} \mathbf{0} & \mathbf{I} \\ \mathbf{X} & \mathbf{Y} \end{bmatrix} \in \Re^{2n \times 2n} \tag{4.22}$$

$$\mathbf{B_c} = \begin{bmatrix} \{\approx \mathbf{0}\} \\ \{\mathbf{Z}\} \end{bmatrix} \in \Re^{2n} \tag{4.23}$$

$$\mathbf{C_c} = \begin{bmatrix} \mathbf{I} & \mathbf{0} \end{bmatrix} \in \Re^{n \times 2n} \tag{4.24}$$

$$\mathbf{D_c} = \{\mathbf{W}\} \in \Re^{n} \tag{4.25}$$

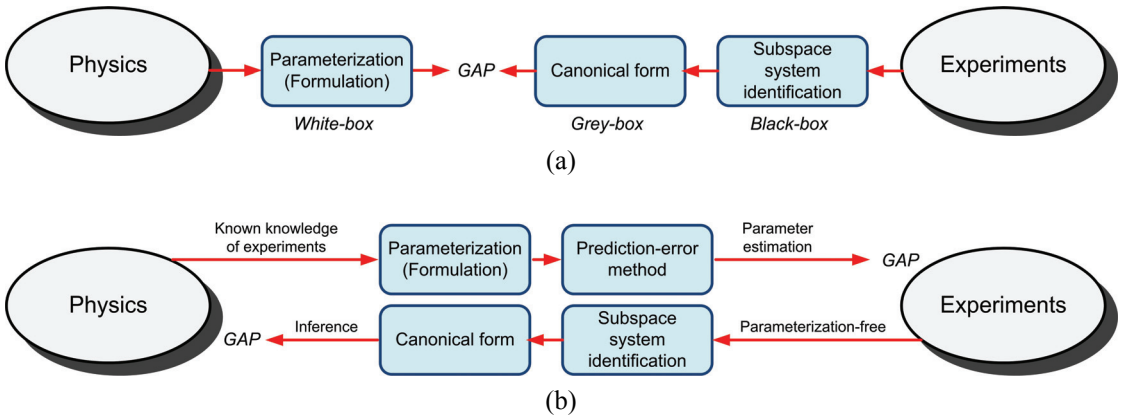

Figure 4.4 System identification of a structural system: (a) the approach proposed in this study; (b) two common approaches taken in the control community.

where $\{\approx \mathbf{0}\} \in \Re^n$ is a column vector which has trivial values and $\mathbf{X} \in \Re^{n \times n}$, $\mathbf{Y} \in \Re^{n \times n}$, $\{\mathbf{Z}\} \in \Re^n$, and $\{\mathbf{W}\}$ are portions of the system matrices that have non-zero values. By the process of observability canonical form conversion and state reordering, the continuous-time state-space mathematical model has effectively been changed to a grey-box model where internal system description is physically identified.

4.4 Physical Parameter Estimations

4.4.1 Methodology

Since the system properties are fully captured in the system matrices $\{\mathbf{A_c}, \mathbf{B_c}\}$, the physical parameters of the structural system can be estimated through a direct comparison of Eqs (4.8) and (4.9) of the physics-based model (*i.e.*, white-box model) and Eqs (4.22) and (4.23) of the data-driven mathematical model (*i.e.*, grey-box model). This approach is depicted in Fig. 4.4-a. However, as seen in Fig. 4.4-a, a gap still exists between the two models due to model discrepancies (or model errors). The existence of this gap was also an issue in the control theory community as depicted in Fig. 4.4-b. This abstract gap problem was solved by Ljung, Åström, and Söderström in the mid 1980's and is often referred to as "Ljung's cleanup" (Gevers 2003). By making a clear distinction between the true system and the model set (Ljung 1999), system identification can be considered as an approximation problem. Thus, the remaining problem is the model quality for an intended application. In this study, model quality is assessed in the context of physical parameter estimation for damage detection. This study essentially adopts the Ljungian

engineering approach. As seen in Fig. 4.3, the two models (*i.e.*, physics-based and data-driven mathematical models) are similar but not identical; the system input matrices $\overline{\mathbf{B}}_\mathbf{c}$ and $\mathbf{B}_\mathbf{c}$ have different physical meaning, especially for support-exited structures. Admitting this difference, this study aims to estimate the physical parameters of the system by comparing the system matrix, $\mathbf{A}_\mathbf{c}$, of the models. It should be noted that this strategy can be equivalently applied to output-only system identification.

Comparing the system matrix, $\mathbf{A}_\mathbf{c}$, of the white-box and grey-box models gives:

$$\mathbf{X} = -\mathbf{M}^{-1}\mathbf{K} \tag{4.26}$$

$$\mathbf{Y} = -\mathbf{M}^{-1}\mathbf{C} \tag{4.27}$$

Pre-multiplying **M** on both sides of Eqs (4.26) and (4.27) yields:

$$\mathbf{M}\,\mathbf{X} = -\mathbf{K} \tag{4.28}$$

$$\mathbf{M}\,\mathbf{Y} = -\mathbf{C} \tag{4.29}$$

Numerous solutions for **M**, **C**, and **K** given the grey-box **X** and **Y** matrices exist mathematically. For the purpose of damage detection through system identification, the structure's spatial distribution of stiffness and damping are more meaningful, since damage is a physical phenomenon that is closely related to structural stiffness and damping rather than mass. Thus, damage is often quantified as a change in the identified **K** and **C** under the assumption of invariant spatial distributions of mass. In this study, *a priori* knowledge on the mass distribution of a structure is utilized for the purpose of extracting **K** and **C**. However, considering the potential difficulty of accurately acquiring full knowledge of a structure's mass, partial *a priori* knowledge of the mass distribution is also considered herein.

If the mass distribution of the structure is accurately known (*i.e.*, **M** can be determined), then by Eqs (4.28) and (4.29), **K** and **C** can be easily calculated. However, if **M** is not known with complete accuracy, the problem is a little bit more challenging. This problem of finding matrices can be effectively formulated using the concept of vectorized expressions (Brewer 1978; Brogan 1991):

$$vec(\mathbf{M}\,\mathbf{X}) = -vec(\mathbf{K}) \in \Re^{n^2} \tag{4.30}$$

$$vec(\mathbf{M}\,\mathbf{Y}) = -vec(\mathbf{C}) \in \Re^{n^2} \tag{4.31}$$

where $vec(\bullet)$ is the vectorized expression of the matrix; in other words, the matrix is stacked into a single column vector. Considering the Kronecker product, $\otimes$, it can be stated:

$$vec(\mathbf{M}\,\mathbf{X}) = \left[\mathbf{X}^T \otimes \mathbf{I}\right] vec(\mathbf{M}) = -vec(\mathbf{K}) \tag{4.32}$$

$$vec(\mathbf{M}\,\mathbf{Y}) = \left[\mathbf{Y}^T \otimes \mathbf{I}\right] vec(\mathbf{M}) = -vec(\mathbf{C}) \tag{4.33}$$

where $\left[\mathbf{X}^T \otimes \mathbf{I}\right] \in \Re^{n^2 \times n^2}$ and $\left[\mathbf{Y}^T \otimes \mathbf{I}\right] \in \Re^{n^2 \times n^2}$. Based on the reciprocal theorem for linear structural systems, **K** and **C** are symmetric, *i.e.*, $\mathbf{K} = \mathbf{K}^T$ and $\mathbf{C} = \mathbf{C}^T$. Applying this fact to Eqs (4.28) and (4.29) yields:

$$\mathbf{M}\,\mathbf{X} = \mathbf{X}^T\mathbf{M} \tag{4.34}$$

$$\mathbf{M}\,\mathbf{Y} = \mathbf{Y}^T\mathbf{M} \tag{4.35}$$

$$\left[\mathbf{X}^T \otimes \mathbf{I}\right] vec(\mathbf{M}) = \left[\mathbf{I} \otimes \mathbf{X}^T\right] vec(\mathbf{M}) \tag{4.36}$$

$$\left[\mathbf{Y}^T \otimes \mathbf{I}\right] vec(\mathbf{M}) = \left[\mathbf{I} \otimes \mathbf{Y}^T\right] vec(\mathbf{M}) \tag{4.37}$$

By combining Eqs (4.30), (4.31), (4.36), and (4.37), the form of a linear regression can be composed as:

$$\begin{bmatrix} \begin{bmatrix}\mathbf{X}^T \otimes \mathbf{I}\end{bmatrix} & \mathbf{0} & \begin{bmatrix}\mathbf{I}\end{bmatrix} \\ \begin{bmatrix}\mathbf{Y}^T \otimes \mathbf{I}\end{bmatrix} & \begin{bmatrix}\mathbf{I}\end{bmatrix} & \mathbf{0} \\ \begin{bmatrix}\mathbf{X}^T \otimes \mathbf{I}\end{bmatrix} - \begin{bmatrix}\mathbf{I} \otimes \mathbf{X}^T\end{bmatrix} & \mathbf{0} & \mathbf{0} \\ \begin{bmatrix}\mathbf{Y}^T \otimes \mathbf{I}\end{bmatrix} - \begin{bmatrix}\mathbf{I} \otimes \mathbf{Y}^T\end{bmatrix} & \mathbf{0} & \mathbf{0} \end{bmatrix} \begin{Bmatrix} vec(\mathbf{M}) \\ vec(\mathbf{C}) \\ vec(\mathbf{K}) \end{Bmatrix} = \{\mathbf{0}\} \tag{4.38}$$

Eq. (4.38) can be symbolized as $\mathbf{P}\,\mathbf{q} = \{\mathbf{0}\}$ where $\mathbf{P} \in \Re^{4n^2 \times 3n^2}$, $\mathbf{q} \in \Re^{3n^2}$, and $\{\mathbf{0}\} \in \Re^{4n^2}$. Depending on the partial *a priori* knowledge on mass, **P** and **q** can be partitioned by pivoting as:

$$\begin{bmatrix}\mathbf{P}_1 & \mathbf{P}_2\end{bmatrix} \begin{Bmatrix} \mathbf{q}_{\mathbf{known}} \\ \mathbf{q}_{\mathbf{TBD}} \end{Bmatrix} = \{\mathbf{0}\} \tag{4.39}$$

where $\mathbf{q}_{\mathbf{known}}$ reflects known mass parameters and $\mathbf{P}_1$ corresponds to a regressor matrix; $\mathbf{q}_{\mathbf{TBD}}$ is the to-be-determined mass, stiffness, and damping parameters and $\mathbf{P}_2$ corresponds to another regressor matrix. The least square solution for the unknown parameter vector, $\mathbf{q}_{\mathbf{TBD}}$, can be calculated from the Moore-Penrose pseudo-inverse as follows:

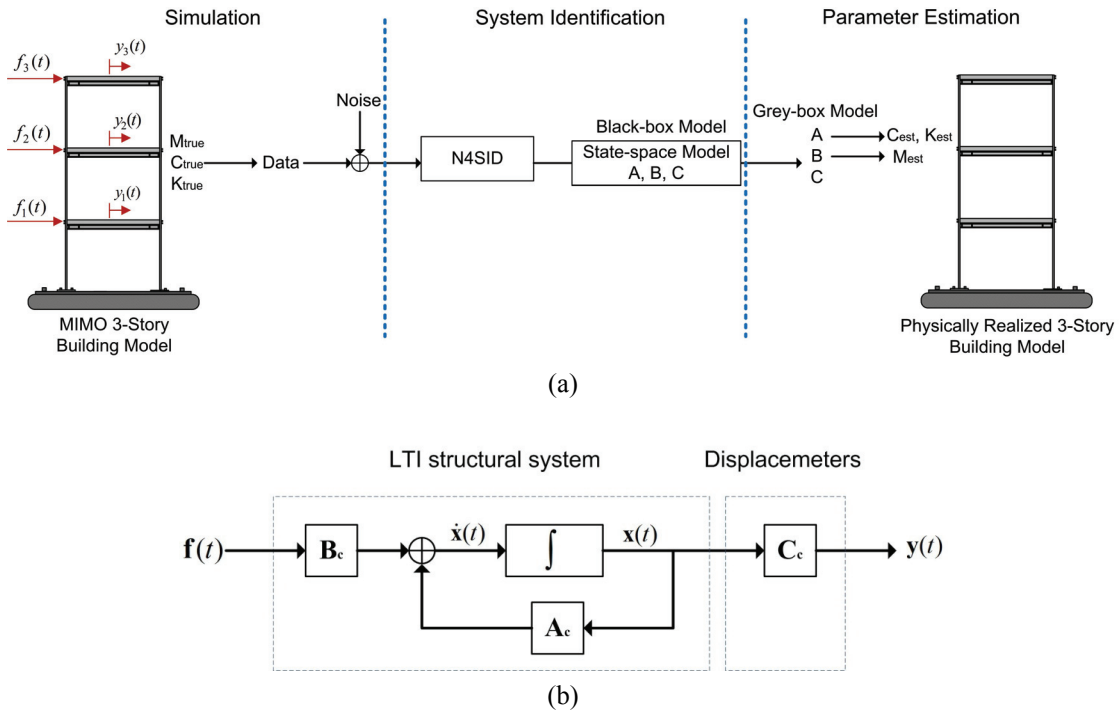

Figure 4.5 Numerical example of a 3-story building structure: (a) numerical procedures from simulation to structural parameter estimation; (b) identical white-box and grey-box model.

$$\mathbf{q}_{\mathbf{TBD}} = \mathbf{P}_2^{\dagger}\left(-\mathbf{P}_1\,\mathbf{q}_{\mathbf{known}}\right) \tag{4.40}$$

4.4.2 Numerical Example

A numerical example is studied to verify the grey-box application of subspace system identification. A simple numerical example is considered here lowering the complexities for the experimental validation state of this study. A multi-story building structure excited at each story by a measured force, *f*, is the simulated and structural responses, *y* , are measured at each story by displacemeters as seen in Fig. 4.5-a. Since the example has an identical white-box and grey-box model (Fig. 4.5-b), the problem is well suited for numerical simulation. Furthermore, the absence of the gap in Fig. 4.4-a allows performance of the physical parameter estimation to be assessed through numerical simulation. The equation of motion of the multi-story building excited at each story is formulated as:

$$\mathbf{M}\ddot{\mathbf{u}}(t) + \mathbf{C}\dot{\mathbf{u}}(t) + \mathbf{K}\mathbf{u}(t) = \mathbf{f}(t) \tag{4.41}$$

By defining the state vector as $\mathbf{x}(t) := \begin{bmatrix}\mathbf{u}(t)^T & \dot{\mathbf{u}}(t)^T\end{bmatrix}^T$, the physics-based model is derived as a continuous-time state-space model with system matrices:

$$\mathbf{A_c} = \begin{bmatrix} \mathbf{0} & \mathbf{I} \\ -\mathbf{M}^{-1}\mathbf{K} & -\mathbf{M}^{-1}\mathbf{C} \end{bmatrix} \in \Re^{2n\times 2n} \tag{4.42}$$

$$\mathbf{B_c} = \begin{bmatrix} \mathbf{0} \\ \mathbf{M}^{-1} \end{bmatrix} \in \Re^{2n\times n} \tag{4.43}$$

$$\mathbf{C_c} = \begin{bmatrix}\mathbf{I} & \mathbf{0}\end{bmatrix} \in \Re^{n\times 2n} \tag{4.44}$$

where $\mathbf{M}^{-1}$ is composed under the assumption of lumped masses as:

$$\mathbf{M}^{-1} = \begin{bmatrix} 1/m_1 & 0 & \cdots & 0 \\ 0 & 1/m_2 & \cdots & 0 \\ \vdots & \vdots & \ddots & 0 \\ 0 & 0 & 0 & 1/m_n \end{bmatrix} \in \Re^{n\times n} \tag{4.45}$$

Using simulated input-output data, a data-driven mathematical model converted to its grey-box form is also calculated as:

$$\mathbf{A_c} = \begin{bmatrix} \mathbf{0} & \mathbf{I} \\ \mathbf{X} & \mathbf{Y} \end{bmatrix} \in \Re^{2n\times 2n} \tag{4.46}$$

$$\mathbf{B_c} = \begin{bmatrix} \approx \mathbf{0} \\ \mathbf{Z} \end{bmatrix} \in \Re^{2n\times n} \tag{4.47}$$

$$\mathbf{C_c} = \begin{bmatrix}\mathbf{I} & \mathbf{0}\end{bmatrix} \in \Re^{n\times 2n} \tag{4.48}$$

where $\approx \mathbf{0} \in \Re^{n\times n}$ is a matrix with trivial values. By comparison of $\mathbf{B_c}$ in Eqs (4.43) and (4.47), the mass matrix can be determined. Then, the stiffness and damping matrices are calculated by comparison of $\mathbf{A_c}$ (*i.e.*, Eq. (4.42) compared to Eq. (4.46)) with the known mass matrix.

The whole procedure consists of five major steps as illustrated in Fig. 4.5-a: 1) physics-based system matrices are composed and numerical simulation is conducted to generate an input-output data set; 2) noise is added to the simulated data prior to system identification; 3) system identification by N4SID is conducted with the input-output data set; 4) grey-box conversion is

implemented to estimate physical parameters; 5) the 3-story shear building model is fully realized physically.

The simulation is conducted using a 3-story shear building model. Later, a 6-story steel frame structure will be experimentally tested. As a result, many of the structural properties of the 6-story test structure will be used for the 3-story structure simulated. For example, identical inter-story stiffness is used (1.9×10^6 N/m) for every story. Furthermore, the inter-story damping is considered with a certain ratio with respect to the stiffness. Three floor masses are considered: 800 kg, 850 kg, and 900 kg for the 1st floor, 2nd floor, and 3rd floor, respectively. White noise forces are applied to each floor mass. The displacement of each floor is considered as the system measured outputs. The sampling rate for the discrete data is 100 Hz.

The convergence of the system identification without consideration of the aforementioned gap is affected by three factors: 1) the size of the data set (as the number of data goes to infinity, the model converges asymptotically under the assumption of a Gaussian stochastic process); 2) noise (white noise contamination deteriorates the convergence); 3) damping components in the system (small damping can be hidden within noise content or the output of the system with large damping might not contain enough dynamic behavior). A parametric study was conducted to evaluate the effect on these three factors. However, some difficulties relating to the parametric study must be first addressed. First, countless combinations of the three factors exist. Second, a statistical analysis should be conducted; this requires numerous simulations to be implemented for each combination. Third, the simulation study is heavily dependent on the performance of the random number generators. Thus, it is challenging to perform a precise quantitative analysis of the results. Rather, the overall trend of effect of the three factors on system identification and physical parameter estimation will be checked.

To cope with such a complex parametric study, a rather simple numerical study is adopted here. Five data set lengths are considered: 3,000, 10,000, 50,000, 100,000, and 500,000. Also, five noise ratios are considered on the system's output: 0.0, 0.001, 0.005, 0.01, and 0.03 (RMS). Finally, five different inter-story damping to stiffness ratios are considered: 0.0, 0.0001, 0.001, 0.005, and 0.01. With these three sets of variables, the numerical study was performed with the following three cases: 1) convergence check depending on the length of data was performed with a RMS noise ratio of 0.01 and a damping ratio of 0.0001; 2) the influence of noise was studied with 50,000 data and a damping ratio of 0.0001; 3) the effect of the damping ratio was explored with 50,000 data and a RMS noise ratio of 0.01. A single numerical simulation was conducted

Table 4.1 Results of numerical parametric study.

	Number of Data Points				
	3,000	10,000	50,000	100,000	500,000
M_e (%)	0.28	0.25	0.28	0.05	0.07
K_e (%)	0.07	0.34	0.23	0.03	0.07
C_e (%)	89.99	70.13	57.71	19.28	18.26

	RMS Noise Ratio				
	0.0	0.001	0.005	0.01	0.03
M_e (%)	0.000	0.088	0.198	0.279	0.484
K_e (%)	0.000	0.072	0.162	0.232	0.404
C_e (%)	0.000	11.023	30.882	57.712	1,071

	Damping Ratio				
	0.0	0.0001	0.001	0.005	0.01
M_e (%)	0.06	0.28	0.67	0.97	1.14
K_e (%)	0.05	0.23	0.64	0.95	1.12
C_e (%)	0.00	57.71	2.75	0.72	0.72

without a statistical analysis. Then, three physical parameters were estimated and relating errors were calculated as:

$$\mathrm{M_e}(\%) = mean\left(\sum_{i,j} \left| \frac{m_{ij}^{true} - m_{ij}^{est}}{m_{ij}^{est}} \right| \right) \times 100 \tag{4.49}$$

where m_{ij}^{true} and m_{ij}^{est} are the entities of the mass matrices corresponding to the true and estimated models, respectively; $\mathrm{K_e}(\%)$ and $\mathrm{C_e}(\%)$ are also calculated similarly. The results of the numerical parametric study are tabulated in Table 4.1.

Estimation errors on the system's mass and stiffness are very small; as the number of data points increases, the accuracy increases in tandem. However, the damping error is still nontrivial in the case of the 0.01 RMS noise ratio and 0.0001 damping ratio. As the noise level increases, all errors increase, especially for the damping error. As the damping ratio increases, the estimation of mass and stiffness are deteriorated. However, the damping estimate is improved but stagnates after 0.005. Through the numerical example, it can be concluded that the true system matrices can be estimated with a probability of one (w.p.1) in the numerical example and this approach does not require any prior knowledge of the system.

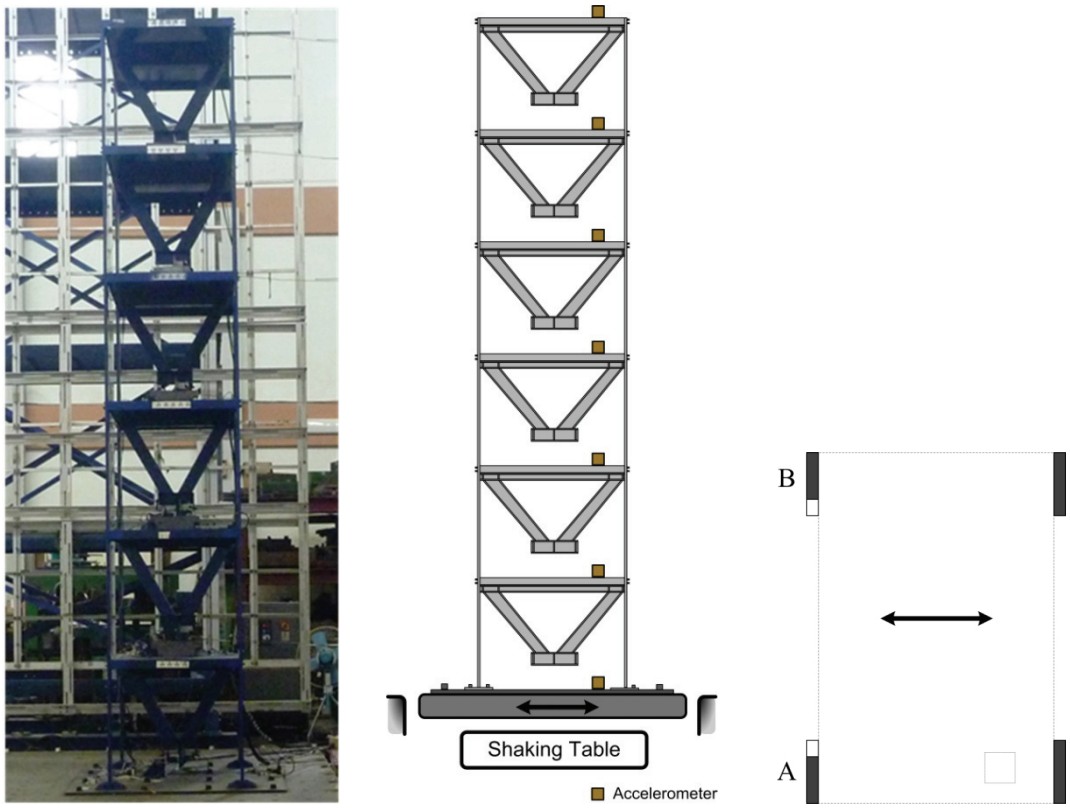

(a) (b) (c)

Figure 4.6 Testbed structure: (a) partial scaled structure for six-story single-bay steel building; (b) planar schematics with sensor installation; (c) emulated damage location for cutting columns and location of accelerometer.

4.5 Experimental Verifications

4.5.1 Testbed Structure and Support-Exciting Testing

The identical steel frame structure (Fig. 4.6) presented in Chapter 3 is used. The structure is built on a shaking table at the National Center for Research in Earthquake Engineering (NCREE). The structure is a six-story single-bay steel frame building with 1.0 m story heights. Each floor is a rigid diaphragm (1.0 m × 1.5 m × 2cm thick) welded along all four edges to 5.0 cm × 0.5 cm rectangular beams. Each floor is rigidly connected by bolts to four steel rectangular (15.0 cm × 2.5 cm) cross-sectioned columns oriented in their flexurally weak axis. The structural parameters of the testbed structure are summarized in Table 4.2.

Table 4.2 Summary of structural parameters of the six-story frame structure.

Floor mass	862 kg
Floor area	1×1.5 m^2
Inter-story height	1 m
Column cross section	15×2.5 cm^2
Inter-story stiffness	1.9×10^6 N/m

Note: Inter-story stiffness is calculated from the Euler-Bernoulli beam equations with fixed-fixed end conditions.

Table 4.3 Damage scenario for cutting columns.

Case	Location	
	Under 1st floor mass	Under 2nd floor mass
Case 1	A(6)	-
Case 2	A(6), B(3)	-
Case 3	A(6), B(6)	-
Case 4	A(9), B(9)	-
Case 5	A(9), B(9)	A(6)
Case 6	A(9), B(9)	A(6), B(6)

Note: The numbers in parenthesis denote induced crack lengths in cm.

Support excitation is applied in one direction as moderate white noise (peak ground acceleration of 0.061 g). This motion is applied along the planar weak axis of the structure. Seven accelerometers that measure the acceleration of the ground motion and each story are installed. A total of seven tests were conducted for the undamaged structure (*i.e.*, baseline) and the damaged structure. Damage is emulated by cutting the columns below the floor connections. The details of the damage cases are illustrated in Fig. 4.6-c and Table 4.3. It should be noted here that the emulated damage scenarios are not intended to represent severe damages, since this study attempts to detect minor damage. The testing of the damaged structure was conducted sequentially after the testing of the undamaged baseline was completed.

4.5.2 Estimation of Baseline Physical Parameters

Estimation of the physical parameters from the experiment is conducted off-line using 30 sec-long data sets (3000 data points). Two different system identifications were considered for both input-output analysis and output-only data sets. Then, considering full *a priori* knowledge on the structure's lumped masses (*i.e.*, 862 kg at each floor), the physical parameters such as the spatial distribution of stiffness **K** and damping **C** were calculated by Eqs (4.28) and (4.29) and for the input-output analysis:

$$\hat{\mathbf{K}} = \begin{bmatrix} 3260436 & -1964009 & 414255 & -104393 & 88381 & -67298 \\ -1788583 & 3032469 & -1939778 & 407177 & 82730 & -99864 \\ 439303 & -1827917 & 2932826 & -1892131 & 534577 & -131916 \\ -145435 & 507923 & -2002127 & 3187329 & -1870920 & 299167 \\ -33299 & -73415 & 440842 & -1907798 & 2969031 & -1462394 \\ 5980 & -116316 & 130940 & 298632 & -1645762 & 1343867 \end{bmatrix} \tag{4.50}$$

$$\hat{\mathbf{C}} = \begin{bmatrix} 1154 & -486 & 1157 & -625 & -59 & 200 \\ 79 & -192 & 1659 & -995 & -917 & 555 \\ -398 & -292 & 1264 & -192 & -1721 & 195 \\ -429 & 175 & -610 & 783 & -1373 & -174 \\ -2 & 146 & -819 & 177 & 693 & -1088 \\ 923 & -109 & -596 & 294 & 2469 & 832 \end{bmatrix} \tag{4.51}$$

and output-only analysis:

$$\hat{\mathbf{K}} = \begin{bmatrix} 3265841 & -1964712 & 420615 & -85008 & 83801 & -76696 \\ -1766359 & 3027363 & -1971765 & 385487 & 80252 & -82615 \\ 478759 & -1863302 & 3007121 & -1903873 & 526180 & -144488 \\ -132824 & 475307 & -2015466 & 3200151 & -1845411 & 300643 \\ -47256 & -41951 & 430675 & -1944562 & 3005266 & -1544925 \\ -27761 & -54718 & 62227 & 330254 & -1619674 & 1378577 \end{bmatrix} \tag{4.52}$$

$$\hat{\mathbf{C}} = \begin{bmatrix} 2180 & 195 & -609 & -613 & -128 & -172 \\ 268 & -4 & 1404 & -702 & -489 & 1198 \\ 1491 & -1697 & 998 & -988 & -483 & -262 \\ 610 & -943 & -164 & 157 & -91 & -19 \\ -247 & 1392 & -181 & 668 & 823 & -520 \\ -1834 & 722 & -1013 & 775 & 214 & 15 \end{bmatrix} \tag{4.53}$$

where the units for each matrix are N/m and N·sec/m, respectively. In both cases, the estimated stiffness matrices $\hat{\mathbf{K}}$ resemble what should be calculated by a finite element formulation based on the underlying physics of the problem. In other words, each inter-story stiffness is placed on the upper and lower diagonals as negative values except at the top story. Furthermore, the sum of inter-story stiffnesses of the adjacent stories are placed along the diagonal, except at the top story. The estimated stiffness matrices, $\hat{\mathbf{K}}$, have significant values along the tri-diagonals with positive values along the diagonals and negative values along the off-diagonals. The values are very close to the analytical values (1.9×10^6 N/m (Table 4.2)).

Estimated damping matrices, $\hat{\mathbf{C}}$, do not imply the underlying physics. For example, no significant tri-diagonals are found. As previously studied in numerical examples, damping

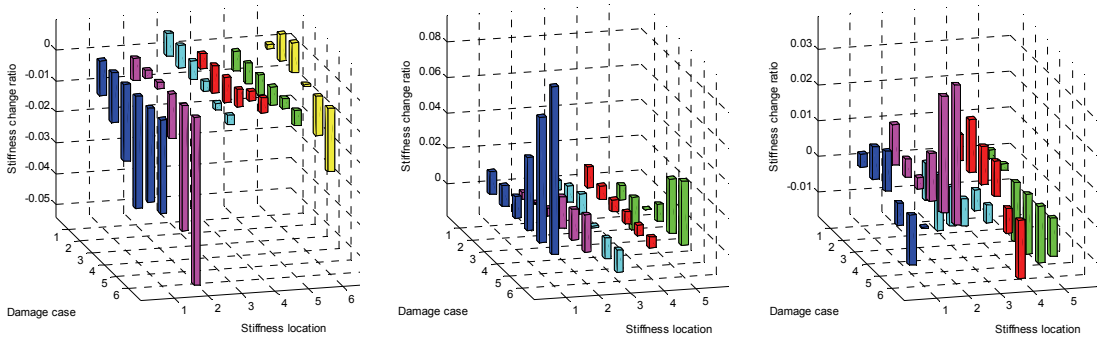

Figure 4.7 Stiffness change ratio (*SCR*) corressponing to cut coulmuns: (a) stiffness matrix diagonal (SCR_{ii}); (b) stiffness matrix superdiagonals ($SCR_{i(i+1)}$); (c) stiffness matrix subdiagonals ($SCR_{(i+1)i}$).

estimation for lightly damped structures with relatively high signal-to-noise ratios is generally very challenging. Thus, a comparison of estimated physical matrices for damage detection is confined only to the estimated stiffness matrice in this study.

4.5.3 Damage Detection for SHM

Damage locations and severities are quantitatively identified by the stiffness change ratio, SCR_{ij} , which is defined as:

$$SCR_{ij} := \left(k_{ij}^{D} - k_{ij}^{0}\right) / k_{ij}^{0} \tag{4.54}$$

where k_{ij}^{0} and k_{ij}^{D} are the elements of the *i*-th row and the *j*-th column in the estimated stiffness matrix $\hat{\mathbf{K}}$ for the baseline and damaged cases, respectively. Stiffness losses (*i.e.*, damages) are represented by a negative stiffness change ratio for the diagonals (SCR_{ii}) and a positive stiffness change ratio for the superdiagonals ($SCR_{i(i+1)}$) and subdiagonals ($SCR_{(i+1)i}$). The damage introduced by cutting the columns results in inter-story stiffness losses. Fig. 4.7 displays the stiffness change ratio for the diagonals, superdiagonals, and subdiagonals, depending on the damage scenario.

As seen in Fig. 4.7-a, the *SCR* of the diagonals closely match the damage on the first and second stories. The *SCR* of location 1 increases proportionally with the damage applied to the

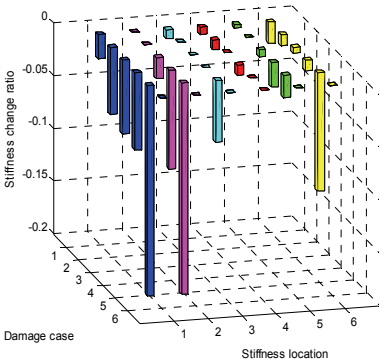

Figure 4.8 Stiffness change ratios of stiffness matrix diagonal (SCR_{ii}) for output-only analysis.

first story columns. The *SCR* of location 2 in damage cases 5 and 6 also accurately represent the applied damage to the second story columns. However, slightly elevated *SCR*s are also found in other locations, especially in location 6. The stiffness change ratios of the subdiagonal stiffness matrix and those of the superdiagonal stiffness matrix are displayed in Fig. 4.7-b and Fig. 4.7-c, respectively.

The location and severity of structural damage is identified using the relative stiffness change between the baseline and damaged structure. This implies that absolute stiffness estimation is not required. As a result, the methodology does not require exact mass information for the purpose of damage detection. Specifically, the requirement for solving Eq. (4.28) is that the mass ratio be known, and not the absolute mass quantity (862 kg).

Damage location and severity can be identified quantitatively by input-output analysis. In the case of output-only analysis, similar damage detection results are confirmed up to a certain amount of damage. Fig. 4.8 displays the stiffness change ratio of the stiffness matrix diagonal based on the output-only analysis. Generally, the stiffness change ratio of the output-only stiffness matrix change more than those in the input-output analysis. Especially for relatively severe damage cases (*e.g.*, damage case 5) large changes in the stiffness change ratio is observed. In the case of damage case 6, which is the most severe damage scenario, output-only system identification by N4SID was unstable yielding unreliable model; as a result, damage detection was not conducted for this case. This implies that the input to the system is needed for precise quantitative detection of a wide range of damage states in a structure.

4.5.4 Damage Detection with Partial Knowledge of the Structure Mass

The estimation of the physical parameters of the system and damage detection are also conducted under the assumption of partial *a priori* knowledge of the structure's mass. In this study, it is assumed that there is no *a priori* knowledge of the 1st floor mass. For the other floors, *a priori* mass information is assumed to be 862 kg. Similar to the previous section, grey-box model is utilized to extract physical parameters of the system. By solving Eq. (4.40), the spatial distribution of the stiffness, **K**, and damping, **C**, are calculated as:

$$\hat{\mathbf{K}} = \begin{bmatrix} 2982389 & -1796520 & 378928 & -95490 & 80844 & -61559 \\ -1788583 & 3032469 & -1939778 & 407177 & 82730 & -99864 \\ 439303 & -1827917 & 2932826 & -1892131 & 534577 & -131916 \\ -145435 & 507923 & -2002127 & 3187329 & -1870920 & 299167 \\ -33299 & -73415 & 440842 & -1907798 & 2969031 & -1462394 \\ 5980 & -116316 & 130940 & 298632 & -1645762 & 1343867 \end{bmatrix} \tag{4.55}$$

$$\hat{\mathbf{C}} = \begin{bmatrix} 1055 & -445 & 1059 & -572 & -54 & 183 \\ 79 & -192 & 1659 & -995 & -917 & 555 \\ -398 & -292 & 1264 & -192 & -1721 & 195 \\ -429 & 175 & -610 & 783 & -1373 & -174 \\ -2 & 146 & -819 & 177 & 693 & -1088 \\ 923 & -109 & -596 & 294 & 2469 & 832 \end{bmatrix} \tag{4.46}$$

Due to the absence of the 1st floor mass, the stiffness and damping parameters associated with the 1st floor mass have changed compared to Eqs (4.50) and (4.51). With the identified physical parameters of the baseline structure, the stiffness change ratio is calculated for the six damage scenarios (Table 4.3) and depicted in Fig. 4.9. The stiffness change ratios of the stiffness matrix diagonal, subdiagonal, and superdiagonal are observed to capture the imposed damage accurately. Compared to Fig. 4.7 which is based on assumed *a priori* full knowledge on mass, Fig. 4.9 presents *SCR* results that the damage scenarios more clearly. This implies that: 1) partial information on mass may result in a lower accuracy in the estimation of the absolute stiffnesses; 2) for the purpose of damage detection, comparable damage detection results are encountered with partial information on the structure mass.

4.6 Chapter Summary and Conclusions

In this chapter, a theoretical framework was presented for the estimation of a structure's physical parameters (*i.e.*, a structure's mass, stiffness, and damping) using measured experimental data (*i.e.*, input-output or output-only data). The framework considered two state-space models: a

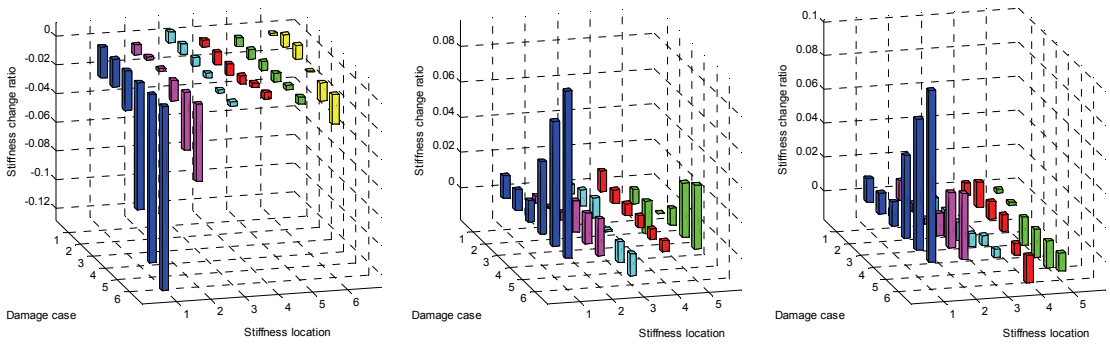

Figure 4.9 Stiffness change ratio (*SCR*) without knowlege of 1st floor mass: (a) stiffness matrix diagonal (SCR_{ii}); (b) stiffness matrix superdiagonal ($SCR_{i(i+1)}$); (c) stiffness matrix subdiagonal ($SCR_{(i+1)i}$).

physics-based model (*i.e.*, white-box model) and a data-driven mathematical model (*i.e.*, black-box model) derived using the subspace system identification method. Observability canonical form conversion was proposed to convert the data-driven mathematical model into a physically interpretable model (*i.e.*, grey-box model). Then, by linking the white-box and grey-box models, physical parameters were estimated in the form of finite element discretization. The proposed framework is experimentally verified using the six-story steel frame structure introduced in Chapter 3. Based on *a priori* knowledge of the lumped mass (*i.e.*, mass distribution) of the structure, the distribution of the structure's stiffness and damping was accurately estimated. Since the physical parameters reflect the structural condition, damage detection was also conducted by comparing the estimated physical parameters (especially stiffness) between a baseline (undamaged) and damaged structural condition. It was proved that the framework was valid for the identification of structural damage (location and severity) based on only the measured acceleration with *a priori* knowledge of the ratio of lumped mass. Furthermore, the framework was shown to be still valid with insufficient *a priori* knowledge of the ratio of lumped mass. The proposed framework has shown great promise to the SHM community for its application to linear time-invariant (LTI) structures, because the approach focused on moderate structural behavior (*i.e.*, non-destructive testing).

CHAPTER 5

IN-NETWORK SYSTEM IDENTIFICATION STRATEGY BY DECENTRALIZED MARKOV PARAMETER ESTIMATION

The emergence of low-cost wireless sensors for the dense monitoring of civil structures is driving interest in the embedment of autonomous data interrogation methods within the computational core of the sensors. Automated system identification of a monitored structure can produce structural models that can serve as part of a more comprehensive structural health monitoring strategy. In this chapter, a system identification strategy based on Markov parameters is studied for embedment within the decentralized computational framework of a wireless sensor network. Markov parameters are calculated by each wireless sensor using input-output and output-only response data of the structure. The data storage and wireless communication requirements of Markov parameters are less than that required by the original raw data, resulting in the preservation of scarce system resources such as communication bandwidth and battery power. Markov parameters are wirelessly communicated to a centralized node where eigensystem realization is used to extract the global modal properties of the structure. For validation, dynamic testing of a cantilevered balcony in a historic building (Hill Auditorium, Ann Arbor, MI) is conducted.

5.1 Introduction

The field of system identification has produced a suite of powerful mathematical tools that can accurately model the dynamic behavior of a complex engineered structure (Ljung 1999). Identified models have historically served as the basis for predicting structural responses to future loads, designing feedback control systems (Juang 1994), and for estimating the health of a

structure (Doebling *et al.* 1998). Modal analysis was one of the earliest forms of parametric-based system identification with modal parameters (*e.g.*, modal frequencies, modal damping ratios, and mode shapes) extracted from measured input-output measurements data (Ewins 2000). By definition, parametric methods seek to map physical variables (*e.g.*, stiffness, damping, *etc.*) of the system to the model derived from the measurement data. Subsequently, parametric prediction-error methods for system identification emerged (Ljung 1999) followed by powerful parameterization-free subspace system identification methods introduced in Chapter 3. Subspace system identification based on time-domain state-space representations of dynamic systems has gained popularity within the engineering community since the 1990's. Subspace system identification seeks mathematical models (*i.e.*, black-box state-space model) that optimally fit the measurement data available without concern for a mapping between the model and physical system parameters. Today, a number of subspace state-space system identification (4SID) techniques have been successfully applied for system identification of civil and mechanical dynamic systems including reference-based stochastic subspace identification (SSI) (Peeters and Roeck 1999) and the eigensystem realization algorithm (ERA) (Juang and Pappa 1984).

Regardless of the system identification technique adopted, the underlying requirement of all system identification methods is the availability of data (*i.e.*, measurement of the system output and input). To collect this data, data acquisition systems are necessary. The vast majority of systems used in the laboratory and field are wire-based systems with centralized architectures. Specifically, sensors installed in the system utilize wires to communicate measurements to the central data server where data is time-synchronized, digitized, and stored for off-line analysis. In some instances, automated data processing occurs in the data server (*i.e.*, on-line analysis). While wires provide a reliable conduit for the communication of measurement data, the extensive cabling requirements of permanent data acquisition systems in large civil structures detracts from their attractiveness. To overcome these limitations, wireless sensors have been proposed for structural monitoring (Straser and Kiremidjian 1998; Lynch *et al.* 2006). In addition to simplifying the installation of sensors in large structural systems, wireless sensors also offer on-board computing resources that can be used to locally process measurement data (Lynch *et al.* 2003; Nagayama and Spencer 2007). On-board computing reduces the amount of data to be transmitted; hence, "smart" wireless sensor nodes can more effectively utilize the shared communication channel (*i.e.*, improved system scalability). Wireless transceivers also consume more power than microprocessors. Therefore, processing data at the node can be more power-efficient than communicating raw data wirelessly (Lynch *et al.* 2004b), an important consideration when powering nodes from battery or power harvesting sources.

The centralized wired monitoring system architecture is often defined by a small number of computing nodes (*i.e.*, data servers), each endowed with large memory and computational throughput capacity. In stark contrast, the computing environment offered by wireless sensor networks is highly decentralized with a large number of light-weight computing nodes (*i.e.*, small memory and computational throughput capacity). Lynch *et al*. first proposed the concept of decentralized computing for structural system identification (Lynch *et al.* 2006): Lynch extracted mode shapes from time-synchronized wireless sensor data by having nodes locally calculate Fourier output spectra and utilize peak-picking (PP) logic to identify modal frequencies; Mode shapes were then extracted in the network by having the imaginary component of the Fourier spectra at modal frequencies wirelessly exchanged. Nagayama and Spencer explored the embedment of the output-only Natural Excitation Technique (NExT) for identification of free decay responses from which state-space models are extracted by the ERA method executed on a centralized server (Nagayama and Spencer 2007). More recently, Sim *et al*. extended the work of Nagayama and Spencer by utilizing the random decrement technique (RDT) instead of NExT (Sim *et al.* 2008). Zimmerman *et al*. proposed the adoption of a parallel computing paradigm to embed the frequency domain decomposition (FDD) method in a wireless sensor network for automated mode shape extraction (Zimmerman *et al.* 2008).

In this study, a single-input multi-output (SIMO) subspace system identification strategy ideally suited for the decentralized computing architecture of a wireless monitoring system is studied. The low-cost *Narada* wireless node (Swartz *et al.* 2005) that is capable of sensing, actuating, computing, and wireless communication is adopted as the primary building block of the wireless monitoring system. The complexity of the linear time-invariant SIMO problem will be handled by decomposing the system analysis into parallel single-input single-output (SISO) systems that can be embedded within the computational framework of the wireless sensor network. Specifically, μ-Markov parameter extraction is embedded in each wireless sensor to extract SISO system information in a compressed manner (namely, the finite number of Markov parameters). After μ-Markov parameter extraction is completed, nodes then wirelessly transmit their results to a centralized server where the global system characteristics of the SIMO system are identified using the ERA method. The proposed decentralized system identification method is experimentally verified using input-output and output-only measurements derived during forced vibration testing of a large cantilevered auditorium balcony. To validate the accuracy of the wireless monitoring system, the dynamic system properties (*i.e.*, modal frequencies, modal damping, and mode shapes) autonomously extracted are compared to those derived from data-driven subspace system identification conducted off-line using the same measurement data.

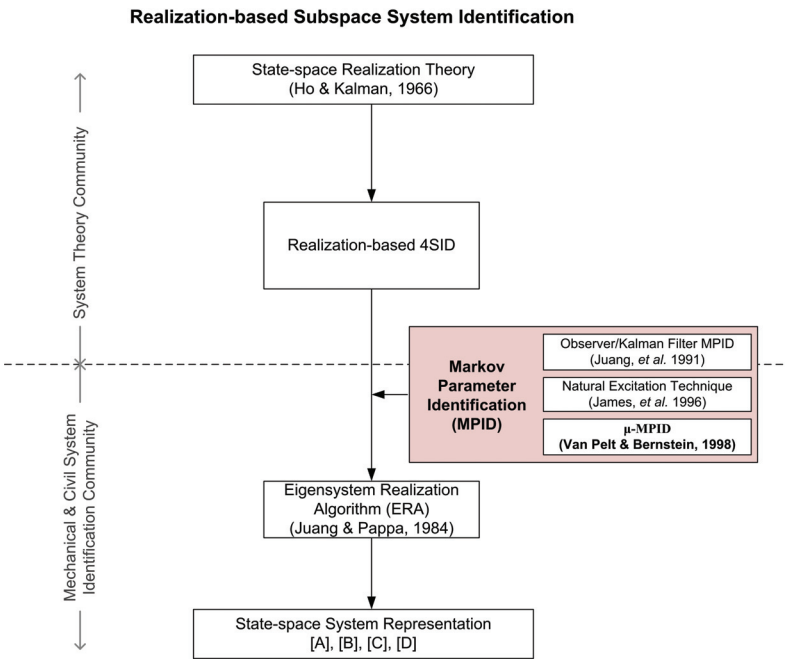

Figure 5.1 Realization-based 4SID methods with the role of MP estimation highlighted.

5.2 Realization-Based Subspace System Identification

Realization-based subspace system identification represents a major group of subspace state-space system identification (4SID) family as explained in Chapter 3. Realization-based 4SID methods (Fig. 5.1) originated from Ho and Kalman (1965) and attempt to estimate state-space models using the system impulse response (*i.e.*, Markov parameters (MP)). Since the realization-based 4SID methods entail the estimation of MPs, the methods are often referred to as indirect 4SID methods (Viberg 1995). Realization-based 4SID methods are computationally less resource-intensive and naturally decompose the SIMO system into SISO systems. Decomposition is an attractive approach in the wireless sensor domain because it allows realization-based 4SID algorithms to be parallelized with each node, simultaneously estimating SISO impulse response functions using a locally-collected system output that corresponds to a known system input. Estimation of impulse response functions corresponding to system outputs can be done by one of three methods: NExT (James *et al.* 1996), observer/Kalman filter identification (Juang *et al.* 1991), and μ-Markov parameter extraction (Van Pelt and Bernstein 1998). The NExT method has been used for impulse response extraction using wireless sensor networks engaged in structural monitoring in the study by Nagayama and Spencer (Nagayama and Spencer 2007).

In this study, a realization-based 4SID method is embedded in a wireless sensor network using μ-Markov parameters to extract system impulse response functions from input-output data sets. The μ-Markov parameters compress the original output time-history data into a small number of parameters that can be wirelessly communicated using significantly less energy and communication bandwidth than by transmitting the original measured time histories. Unlike the observer/Kalman filter identification that require the model order to be established *a priori*, μ-Markov parameters are consistent regardless of the number of parameters selected. This renders them ideal when implementing in an automate monitoring system. For output-only data sets generated by broad-band inputs, the nonparametric NExT method is used to extract system MPs. MP sequences collected by each wireless sensor can be aggregated at a single server where the state-space realization of the SIMO system is formed using the eigensystem realization algorithm (ERA) (Juang and Pappa 1984).

5.2.1 μ-Markov Parameter Estimation Using Input-Output Data

The μ-Markov parameter estimation technique is a time-domain technique used for the extraction of system impulse response functions (Van Pelt and Bernstein 1998; Holzel and Bernstein 2009). Compared to more traditional time-domain techniques, *e.g.*, observer/Kalman filter identification (OKID) (Juang *et al.* 1991), μ-Markov parameter estimation is conceptually simple and well suited for embedment in fixed point microcontrollers commonly integrated with low-power wireless sensor nodes. Furthermore, it does not require *a priori* selection of the system model order (Holzel and Bernstein 2009).

Derivation of μ-Markov parameter estimation for a linear time-invariant SISO system begins with the n-th order auto-regressive moving average (ARMA) model

$$y(k) = -\sum_{j=1}^{n} a_j \, y(k-j) + \sum_{j=0}^{n} b_j \, u(k-j) \tag{5.1}$$

where k is the discrete time step, a_j are coefficients on the system output y, and b_j are coefficients on the system input u. If the at-rest system is excited by an arbitrary load at $k = 0$, then Eq. (1) at $k = 0$ simplifies to $y(0) = b_0$. Since the system output at $k = 0$ is the impulse response function, it can be extracted from the moving average (MA) part. Then, the ARMA model at step k to be rewritten as:

$$y(k) = -\sum_{j=1}^{n} a_j \, y(k-j) + h_0 u(0) + \sum_{j=1}^{n} b_j \, u(k-j) \tag{5.2}$$

By inserting the ARMA model at time k-1 into Eq. (5.2) and extracting another representation of the impulse response function at k=1 from the MA part, the equation can be derived as:

$$y(k) = -\sum_{j=1}^{n} a_j' \, y(k-j-1) + \sum_{j=0}^{1} h_j \, u(k-j) + \sum_{j=1}^{n} b_j' \, u(k-j-1) \tag{5.3}$$

where a_j' and b_j' are modified system coefficients. Repeating this procedure $\mu - 1$ times, an ARMA equation explicitly displaying the first μ values of the impulse response function (h_0, h_1, … $h_{\mu\text{-}1}$) is extracted

$$y(k) = -\sum_{j=1}^{n} a_j^{(\mu-1)} \, y(k-j-\mu+1) + \sum_{j=0}^{\mu-1} h_j \, u(k-j) + \sum_{j=1}^{n} b_j^{(\mu-1)} \, u(k-j-\mu+1) \tag{5.4}$$

where h_0, h_1, … $h_{\mu\text{-}1}$ are also termed the μ-Markov parameters. The modified ARMA model written in Eq. (5.4) has $2n + \mu$ unknowns: $a_j{}^{(\mu\text{-}1)}$, $b_j{}^{(\mu\text{-}1)}$, and h_j. A least-squares problem can be formulated to determine the unknowns using the measured input-output sequences of the LTI system (Verhaegen and Verdult 2007). Consider the system input and output of Eq. (5.4) assembled as a row vector, $\boldsymbol{\varphi}_k$, at time step k:

$$\begin{aligned} &\boldsymbol{\varphi}_k = \\ &\left\{ -y(k-\mu) \quad \cdots \quad -y(k-n-\mu+1) \quad u(k) \quad \cdots \quad u(k-n-\mu+1) \right\} \in \Re^{1\times(2n+\mu)} \end{aligned} \tag{5.5}$$

If the input-output response of the system is considered at each time step from k = 0 to N-1, then the input-output matrix can be formed:

$$\boldsymbol{\Phi} = \left[\boldsymbol{\varphi}_0{}^{\mathrm{T}} \quad \boldsymbol{\varphi}_1{}^{\mathrm{T}} \quad \cdots \quad \boldsymbol{\varphi}_{N-1}^{\mathrm{T}} \right]^{\mathrm{T}} \in \Re^{N\times(2n+\mu)} \tag{5.6}$$

The system output from k = 0 to N-1 assembled as a column vector, $\mathbf{y} = \left[y(0) \quad \cdots \quad y(N-1) \right]^{\mathrm{T}}$, is linearly related to the unknown parameters

$$\boldsymbol{\theta} = \left[a_1^{(\mu-1)} \quad \ldots \quad a_n^{(\mu-1)} \quad h_0 \quad \cdots \quad h_{\mu-1} \quad b_1^{(\mu-1)} \quad \cdots \quad b_n^{(\mu-1)} \right]^{\mathrm{T}} \in \Re^{(2n+\mu)\times 1} \tag{5.7}$$

through the input-output matrix of Eq. (5.6):

$$\mathbf{y} = \mathbf{\Phi\theta} \tag{5.8}$$

If the number of observed points, N, is larger than the number of unknowns ($2n + \mu$), Eq. (5.8) represents an over-determined set of linear equations where the unknown model parameters, $\boldsymbol{\theta}$, can be found by applying the traditional linear least-squares solution:

$$\boldsymbol{\theta} = \left(\mathbf{\Phi}^{\mathrm{T}}\mathbf{\Phi}\right)^{-1}\mathbf{\Phi}^{\mathrm{T}}\mathbf{y} \tag{5.9}$$

The unknown parameter vector, $\boldsymbol{\theta}$, of Eq. (5.9) does not contain any parameterized information of the dynamic system; rather, the estimation of the finite impulse response function of the system is derived. This finite impulse response (FIR) model is in contrast to the infinite impulse response (IIR) model derived by classical parametric estimation methods.

The paramount benefits of μ-Markov parameter estimation as compared to direct application of conventional time series models are the following: the method extracts an accurate representation of the system impulse response function without requiring *a priori* selection of the system model order. Since system order is conventionally determined by manual inspection of stabilization diagrams, this step is difficult to reliably implement in an automated system identification system. In contrast, estimated impulse responses by the μ-Markov parameter estimation are consistent regardless of the system order (Holzel and Bernstein 2009); in addition, the method is well suited for decentralized autonomous computation in WSNs.

5.2.2 Markov Parameter Estimation Using Output-Only Data

Estimation of a system free decay response function from output-only data by the random decrement technique was proposed by Ibrahim (Ibrahim 1977). Shortly thereafter, a new version of the Ibrahim time domain (ITD) technique was proposed based on the cross-correlation between multiple system outputs recorded at different periods in time to extract the modal characteristics of a dynamic system (Ibrahim and Pappa 1982). The modal characteristics of the system are used to calculate the impulse response function of the system. A more effective output-only system identification method termed NExT was proposed by James *et al*. (James *et al.* 1996). Conceptually, this method is analogous to stochastic realization based on canonical correlation analysis (Akaike 1974). The major difference is the use of cross-correlation between a reference output and other system outputs resulting in improved system identification. In this study, the NExT method is adopted to extract Markov parameters of the dynamic system. However, to be consistent with the description of the μ-Markov parameter estimation method previously

described, the NExT method is described using parametric autoregressive models to derive the Markov parameters using output-only measurements of a dynamic system.

First, consider the ARMA model of the system defined in Eq. (5.1) for a defined reference output, $y_{\text{ref}}(k)$:

$$y_{\text{ref}}(k) = -\sum_{j=1}^{n} a_j \, y_{\text{ref}}(k-j) + \sum_{j=0}^{n} b_j \, u(k-j) \tag{5.10}$$

If the left- and right-hand sides of Eq. (5.10) are multiplied by another system output, $y_i(k-\tau)$, shifted by τ, then the expected value of Eq. (5.10) is:

$$\mathrm{E}\left[y_i(k-\tau) y_{\text{ref}}(k)\right] = -\sum_{j=1}^{n} a_j \, \mathrm{E}\left[y_i(k-\tau) y_{\text{ref}}(k-j)\right] + \sum_{j=0}^{n} b_j \, \mathrm{E}\left[y_i(k-\tau) u(k-j)\right] \tag{5.11}$$

The expected value of the product of two time signals time shifted by τ relative to one another is defined as the cross-correlation function:

$$R_{y_i y_{\text{ref}}}(\tau) = \mathrm{E}\left[\, y_i(k-\tau) y_{\text{ref}}(k) \,\right] \tag{5.12}$$

Eq. (5.11) is rewritten in terms of the cross-correlation:

$$R_{y_i y_{\text{ref}}}(\tau) = -\sum_{j=1}^{n} a_j R_{y_i y_{\text{ref}}}(\tau - j) + \sum_{j=0}^{n} b_j \, R_{y_i u}(\tau - j) \tag{5.13}$$

The cross-correlation function between a system output and the input is directly related to the autocorrelation of the system input through convolution (Verhaegen and Verdult 2007):

$$R_{y_i u}(\tau - j) = h(-(\tau - j)) * R_{uu}(\tau - j) \tag{5.14}$$

where $h(t)$ is impulse responses of the system. If the input is assumed to be a stationary Gaussian random process, the autocorrelation function of the system input reduces to the Kronecker delta function, δ, scaled by an arbitrary constant, c_o' (James *et al.* 1996). This allows Eq. (5.14) to be rewritten:

$$R_{y_i y_{\text{ref}}}(\tau) = -\sum_{j=1}^{n} a_j \, R_{y_i y_{\text{ref}}}(\tau - j) + c_0' \, h(0) \delta(\tau - j) \tag{5.15}$$

Hence, the cross-correlation of the system outputs is an infinite impulse response function of a system that has an identical AR model with the original system in Eq. (5.10).

5.2.3 Eigensystem Realization Algorithm

The eigensystem realization algorithm (ERA) (Juang and Pappa 1984) derives a minimal state-space realization of a linear time-invariant system using a finite number of Markov parameters. ERA is therefore used in this study to derive the state-space model of a global SIMO system using the MP sequences of the SISO models previously derived from input-output and output-only measurements. The state-space representation of a fully controllable and observable system in the discrete time-domain is described as:

$$\begin{aligned} \mathbf{x}(k+1) &= \mathbf{A}\,\mathbf{x}(k) + \mathbf{B}\,u(k) \\ \mathbf{y}(k) &= \mathbf{C}\,\mathbf{x}(k) + \mathbf{D}\,u(k) \end{aligned} \tag{5.16}$$

where $\mathbf{x}$ is an n-dimensional state vector, $\mathbf{A} \in \Re^{n \times n}$ is the system matrix, $\mathbf{B} \in \Re^{n}$ is the vector relating the state to the single input u, $\mathbf{C} \in \Re^{l \times n}$ is the matrix relating the system observation vector, $\mathbf{y}$, to the state, and $\mathbf{D} \in \Re^{l}$ is the vector relating the l system outputs to the single input, u.

The controllability and observability matrices ($\mathcal{C}$ and $\mathcal{O}$, respectively) are defined as:

$$\mathcal{C} = \begin{bmatrix} \mathbf{B} & \mathbf{AB} & \cdots & \mathbf{A}^{n-1}\mathbf{B} \end{bmatrix} \tag{5.17}$$

$$\mathcal{O} = \begin{bmatrix} \mathbf{C} \\ \mathbf{CA} \\ \vdots \\ \mathbf{CA}^{n-1} \end{bmatrix} \tag{5.18}$$

The SIMO system is fully controllable and observable if, and only if, $\mathcal{C}$ and $\mathcal{O}$ are of rank n. If an LTI system is fully controllable and observable, then the vector of Markov parameters can be written as (Verhaegen and Verdult 2007):

$$\mathbf{h}(k) = \begin{cases} \mathbf{0} & k < 0 \\ \mathbf{D} & k = 0 \\ \mathbf{CA}^{k-1}\mathbf{B} & k > 0 \end{cases} \tag{5.19}$$

If an infinite sequence of MP are written in block Hankel form:

$$\mathcal{H} = \begin{bmatrix} \mathbf{h}(1) & \mathbf{h}(2) & \mathbf{h}(3) & \cdots \\ \mathbf{h}(2) & \mathbf{h}(3) & \mathbf{h}(4) & \cdots \\ \mathbf{h}(3) & \mathbf{h}(4) & \mathbf{h}(5) & \cdots \\ \vdots & \vdots & \vdots & \ddots \end{bmatrix} \tag{5.20}$$

then Eq. (5.19) allows the Hankel matrix to be factorized into an infinite observability and controllability matrix

$$\mathcal{H} = \begin{bmatrix} \mathbf{C} \\ \mathbf{CA} \\ \mathbf{CA}^2 \\ \vdots \end{bmatrix} \begin{bmatrix} \mathbf{B} & \mathbf{AB} & \mathbf{A}^2\mathbf{B} & \cdots \end{bmatrix} = \mathcal{O}\,\mathcal{C} \tag{5.21}$$

This allows the system matrices **A**, **B**, and **C** to be found by factorization of the Hankel matrix. If the rank of the block Hankel matrix is identical to the dimension of the system *n*, then the system matrices **A**, **B,** and **C** represent the minimal realization of the system. To achieve a minimal realization, the Hankel matrix can be robustly truncated to rank *n* through the use of singular value decomposition (SVD) (Kung 1978).

5.3 Implementation of MP Identification within a Wireless Sensor Network

Input-output and output-only system identification based on Markov parameter extraction is ideally suited for implementation within the distributed computational architecture posed by a wireless structural monitoring system. Sensor-level computing is sufficient for the extraction of MP from raw measurement data recorded by each wireless sensor node. After all sensor nodes have performed their MP extractions in parallel, the MP from each node can be wirelessly communicated to the remaining nodes. Once Markov parameters have been collected from all measured degrees-of-freedom, the eigensystem realization algorithm can be implemented at the network-level to estimate the system matrices **A**, **B**, and **C**. In this study, system identification based on Markov parameter extraction is implemented within a wireless structural monitoring system using three functional components: control server, local coordinator, and wireless sensor nodes (see Fig. 5.2). The control server is a single unit (*e.g.*, a data server or wireless sensor) responsible for initiating and coordinating the data collection, communication, and computing tasks of the wireless monitoring system. The local coordinator is responsible for applying a controlled excitation to the structure based on commands from the control server or serving as a reference node. The wireless sensor nodes are used to collect the acceleration response of a structure at their respective locations. In addition, wireless sensor nodes perform sensor-level

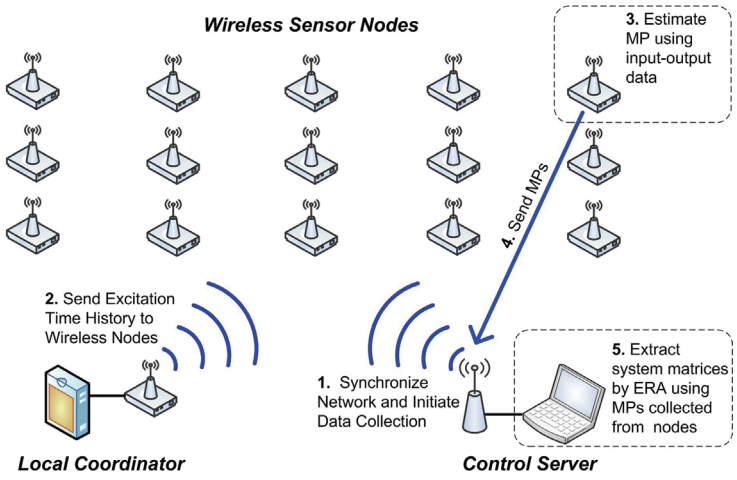

(a)

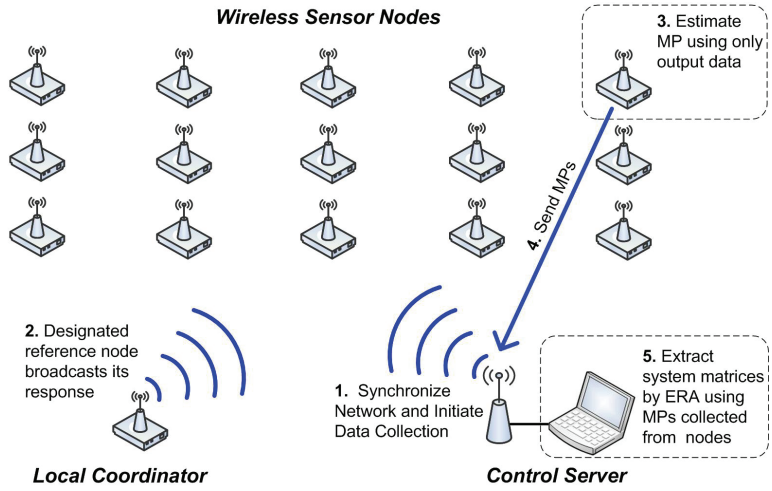

(b)

Figure 5.2 Automated system identification by decentralized MP estimation within a wireless structural monitoring system: (a) input-output and (b) output-only implementations.

computing when commanded by the local coordinator or control server. In this study, the *Narada* wireless sensor platform will serve as the system wireless sensor node and local coordinator; a standard personal computer (PC) will serve as the control server. While *Narada* will be utilized in this study, it should be noted that any wireless sensor platform with on-board data processing capabilities (*e.g.*, Crossbow iMote2) can be used without modification to the proposed computational approach.

5.3.1 Input-Output Implementation

In the input-output implementation of the proposed automated system identification method (Fig. 5.2-a), the control server coordinates the activities of the wireless monitoring system. The control server begins by broadcasting a command packet to the wireless sensor network notifying the local coordinator and the wireless sensor nodes that a test will begin. Upon receipt of that command packet, the coordinator and the wireless sensor nodes each acknowledge the receipt of the command and wait for time synchronization to occur. The control server then sends a beacon packet upon which the local coordinator and wireless sensor nodes initiate their internal clocks and begin their data collection tasks. This beacon-based approach to time-synchronization has been experimentally determined to be accurate with synchronization errors of less than 30 μsec (see Fig. 2.3 in Chapter 2).

Upon receipt of the beacon packet from the control server, the local coordinator will begin the application of a controlled excitation to the structure (*e.g.*, using a shaker) while the wireless sensor nodes record the structure response. After a number of time steps (N_{acc}) have been collected as defined by the control server during initiation of the network, the local coordinator stops its application of the excitation while the wireless sensor nodes simultaneously stop collecting structural response data. Next, the local coordinator broadcasts its raw, excitation time-history record (*i.e.*, in 16-bit integer format) to the network of wireless sensor nodes using a send-acknowledge communication protocol that ensures each wireless sensor node receives the excitation time-history record. Upon receipt of the excitation time-history record, each wireless sensor node converts the raw (16-bit) excitation, u, and acceleration time histories, y_i, into single-precision floating-point representations (32-bit). Next, each wireless sensor node extracts MPs using LU decomposition to solve Eq. (5.9). In total, N_{MP} parameters are estimated by each wireless sensor node.

After the sensor-level computing has been completed, each wireless sensor node confirms the completion of its computational task with the local coordinator. The local coordinator then requests each wireless sensor node to send its single-precision floating point MP one at a time by peer-to-peer communication to the control server. Upon receipt of all MPs, the control server then assembles the MPs into an N_{MP} by N_{MP} Hankel matrix (Eq. (5.20)). Singular value decomposition (SVD) of the Hankel matrix is performed by the central server; the SVD orthogonal matrices are truncated to rank n from which the system matrices **A**, **B**, and **C** are calculated (Verhaegen and Verdult 2007).

The attraction of embedded μ-MP estimation is that sensor-level computing (*i.e.*, MP estimation) results in a substantial compression of the measurement data prior to communication. Consider a wireless monitoring system employing 15 *Narada* wireless sensor nodes ($N_{sensors}$) each

Table 5.1 Analysis of communication requirements of centralized and proposed decentralized system identification methods.

Methods	Transmission payload byte
Centralized Implementation *Analysis performed on control server after all time history records received*	$N_{sensor} \times N_{acc} \times 2\,byte$ $= 16 \times 1200 \times 2 = 38.4\,kbyte$
Decentralized computing *MP estimation conducted on wireless sensor nodes with MP communicated to control server*	$N_{acc} \times 2\,byte + (N_{sensor} - 1) \times N_{MP} \times 4\,byte$ $= 1200 \times 2 + 15 \times 105 \times 4 = 8.7\,kbyte$
	$\therefore$ **Transmission reduction = ~77%**

Note: Network size, $N_{sensor} = 16\,units$

Time history data length, $N_{acc} = 1200\,points$

Number of Markov Parameters, $N_{MP} = 105\,points$

collecting 1200 time samples (N_{acc}) of measurement data at any arbitrary sample rate. If implemented in a centralized monitoring system, all of the wireless sensor nodes and the local coordinator would be required to communicate their raw (16-bit) time history data to the centralized control server where system identification would be conducted. This would result in 38,400 bytes of data to be communicated (see Table 5.1). In the decentralized approach advocated herein, the local coordinator broadcasts its excitation time history record (2,400 bytes) to the network so that each wireless sensor node can extract Markov parameters from their input-output data. Assuming 105 MPs are extracted with each parameter represented by a single-precision floating point number (4 bytes), this generates 420 bytes worth of data to be communicated by each wireless sensor node. If all 15 wireless sensor nodes communicate their MPs to the control server, a total of 6,300 bytes would be communicated. Hence, the total number of bytes to be communicated by the decentralized μ-MP approach to system identification is 8,700 bytes (see Table 5.1). This represents a compression of more than 77%, which translates directly into the preservation of the wireless monitoring system's finite power sources. Another benefit of the approach is that communication reduction allows the network size to grow. For example, if the wireless monitoring system is increased from 15 to 99 wireless sensor nodes, an 82% reduction in communication is achieved as compared to the centralized case.

5.3.2 Output-Only Implementation

In the output-only implementation (Fig. 5.2-b), the local coordinator is no longer responsible for the excitation of the structure but rather represents a reference node at which one additional channel of structural response is collected by the wireless monitoring system. Similar to the

input-output implementation, the control server begins by synchronizing the network through the use of a beacon packet. Upon receipt of the beacon packet, the local coordinator and wireless sensor nodes reset their internal clocks and begin to collect structural response data for the prescribed time period. After N_{acc} time steps have been collected, the local coordinator broadcasts its raw (16-bits) time-history response, y_{ref}, to the wireless sensor nodes. Using Eq. (5.12), each wireless sensor node calculates the cross-correlation between its measured response, y_i, and that of the local coordinator's reference response, y_{ref}. The first 105 terms of the single-precision floating point cross-correlation function, $R_{y_i y_{ref}}$, are treated as MP to be communicated by each wireless sensor node to the control server for use in its ERA analysis. Since the communication requirements are identical to that of the input-output implementation, the amount of communication reduction (and corresponding savings in battery power) are the same as that presented in Table 5.1.

5.4 Experimental Validation, Vibration Testing of Hill Auditorium

Experimental validation of the proposed wireless monitoring system is conducted using a cantilevered balcony of Hill Auditorium, a historic theatre on the University of Michigan's Ann Arbor campus. Constructed in 1913, the theatre has a capacity of 3,500 with its seating distributed between the main floor and two balcony sections (termed the mezzanine and upper balconies). In this study, the mezzanine balcony was selected to serve as a demonstration structure for experimental validation of the decentralized system identification method embedded within a wireless monitoring system. The mezzanine balcony is roughly 42 m wide and is cantilevered 11 m above the main floor of the theatre as shown in Fig. 5.3. The plan view presented in Fig. 5.4-a reveals the supports of the balcony: rigid walls on two sides, a rigid wall on the back of the balcony, and six auxiliary columns distributed along the rear of the balcony.

5.4.1 Instrumentation Strategy

A total of 15 *Narada* units are installed on the mezzanine balcony of Hill Auditorium; the *wireless sensor nodes* are organized into 3 rows of 5 nodes each as shown in Fig. 5.4-a. The wireless sensor nodes are numbered 1 through 15. Attached to each *Narada* node is a MEMS accelerometer mounted to the balcony floor to measure its vertical acceleration response. Two accelerometers are used: Crossbow CXL02 and PCB Piezotronics 3801D1FB3G. The sensitivity of the 3801D1FB3G accelerometer is 0.7 V/g, its acceleration range is ±3 g, and its noise floor level is 0.15 mg. The CXL02 accelerometer sensitivity is 1 V/g, its range is ±2 g, and its noise

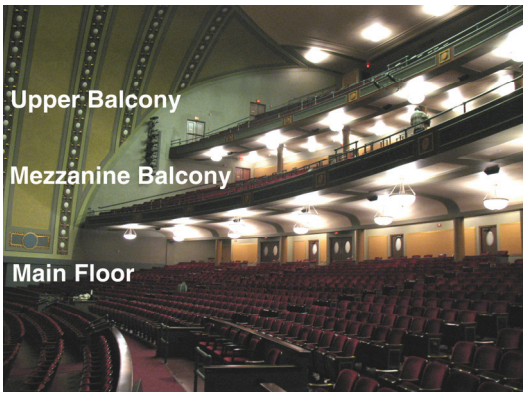

Figure 5.3 Main floor, mezzanine, and upper balcony sections of the University of Michigan's Hill Auditorium.

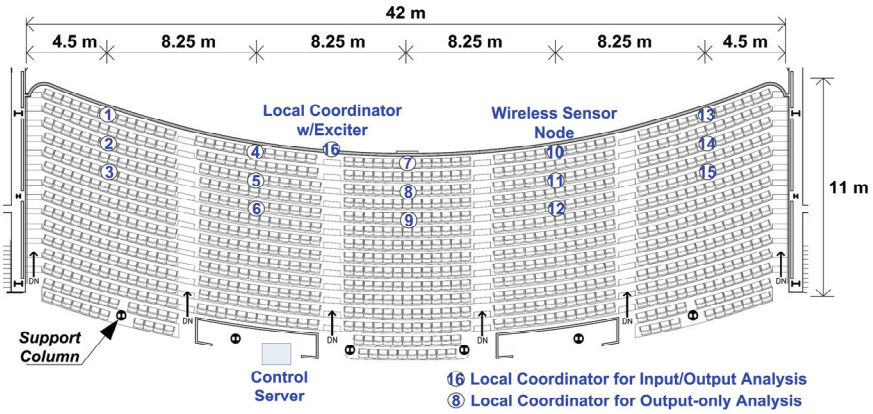

(a)

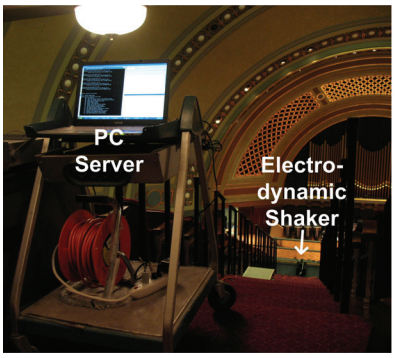

(b)

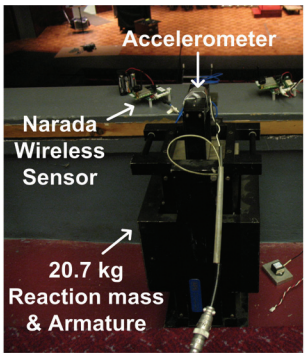

(c)

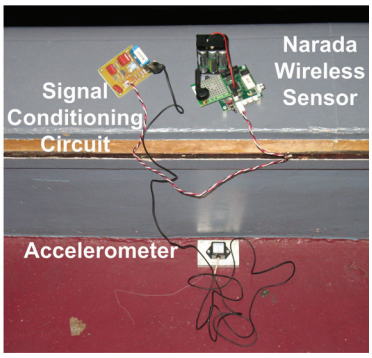

(d)

Figure 5.4 Experimental setup of the wireless monitoring system on the mezzanine balcony of Hill Auditorium: (a) sensor and exciter locations; (b) the control server; (c) electro-dynamic shaker driven by *Narada*; (d) typical *Narada* wireless sensor node with a MEMS-based accelerometer.

floor is 0.5 mg. To improve the signal-to-noise ratio of the accelerometers, a signal conditioning board designed to band-pass (0.014 to 25 Hz) and amplify (by 5, 10 or 20 times) sensor signals is utilized as shown in Fig. 5.5-d. In this study, an amplification of 20 is used on each MEMS accelerometer output before being digitized by the *Narada* ADC. The wireless sensor network is controlled by a standard laptop computer setup to act as the monitoring system's control server as shown in Fig. 5.4-b.

In the input-output implementation of the wireless monitoring system, an electro-dynamic shaker (APS Dynamics 400) is used. The shaker (Fig. 5.4-c) is placed at the front edge of the mezzanine balcony at the end of the third aisle (Fig. 5.4-a). This location is determined to be optimal for exciting a maximum number of modes of the cantilevered balcony. The shaker's total mass is 90.9 kg but its moving reaction mass is 20.7 kg. The shaker is controlled by a *Narada* node setup as a *local coordinator* (denoted as node 16 in Fig. 5.4-a). Prior to application of the *Narada*'s DAC output signal, the signal is boosted by an amplifier (Power Amplifier Model 124). The local coordinator is programmed to generate a saw-tooth chirp excitation whose frequency range is 3 to 15 Hz. In order to measure the motion of the shaker reaction mass, a Crossbow CXL02 accelerometer is mounted to the reaction mass and interfaced to the *Narada* node. During excitation of the balcony, five excitation types are utilized with time of duration the primary differentiator between excitations. The durations of the chirp excitations are varied from 8 to 24 sec in 4 sec increments. During the output-only implementation of the system, the shaker is turned off and wireless sensor node 8 (Fig. 5.4-a) is designated as the local coordinator of the wireless monitoring system. For excitation, a soft-tip 12-lb modal hammer (Dytran Instruments 5803A) is used in the vicinity of the electro-dynamic shaker to deliver broad-band impulse loads.

With the first five modes estimated to be below 10 Hz, a sampling rate of 40 Hz is prescribed for all of the tests conducted in this study. Each test is conducted for 30 sec resulting in the collection of 1200 points of data by the local coordinator and wireless sensor nodes. The input-output and output-only approaches to MP extraction are conducted autonomously by the wireless monitoring system. Each wireless sensor node is programmed to extract 105 Markov parameters.

5.4.2 Experimental Results

The acceleration of the shaker reaction mass during the application of the 20 sec chirp signal as measured by the local coordinator (*Narada* node 16) is presented in Fig. 5.5-a. Due to the presence of a back electromagnetic field (EMF), the amplitude of the acceleration decreases over the direction of the applied excitation. In addition, the coupling between the shaker and the balcony is evident in the measured acceleration toward the end of the time history record (*i.e.*,

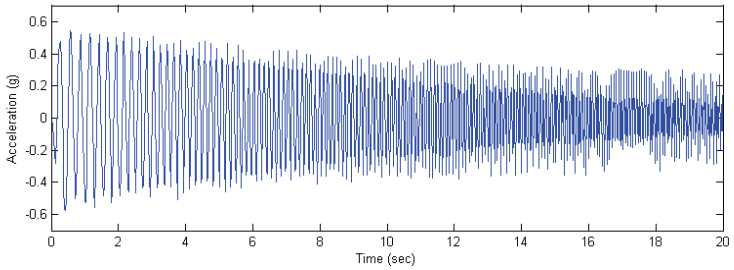

(a)

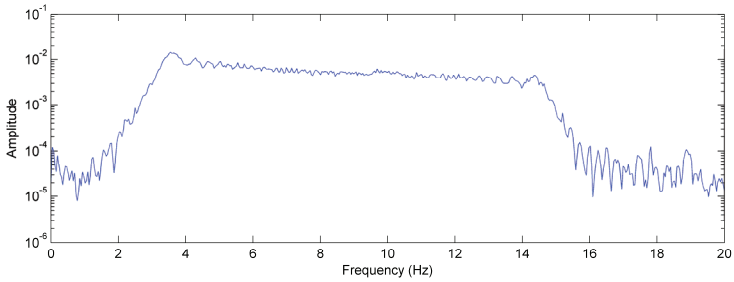

(b)

Figure 5.5 Controlled excitation of the mezzanine balcony: (a) measured acceleration of the electro-dynamic shaker reaction mass; (b) corresponding Fourier spectrum of the excitation.

between 16 and 20 sec). The Fourier spectrum of the reaction mass acceleration is presented in Fig. 5.5-b. The 3 to 15 Hz frequency band of the applied excitation is confirmed although the spectrum amplitude decreases at higher frequencies as a result of the aforementioned back EMF effect inherent to the excitation source. The acceleration response of the mezzanine balcony at the center of the balcony as measured by wireless sensor nodes 7, 8, and 9 is shown in Fig. 5.6. The acceleration response is less than 3 mg as measured in the three locations. In addition, resonance of the lower modes of the mezzanine balcony is evident in the first ten seconds of the measured acceleration response. The power spectral density (PSD) functions corresponding to the response time-histories plotted in Fig. 5.6 are shown in Fig. 5.7; the modes of the system are easy to identify in the PSD plots.

During each test, the wireless monitoring system automatically extracts the MPs at each wireless sensor node using the input-output or output-only data. During the input-output implementation of the decentralized system identification, perfect communications are experienced with data never being lost during the broadcasting of the excitation force by the local coordinator and the communication of the MPs from each wireless sensor node to the control server. Similarly, the output-only implementation also experiences perfect communications with 100% data delivery during the broadcasting of the local coordinator acceleration response and the

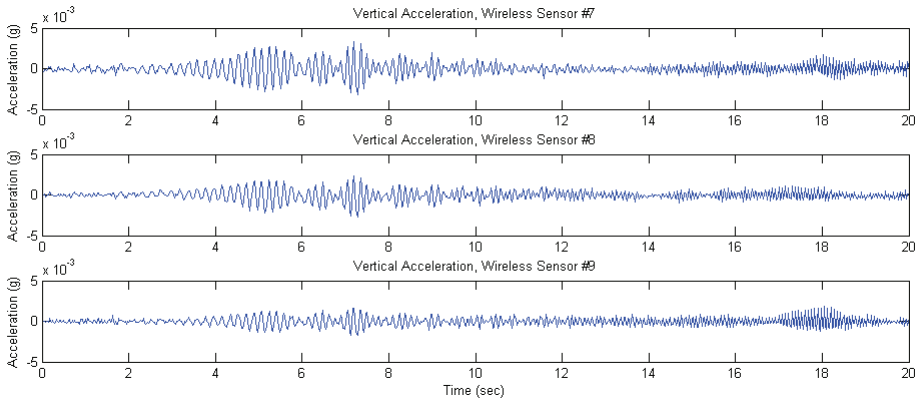

Figure 5.6 Measured acceleration response of the instrumented mezzanine balcony at node 7 (top), 8 (middle), and 9 (bottom) during the application of a 20-second 3 to 15 Hz chirp signal (Fig. 5.5).

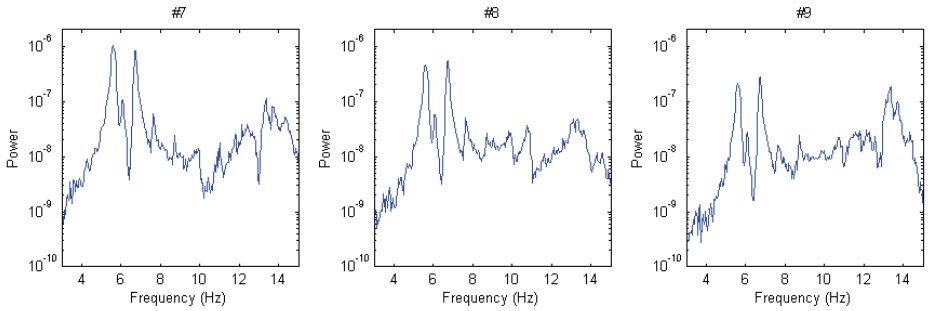

Figure 5.7 Power spectral density functions of the measured acceleration response at sensor node 7 (left), 8 (middle), and 9 (right) during the application of a 20-second 3 to 15 Hz chirp signal (Fig. 5.5).

communication of the MPs from each wireless sensor node. Figs 5.8 and 5.9 depict the estimated MPs as calculated by wireless sensor nodes 7, 8, and 9 during the input-output and output-only implementations, respectively. To check the precision of the extracted MP, offline subspace identification is conducted using the excitation and response time history data collected by the wireless monitoring system. As shown in Figs 5.8 and 5.9, excellent agreement is encountered in the MP time histories, thereby underscoring the accuracy of the automated data processing implemented within the wireless monitoring system. Similar results are encountered in the remaining wireless sensor nodes.

After the estimated MPs are communicated to the control server, the system matrices **A**, **B**, **C**, and **D** are estimated by ERA. The modal characteristics of the system (*i.e.*, modal frequencies, mode shapes, and modal damping ratios) are extracted from the system matrix **A**. For example,

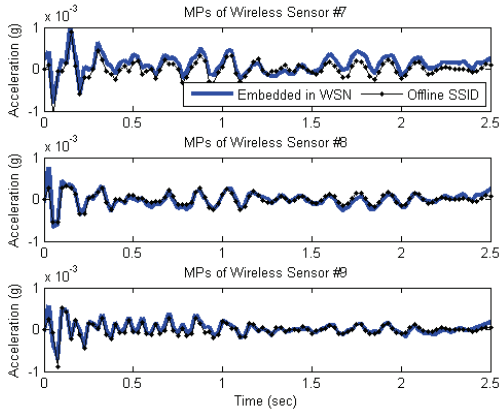

Figure 5.8 Estimated MPs at wireless sensor node 7 (top), 8 (middle), and 9 (bottom) during controlled excitation of the balcony.

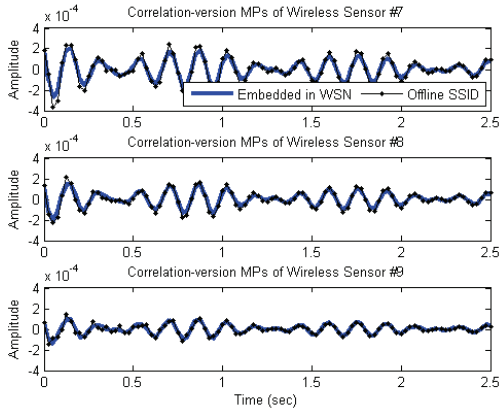

Figure 5.9 Estimated MPs at wireless sensor node 7 (top), 8 (middle), and 9 (bottom) during the output-only implementation of the decentralized system identification method.

the first five mode shapes of the mezzanine balcony as extracted by the input-output and output-only MP estimation are presented in Fig. 5.10-a and Fig. 5.10-b, respectively. For comparison, the first five mode shapes of the balcony calculated offline by subspace identification are also presented in Fig. 5.10-c. Strong agreement is visually observed in the mode shapes as estimated by the three independent system identification methods. To compare the modal characteristics extracted by the input-output and output-only implementations in a more quantitative manner, Table 5.2 tabulates the modal frequencies and modal damping ratios extracted by the three system identification methods (*i.e.*, the in-network input-output implementation, in-network output-only implementation, and offline subspace identification). During the input-output implementation, the five tests correspond to the same excitation but of differing duration (*i.e.*, 8, 12, 16, 20, and 24

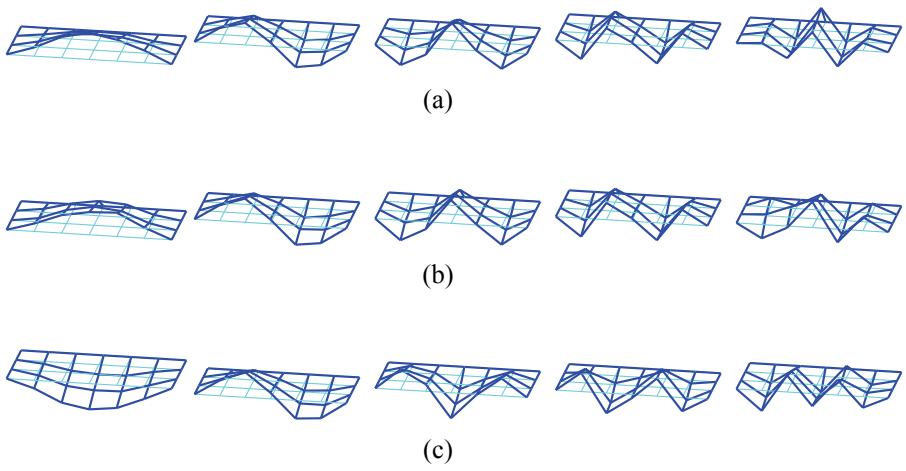

Figure 5.10 Estimated five global mode shapes of the Hill Auditorium mezzanine balcony: (a) network-level ERA from sensor-level MP estimations from input/output data; (b) network-level ERA from sensor-level MP estimations from output-only data; (c) off-line subspace method from input/output data.

sec). The five tests corresponding to the output-only implementation are separate modal hammer blows delivered to the balcony. The first four modal frequencies (5.6, 6.1, 6.7, and 7.6 Hz) and damping ratios (1.4, 1.1, 0.8, and 0.8 %) are all in strong agreement between the three system identification methods. However, the in-network implementation (both the input-output and output-only implementations) is not as accurate for the fifth mode (9.1 Hz). In comparison to the offline subspace identification method, the frequency and damping ratio of the fifth mode for the in-network input-output system identification method is in error by 5.5 and 81.6 %, respectively. The modal frequency is more accurate for the output-only implementation (with an error of less than 1 %); however, the estimated damping ratio is in error by 73.5 %. To compare the mode shapes, the modal assurance criteria (MAC) is adopted (Ewins 2000). The mode shapes estimated by the wireless monitoring system are compared to the mode shapes extracted offline. Again, consistent modes are extracted by the monitoring system as seen by MAC values close to 1. However, disagreement exists in the fifth mode with MAC values well below 1. The lack of general agreement of the 5th mode can be attributed to the limited number of Markov parameters extracted. Longer time history records, higher sampling rates, and the extraction of more Markov parameters would all lead to improvements in the accuracy of the extracted 5th mode.

Table 5.2 Summary of identified modal parameters from the Hill Auditorium mezzanine balcony.

	Input/output Analysis					Output-only Analysis				
Frequency (Hz)	Mode 1	Mode 2	Mode 3	Mode 4	Mode 5	Mode 1	Mode 2	Mode 3	Mode 4	Mode 5
Test 1	5.616	6.052	6.724	7.618	8.606	5.629	6.064	6.731	7.616	9.958
Test 2	5.629	6.046	6.720	7.613	8.591	5.617	6.030	6.727	7.638	8.535
Test 3	5.617	6.047	6.713	7.612	8.642	5.618	6.054	6.720	7.613	10.055
Test 4	5.612	6.047	6.717	7.610	8.663	5.611	6.045	6.718	7.620	8.660
Test 5	5.612	6.047	6.715	7.602	8.596	5.622	6.044	6.716	7.602	8.591
Mean	5.617	6.048	6.718	7.611	8.619	5.619	6.047	6.722	7.618	9.160
Subspace Method	5.631	6.056	6.727	7.626	9.116					
Damping Ratio	Mode 1	Mode 2	Mode 3	Mode 4	Mode 5	Mode 1	Mode 2	Mode 3	Mode 4	Mode 5
Test 1	0.014	0.011	0.007	0.008	0.011	0.011	0.008	0.007	0.007	0.022
Test 2	0.013	0.011	0.008	0.008	0.009	0.013	0.010	0.009	0.007	0.008
Test 3	0.013	0.012	0.008	0.008	0.005	0.014	0.011	0.007	0.007	0.014
Test 4	0.014	0.012	0.009	0.007	0.010	0.015	0.009	0.008	0.007	0.015
Test 5	0.013	0.012	0.009	0.008	0.008	0.015	0.011	0.008	0.006	0.007
Mean	0.013	0.011	0.008	0.008	0.009	0.013	0.010	0.008	0.007	0.013
Subspace Method	0.014	0.011	0.008	0.008	0.049					
MAC	Mode 1	Mode 2	Mode 3	Mode 4	Mode 5	Mode 1	Mode 2	Mode 3	Mode 4	Mode 5
Test 1	0.998	0.969	0.999	0.933	0.480	0.977	0.994	0.992	0.972	0.543
Test 2	0.999	0.989	0.996	0.932	0.598	0.966	0.990	0.984	0.965	0.621
Test 3	0.999	0.983	0.996	0.935	0.495	0.972	0.996	0.994	0.973	0.474
Test 4	0.996	0.986	0.994	0.931	0.710	0.972	0.994	0.991	0.960	0.233
Test 5	0.999	0.982	0.992	0.933	0.455	0.975	0.992	0.990	0.969	0.524
Mean	0.998	0.982	0.995	0.933	0.548	0.973	0.993	0.990	0.968	0.479

5.5 Chapter Summary and Conclusions

As wireless monitoring systems emerge as a viable alternative to traditional wired counterparts, scalable approaches to autonomously processing measurement data in the network are necessary. Embedded data processing has the benefit of improving system scalability, reducing demand on the wireless communication channel, and reducing the power consumption of the system battery-operated nodes. In this study, a decentralized approach to system identification is proposed for embedment within a wireless structural monitoring system. Specifically, extraction of nonparametric Markov parameters using input-output and output-only data locally stored at individual wireless sensor nodes allows each node to convert its raw measurement data into a more compact representation prior to communication to a control server

where ERA analysis is performed. The approach is scalable to large nodal densities because: 1) the need for broadcasting data to the entire network is minimized (*i.e.*, only the excitation or reference response time history must be broadcast herein), and 2) calculations (*i.e.*, MP extraction) are performed in parallel independently by the pervasive wireless sensor nodes. By extracting 105 MPs from 1200 point response time history records at 15 wireless sensor nodes, over 77 % compression was accomplished. While significant data compression is attained, system properties are identified with a high-degree of accuracy.

For validation, a wireless monitoring system consisting of *Narada* nodes was installed on the mezzanine balcony of the Hill Auditorium. The wireless monitoring system is installed to control the excitation applied to the balcony, to sense the balcony response under the applied load, to communicate data, and to process measurement data in a scalable and autonomous manner. To validate the input-output MP extraction method embedded in-network, an electro-dynamic shaker was also adopted. The MPs extracted in-network were found to be in complete agreement with MP estimated offline by a direct subspace identification method. The wireless monitoring system control server performed an ERA analysis using the MPs collected from the wireless sensor nodes resulting in complete characterization of the system modal properties. The modal characteristics autonomously extracted by the wireless monitoring system using its in-network data processing were found to be within 2 % of those extracted offline by subspace identification for the first four modes.

CHAPTER 6

MOBILE WIRELESS SENSOR NETWORKS FOR EXPERIMENTAL OBSERVATION OF VEHICLE-BRIDGE INTERACTION

Heavy vehicles driving over a bridge create a complex dynamic phenomenon known as vehicle-bridge interaction. In recent years, interest in vehicle-bridge interaction has grown because deeper understanding of the phenomena can lead to improvements in bridge design methods while enhancing the accuracy of structural health monitoring techniques. The mobility of wireless sensors can be leveraged to directly monitor the dynamic coupling between the moving vehicle and the bridge. In this chapter, a mobile wireless sensor network is proposed for installation on a heavy truck to capture the vertical acceleration, horizontal acceleration, and gyroscopic pitching of the truck as it crosses a bridge. The vehicle-based wireless monitoring system is designed to interact with a static, permanent wireless monitoring system installed on the bridge. Specifically, the mobile wireless sensors time synchronize with the bridge's wireless sensors before transferring vehicle response data. Vertical acceleration and gyroscopic pitching measurements of the vehicle are combined with bridge accelerations to create a time synchronized vehicle-bridge response data set. In addition to observing the vehicle vibrations, Kalman filtering is adopted to accurately track the vehicle position using the measured horizontal acceleration of the vehicle and positioning information derived from piezoelectric strip sensors installed on the bridge deck as part of the bridge monitoring system. Using the Geumdang Bridge (Korea), extensive field testing of the proposed vehicle-bridge wireless monitoring system is conducted. Experimental results verify the reliability of the wireless system and the accuracy of the vehicle positioning algorithm.

6.1 Introduction

Vehicle-bridge interaction refers to the dynamic coupling that occurs between a vehicle and bridge when the vehicle crosses at high speeds. A vehicle can be viewed as a large rigid mass (*i.e.*, vehicle body) that is supported by vertical spring-damper connections at each of its wheels. When crossing a bridge, the vehicle vertically vibrates and pitches, leading to the introduction of dynamic loading on the bridge. In turn, the vibrations of the bridge influence the dynamics of the vehicle. Complete understanding of this complex coupling between the vehicle and bridge is critical in fully understanding the dynamic behavior of bridges under live load conditions. In the design of highway bridges, vehicle-bridge interaction is accommodated through the use of dynamic impact factors. Dynamic impact factors allow the bridge designer to account for the dynamic response of a bridge when using an equivalent static load design methodology (AASHTO 2002). The current set of dynamic impact factors were obtained from finite element method (FEM) simulation of bridge systems in which the dynamics of the bridge, the behavior of the vehicle, and the bridge road roughness have all been explicitly considered (Hwang and Nowak 1991). However, the limitation of FEM modeling render the dynamic impact factors potentially inaccurate for some bridge designs (Kwasniewski *et al.* 2006). To more accurately determine suitable dynamic impact factors, direct experimental observation of vehicle-bridge interaction is necessary. There are many additional benefits that can be derived from experimental observation of vehicle-bridge interaction. For example, recent increases in the weight of heavy trucks has led to an acceleration of bridge deterioration (Green and Cebon 1994). Experimental observation of vehicle-bridge interaction could lead to more accurate determination of bridge load capacities. Furthermore, experimental data would improve understanding of vehicle-induced structural degradation.

Over the past two decades, powerful new sensor technologies have emerged including microelectromechanical systems (or MEMS) (Oppenheim 2003; Ozevin *et al.* 2006), wireless sensor networks (Pakzad *et al.* 2008; Mascarenas *et al.* 2009; Whelan and Janoyan 2009), guided wave sensors (Greve *et al.* 2007; Salas and Cesnik 2010) and fiber optic sensors (Ansari 2007; Suzhen and Zhishen 2007), just to name a few. Structural health monitoring (SHM) of bridge structures has served as the primary motivator for many of these developments. However, most of the sensors developed are designed to monitor structural response but not the loading inducing those responses. This is unfortunate because system identification and damage detection using output-only data sets are challenging inverse problems to solve when high uncertainty surrounds the bridge loading. Hence, the accuracy of current damage detection methods would be improved if the structural demand (*i.e.*, the vehicle loading) was precisely known. Historically, weigh-in-

motion systems (WIMS) have been used to observe the weight of vehicles crossing a bridge at a specific position. While WIMS can provide data sets from which bridge loads and their temporal variations can be modeled, such systems are inadequate for direct observation of vehicle-bridge interaction due to the fact that they only measure vehicle loading at a static location on the bridge. Another issue associated with WIMS is that their measurements contain significant uncertainty due to the temperature and time variation of their voltage outputs (Szary and Maher 2009). Alternatively, researchers have explored the use of video sensing to observe the motion of vehicles as they cross a bridge. For example, a piezoelectric-based WIMS can be replaced with a high-speed camera that can capture vehicles entering and leaving the view of the camera. Captured video can then be used to accurately assess the speed of the vehicle, the number of vehicle axels, and the general class of vehicle (*e.g.*, car, sport utility vehicle, truck, *etc.*) through image processing (Chen *et al.* 2009). While Chen *et al*. position their camera to view the road at a localized position, Fraser *et al*. alternatively propose the use of video cameras positioned to capture a view of an entire bridge (Fraser *et al.* 2010). Using feature extraction and pattern recognition, vehicle types and position trajectories can be derived for all of the vehicles on the bridge. While knowledge of average vehicle weight and trajectory can be used to model vehicle-bridge interaction in a simulation environment, the actual interaction is not directly sensed in these video-based sensing systems.

The bridge and vehicle must both be instrumented to capture the dynamic coupling that exists during vehicle-bridge interaction. In particular, instrumentation installed in the vehicle can provide data corresponding to the vehicle's vibratory response to the bridge as well as its position on the bridge as a function of time. When combined with response data collected from the bridge, a rich data set corresponding to the system input (*i.e.*, vehicle) and output (*i.e.*, bridge) is created. The field has explored the monitoring of vehicles as they interact with roads, rail tracks, and bridges. For example, Mizuno *et al.* propose the installation of MEMS accelerometers, global positioning system (GPS) receivers, and a wired data acquisition system within railcars to capture their dynamic behavior as they travel over rail tracks (Mizuno *et al.* 2008). While the prototype system can measure the dynamic response of the vehicle, the system does not directly record the dynamic response of the rail or that of railway bridges. Even though bridges and vehicles have been independently monitored, monitoring both the vehicle and bridge within a single monitoring system architecture has not yet been attempted. This is due largely to the challenges a moving vehicle poses to tethered monitoring system architectures. Specifically, the mobility of the vehicle rules out the possibility of connecting vehicle sensors to the bridge monitoring system via coaxial wiring. Rather, two independent data acquisition systems would

be needed with one dedicated to monitoring the vehicle and the other monitoring the bridge. After collection, the vehicle and bridge response data sets would need to be combined with accurate time synchronization. In contrast, this study explores the use of wireless telemetry to eliminate the wires that limit the unification of vehicle-based mobile sensors within a bridge monitoring system.

In this study, extended-range *Narada* wireless sensors are utilized as a building block of a comprehensive monitoring system designed for monitoring vehicle-bridge interaction. The work builds on recent research that has established the accuracy, reliability, and cost-effectiveness of wireless monitoring systems for bridges (Lynch *et al.* 2006; Pakzad *et al.* 2008; Whelan and Janoyan 2009). A wireless sensor network is proposed for installation in a heavy vehicle (*i.e.*, truck) to record the dynamic response of the vehicle as it crosses a bridge instrumented with a permanent wireless monitoring system. The sensing transducers installed in the vehicle include accelerometers to measure vertical and horizontal acceleration and a gyroscope to capture the vehicle pitching motion. The bridge is instrumented with accelerometers to measure the vertical vibration of the bridge. Piezoelectric tactile sensors are also installed on the bridge road surface to sense the vehicle position. As the instrumented vehicle approaches the bridge, the permanent wireless monitoring system on the bridge establishes communication with the vehicle's mobile monitoring system to synchronize time and to initiate data collection. After the truck crosses the bridge, the wireless sensors on the truck wirelessly transmit their synchronized response data to the bridge monitoring system where it is automatically combined with the bridge response data. The horizontal acceleration of the vehicle and the position information acquired from the piezoelectric tactile sensors are combined by the wireless monitoring system using Kalman filtering to estimate the vehicle trajectory. The chapter begins with a description of the components of the proposed wireless monitoring system for experimentally observing vehicle-bridge interaction. Next, a theoretical description of the Kalman filter used to extract an accurate vehicle position trajectory is presented. Experimental validation of the proposed wireless monitoring system on Geumdang Bridge (Icheon, Korea) is then presented. Finally, the chapter concludes with a summary of the key project results and offers insight to future work aimed towards acquiring measurement data for vehicle-bridge interaction analysis (Chapter 7).

6.2 Overview of the Wireless Vehicle-Bridge Monitoring System

6.2.1 Geumdang Bridge, Korea

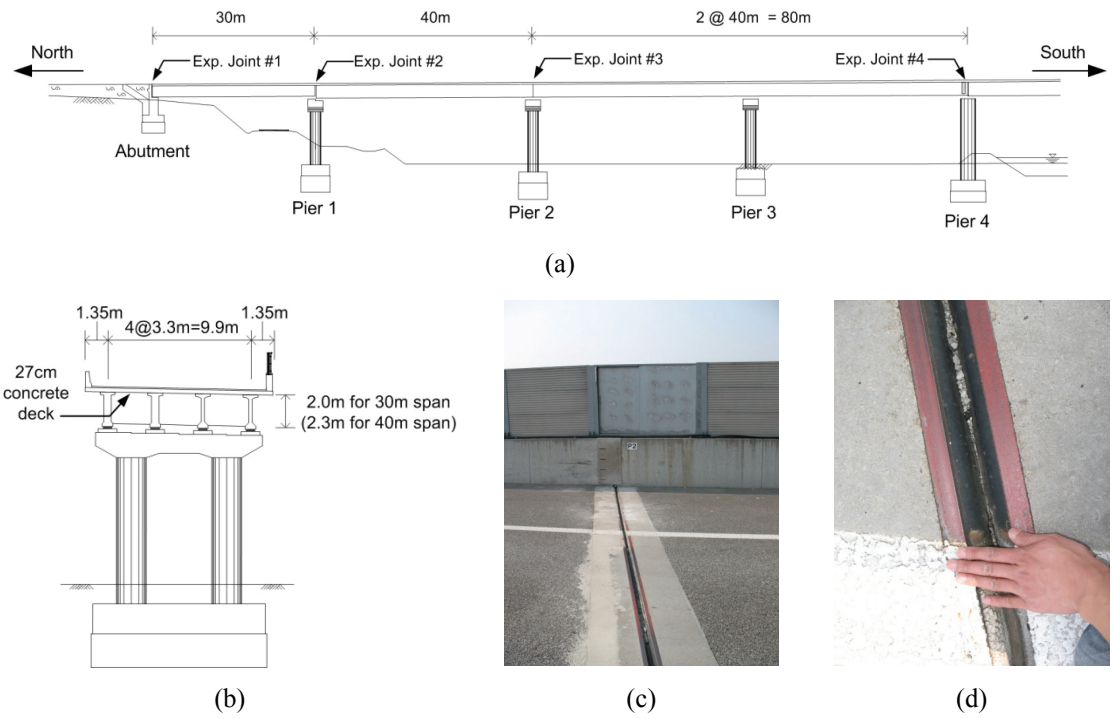

Figure 6.1 The Geumdang Bridge: (a) profile plan of the northern-most spans of the bridge; (b) cross-section profile; (c) expansion joint typical between adjacent spans; (d) close-up view of the third expansion joint.

This study selects the Geumdang Bridge located in the KEX test road (Fig. 2.5 in Chapter 2) to validate the performance of the proposed wireless monitoring system for vehicle-bridge interaction monitoring. The design of the Geumdang Bridge is very unique because it employs two different span types in its design. The northern half of the bridge spans 150 m and is constructed using 4 pre-cast concrete girders with a 27 cm thick concrete deck placed in composite action with the girders (Fig. 6.1-b). The southern half of the bridge spans 122 m and is constructed as a continuous prestressed concrete box-girder. In 2006, the southern spans of the Geumdang Bridge were instrumented with an array of wireless sensors to measure the vertical acceleration of the bridge under traffic loads (Lynch *et al.* 2006). In this study, the northern span of the bridge will be instrumented with a wireless monitoring system to record the behavior of the bridge during loading by a test vehicle simultaneously monitored using wireless sensors. The northern portion of the bridge (Fig. 6.1-a) is divided into three independent spans separated by expansion joints (Figs 6.1-c and -d) that accommodate thermal expansion of the bridge. The first span is 30 m long and is supported by the abutment structure and a pier. The second span is 40 m long and is supported by two piers at its ends. The third span is 80 m long and is again supported

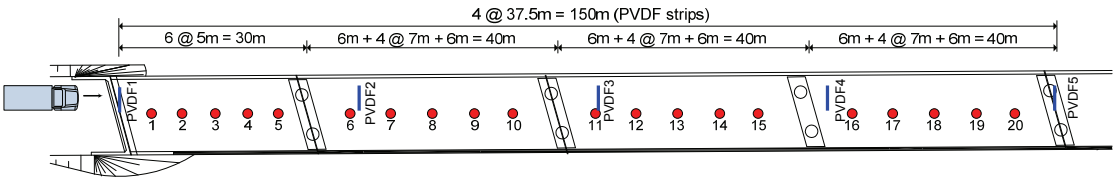

Figure 6.2 Stationary wireless monitoring system assembled from *Narada* wireless sensor nodes. Twenty (20) uni-axial accelerometers installed in the center of the bridge deck with five (5) PVDF tactile sensors installed at multiple locations along the bridge length.

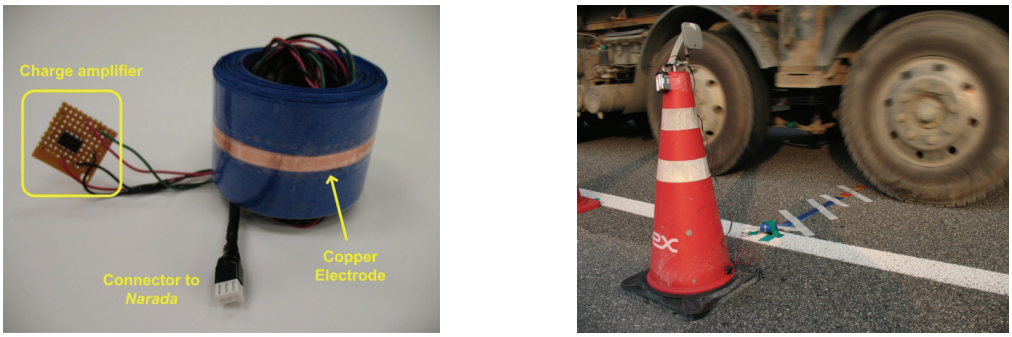

(a) (b)

Figure 6.3 (a) PVDF tactile strip sensor rolled up prior to deployment on the bridge. Copper electrode and charge amplifier circuit clearly shown. (b) PVDF tactile strip sensor installed on the bridge deck (at sensor location #1) with *Narada* wireless sensor shown on top of the orange traffic cone.

by two piers at its span ends; however, a redundant pier is placed midway along its length to offer additional support.

6.2.2 Stationary Wireless Monitoring System on the Bridge

The 150 m northern span of the Geumdang Bridge is instrumented with a dense network of *Narada* wireless sensor nodes to which MEMS accelerometers and tactile sensors (*i.e.*, piezoelectric strips) have been interfaced. As shown in Fig. 6.2, a total of 20 *Narada* wireless sensor nodes, each with a uniaxial MEMS accelerometer oriented in the vertical direction, is installed in the center lane of the bridge deck; the accelerometers are spaced equidistantly on each span. The Silicon Designs SD2012 accelerometer is selected for monitoring the vertical acceleration response of the bridge. While a large fraction of sensors for structural monitoring are single-ended, the SD2012 offers a low noise floor when utilized in differential output mode. The *Narada* ADC can accommodate differential sensor outputs by combining two of its available channels. In differential output mode, the sensitivity of the SD2012 accelerometer is 2 V/g while

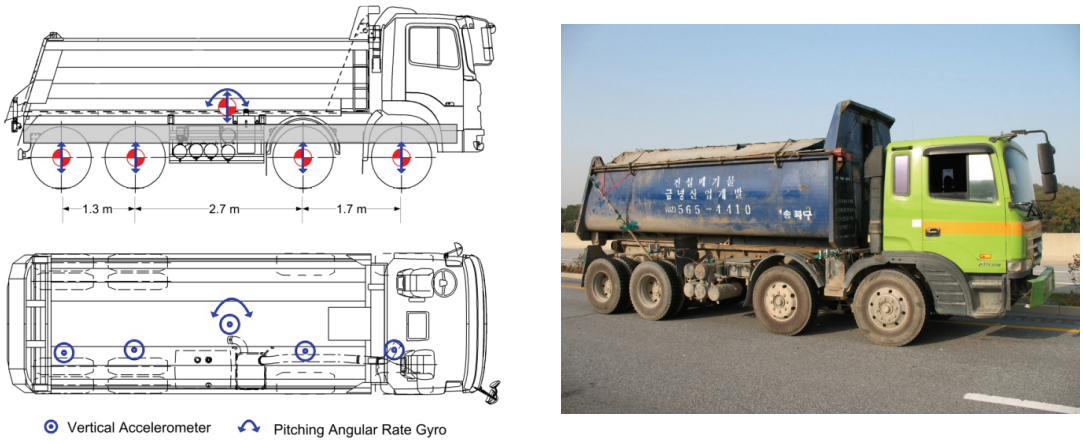

(a) (b)

Figure 6.4 Experimental 4-axle 20.9 ton truck with instrumentation: (a) pitch-plane model of the truck with 6 DOFs identified for one sprung mass and four unsprung masses. (b) picture of the truck on the Geumdang Bridge.

its noise floor is 13 μg/√Hz. The dynamic range of the accelerometer is ±1 g which is ample for measuring bridge vibrations. Accelerometers are mounted on aluminum blocks that are bonded to the surface of the roadway by epoxy.

Tactile sensors are installed on the bridge deck to identify points in time when the truck drives over the sensors. The tactile sensors are designed from poly(vinylidene) fluoride, or PVDF, which is a piezoelectric polymeric material that exhibits a voltage change when dynamically strained. PVDF strips will capture in time when each axel of the truck drives over the strip. In this application, PVDF is selected because of its ductility and toughness which will give it great durability when being repeatedly driven over by heavy trucks. The tactile sensors are constructed from commercial PVDF sheets acquired from Measurement Specialties. The sheets are cut into 5 mm wide strips roughly 1.5 m long. Copper tape (5 mm wide) is bounded to the top and bottom surfaces of the PVDF strip to serve as electrodes (Fig. 6.3-a). A charge amplifier circuit is integrated with each PVDF strip to amplify its voltage before being interfaced to a *Narada*. In total, five (5) PVDF strips interfaced to *Narada* nodes are bounded to the surface of the road (Fig. 6.3-b); the locations of the PVDF tactile sensors are presented in Fig. 6.3.

6.2.3 Mobile Wireless Sensor Instrumentation on the Truck

To dynamically load the Geumdang Bridge, a 4-axel truck is used (Fig. 6.4). Prior to the truck's arrival to the bridge, the weight of the truck is measured at a local weigh-station. The

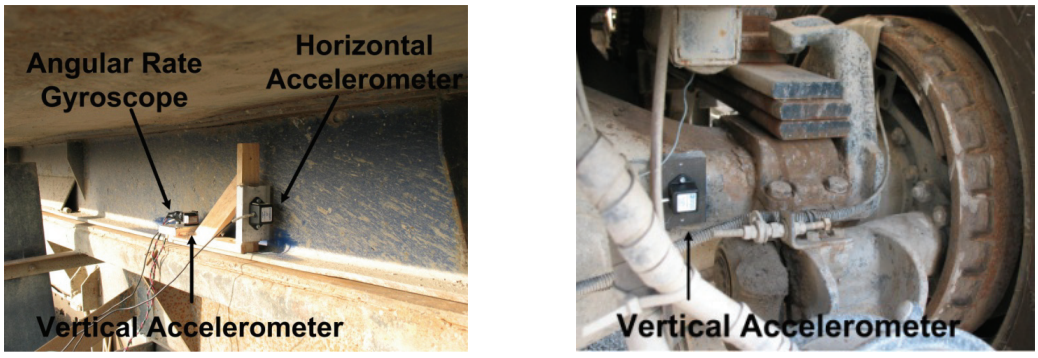

(a) (b)

Figure 6.5 Installation of sensors on the experimental truck to monitor the 6 DOF associated with the truck pitch-plane model (Fig. 6.4-a): (a) accelerometers and gyroscope installed at the truck body center of gravity; (b) accelerometer on the axle cover at the fourth (back) axel.

total weight of the truck is 20.9 tons with the front, second, third, and back axels each taking 4.3, 8.0, 4.6, and 4.0 tons, respectively. The truck dynamics can be modeled using a pitch-plane model with multiple rigid bodies connected by spring-damper linkages (Gillespie and Karamihas 2000). First, the truck body is comprised of a single sprung mass supported by the vehicle suspension system. Second, the wheels, axels, brakes, and steering knuckle are modeled as concentrated masses centered at each axel. In total, the dynamics of the vehicle are modeled using five lumped masses and six degrees-of-freedom (DOF): vertical translation of the truck body, rotation of the truck body, and vertical translation of each axel. Finally, the rigid body motion of the vehicle is modeled by its horizontal translation.

To monitor the dynamics of the truck body (*i.e.,* the sprung mass of the pitch-plane model), sensors are concentrated in the truck body's center of gravity to monitor vertical acceleration, horizontal acceleration, and gyroscopic motion associated with truck pitching (Fig. 6.5-a). To monitor the vertical acceleration of the truck body, the Crossbow CXL02 capacitive accelerometer is selected. The CXL02 has a dynamic range of ± 2g, a sensitivity of 1 V/g, and a noise floor of 0.15 mg. A second CXL02 is utilized to monitor the horizontal acceleration of the vehicle; this acceleration data will be used for truck positioning. A MEMS angular rate gyroscope (Analog Devices ADXRS624) is also installed at the center of gravity to capture the pitching motion of the truck. The ADXRS624 has a dynamic range of ±50º/sec and a sensitivity of 25 mV/º/sec. Each axel of the truck is monitored using an accelerometer bonded to the axel oriented in the vertical direction. The Analog Devices ADXL105 accelerometer is selected for its high ± 10g measurement range and low 2 mg noise floor; the sensitivity of the ADXL105 is 250 mV/g. The accelerometer is attached by epoxy to the underside of the leaf-spring of each front

axle. For the two back axels, the accelerometers are installed on the metallic cover of the axel (Fig. 6.5-b). To record the sensor outputs, a *Narada* wireless sensor is interfaced with each sensing transducer installed on the truck. To enhance the performance of the wireless communications, the antennas of each wireless sensor are mounted to a 1.2 m wood post with the post installed in a near vertical orientation (70 to 75°) on the passenger side of the truck.

6.2.4 Operation of the Wireless Monitoring System During Dynamic Load Testing

The proposed wireless monitoring system for experimental observation of vehicle-bridge interaction is architecturally centralized with a central base station installed on the bridge. The base station consists of an IEEE 802.15.4 receiver interfaced to a small single-board computer that coordinates the activity of the wireless monitoring system. The base station continuously transmits a beacon signal that can be received by a truck instrumented with *Narada* wireless sensors. Similarly, *Narada* sensors on the truck are designed to be in a receive-mode waiting to receive the beacon packet from the bridge base station. As the truck drives closer to the bridge (*i.e.,* within 800 m of the bridge receiver), it will fall within communication range of the bridge monitoring system base station. Upon receipt of the beacon packet, the *Narada* wireless sensors on the truck acknowledge their existence by sending their identification numbers wirelessly back to the base station. As soon as the truck's wireless sensor nodes send their identification numbers, they enter a state ready to receive a second beacon packet from the bridge receiver to which their local clocks will be synchronized. Once the base station acknowledges that an instrumented truck is in vicinity, it sends a command packet to the network of wireless sensor nodes on the bridge and truck commanding them to all synchronize their clocks to the arrival of the packet and to collect data for a set period of time at a specific sampling rate. This approach to time synchronization has been previously verified to be within 11 μs (see Fig. 2.3 in Chapter 2) which is negligible when compared to the normal sample rates used in bridge monitoring (*i.e.*, less than 1 kHz). After all of the sensors have collected their response data, they notify the base station that they are ready to transmit their response data back to the server. The server queries them one at a time for their data; the sensors on the truck are queried first because they may shortly be out of range. In this study, the base station commands the mobile and static wireless sensor nodes to collect 90 seconds of data at a sample rate of 100 Hz. This time duration provides the monitoring system ample time to register the mobile wireless sensors, collect bridge and vehicle response data, and collect the data at the base station.

During experimental validation on the Geumdang Bridge, the KEX closes the test road to allow the 4-axel truck unfettered access to the bridge. The base station with a receiver (Fig. 6.6-

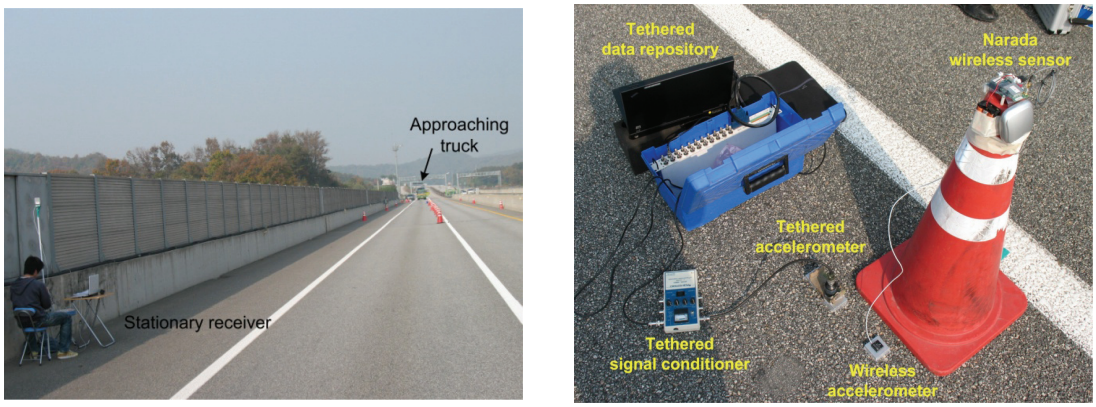

(a) (b)

Figure 6.6 Dynamic load testing by wireless sensor networks: (a) base station at the start of a test with the truck north of the bridge. (b) Wireless accelerometer on the bridge deck side-by-side with a tethered piezoelectric accelerometer at sensor location #8 (see Fig. 6.2).

a) is installed on the shoulder of the southern end of the bridge. On site, the effective communication range of the base station is determined to be roughly 800 m. The seven mobile *Narada* wireless sensors on the truck and the twenty five static *Narada* wireless sensors on the bridge are set to communicate on the same wireless channel as the base station. Once the installation of the sensors on the truck and bridge is complete, the bridge is loaded by driving the truck across the bridge at three different velocities (30, 50, and 60 km/hr). The starting position of the truck is roughly 500 m up the road. The truck is commanded by the researchers on site to accelerate until it achieves the desired test speed at which time the truck driver holds the velocity of the truck constant. Once the truck leaves the bridge, the truck driver brings the truck to a stop roughly 200 m past the southern bridge abutment. The truck is driven in the left-most lane to ensure it drives over the PVDF tactile sensors installed on the road deck.

6.3 Theory of Trajectory Estimation

6.3.1 Review of Trajectory Estimation and Integration of Acceleration

During vehicle-bridge interaction analysis, accurate positioning of the vehicle provides the location of the dynamic load imposed on the bridge by the vehicle. Many trajectory estimation algorithms are available from the geodetic and navigation fields that integrate inertial measurements derived from accelerometers and gyroscopes to track bodies in space (Lawrence 1998). Closely related to inertial navigation is the work conducted in the civil engineering field in determining the displacement of structures based on their measured acceleration responses.

For example, Lee *et al.* have proposed an acceleration-based low-pass filtering algorithm to derive the displacement of low-frequency dominant structures using acceleration measurements (Lee *et al.* 2010). While the method works well for structural responses dominated by sinusoidal motion, it is not capable of reconstructing the pseudo-static response common during vehicle loading. In contrast, Smyth and Wu propose a novel data fusion algorithm that combines acceleration and displacement measurements to overcome the challenge of low frequency noise that is amplified when numerically integrating an acceleration signal (Smyth and Wu 2007).

Similar to Smyth and Wu, this study takes a data fusion approach to positioning an instrumented vehicle on a bridge by combining acceleration measurements of the vehicle with position information obtained from PVDF tactile sensors installed on the bridge deck. The proposed trajectory estimation algorithm explicitly considers measurement bias to account for sensor bias (*e.g.*, non-zero offsets), the tilting of the sensor during installation, among other biasing factors. Each sensor used has a unique bias that must be accounted for to achieve high precision inertial sensing (Ryu 2004; Zarchan *et al.* 2009). Kalman filtering and fixed interval smoothing is then used to yield a highly accurate estimate of the vehicle location on the bridge.

6.3.2 Tracking Model Formulation

A mathematical model for the vehicle tracking begins with consideration of a vehicle in which an accelerometer is installed at the center of gravity to measure horizontal acceleration. The one-dimensional trajectory of the horizontally moving vehicle is:

$$\ddot{\bar{x}}(t) = a(t) - \delta a(t) \qquad \text{with initial conditions } \bar{x}(0) \text{ and } \dot{\bar{x}}(0) \tag{6.1}$$

where $\ddot{\bar{x}}(t)$ is true horizontal acceleration of the vehicle and $a(t)$ is the measured horizontal acceleration. Hence, $\delta a(t)$ corresponds to the acceleration measurement error. The measurement error, $\delta a(t)$, consists of a deterministic unknown bias, $b(t)$, and stochastic process noise, $w(t)$, as follows:

$$\delta a(t) = bias(t) + w(t) \tag{6.2}$$

By numerically integrating Eq. (6.1) in the discrete-time domain, the horizontal velocity and position of the vehicle can be estimated:

$$\dot{\bar{x}}(k+1) = \dot{\bar{x}}(k) + (a(k) - \delta a(k))\Delta t \tag{6.3}$$

$$\bar{x}(k+1) = \bar{x}(k) + \dot{\bar{x}}(k)\Delta t + 0.5(a(k) - \delta a(k))\Delta t^2 \tag{6.4}$$

where Δt is the time step.

The problem of estimating the position and velocity of the vehicle is confined to estimating the measurement error, $\delta a(k)$ which consists of the bias, $b(k)$, and Gaussian process noise, $w(k)$, with zero mean and variance, Q (*i.e.*, $w(k) = N(0,Q(k))$). A model-based data fusion approach that combines the horizontal acceleration of the vehicle with position and velocity measurements obtained from PVDF tactile sensors is adopted. A state-space model that captures the evolution of the measurement error is proposed. Towards this end, a state vector, **x**, is introduced as:

$$\mathbf{x}(t) = \left[\delta\dot{x}(t)\ \delta x(t)\ b(t)\right]^T \tag{6.5}$$

where $\delta\dot{x}$ is the velocity measurement error and δx is the position measurement error. Based on the state defined in Eq. (6.5), a continuous-time state-space equation can be written to model the measurement error in the system:

$$\dot{\mathbf{x}}(t) = \begin{bmatrix} 0 & 0 & 1 \\ 1 & 0 & 0 \\ 0 & 0 & 0 \end{bmatrix} \mathbf{x}(t) + \begin{bmatrix} 1 \\ 0 \\ 0 \end{bmatrix} w(t) = \mathbf{A}\mathbf{x}(t) + \mathbf{w}(t) \tag{6.6}$$

Eq. (6.6) is converted to a discrete-time state-space representation as:

$$\mathbf{x}(k+1) = \mathbf{A}_{\mathrm{d}}\,\mathbf{x}(k) + \mathbf{w}(k) \tag{6.7}$$

where state transition matrix is calculated as:

$$\mathbf{A}_{\mathrm{d}} = e^{\mathbf{A}\Delta t} = \begin{bmatrix} 1 & 0 & \Delta t \\ \Delta t & 1 & 0.5\Delta t^2 \\ 0 & 0 & 1 \end{bmatrix} \tag{6.8}$$

When additional measurements are available from the PVDF tactile sensors (*i.e.*, vehicle position and velocity), the measurement error in the estimated vehicle position and velocity can be captured in the observation of the state:

$$\mathbf{y}(k) = \begin{bmatrix} 1 & 0 & 0 \\ 0 & 1 & 0 \end{bmatrix} \mathbf{x}(k) + \mathbf{v}(k) = \mathbf{C}_{\mathbf{d}}\mathbf{x}(k) + \mathbf{v}(k) \tag{6.9}$$

Process noise is included in the observation model to capture the uncertainty in the measured truck position and velocity as measured by the PVDF tactile sensors. Here, $\mathbf{v}(k)$ is simply:

$$\mathbf{v}(k) = \begin{bmatrix} N(0, R_1(k)) \\ N(0, R_2(k)) \end{bmatrix} \tag{6.10}$$

In Eq. (6.10), R_1 and R_2 correspond to the variance of the Gaussian noise inherent to the velocity and displacement and measurements, respectively.

6.3.3 Data Fusion by Kalman Filtering

Due to the assumption of zero-mean Gaussian noise on the acceleration (*i.e.*, $w(k)$), velocity and position (*i.e.*, $\mathbf{v}(k)$) measurements, Kalman filtering is ideally suited to extract an accurate estimate of the hidden state of the system, $\mathbf{x}(k)$ (Stengel 1994). By estimating the state of the system, the deterministic bias error, $b(k)$, can be accurately estimated. The Kalman filter algorithm consists of two main stages: state/covariance prediction and correction. Because the state-space model (*i.e.*, Eqs (6.6) and (6.9)) of the system is based on error dynamics, special considerations for the Kalman filter will be addressed during the correction stage.

Prediction stage: As seen in Eq. (6.6), there is no external input driving the system dynamics. The *a priori* state, $\mathbf{x}(k+1|k)$ and covariance, $\mathbf{P}(k+1|k)$ are expressed, respectively, as:

$$\mathbf{x}(k+1|k) = \mathbf{A}_\mathrm{d}\, \mathbf{x}(k|k) \tag{6.11}$$

$$\mathbf{P}(k+1|k) = \mathbf{A}_\mathrm{d}\mathbf{P}(k|k)\mathbf{A}_\mathrm{d}^\mathrm{T} + \mathbf{Q}_\mathrm{d} \tag{6.12}$$

where $\mathbf{Q}_\mathrm{d}$ is a discrete noise covariance matrix corresponding to horizontal acceleration sensing.

Correction stage: At the time step $k+1$, when the wheels of the vehicle hit a PVDF tactile sensor, an observation of the state-space system (*i.e.*, Eq. (6.9)) is made. Specifically, the estimated velocity, $\dot{\bar{x}}$, and displacement, $\bar{x}$, is derived from Eqs (6.3) and (6.4). These estimates are compared to the measured vehicle position, $x_{\mathrm{PVDF}}(k+1)$, and velocity, $\dot{x}_{\mathrm{PVDF}}(k+1)$, obtained from the PVDF tactile sensor. Position is based on the time when the first two axels have crossed over the PVDF. Similarly, the velocity is based on the timing between the axel crossings as measured by the PVDF sensor. The observation of the system can be written:

$$\mathbf{y}(k+1) = \begin{bmatrix} \delta\dot{x}(k+1) \\ \delta x(k+1) \end{bmatrix} = \begin{bmatrix} \dot{\bar{x}}(k+1) - \dot{x}_{\mathrm{PVDF}}(k+1) \\ \bar{x}(k+1) - x_{\mathrm{PVDF}}(k+1) \end{bmatrix} \tag{6.13}$$

The *a posteriori* state and covariance matrices can be expressed, respectively, as:

$$\mathbf{x}(k+1|k+1) = \mathbf{x}(k+1|k) + \mathbf{K}(k+1)\left(\mathbf{y}(k+1) - \mathbf{C}_{\mathrm{d}}\,\mathbf{x}(k+1|k)\right) \tag{6.14}$$

$$\mathbf{P}(k+1|k+1) = \left(\mathbf{I} - \mathbf{K}(k+1)\mathbf{C}_{\mathrm{d}}\right)\mathbf{P}(k+1|k) \tag{6.15}$$

The Kalman gain matrix, $\mathbf{K}(k+1)$, in Eqs (6.14) and (6.15) can be calculated using the algebraic Riccati equation:

$$\mathbf{K}(k+1) = \mathbf{P}(k+1|k)\mathbf{C}_{\mathrm{d}}^{\mathrm{T}}\left(\mathbf{C}_{\mathrm{d}}\mathbf{P}(k+1|k)\mathbf{C}_{\mathrm{d}}^{\mathrm{T}} + \mathbf{R}_{\mathrm{d}}\right)^{-1} \tag{6.16}$$

where $\mathbf{R}_{\mathrm{d}}$ is the covariance matrix corresponding to the position and velocity measurements yielded by the PVDF tactile sensor.

The vehicle velocity and location are finally estimated, respectively, as:

$$\begin{aligned} \dot{\hat{x}}(k+1) &= \dot{\bar{x}}(k+1) - \dot{x}(k+1\,|\,k) \quad \textit{with a priori state} \\ &= \dot{\bar{x}}(k+1) - \dot{x}(k+1\,|\,k+1) \quad \textit{with a posteriori state} \end{aligned} \tag{6.17}$$

$$\begin{aligned} \hat{x}(k+1) &= \bar{x}(k+1) - x(k+1\,|\,k) \quad \textit{with a priori state} \\ &= \bar{x}(k+1) - x(k+1\,|\,k+1) \quad \textit{with a posteriori state} \end{aligned} \tag{6.18}$$

6.3.4 Fixed-Interval Smoothing

To enhance the accuracy of the unique Kalman filter formulated, fixed-interval smoothing is adopted. Since the precise timing of when the vehicle enters and exits the bridge is known based on PVDF tactile sensors installed at the bridge end-points, fixed interval smoothing (Simon 2006) over the time period when the vehicle is on the bridge is prudent. The aforementioned Kalman filter is implemented off-line forward in time (from the time when the vehicle enters the bridge) and backwards in time (from the time when the vehicle exits the bridge) resulting in two estimates for the system state: $\hat{\mathbf{x}}_{\mathrm{f}}(k)$ and $\hat{\mathbf{x}}_{\mathrm{b}}(k)$, respectively. The smoothing process derives a smoothed state, $\hat{\mathbf{x}}_{\mathrm{s}}(k)$, as:

$$\hat{\mathbf{x}}_{\mathrm{s}}(k) = \mathbf{K}_{\mathrm{f}}(k)\hat{\mathbf{x}}_{\mathrm{f}}(k) + \mathbf{K}_{\mathrm{b}}(k)\hat{\mathbf{x}}_{\mathrm{b}}(k) \tag{6.19}$$

where $\mathbf{K}_{\mathrm{f}}(k)$ and $\mathbf{K}_{\mathrm{b}}(k)$ are coefficient matrices that weigh the relative contribution of the forward and backward state estimates. To guarantee unbiased state estimates, it requires that the sum of the coefficient matrices yield the identify matrix (*i.e.*, $\mathbf{K}_{\mathrm{f}}(k) + \mathbf{K}_{\mathrm{b}}(k) = \mathbf{I}$). As a result, Eq. (6.19) can be further simplified as:

$$\hat{\mathbf{x}}_s(k) = \mathbf{K}_f(k)\hat{\mathbf{x}}_f(k) + (\mathbf{I} - \mathbf{K}_f(k))\hat{\mathbf{x}}_b(k) \tag{6.20}$$

The covariance matrix of the smoothed state, $\mathbf{P}_s(k)$, can be calculated as:

$$\begin{aligned}\mathbf{P}_s(k) &= \mathrm{cov}\left(\hat{\mathbf{x}}_s(k)\hat{\mathbf{x}}_s^T(k)\right) \\ &= \mathbf{K}_f(k)\mathbf{P}_f(k)\mathbf{K}_f^T(k) + (\mathbf{I} - \mathbf{K}_f(k))\mathbf{P}_b(k)(\mathbf{I} - \mathbf{K}_f(k))^T\end{aligned} \tag{6.21}$$

where $\mathbf{P}_f(k)$ and $\mathbf{P}_b(k)$ are the covariance matrices of the forward and backward Kalman filtering processes. Minimizing $\mathbf{P}_s(k)$ with respect to $\mathbf{K}_f(k)$ in Eq. (6.21) leads to a condition for an optimal forward coefficient matrix, $\mathbf{K}_f(k)$:

$$\mathbf{K}_f(k) = \mathbf{P}_b(k)(\mathbf{P}_f(k) + \mathbf{P}_b(k))^{-1} \tag{6.22}$$

Finally, by substituting the optimal forward coefficient matrix into Eqs (6.20) and (6.21), the smoothed state and its covariance matrix can be determined, respectively, as:

$$\hat{\mathbf{x}}_s(k) = \mathbf{P}_b(k)(\mathbf{P}_f(k) + \mathbf{P}_b(k))^{-1}\hat{\mathbf{x}}_f(k) + \mathbf{P}_f(k)(\mathbf{P}_f(k) + \mathbf{P}_b(k))^{-1}\hat{\mathbf{x}}_b(k) \tag{6.23}$$

$$\mathbf{P}_s(k) = \left(\mathbf{P}_f^{-1}(k) + \mathbf{P}_b^{-1}(k)\right)^{-1} \tag{6.24}$$

6.4 Experimental Validation

6.4.1 Accuracy of the Wireless Monitoring System

The measurement accuracy of the *Narada* wireless sensors installed on the Geumdang Bridge is verified using a traditional tethered data acquisition system. A National Instruments 16-bit data acquisition system (Model 60362E) is used with a PCB Piezotronics 393B12 integrated circuit piezoelectric (ICP) accelerometer interfaced. The accelerometer measurement range is ± 0.5 g and its noise floor is 1.3 μg/(√Hz). The accelerometer is well suited for bridge monitoring because of its high sensitivity (10 V/g). To provide a constant excitation to the ICP accelerometer and to amplify the accelerometer output by a factor of 10, the PCB Piezotronics 480B21 signal conditioner is adopted. The tethered 393B12 ICP accelerometer is installed adjacent to the wireless accelerometer at sensor location #8 (as denoted in Fig. 6.2). A picture of

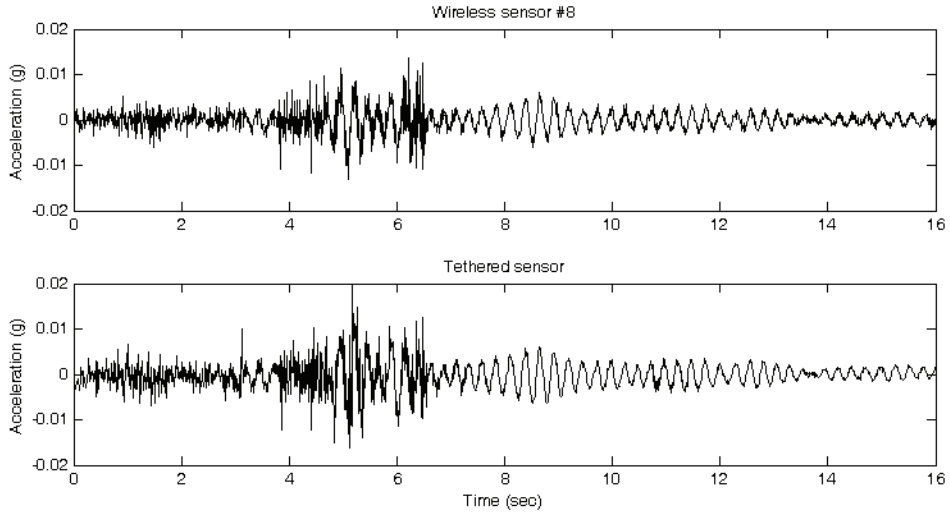

Figure 6.7 Comparision of the bridge vertical acceleration at sensor location #8 (Fig. 6.2) as measured by the *Narada* wireless (top) and tethered accelerometers (bottom) when loaded by a 20.9 ton truck driving at 65 km/hr with the truck north of the bridge.

the side-by-side accelerometer installation is depicted in Fig. 6.6-b. Fig. 6.7 presents the measured vertical acceleration of the bridge at sensor #8 as measured by the *Narada* wireless and tethered systems. The response measured corresponds to the test vehicle (*i.e.,* the 20.9 ton truck) driving over the bridge at 65 km/hr. In general, both time-history responses are in excellent agreement. As expected, the *Narada* wireless sensor has a slightly elevated level of noise in the measured acceleration data due to the lower sensitivity and higher noise floor of the SD2012 accelerometer as compared to the PCB 393B12 accelerometer.

6.4.2 Truck Trajectory Estimation

The test vehicle is parked 500 m north of the Geumdang Bridge at the start of testing. After the wireless monitoring system initiates data collection using the mobile wireless sensors on the truck and the static wireless sensors on the bridge, the truck is commanded to accelerate to achieve a desired speed (*e.g.*, 30 km/hr) before entering the bridge. After crossing the bridge, the truck decelerates until it comes to a stop approximately 200 m past the south end of the bridge. At the end of the test, the wireless monitoring system collects the horizontal acceleration of the vehicle as shown in Fig. 6.8-a. Based on the measured horizontal acceleration time history, the acceleration of the truck is zero at the start due to it being at rest. The truck accelerates with positive horizontal acceleration at 2.1 sec until it achieves 30 km/hr before entering the bridge at

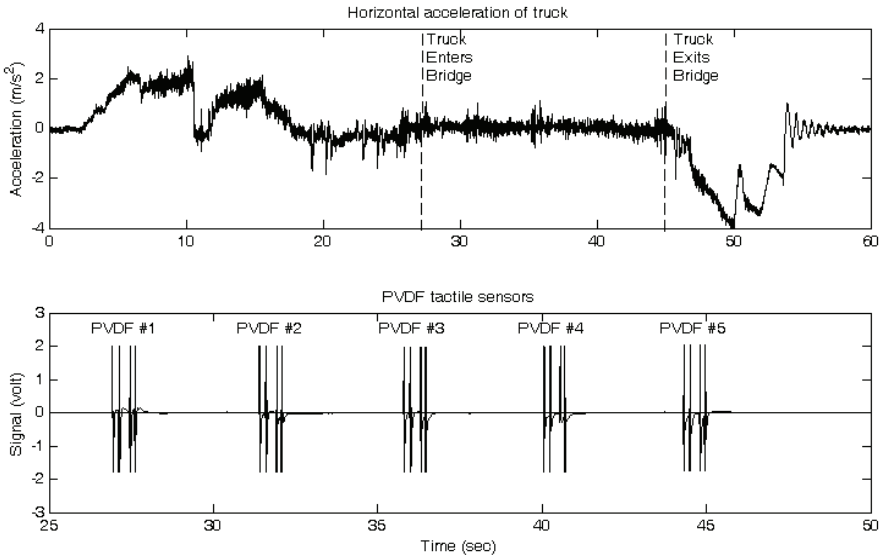

Figure 6.8 Trajectory sensing of the 4-axle truck crossing the Geumdang Bridge at 30 km/hr. Horizontal acceleration time-history of the truck (top) and its position information measured by the 5 PVDF tactile sensors (bottom) with all four truck axels evident from the PVDF tactile sensor response.

26.9 sec. During the time the truck is on the bridge (26.9 to 44.9 sec), the truck has a constant velocity and hence experiences zero horizontal acceleration. However, after exiting the bridge at 44.9 sec, the truck rapidly decelerates until it comes to a full stop at approximately 55 sec. In addition, the 5 PVDF tactile sensors on the bridge capture the time at which each axel of the truck rides over the sensor. Fig. 6.8-b superimposes the PVDF output voltage at all 5 PVDF tactile sensor locations. Each of the 4 truck axels are evident (*e.g.*, 4 major voltage spikes) in the response measured at each PVDF tactile sensor. To determine the truck velocity, the spacing between the truck axels and the time of their crossing each PVDF tactile sensor is used.

The measured horizontal acceleration of the truck and the truck position and velocity (as measured at each of the 5 PVDF tactile sensors) serve as inputs to the trajectory estimation algorithm previously derived. Based on the time the truck enters and exits the bridge (26.9 sec and 44.9 sec, respectively), the Kalman filter is applied to the data in both a forward and backward manner. The output of the forward and backward Kalman filters are presented in Fig. 6.9 and Fig. 6.10, respectively. In each figure, the estimated truck position, velocity and acceleration bias are plotted over the 18 seconds the truck is on the bridge. In each figure, 0 sec denotes the time when the first truck axel enters the bridge while 18 sec denotes when the last axel exits the bridge. For both the forward and backward Kalman filters, the position of the truck at the end of the analysis is 150 m away from the start which corresponds to the length of the

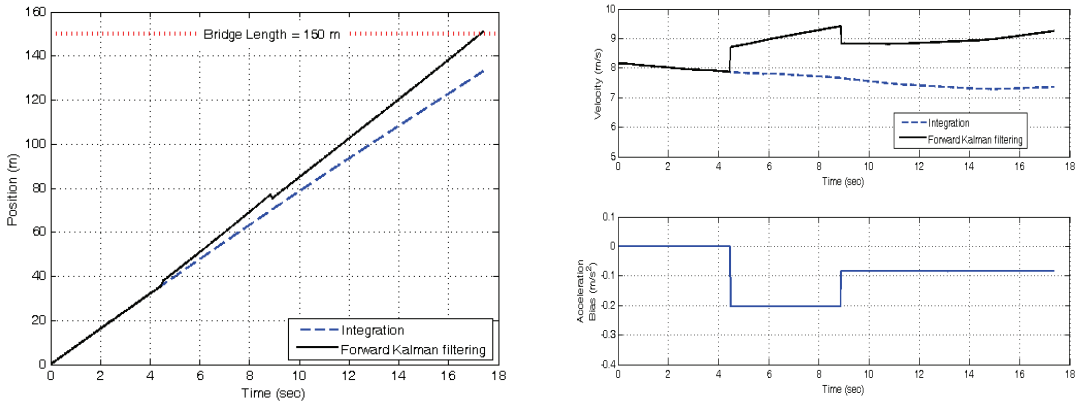

(a) (b)

Figure 6.9 Results from the forward Kalman filter: (a) estimated truck trajectory along the 150 meter bridge; (b) estimated velocity (top) and estimated accelerometer bias (bottom).

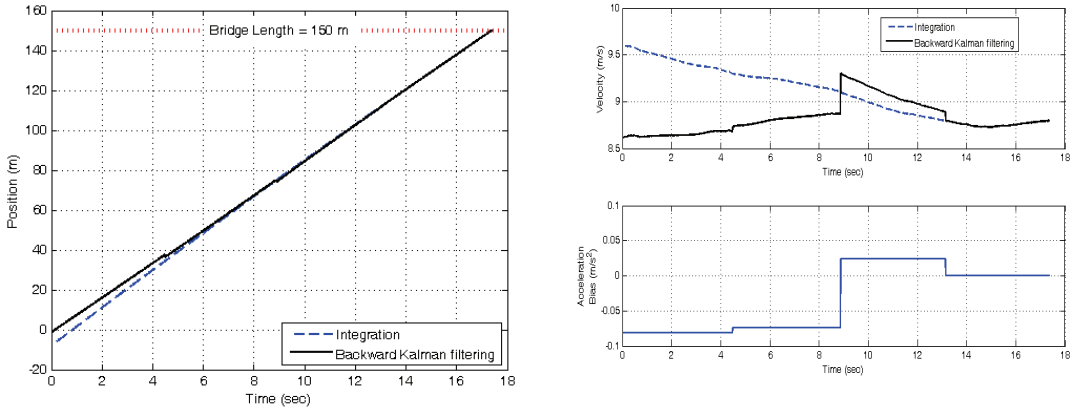

(a) (b)

Figure 6.10 Results from the backward Kalman filter: (a) estimated truck trajectory along the 150 meter bridge; (b) estimated velocity (top) and estimated accelerometer bias (bottom).

bridge (150 m). In comparison, the position based on pure forward integration of the horizontal acceleration results in a final position of 132.9 m at the end of the test; this inaccurate position estimate corresponds to an error of 11.4%. Similarly, backward Kalman filtering places the truck at -1.3 m which is an error of 0.9%. In contrast, backward numerical integration estimates the truck at -8.0 m which corresponds to a 5.3% error. Similar results are observed for the predicted truck velocity. One drawback of the forward and backward Kalman filtering approach is the step-wise discontinuity in the position and velocity trajectories at locations when the PVDF position

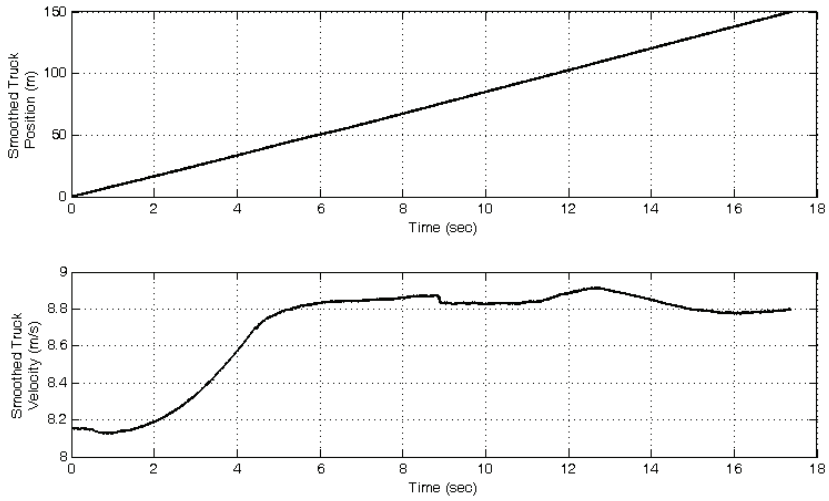

Figure 6.11 Final estimated truck position (top) and velocity (bottom) based on fixed-interval smoothing.

and velocity information is utilized. However, fixed-interval smoothing successfully averages the forward and backward Kalman filtered position and velocity data as shown in Fig. 6.11.

6.4.3 Time-Synchronized Vehicle-Bridge Response

During dynamic testing of the Geumdang Bridge, the wireless monitoring system proves reliable in its data collection functionality. When the truck is kept within 700 m of the wireless monitoring system base station, a data delivery rate of 100% is achieved. Outside of 700 m, communication between the system base station and the truck-based wireless sensor nodes experience some intermittent data losses. A total of 18 tests are conducted on the bridge with the truck driven at different velocities over the bridge (ranging from 30 to 65 km/hr). For example, the vertical acceleration response of the truck when driving at 30 km/hr is shown in Fig. 6.12. Based on the estimated truck trajectory (*i.e.*, Fig. 6.11), the point in time when each of the truck axels drives over the bridge expansion joints is superimposed on the truck response plots. The truck body and individual axels all experience significant vertical accelerations when driving over the expansion joints. However, the vertical acceleration response of the truck body and axels is damped out quickly by the truck suspension system. Aside from the large vertical accelerations experienced when driving over the expansions joints, smaller vertical accelerations are observed at each of the axels when the truck is driving over the spans. These accelerations are suspected to

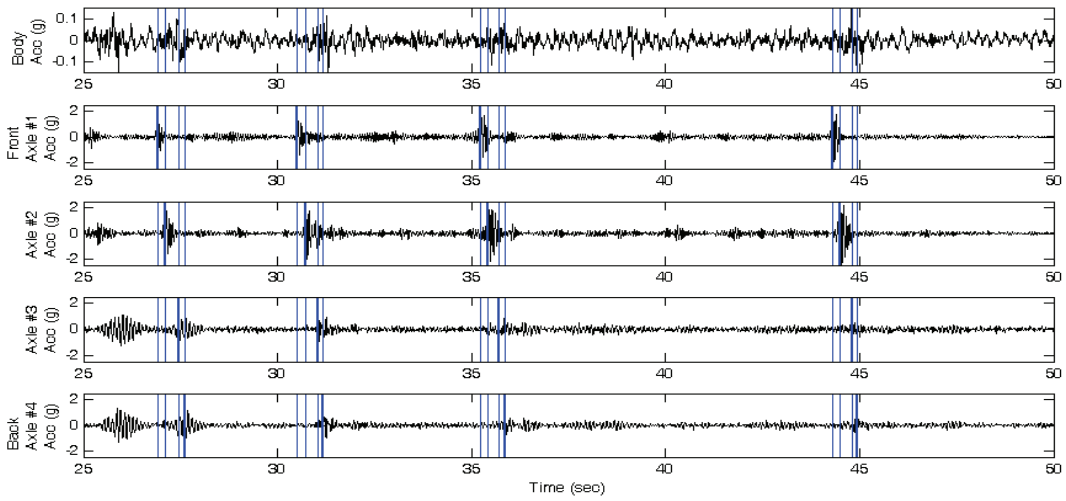

Figure 6.12 Measured truck vertical acceleration response when driven at 30 km/hr over the Geumdang Bridge. Vertical lines denote time when each axel crosses a bridge expansion joint. The thicker of the four vertical lines denotes the time of crossing of that specific instrumented axel.

result from the interaction of the vehicle with the road surface (*e.g.*, due to road roughness) and with the bridge itself.

For the same test (*i.e.*, truck crossing at 30 km/hr), the corresponding response of the bridge is presented in Fig. 6.13. The vertical acceleration response of the Geumdang Bridge is strongly influenced by the location of the truck relative to the individual spans of the bridge. In Fig. 6.13-a, the acceleration measured by sensors #1 through 5 (see Fig. 6.2), which are installed along the centerline of the first independent span, clearly show the global response of the span when the truck is on that particular span. This low-frequency response corresponds to the global dynamic response of the girders. It is likely some small amplitude, high-frequency localized response of the bridge deck (acting as a dynamic diaphragm), is also present in the acceleration response. In Fig. 6.13-b, the truck has crossed into the second independent span resulting in strong vertical accelerations in sensors #6 through 10. When the truck is on the second span, only minor small-amplitude vibrations are observed on the first and third spans. The third span of the Geumdang Bridge is a more complicated span with a pier situated at the mid-point of the continuous span; this results in a more complex bridge response. In Fig. 6.13-c, the truck is on the third span but to the north side of the center pier. This results in high amplitude accelerations with higher frequency content for sensors #11 through 15. However, Fig. 6.13-d reveals sensors #16 through 20 (which are on the south side of the center pier) also experience high amplitude accelerations but are characterized by lower frequency content. The opposite situation occurs when the truck

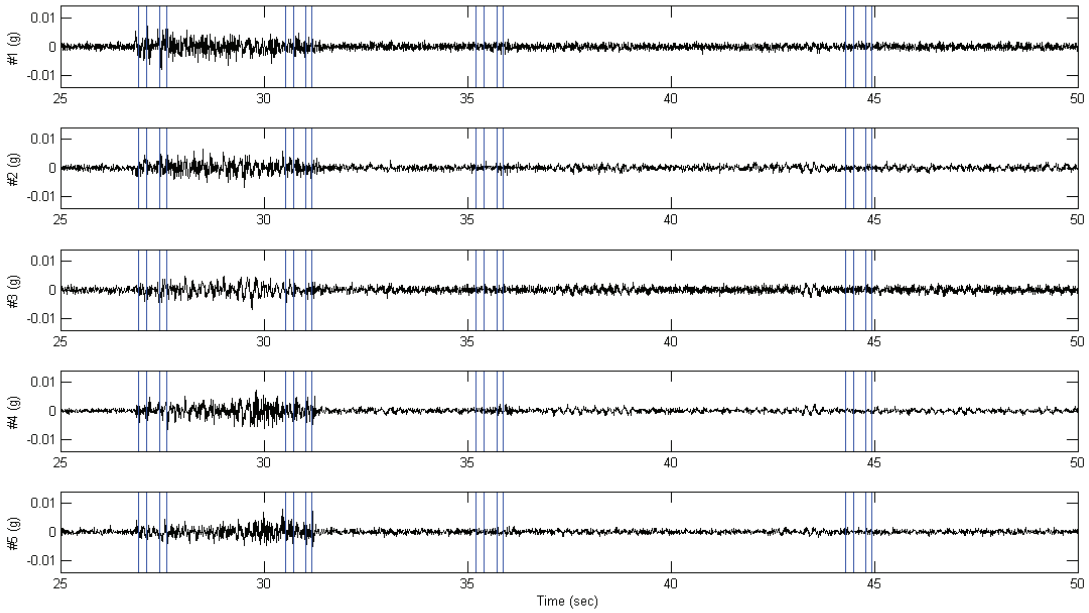
#1 (g)
#2 (g)
#3 (g)
#4 (g)
#5 (g)
0.01
0
-0.01
25
30
35
40
45
50
Time (sec)

(a)

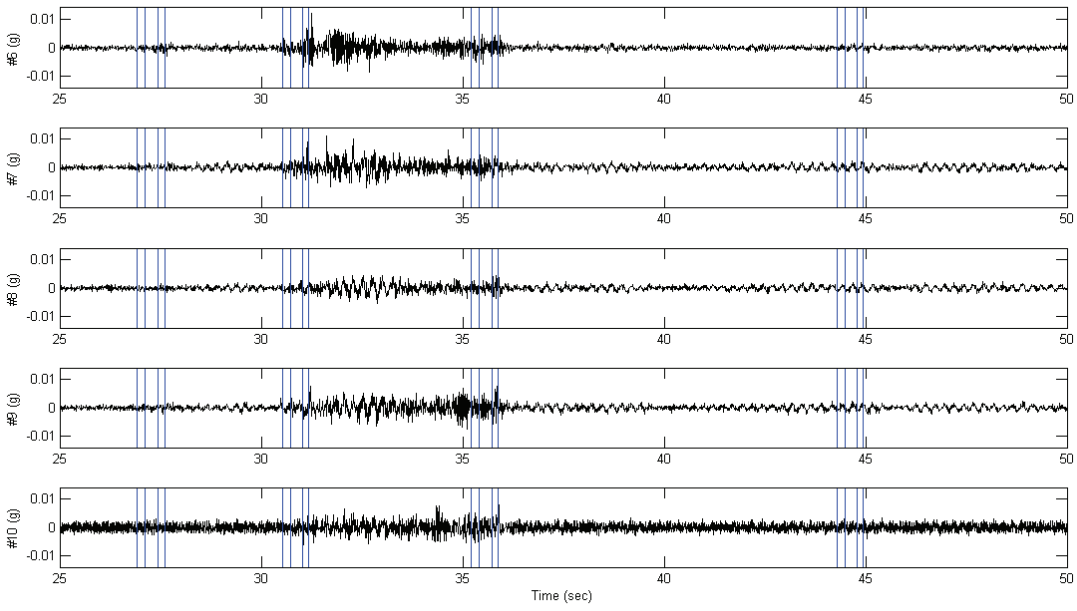
#6 (g)
#7 (g)
#8 (g)
#9 (g)
#10 (g)
0.01
0
-0.01
25
30
35
40
45
50
Time (sec)

(b)

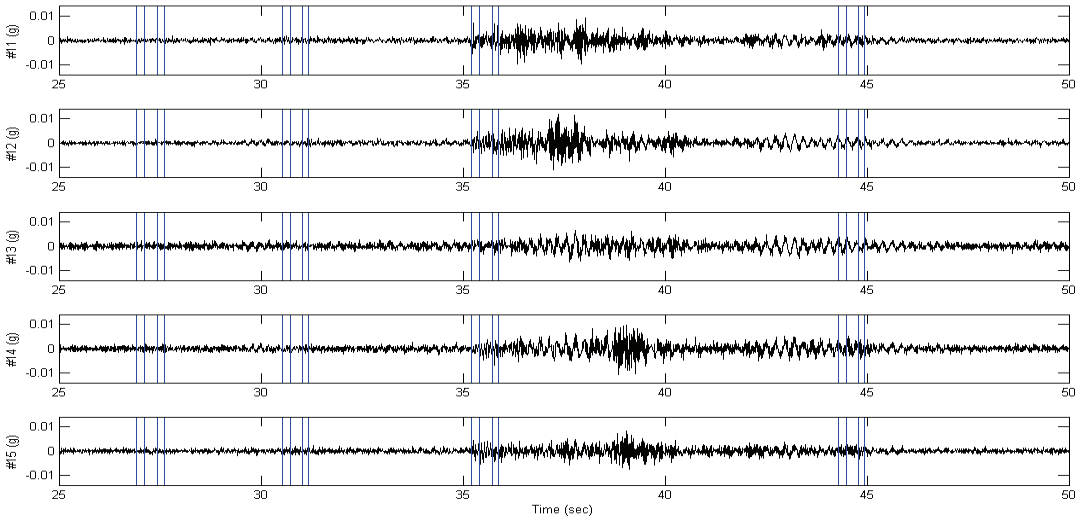

(c)

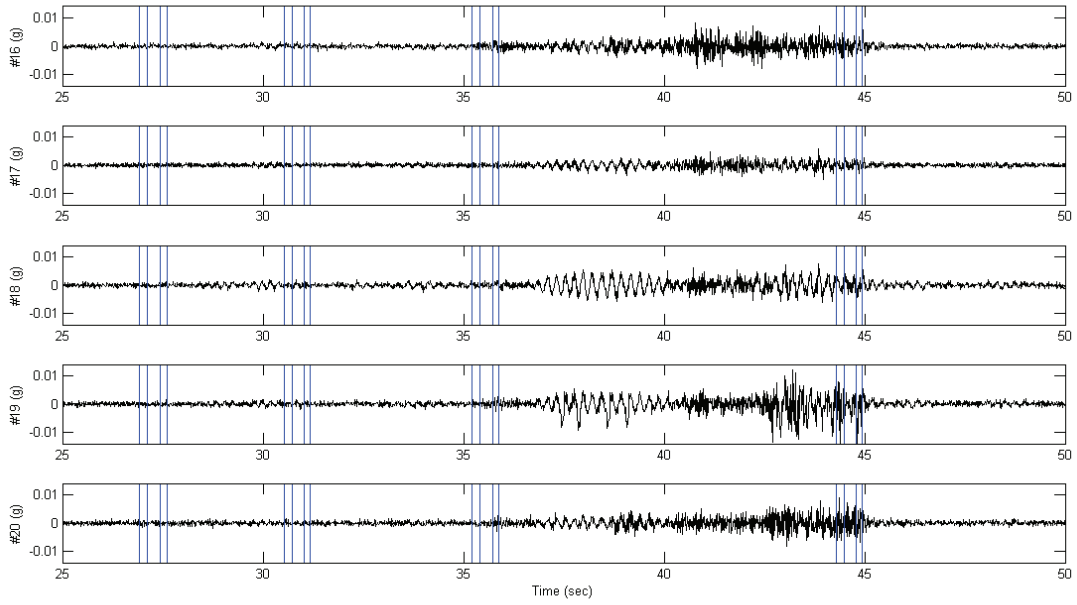

(d)

Figure 6.13 Measured vertical acceleration response of the Geumdang Bridge during the 30 km/hr truck run: (a) sensors #1 through #5 on Span 1 (30 m long); (b) sensors #6 through #10 on Span 2 (40 m long); (c) sensors #11 through #15 on the first part of Span 3 (40 m long); (d) sensors #16 through #20 on the second part of Span 3 (40 m long). Vertical lines denote time when each axel crosses a bridge expansion joint.

moves to the south-side of the central pier. This complex dynamic behavior is due to the dynamic coupling of the vehicle and bridge.

6.5 Chapter Summary and Conclusions

Vehicle-bridge interaction is successfully observed using a comprehensive wireless monitoring system capable of unifying data acquisition from mobile wireless sensors on a truck with permanent wireless sensors installed on a bridge. The wireless vehicle-bridge monitoring system is scalable, low-cost, and proven reliable during dynamic testing. In this study, the Geumdang Bridge in Icheon, Korea is selected for dynamic testing using a 20.9 ton truck. Installed along the 150 m northern span of the bridge is a wireless sensor network with 20 wireless vertical accelerometers and 5 wireless PVDF tactile sensors to measure the bridge response and the location of the truck. Similarly, the truck is instrumented with 5 wireless vertical accelerometers, 1 wireless horizontal accelerometer, and 1 wireless gyroscope. The 32 wireless sensor nodes are time synchronized by the wireless monitoring system base station installed on the bridge. The system proved reliable with 100% data delivery when the truck was within 700 m of the base station. Using the Kalman filter combined with fixed-interval smoothing, the trajectory of the truck is accurately identified using the horizontal truck acceleration and the PVDF tactile sensor outputs. Furthermore, the time-history data collected from the vehicle and bridge revealed the dynamic coupling that exists between the vehicle and the bridge. By exploring the time-synchronized vibration data of the position-identified vehicle and the bridge, the dominant sources of vehicle-bridge interaction are found experimentally. The main source of vehicle-bridge interaction is the road roughness (*e.g.*, the irregularity of the deck surface) and the sudden change in the pavement topology (*e.g.,* the existence of expansion joints). Two dominant bridge vibration responses are induced by the moving, vertically vibrating vehicle: low frequency global structure dynamic responses and high frequency member-level localized responses (*e.g.*, diaphragm vibrations). The experimental findings of this study will ultimately help researchers in the smart structure field by offering a scalable means of monitoring both structural demand and response in bridge structures.

CHAPTER 7

TWO-STAGE SYSTEM IDENTIFICATION FOR EXPERIMENTAL ANALYSIS OF VEHICLE-BRIDGE INTERACTION

Deterioration of bridges under repeated traffic loading has called attention to the need for improvements in the understanding of vehicle-bridge interaction. While analytical and numerical models have been previously explored to describe the interaction that exists between sprung mass and an elastic beam system, comparatively less research has been focused on the experimental study of vehicle-bridge interaction. As an extension of the experimental observation of vehicle-bridge interaction based on a wireless monitoring system (Chapter 6), a strategy for estimation of a data-driven model for an elastic beam system excited by a moving sprung mass vehicle is proposed in this chapter. Time-synchronized vehicle-bridge response data is used within a two-stage system identification methodology. In the first stage, the free-vibration response of the bridge is used to identify the dynamic characteristics of the bridge. In the second stage, the vehicle-bridge response data is used to identify the time varying load imposed on the bridge from the vehicle. Excellent agreement between measured bridge response and predicted response by an estimated vehicle-bridge interaction model validates the proposed strategy.

7.1 Introduction

Bridges represent a critical structural link within a nation's transportation system; in the case of the United States, there are 603,307 bridges currently in operation (USDOT 2009). Bridges support the economic activity of a nation by providing a convenient means of moving people and goods over bodies of water, mountain valleys, and other topological obstructions. The collapse of the I-35W Bridge in Minneapolis, MN (August 1, 2007) underscored the economic importance of bridges; the loss of the I-35W Bridge is estimated to have resulted in a total economic loss of

$200 million to the Minneapolis region (NIST 2008). In many developed nations, there is growing concern over the general health and well-being of growing inventories of aging bridges. For example, the United States is facing a serious baby-boomer bridge problem; the average age of the nation's bridges is 43 years old with most of these bridges designed for 50 year service lives (AASHTO 2008). Over time, daily traffic and extreme environmental factors naturally lead to structural deterioration. To better understand the behavior of bridges under traffic loads and to comprehend causal relationships in bridge deterioration processes, there has been renewed interest in the study of vehicle-bridge interaction as it pertains to structural health.

The dynamic behavior of bridge systems under the influence of a moving load (*i.e.*, vehicle) is one of the oldest problems in the civil engineering profession. The first reported study of the influence of a moving vehicle on a bridge dates back to 1849 when R. Willis reported on the behavior of a massless beam loaded by an unsprung moving mass (Timoshenko *et al.* 1974). In the Willis study and the many that followed (Timoshenko 1922; Jeffcott 1929), the inertia effect of the vehicle was ignored. To begin to account for the vehicle dynamics in the response of the bridge, a variety of solutions were proposed in the 1920's including models that analyze the vehicle as a moving harmonic force (Timoshenko 1922) and those that account for the vertical inertia effect of the vehicle mass (Jeffcott 1929). Hillerborg (Hillerborg 1951) is one of the earliest to offer a solution to the problem of a sprung mass moving across an elastic beam. Other notable contributions to the moving oscillator problem have been reported by Biggs *et al.* (Biggs *et al.* 1959), Fryba (Fryba 1972) and more recently by Pesterev and Bergman (Pesterev and Bergman 1997). With the emergence of computers in the 1960's, finite element method (FEM) models were used to study the dynamic interaction between vehicles and bridges (Yang *et al.* 2004b). The use of FEM models in the study of vehicle-bridge interaction is significant because FEM allows for countless variations in: 1) the type of vehicle (*e.g.*, multi-axle trucks, railroad trains), 2) vehicle suspension system, and 3) bridge type (*e.g.,* multi-girder bridge, truss bridge, cable-stayed bridge). The FEM approach entails the creation of two separate models that analyze the vehicle and bridge dynamics separately. Given the profile of road roughness, the vehicle and bridge displacements are solved in an iterative manner to satisfy both dynamic models at each time-step.

While great advances have been made in the analytical and numerical modeling of vehicle-bridge interaction, comparatively less research has been aimed towards experimental study. The measurement of vehicle and bridge dynamics in real, operational bridges is critical towards understanding how repeated vehicular loading leads to long-term structural deterioration of the bridge. However, due to the nature of the moving vehicle in contrast to stationary bridges, the use

of a wired monitoring system to measure vehicle and bridge dynamic interaction is infeasible. Alternatively, independent monitoring systems can be installed in the bridge and vehicle (Mizuno *et al.* 2008), but accurate time synchronization of the two monitoring systems can prove challenging. Addressing the technological challenge relating observation of vehicle-bridge interaction, the preliminary work in Chapter 6 has validated the feasibility of using wireless sensors to measure the position and vibratory behavior of a vehicle while driving on a bridge instrumented with a permanent wireless monitoring system. The proposed wireless monitoring system provides a rich input-output data set from which the dynamic coupling between a vehicle and bridge can be analyzed.

The vibratory response of the bridge subjected to a moving random force is effectively a non-stationary random process (Fryba 1976). In the context of system identification, vehicle-bridge interaction can be considered as a complex time-variant problem that prohibits direct application of the batch system identification algorithms, *i.e.*, subspace system identification techniques in Chapter 3, that require the system to be linear, time-invariant. Alternatively, classical parameterized model-based system identification algorithms such as the prediction-error method (Ljung 1999) can be utilized. However, such methods are challenging to apply to time-varying systems with poor convergence expected during recursive optimization in the time-domain.

In this study, a novel two-stage approach to system identification is proposed. In the first stage, the free-vibration response of the bridge is used to characterize the dynamic properties of a linear time invariant state-space model corresponding to the unloaded bridge. In the second stage, vehicle position and vibratory response time-histories are used to identify a linear, time-variant model that encapsulates the vehicle-bridge interaction. A key innovation of the second stage on the system identification process is the use of a kernel approximation of the bridge loading based on the vehicle position. The proposed two-stage system identification process is applied to the Yeondae Bridge (KEX test road, Korea) data set so that the accuracy of the system identification process can be quantified.

7.2 Experiments of Vehicle-Bridge Interaction

7.2.1 Yeondae Bridge, Korea

The Yeondae Bridge (Fig. 2.6 in Chapter 2) is selected for the experimental study on vehicle-bridge interaction. As introduced in Chapter 2, the Yeondae Bridge is a continuous steel box girder bridge that is 180 m long with a slight curve in plane at one end (1718 m radius of curvature). The cross-section of the bridge consists of two symmetric trapezoidal box girders that

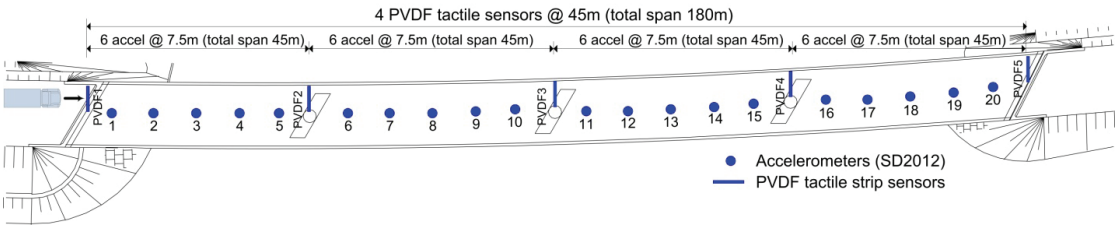

Figure 7.1 Installation strategy of *Narada* wireless sensor nodes on the Yeondae Bridge with 20 capacitive vertical accelerometers (Silicon Design SD2012) and 5 PVDF strip sensors interfaced.

are 2.2 m tall and with a width of 3.1 and 2.1 m at the top and bottom of the trapezoid section, respectively. The box girders are placed in composite action with the 27 cm thick reinforced concrete bridge deck. Along the length of the bridge are three reinforced concrete piers that support the continuous steel box girder using elastomeric pads. The two ends of the bridge are supported on reinforced concrete abutment structures with rubber expansion joints installed between the bridge deck and the abutment structures. The bridge has a 40° skew angle at the abutment supports.

7.2.2 Dynamic Load Testing

Similar dynamic load testing with that on the Geundang Bridge (Chapter 6) was conducted on the Yeondae Bridge. The Yeondae Bridge was instrumented with *Narada* wireless sensors interfaced with two types of sensor (*i.e.*, vertical accelerometers and PVDF tactile strips) (Fig. 7.1). The same truck used in Chapter 6 (Fig. 6.4) was used in this study and instrumented with accelerometers and a gyroscope (Fig. 6.5) in order to monitor the dynamics of the truck. Once the installation of the sensors on the truck and bridge was completed, the bridge was loaded by driving the truck across the bridge at four different target velocities (30, 50, 65, and 70 km/hr). The starting position of the truck was roughly 200 to 500 m from the north end of the bridge depending on the desired truck velocity when crossing the bridge. Once the wireless sensor network was synchronized, each wireless sensor collected the acceleration response of the bridge using a sample rate of 100 Hz. The truck was directed to accelerate until it achieved the desired velocities and successfully crossed the bridge (Fig. 7.2). The unified wireless monitoring system simultaneously collected: 1) the dynamics of the truck; 2) the truck passing time as measured by the PVDF tactile strips; and 3) the vibration of the bridge. In total, eleven separate tests were conducted on the bridge during forced-vibration testing: the truck was driven over the bridge at four different speeds (*i.e.*, 30, 50, 65, and 70 km/hr) three times each except for 70 km/hr which

Figure 7.2 Vehicle-bridge interaction testing with a 20.9-ton test truck on the Yeondae Bridge.

was conducted only twice. During all tests, the wireless monitoring system architecture proved to be an extremely reliable system that yielded a rich set of time-synchronized truck-bridge response time-histories.

7.2.3 Time- and Frequency-Domain Analysis

Fig. 7.3 depicts a representative set of acceleration time-histories for the bridge at the center of each free span (*i.e.*, accelerometers at sensor locations #3, 8, 13, and 18 in Fig. 7.1) when the 20.9 ton dump truck was driven at 65 km/hr. Superimposed on each of the acceleration time-histories are the times when the truck crosses each of the five PVDF tactile sensors; the four vertical lines at each PVDF tactile sensor denote when each of the four truck axel generated a sensor output. Before the truck entered the bridge, a trivial amount of vibration was measured; however, once the truck entered the bridge (*e.g.*, at 34 sec in Fig. 7.3) the bridge experienced significant vibration everywhere as is expected for a continuous span bridge. The truck exited the bridge at approximately 44 sec; once the truck was off the bridge, the measured response corresponded to the bridge free-vibration response. When the truck was positioned on the same free span as the sensors plotted in Fig. 7.3, the vertical acceleration of the bridge was characterized by higher frequency content in the measured response. This higher frequency content was attributed to the dynamic interaction between the truck wheels and the bridge due to the road roughness in the local vicinity of the sensor (*e.g.,* dynamic response of the concrete slab). In contrast, the high amplitude, low frequency response that is persistent in the bridge accelerations is associated with the global vibration response of the continuous box-girder. In Fig. 7.4, the measured dynamic responses of the truck are plotted. The truck time-history

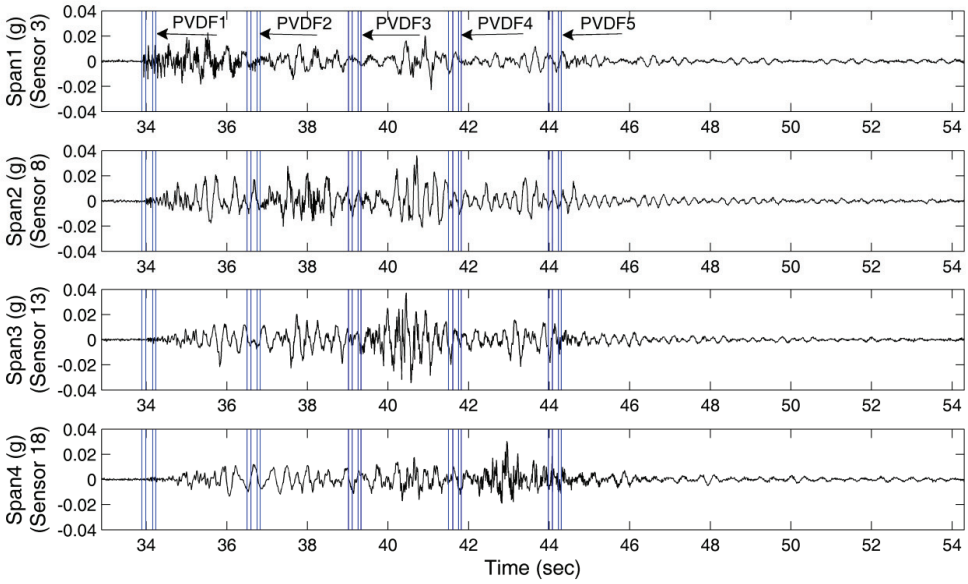

Figure 7.3 Bridge vertical acceleration measured at the center of each span of the Yeondae Bridge. Bridge excited with a heavy-duty dump travel crossing the bridge at 65km/hr. Vertical lines denote the time each truck axel crosses the PVDF tactile sensor.

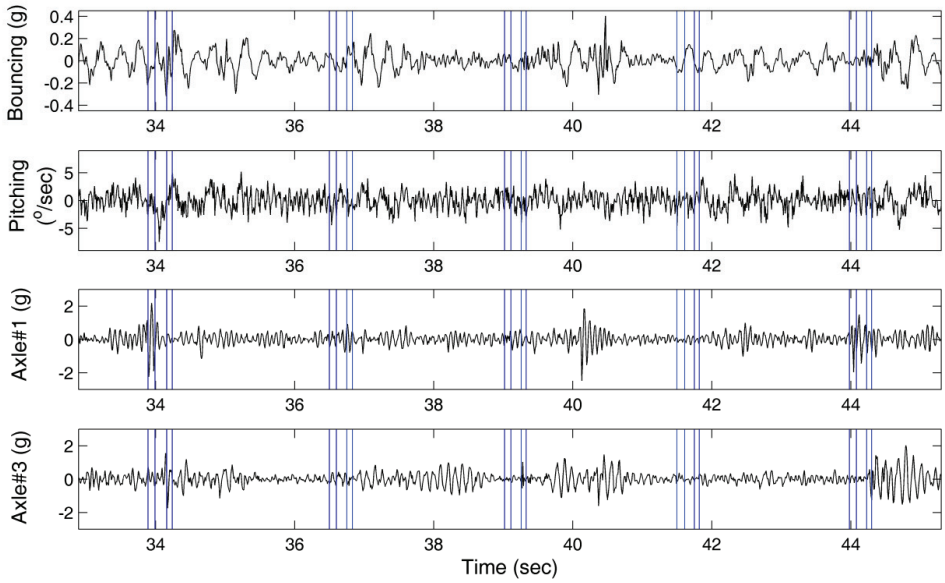

Figure 7.4 Measured truck response as truck crosses the Yeondae Bridge at 65km/hr; response is time synchronized with the bridge response data of Fig. 7.3. Vertical lines denote the time each truck axel crosses the PVDF tactile sensor.

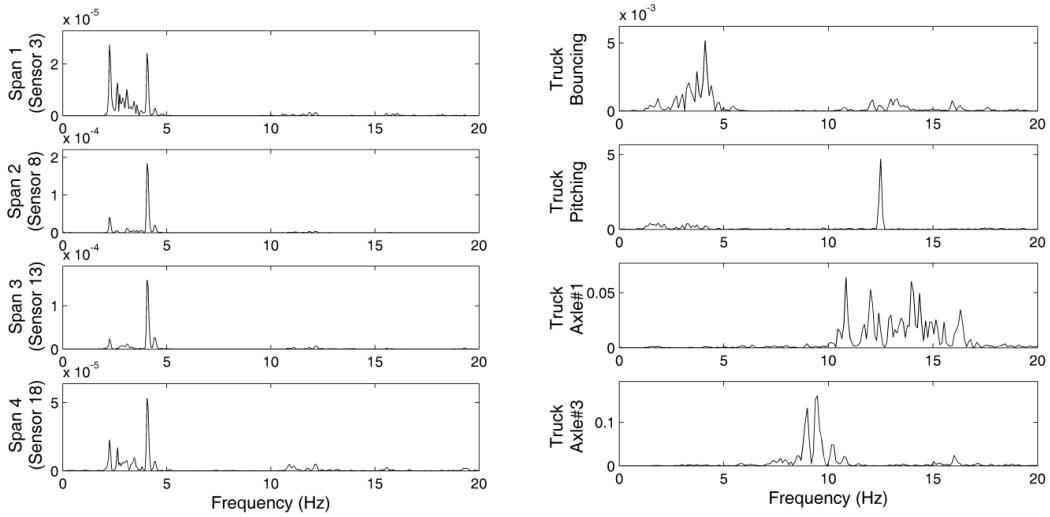

(a) (b)

Figure 7.5 Power spectral density (PSD) function of the measurement data: (a) PSD of span accelerations during the forced-vibration response of the bridge in Fig. 7.3; (b) PSD of the truck response during the forced-vibration response period in Fig. 7.4.

responses in Fig. 7.4 correspond to the same test plotted in Fig. 7.3. The truck axles underwent high frequency vibration when travelled the bridge expansion joints at both ends of the bridge (*i.e.*, at PVDF1 and PVDF5). The high frequency response observed in the axels was effectively filtered out by the truck suspension system when analyzing the truck vertical acceleration; however, the high frequency axel responses translated directly to the pitching motion of the truck body as seen in Fig. 7.4.

To confirm the observations made in the time-domain, the forced-vibration response of the bridge and truck (*i.e.*, the response shown from 34 to 44 sec in Fig. 7.3 and Fig. 7.4, respectively) were converted to the frequency-domain in the form of power spectral density (PSD) functions as shown in Fig. 7.5. The PSD functions of the mid-span accelerations plotted in Fig. 7.7-a revealed distinct peak frequencies at 2.25, 2.64, 3.08, 3.42, 4.05, and 4.44Hz. These peak frequencies were in strong agreement with modes (at 2.25, 2.64, 3.35, and 4.00 Hz) extracted during past modal analysis of the Yeondae Bridge in Chapter 2 as seen in Fig. 2.12. The dynamic response of the truck was more complex. The dynamic behavior of the truck axels were defined by high frequency content. For example, the first axel exhibited a dynamic response in the 10 to 16 Hz frequency band while the third axel response had response energy in the 8 to 12 Hz frequency band. While some of the high frequency axel was observed in the truck body vertical acceleration PSD, axel dynamics were greatly attenuated by the truck suspension system with the

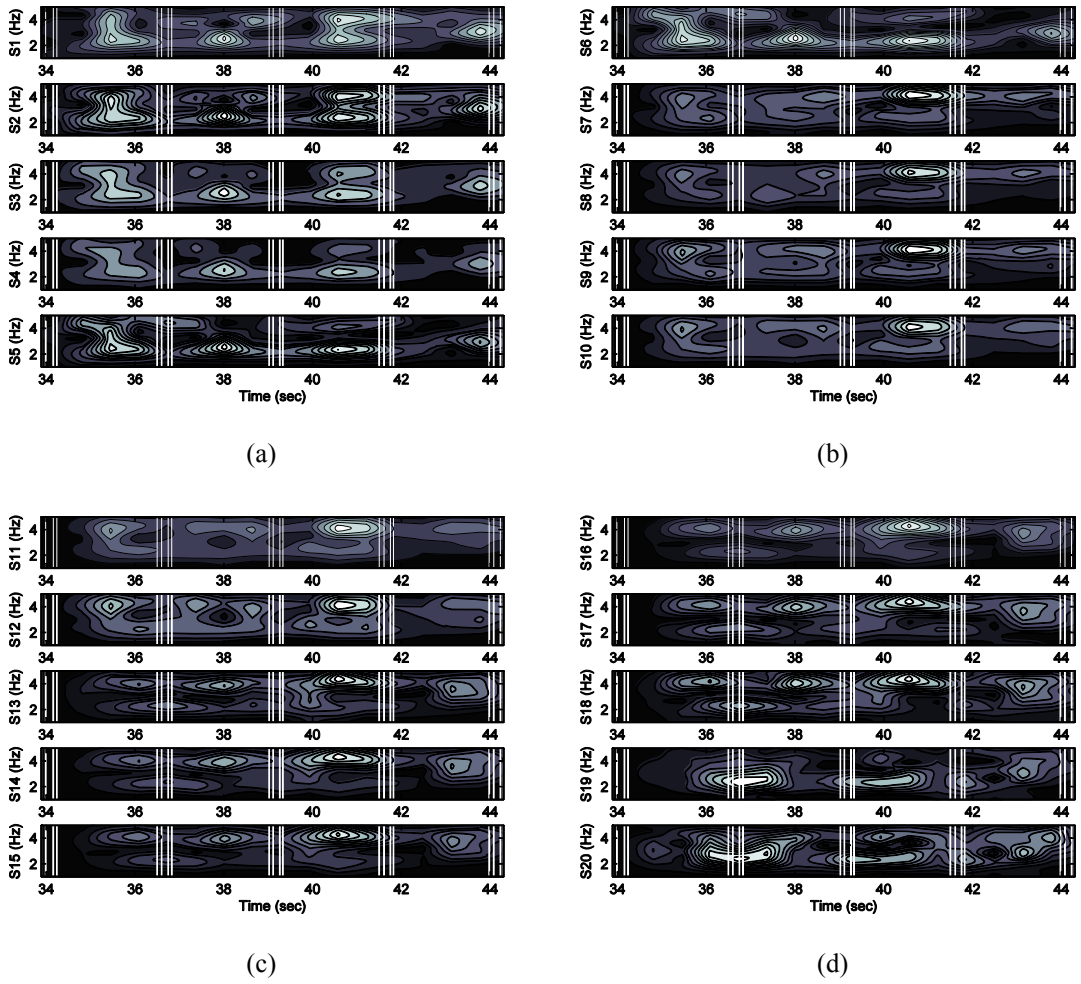

Figure 7.6 Spectrograms of the measured bridge accelerations of the Yeondae Bridge for the truck driven at 65 km/hr: (a) span 1; (b) span 2; (c) span 3; (d) span 4.

vertical bouncing of the truck body defined by lower frequency content centered at 4 Hz. The lower amplitude peaks found at frequencies less than 4 Hz in the truck vertical acceleration PSD were attributed to nonlinearities present in the suspension system (Gillespie *et al.* 1992). The pitching action of the truck body was defined by narrow band behavior centered at 12.5 Hz.

To illuminate the time dependency of the frequency-domain behavior of the bridge, time-frequency plots (spectrograms) of the bridge's vertical accelerations were calculated as presented in Fig. 7.6. The spectrograms are plotted for each of the twenty accelerometers on the bridge deck with each bridge span grouped separately. Depending on the moving truck location, the dominant modes of the bridge in the frequency-domain changed. Even though the fourth mode of the bridge at 4.00 Hz would normally have a lower participation factor in the overall system behavior, this mode contained significant energy as was evident by the high amplitudes in the

spectrograms; the fourth mode amplitude was often as large as the first mode amplitude at 2.25 Hz. Since the natural frequency of the truck sprung mass coincides with the fourth mode, it can be concluded that the bridge is undergoing forced-vibration by the bouncing motion of the moving truck body.

A number of preliminary conclusions can be drawn from analysis of the time- and frequency-domain data presented:

- While the axels of the truck at the bridge-truck interface are characterized by high frequency content, this frequency response is poorly matched to the low frequency global behavior of the bridge. As a result, the high frequency content does not effectively induce the global response of the large mass bridge. Rather, bridge components (*e.*g., bridge deck) defined by lower effective mass are more prone to excitation by the higher frequency content of the truck axels.
- The large mass of the truck body (*i.e.,* unsprung mass) coupled with its low frequency vibratory behavior represents a more influential source of global excitation for a bridge defined by primary modes within the same frequency regime. This conclusion is consistent with the literature where evidence of truck bouncing-induced excitation has been widely reported (Yang *et al.* 2004a; Lin and Yang 2005).
- The speed of the truck has a strong influence on the vehicle-bridge interaction (Lin and Yang 2005). At low speeds (20 km/hr or less), the truck acts like an unsprung mass exciting the bridge with the bridge first mode dominant in the vertical response of the truck body. However, as the speed of the vehicle increases, the sprung mass vibration of the vehicle drives more of the system dynamics with the sprung mass (*i.e.*, truck bouncing motion) dominant in both the truck vertical acceleration PSD function (as was the case in Fig. 7.5-b) and in the bridge responses (as was the case in Fig. 7.6).

7.2.4 Effect of the Truck on the Extraction of Bridge Modal Properties

Based on the bridge drawings, the weight of the Yeondae Bridge superstructure was calculated to be 2,800 tons. The additional weight added to the bridge by the 20.9 ton truck was only 0.75% of the bridge superstructure weight. Even though this additional mass is expected to be trivial, the effects of the additional mass on the bridge modal properties should be checked prior to system identification. To assess this potential influence, two separate modal analyses were conducted using forced and free-vibration response data of the bridge, respectively. Modal analysis of forced-vibration data would contain the influence of the vehicle (*i.e*., additional mass, and truck dynamics). In contrast, free-vibration response data would not be affected by the

Table 7.1 Comparison of estimated modal frequencies (unit: Hz).

Truck velocity		Free vibration				Forced vibration			
		mode 1	mode 2	mode 3	mode 4	mode 1	mode 2	mode 3	mode 4
30 km/hr	test 1	2.26	2.68	3.57	4.03	2.24	2.66	3.64	4.10
	test 2	2.26	2.67	3.56	4.01	2.24	2.68	3.34	4.11
	test 3	2.25	2.68	3.52	4.05	2.24	2.67	3.52	4.13
	mean	**2.26**	**2.68**	**3.55**	**4.03**	**2.24**	**2.67**	**3.50**	**4.11**
50 km/hr	test 4	2.26	2.67	3.71	4.06	2.22	2.62	3.39	3.93
	test 5	2.25	2.66	3.58	4.05	2.22	2.66	3.42	4.03
	test 6	2.25	2.67	3.60	4.05	2.20	2.60	3.52	4.03
	mean	**2.25**	**2.67**	**3.63**	**4.06**	**2.21**	**2.63**	**3.44**	**4.00**
65 km/hr	test 7	2.25	2.67	3.61	4.04	2.24	2.65	3.78	4.05
	test 8	2.25	2.66	3.58	4.12	2.23	2.68	3.52	4.06
	test 9	2.25	2.66	3.58	4.04	2.25	2.66	3.88	4.28
	mean	**2.25**	**2.66**	**3.59**	**4.07**	**2.24**	**2.66**	**3.73**	**4.13**
70 km/hr	test 10	2.25	2.66	3.56	4.07	2.23	2.65	3.31	3.73
	test 11	2.24	2.69	3.52	4.05	2.18	2.65	3.34	3.96
	mean	**2.25**	**2.67**	**3.54**	**4.06**	**2.21**	**2.65**	**3.32**	**3.85**

vehicle. To make a fair comparison, the same system identification technique was applied to the bridge forced- and free-vibration response data. In this study, the output-only stochastic subspace identification (SSI) system identification was applied to all 11 data sets during forced and free-vibration, resulting in 22 sets of estimated modal parameters for the Yeondae Bridge (as tabulated in Table 7.1).

The modal frequencies extracted from the free-vibration response data were consistent with the modal frequencies previously identified for the Yeondae Bridge in Chapter 2. This result was expected because the frequency content contained in the free-vibration response is independent of the truck. In contrast, there was notable variation in the modal frequencies identified from the forced-vibration data. While strong agreement existed for the first two modes of the bridge, the third and fourth modes extracted from the forced-vibration data differed significantly from those extracted from the bridge free-vibration response. In addition, notable variability existed in the identified forced-vibration modes for the differing truck speeds, especially in the third and fourth modes. These observations lead to the conclusion that:

- Discrepancies observed in the modal frequencies of modes 3 and 4 extracted from forced-vibrations imply different truck dynamics affecting the results of the output-only SSI method. Thus, output-only system identification with forced-vibration data is not appropriate.

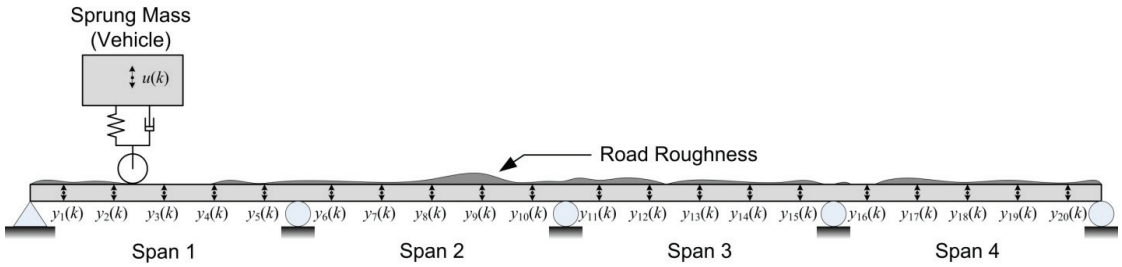

Figure 7.7 Simplified SIMO model of vehicle-bridge interaction: 20 degrees-of-freedom measured in the bridge system under a position-changing single degree-of-freedom (bouncing) vehicle.

- The similarities in the modal frequencies of mode 1 and mode 2 for both the free and forced-vibration imply that the additional truck mass is trivial and that the truck dynamics do not strongly influence these modes. Thus, the mass of the truck can be ignored during the system identification.

7.3 Two-Stage System Identification of Vehicle-Bridge Interaction

7.3.1 Mathematical Formulation of Vehicle-Bridge Interaction

A simplified physical model of vehicle-bridge interaction is presented in Fig. 7.7. A discrete-time linear time-variant state-space model for this single input, multiple output (SIMO) system can be written as

$$\mathbf{x}(k+1) = \mathbf{A}(k)\mathbf{x}(k) + \mathbf{B}(k)u(k) + \mathbf{w}(k) \tag{7.1}$$

$$\mathbf{y}(k) = \mathbf{C}(k)\mathbf{x}(k) + \mathbf{v}(k) \tag{7.2}$$

where, $u(k) \in \Re$ is the measured bouncing acceleration of the truck body at discrete time step k and is considered a deterministic input to the bridge system. Furthermore, $\mathbf{y}(k) \in \Re^l$ is the measured bridge vertical acceleration at time step k, $\mathbf{x}(k) \in \Re^n$ is an unknown n-dimension state vector of the system, $\mathbf{w}(k) \in \Re^n$ is process noise associated with the system state, and $\mathbf{v}(k) \in \Re^l$ is process noise associated with the system observation (*i.e.*, measurement). Process noise **v** and **w** are assumed to be uncorrelated, zero-mean stationary white noise sequences. Due to the moving nature of the bridge loading, the state-space model is written with time varying system, loading, and observation matrices (*i.e.*, $\mathbf{A}(k) \in \Re^{n \times n}, \mathbf{B}(k) \in \Re^n, \mathbf{C}(k) \in \Re^{l \times n}$, respectively). However, if it is assumed the bridge response amplitude is small (this is valid for vibration) and the mass of the vehicle is trivial, then **A** and **C** can be treated as time-invariant. However, the

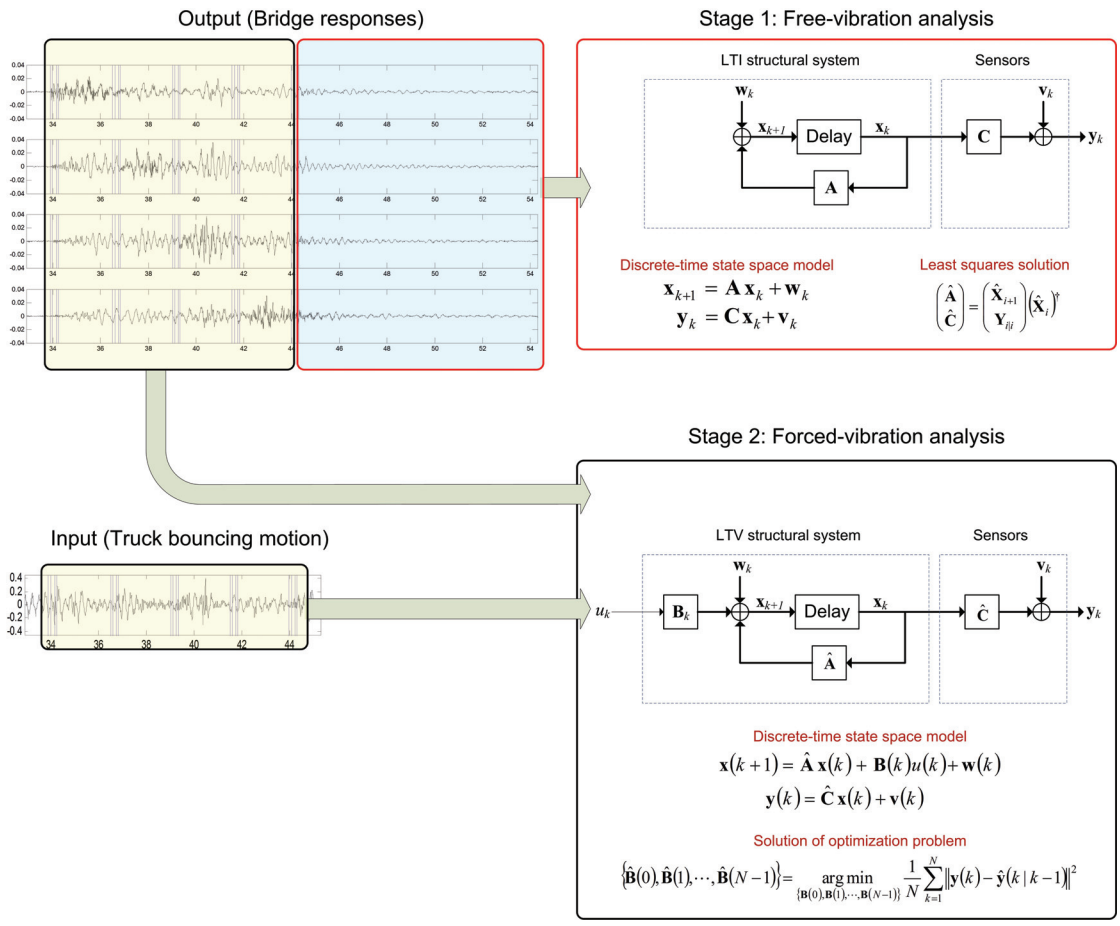

Figure 7.8 Two-stage system identification strategy that delineates the measured bridge response into free- and forced-vibration components in order to identify time-invariant and time-variant system components, respectively.

position-changing nature of the truck load mandates that the load distribution vector, **B**, remain time-variant:

$$\mathbf{x}(k+1) = \mathbf{A}\,\mathbf{x}(k) + \mathbf{B}(k)u(k) + \mathbf{w}(k) \tag{7.3}$$

$$\mathbf{y}(k) = \mathbf{C}\,\mathbf{x}(k) + \mathbf{v}(k) \tag{7.4}$$

Now, the system identification problem for vehicle-bridge interaction can be stated as the estimation of the state-space model system matrices {**A**, **B**(k), **C**} given the measured system input and output ($u(k)$ and $\mathbf{y}(k)$, respectively) over the time trajectory k =1 (the discrete time-step when the vehicle enters the bridge) to N (the discrete time-step when the vehicle exits the bridge).

To solve this complex system identification problem, a two-stage system identification approach is proposed as depicted in Fig. 7.8. First, the time-invariant system, **A**, and observation,

C, matrices are estimated using the free-vibration response of the bridge (*i.e.*, $\mathbf{y}(k)$ for $k > N$). Once the system and observation matrices are identified, the loading matrix, $\mathbf{B}(k)$ is estimated at each discrete time-step from $k = 1$ to N. This second-stage in the system identification process will utilize the system input, $u(k)$ and measured forced-vibration response, $\mathbf{y}(k)$ measured from the coupled vehicle-bridge system. Due to the nature of the acceleration measurement, the measured vehicle acceleration, $u(k)$, may be corrupted by the bridge vertical accelerations, $\mathbf{y}(k)$. Based on the level of acceleration measured on the truck body and that on the bridge, the level of contamination in the measured truck vertical acceleration from the bridge acceleration was considered trivial and was therefore ignored in the analysis. The trivial effect of the output contamination in input acceleration measurement was also proven in Chapter 5 (Section 5.4.2).

7.3.2 Stage 1: System Identification with Free-Vibration Data

After the vehicle departs the bridge ($k = N+1, N+2, \cdots$), the bridge undergoes free-vibration without a deterministic input. Hence, the behavior of the bridge can be modeled as a stochastic discrete-time state-space model as:

$$\mathbf{x}(k+1) = \mathbf{A}\,\mathbf{x}(k) + \mathbf{w}(k) \tag{7.5}$$

$$\mathbf{y}(k) = \mathbf{C}\,\mathbf{x}(k) + \mathbf{v}(k) \tag{7.6}$$

The system identification solution for Eqs (7.5) and (7.6) has been previously derived by Van Overschee and De Moore (Van Overschee and De Moor 1996) and named stochastic subspace identification (SSI) as an output-only numerical algorithm of subspace state-space system identification (N4SID). In Chapter 3, a detailed theory of the N4SID was explained focusing on combined deterministic and stochastic subspace identification (*i.e.*, system identification algorithm using input-output data). Thus, the output-only SSI algorithm is briefly explained herein. The output block Hankel matrix is constructed from the measured bridge free-vibration response and partitioned as past output and future output as follows

$$\mathbf{Y}_{0|2i-1} = \left[\begin{array}{cccc} \mathbf{y}_0 & \mathbf{y}_1 & \cdots & \mathbf{y}_{j-1} \\ \vdots & \vdots & \ddots & \vdots \\ \mathbf{y}_{i-1} & \mathbf{y}_i & \cdots & \mathbf{y}_{i+j-2} \\ \hline \mathbf{y}_i & \mathbf{y}_{i+1} & \cdots & \mathbf{y}_{i+j-1} \\ \vdots & \vdots & \ddots & \vdots \\ \mathbf{y}_{2i-1} & \mathbf{y}_{2i} & \cdots & \mathbf{y}_{2i+j-2} \end{array}\right] = \left[\begin{array}{c} \mathbf{Y}_{0|i-1} \\ \hline \mathbf{Y}_{i|2i-1} \end{array}\right] = \left[\begin{array}{c} \mathbf{Y}_p \\ \hline \mathbf{Y}_f \end{array}\right] \tag{7.7}$$

where **y.** is notation for **y**(•). Two orthogonal projections of the row space of the future output, $\mathbf{Y}_f$, on the row space of the past output, $\mathbf{Y}_p$, can be determined through LQ decomposition of the output block Hankel matrix:

$$\mathbf{P}_i := \mathbf{Y}_f / \mathbf{Y}_p ; \quad \mathbf{P}_{i-1} := \mathbf{Y}_f^- / \mathbf{Y}_p^- \tag{7.8}$$

where $\mathbf{Y}_f^-$ and $\mathbf{Y}_p^-$ are defined as a one block row down-shift in Eq. (7.7) as $\mathbf{Y}_{0|i}$ and $\mathbf{Y}_{i+1|2i-1}$, respectively. Since the projection is equal to the product of the extended observability matrix and the non-stationary the Kalman state sequence, singular value decomposition can be applied to factorize the projection $\mathbf{P}_i$:

$$\mathbf{P}_i = \mathbf{U}\mathbf{S}\mathbf{V}^T \cong \begin{bmatrix}\mathbf{U}_1 & \mathbf{U}_2\end{bmatrix}\begin{bmatrix}\mathbf{S}_1 & \mathbf{0} \\ \mathbf{0} & \mathbf{0}\end{bmatrix}\begin{bmatrix}\mathbf{V}_1^T \\ \mathbf{V}_2^T\end{bmatrix} = \mathbf{U}_1\mathbf{S}_1\mathbf{V}_1^T \tag{7.9}$$

Now, the extended observability matrix

$$\Theta_i = \mathbf{U}_1\mathbf{S}_1^{1/2} \tag{7.10}$$

and the non-stationary Kalman state sequence can be calculated respectively as:

$$\hat{\mathbf{X}}_i = \mathbf{S}_1^{1/2}\mathbf{V}_1^T \tag{7.11}$$

The one-step shifted state sequence is also calculated as

$$\hat{\mathbf{X}}_{i+1} = \left(\Theta_{i-1}\right)^{\dagger}\mathbf{P}_{i-1} \tag{7.12}$$

where Θ_{i-1} is equivalent to Θ_i with the last block row omitted; $\bullet^{\dagger}$ is the pseudo-inverse. Finally, estimates of **A** and **C** can be calculated by a least-squared solution:

$$\begin{bmatrix}\hat{\mathbf{A}} \\ \hat{\mathbf{C}}\end{bmatrix} = \begin{bmatrix}\hat{\mathbf{X}}_{i+1} \\ \mathbf{Y}_{i|i}\end{bmatrix}\hat{\mathbf{X}}_i^{\dagger} \tag{7.13}$$

It should be noted that the estimated system $\left\{\hat{\mathbf{A}},\hat{\mathbf{C}}\right\}$ is a specific realization of a system with an arbitrary state basis. Namely, the estimated system $\left\{\hat{\mathbf{A}},\hat{\mathbf{C}}\right\}$ in Eq. (7.13) is a black-box mathematical model. By using the similarity transformation (Eq. (4.17)), the estimated system $\left\{\hat{\mathbf{A}},\hat{\mathbf{C}}\right\}$ can be converted into discrete-time observability canonical form (Chapter 4).

7.3.3 Stage 2: System Identification with Forced-Vibration Data

In the second stage of system identification analysis, the bridge dynamics under the influence of the moving vehicle can be formulated using the system matrices estimated in Stage 1:

$$\mathbf{x}(k+1) = \hat{\mathbf{A}}\,\mathbf{x}(k) + \mathbf{B}(k)u(k) + \mathbf{w}(k) \tag{7.14}$$

$$\mathbf{y}(k) = \hat{\mathbf{C}}\,\mathbf{x}(k) + \mathbf{v}(k) \tag{7.15}$$

The objective of the second stage of the system identification problem is to estimate the time varying load matrix, $\mathbf{B}(k)$. This objective is accomplished by formulating the problem as an unconstrained optimization problem over an extended horizon where the difference in measured and predicted model output, $\mathbf{y}(k)$ and $\hat{\mathbf{y}}(k)$, respectively, is minimized as follows

$$\left\{\hat{\mathbf{B}}(0), \hat{\mathbf{B}}(1), \cdots, \hat{\mathbf{B}}(N-1)\right\} = \underset{\{\mathbf{B}(0),\mathbf{B}(1),\cdots,\mathbf{B}(N-1)\}}{\arg\min} \frac{1}{N}\sum_{k=1}^{N} \left\|\mathbf{y}(k) - \hat{\mathbf{y}}(k \mid k-1)\right\|^2 \tag{7.16}$$

where $\hat{\mathbf{y}}(k \mid k-1)$ is the one-step ahead prediction of the bridge acceleration calculated at discrete time-step k-1. This output prediction is formulated by the underlying system physics encapsulated in Eqs (7.14) and (7.15)

$$\hat{\mathbf{y}}(k \mid k-1) = \hat{\mathbf{C}}\,\hat{\mathbf{A}}^{k}\,\mathbf{x}(0) + \sum_{q=1}^{k} \hat{\mathbf{C}}\,\hat{\mathbf{A}}^{k-q}\,\mathbf{B}(k-1)u(q) \tag{7.17}$$

where $\mathbf{x}(0)$ is the initial state of the system. Since the bridge is initially at rest before the truck arrives, a zero initial state is assumed herein. Hence, Eq. (7.17) can be further simplified as:

$$\hat{\mathbf{y}}(k \mid k-1) = \sum_{q=1}^{k} u(q)\,\hat{\mathbf{C}}\,\hat{\mathbf{A}}^{k-q}\,\mathbf{B}(k-1) \tag{7.18}$$

The predicted system output formulated in Eq. (7.18) can be combined with the unconstrained optimization problem of Eq. (7.16):

$$\left\{\hat{\mathbf{B}}(0), \hat{\mathbf{B}}(1), \cdots, \hat{\mathbf{B}}(N-1)\right\} = \underset{\{\mathbf{B}(0),\mathbf{B}(1),\cdots,\mathbf{B}(N-1)\}}{\arg\min} \frac{1}{N}\sum_{k=1}^{N} \left\|\mathbf{y}(k) - \sum_{q=1}^{k} u(q)\,\hat{\mathbf{C}}\,\hat{\mathbf{A}}^{k-q}\,\mathbf{B}(k-1)\right\|^2 \tag{7.19}$$

In order to solve this unconstrained optimization problem by the least-squared method, a kernel approximation based on the identified vehicle position will be proposed.

7.3.4 Vehicle Position-Load Effect Kernel

Prior work in forced vibration testing of bridge structures focused on estimating an accurate position vector of the truck using Kalman filtering in Chapter 6. In this framework, the accelerometer installed in the truck to measure horizontal acceleration was fused with the output of the PVDF tactile sensors to estimate the truck trajectory. This methodology was used in this study to extract a precise truck position time history function for inclusion in the two-stage system identification analysis. Knowledge on the truck position during forced vibration testing can be leveraged to reduce the complexity of the unconstrained optimization problem posed in Eq. (7.19). Specifically, the position of the vehicle will be used to estimate a vehicle position-load effect kernel function, $\mathbf{\Phi}(k) \in \Re^n$, that will allow the load effect of the vehicle in the bridge system (Eq. (7.14)) to be estimated through a scalar time-varying function, $\alpha(k)$:

$$\mathbf{B}(k) := \alpha(k)\mathbf{\Phi}(k) \tag{7.20}$$

First, consider the conversion between the continuous and discrete time representation of the vehicle-bridge interaction model. A power series approximation for the conversion of the discrete-time system matrix, **A**, and load matrix, **B**, can be specified as

$$\mathbf{A} = e^{\mathbf{A}_c \Delta t} = \mathbf{I} + \mathbf{A}_c \Delta t + \frac{1}{2!}\mathbf{A}_c^2 \Delta t^2 + \frac{1}{3!}\mathbf{A}_c^3 \Delta t^3 + \cdots \tag{7.21}$$

$$\mathbf{B}(k) = \left(\int_0^{\Delta t} e^{\mathbf{A}_c \tau} d\tau \right) \mathbf{B}_c(t) = \left(\mathbf{I}\Delta t + \frac{1}{2!}\mathbf{A}_c \Delta t^2 + \frac{1}{3!}\mathbf{A}_c^2 \Delta t^3 + \cdots \right) \mathbf{B}_c(t) \tag{7.22}$$

where Δt is the time-step in discrete time, $\mathbf{A}_c$ is the continuous time system matrix, and $\mathbf{B}_c(t)$ is the continuous-time load matrix. By using Eq. (7.21) and the estimated $\hat{\mathbf{A}}$ in Stage 1, Eq. (7.22) can be written as

$$\mathbf{B}(k) = \hat{\mathbf{A}}_c^{-1}\left(\hat{\mathbf{A}} - \mathbf{I}\right)\mathbf{B}_c(t) = \left(\frac{1}{\Delta t} \ln \hat{\mathbf{A}} \right)^{-1} \left(\hat{\mathbf{A}} - \mathbf{I}\right)\mathbf{B}_c(t) = \mathbf{L}\mathbf{B}_c(t) \tag{7.23}$$

where $\mathbf{L} \in \Re^{n \times n}$. Hence, the vehicle position-load effect kernel function in the discrete time-domain, $\mathbf{\Phi}$, is related to the vehicle position-load effect kernel function in the continuous time-domain, $\mathbf{\Phi}_c$, through the same linear operator, **L**:

$$\mathbf{\Phi}(k) = \mathbf{L}\mathbf{\Phi}_c(t) \tag{7.24}$$

Using the known truck trajectory, the vehicle position-load effect kernel function in the continuous time domain, $\mathbf{\Phi}_c(t)$, takes on the value of 1 at the output node closest to the truck position at that time, t, and zero everywhere else.

The representation of $\mathbf{B}$ in Eq. (7.20) can be included in Eq. (7.18) to yield:

$$\hat{\mathbf{y}}(k \mid k-1) = \sum_{q=1}^{k} u(q)\,\hat{\mathbf{C}}\,\hat{\mathbf{A}}^{k-q}\,\mathbf{\Phi}(k-1)\alpha(k-1) \tag{7.25}$$

The output predictor of Eq. (7.25) can be written at each time-step increment in the following manner:

$$\begin{Bmatrix} \hat{\mathbf{y}}(1 \mid 0) \\ \hat{\mathbf{y}}(2 \mid 1) \\ \vdots \\ \hat{\mathbf{y}}(k \mid k-1) \\ \vdots \\ \hat{\mathbf{y}}(N \mid N-1) \end{Bmatrix} = \begin{bmatrix} u(1)\hat{\mathbf{C}}\hat{\mathbf{A}}^{0}\mathbf{\Phi}(0) & \mathbf{0} & \mathbf{0} & \cdots & \mathbf{0} \\ u(1)\hat{\mathbf{C}}\hat{\mathbf{A}}^{1}\mathbf{\Phi}(0) & u(2)\hat{\mathbf{C}}\hat{\mathbf{A}}^{0}\mathbf{\Phi}(1) & \mathbf{0} & \cdots & \mathbf{0} \\ \vdots & \vdots & \vdots & \ddots & \vdots \\ u(1)\hat{\mathbf{C}}\hat{\mathbf{A}}^{k-1}\mathbf{\Phi}(0) & u(2)\hat{\mathbf{C}}\hat{\mathbf{A}}^{k-2}\mathbf{\Phi}(1) & u(3)\hat{\mathbf{C}}\hat{\mathbf{A}}^{k-3}\mathbf{\Phi}(2) & \cdots & \mathbf{0} \\ \vdots & \vdots & \vdots & \ddots & \vdots \\ u(1)\hat{\mathbf{C}}\hat{\mathbf{A}}^{N-1}\mathbf{\Phi}(0) & u(2)\hat{\mathbf{C}}\hat{\mathbf{A}}^{N-2}\mathbf{\Phi}(1) & u(3)\hat{\mathbf{C}}\hat{\mathbf{A}}^{N-3}\mathbf{\Phi}(2) & \cdots & u(N)\hat{\mathbf{C}}\hat{\mathbf{A}}^{0}\mathbf{\Phi}(N-1) \end{bmatrix} \begin{Bmatrix} \alpha(0) \\ \alpha(1) \\ \vdots \\ \alpha(k-1) \\ \vdots \\ \alpha(N-1) \end{Bmatrix} \tag{7.26}$$

Eq. (7.26) can be symbolized as:

$$\hat{\mathbf{Y}} = \mathbf{\Psi}\,\boldsymbol{\alpha} \tag{7.27}$$

where $\hat{\mathbf{Y}} \in \Re^{lN}$, $\mathbf{\Psi} \in \Re^{lN \times N}$, and $\boldsymbol{\alpha} \in \Re^{N}$. The optimization problem of Eq. (7.19) can be written with the argument $\boldsymbol{\alpha}$ and simplified as:

$$\begin{aligned} \{\hat{\alpha}(0), \hat{\alpha}(1), \cdots, \hat{\alpha}(N-1)\} &= \underset{\{\alpha(0),\alpha(1),\cdots,\alpha(N-1)\}}{\arg\min} \frac{1}{N} \sum_{k=1}^{N} \left\| \mathbf{y}(k) - \sum_{q=1}^{k} u(q)\,\hat{\mathbf{C}}\,\hat{\mathbf{A}}^{k-q}\,\mathbf{\Phi}(q)\alpha(k-1) \right\|^2 \\ &= \underset{\{\alpha(0),\alpha(1),\cdots,\alpha(N-1)\}}{\arg\min} \frac{1}{N} \left\| \sum_{k=1}^{N} \mathbf{y}(k) - \sum_{k=1}^{N} \sum_{q=1}^{k} u(q)\,\hat{\mathbf{C}}\,\hat{\mathbf{A}}^{k-q}\,\mathbf{\Phi}(q)\alpha(k-1) \right\|^2 \\ &= \underset{\{\alpha(0),\alpha(1),\cdots,\alpha(N-1)\}}{\arg\min} \frac{1}{N} \left\| \mathbf{Y} - \mathbf{\Psi}\,\boldsymbol{\alpha} \right\|^2 \end{aligned} \tag{7.28}$$

where $\mathbf{Y} = \begin{bmatrix} \mathbf{y}(1)^T & \mathbf{y}(2)^T & \cdots & \mathbf{y}(N)^T \end{bmatrix}^T$ is a stack of measured output vector. The least square solution of Eq. (7.28) is calculated as:

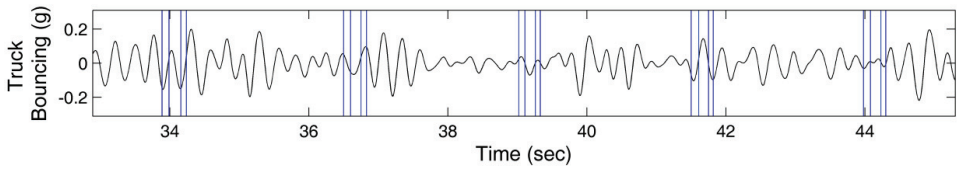

Figure 7.9 Low-pass 10 Hz filtered bouncing acceleration of the truck during the 65 km/hr test.

$$\hat{\boldsymbol{\alpha}} = \boldsymbol{\Psi}^{\dagger}\ \mathbf{Y} \tag{7.29}$$

Thus, estimates of $\mathbf{B}(k)$ are calculated from estimates of $\alpha(k)$ as:

$$\left\{\hat{\mathbf{B}}(0), \hat{\mathbf{B}}(1), \cdots, \hat{\mathbf{B}}(N-1)\right\} = \left\{\hat{\alpha}(0)\boldsymbol{\Phi}(0), \hat{\alpha}(1)\boldsymbol{\Phi}(1), \cdots, \hat{\alpha}(N-1)\boldsymbol{\Phi}(N-1)\right\} \tag{7.30}$$

7.3.5 System Identification of Vehicle-Bridge Interaction

Using the aforementioned two-stage system identification methodology, identification of the vehicle-bridge interaction on the Yeondae Bridge was conducted using the experimentally measured data sets collected for each of the 11 tests. Before execution of the two-stage system identification process, data polishing of the measured truck vertical acceleration response, *u*, (as advocated by Ljung (Ljung 1999)) was conducted using a low-pass filter with a 10 Hz cut-off frequency. The filtered vertical bouncing acceleration of the truck body during the 65 km/hr tests is presented in Fig. 7.9. In addition, the position of the truck using the Kalman estimation framework proposed in Chapter 6 was used. Using the filtered truck bouncing response, $u(k)$ and the vehicle position-load effect kernel function, $\boldsymbol{\Phi}(k)$, derived from the truck position, the two-stage system identification procedure was carried out. The system output predicted for the forced- and free-vibration response of the Yeondae Bridge is plotted in Fig. 7.10. The predicted response (thick line) is superimposed over the measured bridge output (thin line) for all 20 sensor locations.

Excellent agreement was found in the system identification results. The results validate that the proposed two-stage system identification strategy under a non-stationary input was a suitable model when considering the bridge response to the bouncing motion of a sprung mass truck model. While the model does an excellent job in predicting the bridge response, some notable discrepancies were encountered in the time history plots of Fig. 7.10. For example, when the

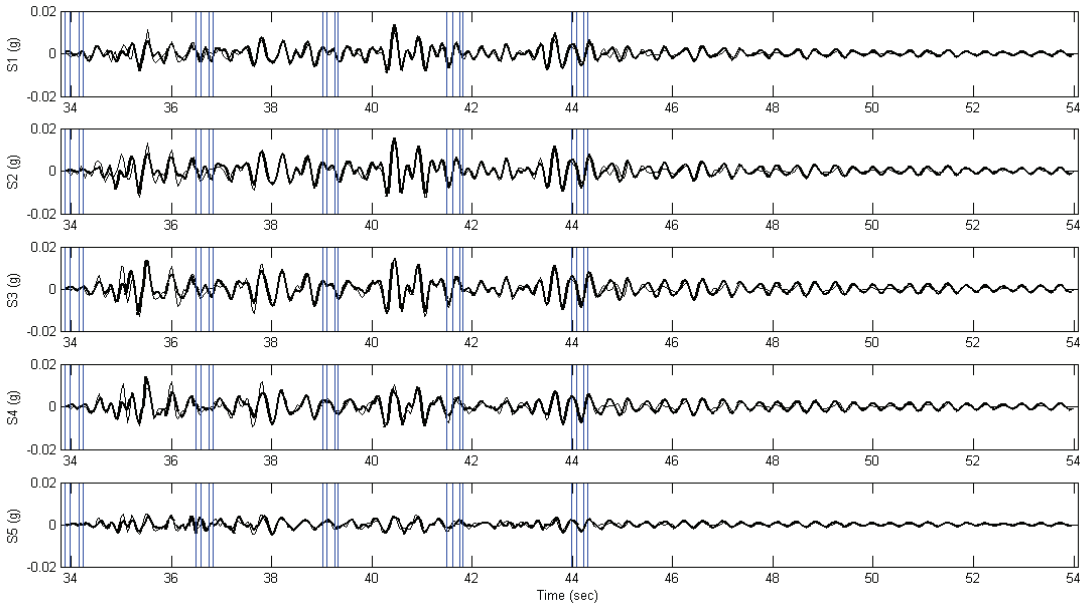
S1 (g)
S2 (g)
S3 (g)
S4 (g)
S5 (g)
0.02
0
-0.02
34
36
38
40
42
44
46
48
50
52
54
Time (sec)

(a)

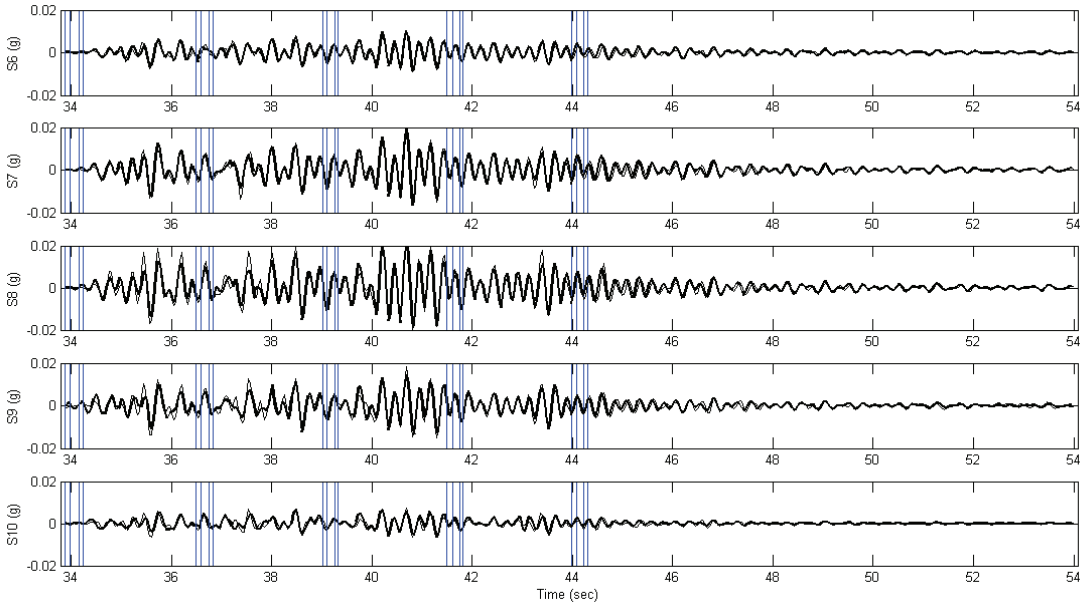
S6 (g)
S7 (g)
S8 (g)
S9 (g)
S10 (g)
0.02
0
-0.02
34
36
38
40
42
44
46
48
50
52
54
Time (sec)

(b)

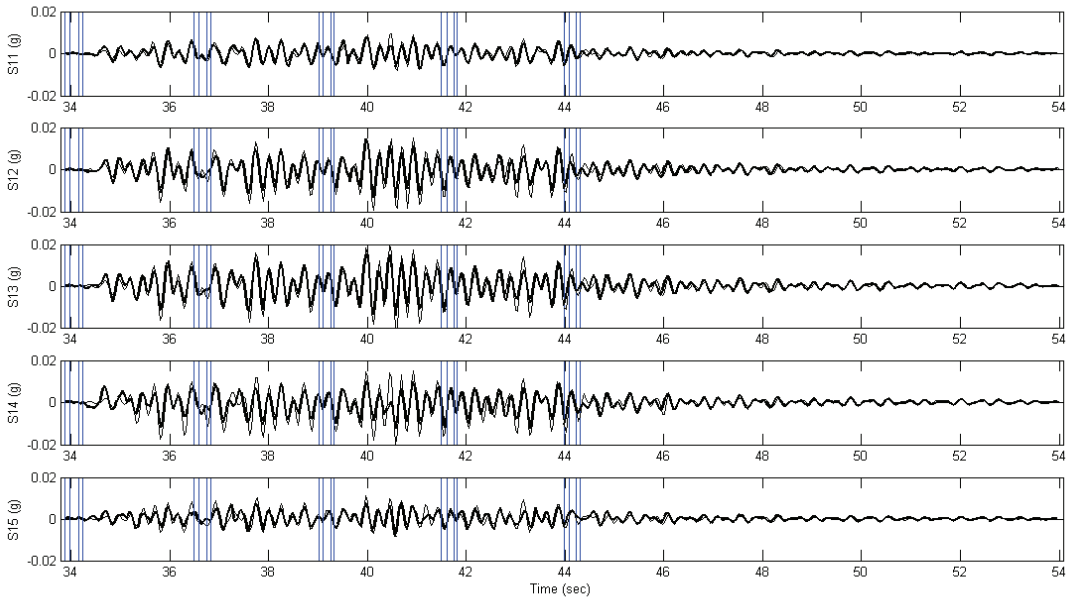

(c)

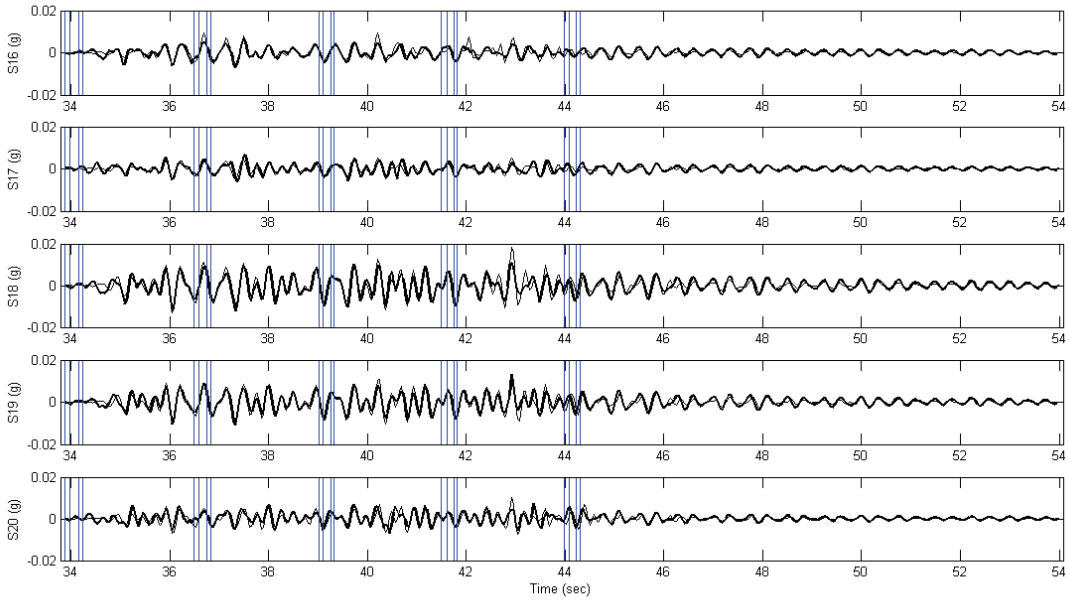

(d)

Figure 7.10 Two-stage system identification of the Yeondae Bridge during the 65 km/hr truck test with the thick line denoting the predicted system output and the thin line the measured response: (a) span 1; (b) span 2; (c) span 3; (d) span 4.

truck and sensors were on the same span, the differences between the measured and predicted system response were notable (*i.e.*, between 34 and 36.5 sec in Fig. 7.10-a; between 36.5 to 39 sec in Fig. 7.10-b; between 39 to 41.5 sec in Fig. 7.10-c; between 41.5 and 44 sec in Fig. 7.10-d). This discrepancy may be attributed to some local nonlinearities in the bridge system when the truck is over a given span.

7.4 Chapter Summary and Conclusions

In this chapter, an effective strategy for the system identification of vehicle-bridge interaction was proposed. A data-driven mathematical model was derived from the experimental data collected from a heavy truck and highway bridge using wireless sensors contained within the same wireless monitoring system architecture. Based on the preliminary data analysis of the measured bridge and truck response in the time- and frequency-domains, the reaction force of the bouncing truck body was revealed to be the primary exciter of the bridge. The bouncing motion of the truck sprung mass worked as a fundamental input to an input-output system model formulated for the modeling of vehicle-bridge interaction. To identify the key parameters of a state-space input-output model, a two-step identification strategy was explored in detail. In the first stage, the time-invariant properties of the bridge are estimated using the free vibration response of the bridge. In the second stage, the vehicle bouncing motion and the truck position history were combined with the bridge forced vibration response to estimate the time variant load matrix of the system model. Excellent system identification results were obtained with the model predicting closely the measured system response.

CHAPTER 8

CONCLUSIONS

Based on the previous development of the *Narada* wireless sensor node and its use in structural health monitoring and control application (Swartz 2009; Zimmerman 2010), the present study has intensively extended the application of wireless sensing technology to a broad range of problems pertaining to system identification of operational civil engineering structures (*e.g.*, highway bridges, building structures, cantilevered balconies, *etc.*). The thesis combined a number of interdependent research threads that all aimed to demonstrate the concept of model-based framework for structural health monitoring (SHM).

8.1 Summary of Achieved Research Objectives

Four major research objectives were defined for this study in Chapter 1: 1) field validation of extended-range wireless sensors; 2) physical interpretation on identified system models; 3) decentralized system identification for in-network execution; and 4) monitoring and identification of vehicle-bridge interaction. These objectives were successfully achieved as presented in this thesis and summarized as follows:

- The extended-range *Narada* wireless sensors were validated; field studies revealed their excellent performance (*i.e.*, high resolution digitization, time synchronization, and robust long-range communication) during dynamic testing of highway bridges as demonstrated in Chapter 2.

- A theoretical framework for the estimation of the physical parameters of a structure (*i.e.*, mass, stiffness, and damping) using measured experimental data (*i.e.*, input-output or output-only data) was proposed in Chapter 4. This framework allows the extracted physical parameters to be used within a large SHM system.

● A decentralized approach to system identification (*i.e.*, Markov parameter identification followed by realization-based subspace system identification) was proposed for embedment within a wireless structural monitoring system during vibration testing on a cantilevered balcony structure in Chapter 5.

● A strategy of a single wireless monitoring system architecture was proposed for vehicle-bridge interaction monitoring in Chapter 6. A key innovation was the use of vehicle-based mobile sensors time-synchronized with a wireless bridge monitoring system. In addition, an analytical strategy for the estimation of a data-driven model for an elastic beam system (*i.e.*, a bridge) excited by a moving sprung mass vehicle was proposed in Chapter 7.

8.2 Summary of Key Contributions

Numerous significant contributions were made to the structural dynamics and SHM research communities ranging from wireless sensing technology to data processing algorithms. The key intellectual contributions are summarized:

● *Chapter 2*: By testing the extended-radio *Narada* wireless sensor in the field, its performance in large-scale civil structures was confirmed. Furthermore, the proposed reconfigurable wireless sensor installation proved to be a very effective strategy for the achievement of a dense sensor network for frequency-domain system identification. A key contribution of the chapter was the estimated modal parameters of medium-span bridge extracted from truck-induced bridge vibrations. This modal analysis later served as a solid basis for the study of vehicle-bridge interaction.

● *Chapter 3*: Since the subspace identification method was developed by the control theory community as a pure mathematical algorithm, it has historically been accepted by the structural engineering community without direct relation to the underlying physics of the structural system (*i.e.*, conventional structural dynamics). The chapter provided an explanation of the direct subspace identification method in a user-friendly manner for structural engineers. Furthermore, the chapter also proposed a methodology for the evaluation of output-only system identification (one of the most popular approaches in the structural engineering field due to the difficulties in measuring ambient loads) for support-excited structures.

● *Chapter 4*: One of the most significant contributions of this thesis was introduced. A framework for the physical interpretation of a data-driven model was proposed and termed as "grey-box model". This can be interpreted as a major achievement, because it allows the highly accurate subspace system identification methods to be used more readily within a SHM system. For the problem of support-excited structures, the mathematical formulation of structural parameters in the form of finite elements discretization was proposed for baselining a structures and for later assessing if structural damage is present.

● *Chapter 5*: Leveraging the computational functionality of the *Narada* wireless sensor, a novel strategy of in-network data processing for realization-based subspace identification and decentralized Markov parameter estimation was proposed. The decentralized data processing architecture presented for data-driven model identification resulted in a dramatic increase in the power-efficiency and system scalability of the wireless sensor network. To the author's knowledge, this is the first implementation of in-network subspace system identification using input-output data for structural health monitoring.

● *Chapter 6*: To cope with the challenges of monitoring the dynamics of a mobile vehicle on a bridge, the strategy of a single wireless sensing network architecture was proposed. The architecture unified vehicle-based mobile sensors with a wireless bridge monitoring system. The novel wireless monitoring system was intensively verified with a series of field tests. Numerous noteworthy experimental findings on vehicle-bridge interaction were presented in this chapter and served as the basis for the development of an analytical vehicle-bridge interaction model presented in Chapter 7.

● *Chapter 7*: As the grand finale of the thesis, the chapter proposed a methodology to estimate a data-driven model for a bridge under a moving vehicle. This chapter will likely serve as a cornerstone for future SHM of bridge structures, because it provides a direct but cost-effective means of measuring the loading on the bridge from a moving vehicle. Based on the previous examples of identification for structures in stationary random processes (*i.e.*, support-excited structure), the study extended subspace system identification to problems of structures exposed to nonstationary random process (*i.e.*, a bridge under a moving vehicle).

8.3 Future Directions

As previously mentioned, the subspace system identification method in Chapter 3 is a universal method for black-box model identification that is applicable to any linear time-invariant dynamic system. However, if the fundamental physics of the system are available, physical interpretation of this data-driven model can be achieved through the grey-box model in Chapter 4. Therefore, numerous applications of black-box and grey-box model estimation by subspace system identification methods, depending on the users' application. As an extension of the work in Chapter 4, four areas for future study are suggested: 1) extension of the methodology to an incomplete set of sensors for finite lumped mass structural systems; 2) application to distributed mass structural systems (*e.g.*, beams, plates, *etc.*); 3) experimental study of grey-box modeling applied to different types of structural damage (*e.g.*, tension loss in cables, loss of bolted connections, *etc.*); and 4) quantitative studies on the impact of environmental effects (*e.g.*, temperature, humidity, sunshine, and rain) on the data-driven models.

As an extension of the study delineated in Chapter 5, in-network implementation of the direct 4SID methods (*i.e.*, N4SID or MOESP in Chapter 3) is suggested as a future research avenue for more accurate system identification. Since the direct 4SID methods are numerically robust and do not require any parameters (once the system order is set), an autonomous decentralized implementation of the direct 4SID methods in a wireless sensors network is expected. To successfully implement the in-network execution of the direct 4SID methods, some hardware improvements (especially the need for large memory resources) of wireless sensors is required. For example, these methods require large amounts of data processed by intensive computational tools (*e.g.*, singular value decomposition). For optimal management of the computational resources in a wireless sensor network, a hierarchical sub-network implementation is also recommended.

For development of a more effective wireless monitoring system for observation of vehicle-bridge interaction, a novel wireless monitoring system architecture, which facilitates ad-hoc connectivity between the wireless sensors in the vehicle and the wireless sensors on the bridge is recommended as a future extension of the work in Chapter 6. The ad-hoc wireless monitoring system is also an essential strategy for monitoring the interaction between a bridge and multiple vehicles (multiple moving vehicles are more realistic situations for operational bridges). Unlike the proposed tactile piezoelectric strip sensor, alternative positioning sensors (*e.g.*, laser-based non-contact sensors or global positioning system (GPS) receivers) can be also considered for accurate vehicle tracking. More advanced filtering algorithms (such as the extended Kalman filter,

the unscented Kalman filter, the particle filter, *etc.*) can be applied to provide more precise vehicle tracking.

Numerous research extensions of the vehicle-bridge interaction analysis in Chapter 7 are suggested. For a detailed exploration of the complex coupled dynamics between a truck and bridge, denser sensor instrumentations on the truck, as well as on the bridge are required. It is also recommended the three-dimensional dynamic motion of the truck be measured. A denser sensor array on a bridge deck is also recommended for the detailed allocation of moving load position (which is referred to as the kernel approximation in Chapter 7). A system identification technique for closed-loop systems is also recommended for the identification of the coupled dynamics between a truck and bridge. Based on the enhanced data-driven model from the truck and bridge response data, the estimated model can be utilized in various ways. For example, realistic system response prediction allows engineers to study long-term bridge deterioration by arbitrary traffic loads (*e.g.*, fatigue analysis of steel bridges). Similar to weighing-in-motion systems, traffic load estimation is achievable since the load input is identified from the estimated data-driven model and other measured bridge responses.

8.4 Model-Based Structural Health Monitoring

A model-based structural health monitoring framework has been emphasized throughout this thesis. Based on cost-effective "***wireless sensor technology***", dense sensor networks are realizable for large-scale civil structures. Density translates into large data sets collected by sensors. Fundamental to the framework is a universal approach to establishing a "***data-driven state-space model***" through system identification. This is mainly achievable 1) by recently developed subspace identification methods (Chapters 3 and 5) or 2) by a combined approach (Chapter 7) of the classical prediction error method (PEM) and subspace identification methods, as demonstrated in this thesis.

The data-driven model offers numerous promising benefits relevant to the SHM and civil engineering community. For example, the data-driven model provides a numerical tool for the prediction of structural responses. Using these models, the structural response of an arbitrary load can be predicted within a linear range. By grey-box modeling, physical interpretation of the data-driven model is possible up to a certain point; physical interpretation is critical in solving traditional SHM problems (*e.g.*, baselining an existing structure performance and damage detection). The data-driven model also consists of a limited number of parameters. Thus, the data-driven model can be considered as a compressed information structure; This data compression approach is very useful, especially for long-term SHM practices, since it can prevent data

inundation. Finally, the data-driven model can be used to illuminate some complex physical phenomena in real structures, thereby providing an effective tool for fundamentally learning about structural behavior from data. Thus, conventional analytical tools for SHM (*i.e.*, finite element analysis) can be enhanced/updated by the data-driven model.

REFERENCES

AASHTO (2002). Standard Specifications for Highway Bridges. Washington D.C., American Association of State Highway and Transportation Officials.

AASHTO (2008). Bridging the Gap: Restoring and Rebuilding the Nation's Bridges. Washington D.C., Association of State Highway and Transportation Officials.

Abdelghani, M., Verhaegen, M., Van Overschee, P. and De Moor, B. (1998). "Comparison Study of Subspace Identification Methods Applied to Flexible Structures." Mechanical Systems and Signal Processing 12(5): 679-692.

Akaike, H. (1974). "Stochastic Theory of Minimal Realization." IEEE Transactions on Automatic Control 19(6): 667-674.

Aktan, A. E., Catbas, F. N., Grimmelsman, K. A. and Tsikos, C. J. (2000). "Issues in Infrastructure Health Monitoring for Management." ASCE Journal of Engineering Mechanics 126(7): 711-724.

Ansari, F. (2007). "Practical Implementation of Optical Fiber Sensors in Civil Structural Health Monitoring." Journal of Intelligent Material Systems and Structures 18(8): 879-889.

Arici, Y. and Mosalam, K. M. (2005). "Modal Identification of Bridge Systems Using State-Space Methods." Structural Control and Health Monitoring 12: 381-404.

Balmes, E. (1997). "New Results on the Identification of Normal Modes from Experimental Complex Modes." Mechanical Systems and Signal Processing 11(2): 229-243.

Bensky, A. (2004). Short-Range Wireless Communication. Oxford, UK, Elsevier.

Bernal, D. (2002). "Load Vectors for Damage Localization." ASCE Journal of Engineering Mechanics 128(1): 7-14.

Betti, R. (2008). Time-Domain Identification of Structural Systems from Input-Output Measurements. Vienna, Austria, Springer.

Biggs, J. M., Suer, H. S. and Louw, J. M. (1959). "Vibration of Simple Span Highway Bridges." ASCE Journal of the Structural Division 83: 1186-1132.

Brewer, J. W. (1978). "Kronecker Products and Matrix Calculus in System Theory." IEEE Transactions on Circuits and Systems 25(9): 772-781.

Brogan, W. L. (1991). Modern Control Theory. Upper Saddle River, NJ, Prentice Hall.

Brownjohn, J. M. W. (2003). "Ambient Vibration Studies for System Identification of Tall Buildings." Earthquake Engineering and Structural Dynamics 32(1): 71-95.

Brownjohn, J. M. W. (2007). "Structural Health Monitoring of Civil Infrastructure." Philosophical Transactions of the Royal Society 365: 589-622.

Cantieni, R. (1983). Dynamic Load Tests on Highway Bridges in Switzerland - 60 Years of Experience, Federal Laboratory for Testing of Materials, Switzerland.

Capecchi, D., De Angelis, M. and Sepe, V. (2004). "Modal Model Identification with Unknown Nonstationary Base Motion." Meccanica 39(1): 31-45.

Celebi, M. (2002). Seismic Instrumentation of Buildings with Emphasis on Federal Buildings. Menlo Park, CA, USGS.

Celebi, M. (2006). "Real-Time Seismic Monitoring of the New Cape Girardeau Bridge and Preliminary Analyses of Recorded Data: An Overview." Earthquake Spectra 22(3): 609-630.

Chaudhary, M. T. A., Abe, M., Fujino, Y. and Yoshida, J. (2000). "System Identification of Two Based-Isolated Brdiges Using Seismic Records." Journal of Structural Engineering, ASCE 126(10): 1187-1195.

Chen, C. T. (1984). Linear Systems Theory and Design. New York, NY, CBS College Publishing.

Chen, Y., Feng, M. Q. and Tan, C.-A. (2009). "Bridge Structural Condition Assessment Based on Vibration and Traffic Monitoring." Journal of Engineering Mechanics 135(8): 747-758.

Cho, S., Jo, H., Jang, S., Park, J., Jung, H. J., Yun, C. B., Spencer, B. F. and Seo, J. W. (2010). "Strcutural Health Monitoring of a Cable-Stayed Bridge Using Smart Sensor Technology: Data Analyses." Smart Structures and Systems 6(5-6): 461-480.

Cunha, A. and Caetano, E. (2006). Experimental Modal Analysis of Civil Engineering Structures. Sound and Vibration Magazine**:** 12-20.

De Angelis, M., Lus, H., Betti, R. and Longman, R. W. (2002). "Extracting Pysical Parameters of Mechanical Models from Identified State-Space Representations." Journal of Applied Mechanics, ASME 69: 617-625.

Doebling, S. W., Farrar, C. R. and Prime, M. B. (1998). "Summary Review of Vibration-Based Damage Identification Methods." Shock and Vibration Digest 30(2): 91-105.

Ewins, D. J. (2000). Modal Testing: Theory, Practice and Application. West Sussex, England, Wiley.

Farrar, C. R., Doebling, S. W. and Nix, D. A. (2001). "Vibration-Based Structural Damage Identificaiton." Philosophical Transactions of the Royal Society 359: 131-149.

Farrar, C. R. and Worden, K. (2007). "An Introduction to Structural Health Monitoring." Philosophical Transactions of the Royal Society 365: 303-315.

Franco, G., Betti, R. and Longman, R. W. (2006). "On the Uniqueness of Solutions for the Identification of Linear Structural Sytems." Journal of Applied Mechanics, ASME 73(1): 153-162.

Frangopol, D. M., Strauss, A. and Kim, S. (2008). "Bridge Reliability Assessment Based on Monitoring." ASCE Journal of Bridge Engineering 13(3): 258 - 270.

Fraser, M., Elgamal, A., Xianfei, H. and Conte, J. P. (2010). "Sensor Network for Structural Health Monitoring of a Highway Bridge." Journal of Computing in Civil Engineering 24(1): 11-24.

Fryba, L. (1972). Vibration of Solids and Structures under Moving Loads. Groningen, Netherlands, Noordhoof Publishing.

Fryba, L. (1976). "Non-Stationary Response of a Beam to a Moving Random Force." Journal of Sound and Vibration 46(3): 323-338.

Gevers, M. (2003). A Personal View on the Development of System Identification. 13th Federation of Automatic Control Symposium on System Identification (IFAC SYSID), Rotterdam, Netherlands.

Gillespie, T. and Karamihas, S. M. (2000). "Simplified Models for Truck Dynamic Response to Road Inputs." International Journal of Heavy Vehicle Systems 7: 52-63.

Gillespie, T., Karamihas, S. M., Cebon, D., Sayers, M. W., Nasim, M. A. and Ehsan, N. (1992). Effects of Heavy Vehicle Charateristics on Pavement Response and Performance. Ann Arobor, MI, University of Michigan Transportation Reaserch Institute.

Ginsberg, J. H. (2001). Mechanical and Structural Vibrations: Theory and Applications. New York, NY, Wiley.

Golub, G. H. and Van Loan, C. F. (1996). Matrix Computations. Baltimore, Maryland, The Johns Hopkins University Press.

Green, M. F. and Cebon, D. (1994). "Dynamic Response of Highway Bridges to Heavy Truck Loads: Theory and Experimental Validation." Journal of Sound and Vibration 170(1): 51-78.

Greve, D. W., Sohn, H., Yue, C. P. and Oppenhiem, I. J. (2007). "An Inductively Coupled Lamb Wave Transducer." IEEE Sensors Journal 7(2): 295-301.

Grini, D. (2006). CC2420 with External PA. Dallas, TX, Texas Instruments Inc.

Haykin, S. (1999). Neural Networks. Upper Saddle River, NJ, Prentice Hall.

Hermans, L. and Van Der Auweraer, H. (1999). "Modal Testing and Analysis of Structures under Operational Conditions: Industrial Applications." Mechanical Systems and Signal Processing 13(2): 193-216.

Hillerborg, A. (1951). Dynamic Influences of Smoothly Running Loads on Simply Suppported Girders. Stockholm, Kungliga Tekniska Högskolan.

Hipley, P. (2001). Caltrans' Current State-of-Practice. Instrumental Systems for Diagnostics of Seismic Response of Brdiges and Dams, Consortium of Organizations for Strong-motion Obervation Systems, Richmond, CA.

Ho, B. L. and Kalman, R. E. (1965). "Effective Construction of Linear State-Variable Models from Input-Output Functions." Regelungtechnik 12: 545-548.

Holzel, M. S. and Bernstein, D. S. (2009). On the Accuracy of Least Squares Estimations of Markov Parameters Based on μ-Markov Models. 15th International Federation of Automatic Control Symposium on System Identification (IFAC SYSID), Saint-Malo, France.

Hwang, E. and Nowak, A. S. (1991). "Simulation of Dynamic Load for Bridges." Journal of Structural Engineering, ASCE 117(5): 1413-1425.

Ibrahim, S. R. (1977). "Random Decremental Technique for Modal Identification of Structures." Journal of Spacecraft and Rockets 14(11): 696-700.

Ibrahim, S. R. (1983). "Computation of Normal Modes from Identified Complex Modes." AIAA Journal 21: 446-451.

Ibrahim, S. R. and Pappa, R. S. (1982). "Large Modal Survey Testing Using the Ibrahim Time Domain Identification Technique." Journal of Spacecraft and Rockets 19(5): 459-465.

Inaudi, D. and Deblois, R. (2009). Overview of 40 Bridge Structural Health Monitoring Projects. 26th International Bridge Conference Pennsylvania, PA.

James, G. H., Carne, T. G. and Lauffer, J. P. (1996). "The Natural Excitation Technique (NExT) for Modal Parameter Extraction from Operating Structures." The International Journal of Analytical and Experimental Modal Analysis 10(4): 260-277.

Jang, S., Jo, H., Cho, S., Mechitov, K., Rice, J. A., Sim, S. H., Jung, H. J., Yun, C. B., Spencer, B. F. and Agha, G. (2010). "Strcutural Health Monitoring of a Cable-Stayed Bridge Using Smart Sensor Technology: Development and Evaluation." Smart Structures and Systems 6(5-6): 439-459.

Jeffcott, H. H. (1929). "On the Vibrations of Beams under the Action of Moving Loads." Philosophical Magazine 7(8).

Jones, J. D. and Pei, J. S. (2009). "Embedded Algorithms within an FPGA to Classify Nonlinear Single-Degree-of-Freedom Systems." IEEE Sensors Journal 9(11): 1486-1493.

Juang, J. N. (1994). Applied System Identification. Upper Saddle River, NJ, Prentice Hall.

Juang, J. N. and Pappa, R. S. (1984). "An Eigensystem Realization Algorithm for Modal Parameter Identification and Model Reduction." Journal of Guidance 8(5): 620-627.

Juang, J. N., Phan, M. and Horta, L. G. L., R.W. (1991). Identification of Observer/Kalman Filter Markov Parameters: Theory and Experiment. Hampton, Virginia, Langley Research Center.

Kailath, T. (1980). Linear Systems. Englewood Cliffs, NJ, Prentice-Hall.

Kalman, R. E. (1960). "New Results in Linear Filtering and Prediction Problems." Journal of Basic Engineering, ASME 82(Series D): 95-108.

Katoua, M., Matsuoka, A., Yoshiokab, T. O., Sanadac, Y. and Miyoshia, T. (2008). "Numerical Simulation Study of Ground Vibrations Using Forces from Wheels of a Running High-Speed Train." Journal of Sound and Vibration 318: 830-849.

Kijewski-Correa, T. and Su, S. (2009). "BRAIN: A Bivariate Data-Driven Approach to Damage Detection in Multi-Scale Wireless Sensor Networks." Smart Structures and Systems 5(4): 415-426.

Kim, J. and Lynch, J. P. (2010). "Experimental Analysis of Vehicle-Bridge Interaction Using a Wireless Monitoring System and a Two-Stage System Identification Technique." Mechanical Systems and Signal Processing (submitted).

Kim, J., Lynch, J. P., Lee, J. J. and Lee, C. G. (2010a). "Truck-Based Mobile Wireless Sensor Networks for Experimental Observation of Vehicle-Bridge Interaction." Smart Materials and Structures (submitted).

Kim, J., Lynch, J. P., Lee, J. J. and Lee, C. G. (2010b). Vehicle Tracking Using Mobile Wireless Sensor Networks During Dynamic Load Testing of Highway Bridges. The 5th European Workshop on Structural Health Monitoring, Sorrento, Italy.

Kim, J., Lynch, J. P., Zonta, D., Yun, C. B. and Lee, J. J. (2009). Modal Analysis of the Yeondae Bridge Using a Reconfigurable Wireless Monitoring System. 10th International Conference on Structural Safety and Reliability (ICOSSAR'09), Osaka, Japan.

Kim, J., Swartz, R. A., Lynch, J. P., Lee, J. J. and Lee, C. G. (2010c). "Rapid-to-Deploy Reconfigurable Wireless Structural Monitoring Systems Using Extended-Range Wireless Sensors." Smart Structures and Systems 6(5-6).

Ko, J. M. (2003). Health Monitoring and Intelligent Control of Cable-Supported Bridges. Strcutural Health monitoring and Intelligent Infrastructure, Tokyo, Japan.

Ko, J. M. and Ni, Y. Q. (2005). "Technology Developments in Structural Health Monitoring of Large-Scale Bridges." Engineering Structures 27: 1715-1725.

Koh, H. M., Choo, J. F., Kim, S. K. and Kim, C. Y. (2003). Recent Application and Development of Structural Health Monitoring Systems and Intelligent Structures in Korea. Strcutural Health monitoring and Intelligent Infrastructure Tokyo, Japan.

Koo, K. Y., Hong, J. Y., Park, H. J. and Yun, C. B. (2008). Remotely Controllable Structural Health Monitoring Systems for Bridges Using 3.5 Generation Mobile Telecommunication Technology. IABMAS 2008: Bridge Maintenance, Safety, Management, Health Monitoring and Informatics, Seoul, Korea.

Kung, S. (1978). A New Identification and Model Reduction Algorithm Via Singular Value Decomposition. 12th Asilomar Conference on Circuits, Systems and Computers, Pacific Groove, CA.

Kwasniewski, L., Wekezer, J., Roufa, G., Li, H. Y., Ducher, J. and Malachowski, J. (2006). "Experimental Evaluation of Dynamic Effects for a Selected Highway Bridge." Journal of Performance of Constructed Facilities 20(3): 253-260.

Larimore, W. E. (1990). Canonical Variate Analysis in Identification, Filtering, and Adaptive Control. 29th Conference on Decision and Control, Honolulu, HI.

Lawrence, A. (1998). Modern Inertial Technology: Navigation, Guidance, and Control New York, NY, Springer.

Lee, C. G., Lee, W. T., Yun, C. B. and Choi, J. S. (2004). Development of Integrated System for Smart Evaluation of Load Carrying Capacity of Bridges. Daejeon, Korea, Korea Advanced Institute of Science and Technology.

Lee, H. S., Hong, Y., H. and Park, H., W. (2010). "Design of an FIR Filter for the Displacement Reconstruction Using Measured Acceleration in Low-Frequency Dominant Structures." International Journal for Numerical Methods in Engineering 82: 403-434.

Lee, J. J., Fukuda, Y., Shinozuka, M., Cho, S. and Yun, C. B. (2007). "Development and Application of a Vision-Based Displacement Measurement System for Structural Health Monitoring of Civil Structures." Smart Structures and Systems 3(3): 373-384.

Lei, Y., Kiremidjian, A. S., Nair, K. K., Lynch, J. P. and Law, K. H. (2005). "Algorithms for Time Synchronization of Wireless Structural Monitoring Sensors." Earthquake Engineering and Structural Dynamics 34(6): 555-573.

Lian, F. L., Moyne, J. R. and Tilbury, D. M. (2005). Network Protocols for Networked Control Systems. Handbook of Networked and Embedded Control Systems. D. L. Hristu-Varsakelis, W.S. Boston, MA, Springer.

Lin, C. W. and Yang, Y. B. (2005). "Use of a Passing Vehicle to Scan the Fundamental Bridge Frequencies: An Experimental Verificatioin." Engineering Structures 27: 1865-1878.

Ljung, L. (1999). System Identification: Theory for the User. Upper Saddle River, NJ, Prentice Hall.

Ljung, L. (2009). System Identification Toolbox 7, The Mathworks.

Lu, K. C., Wang, Y., Lynch, J. P., Loh, C. H., Chen, Y. J., Lin, P. Y. and Lee, Z. K. (2006). Ambient Vibration Study of the Gi-Lu Cable-Stay Bridge: Application of Wireless Sensing Units. SPIE - The International Society for Optical Engineering, San Diego, CA.

Lus, H., De Angelis, M. and Betti, R. (2003). "A New Approach for Reduced Order Modeling of Mechanical Systems Using Vibration Measurements." Journal of Applied Mechanics, ASME 70: 715-723.

Lynch, J. P., Law, K. H., Kiremidjian, A. S., Carryer, E., Farrar, C. R., Sohn, H., Allen, D. W., Nadler, B. and Wait, J. R. (2004a). "Design and Performance Validation of a Wireless Sensing Unit for Structural Monitoring Applications." Structural Engineering and Mechanics 17(3-4): 393-408.

Lynch, J. P. and Loh, K. J. (2006). "A Summary Review of Wireless Sensors and Sensor Networks for Structural Health Monitoring." Shock and Vibration Digest 38(2): 91-128.

Lynch, J. P., Sundararajan, A., Law, K. H., Kiremidjian, A. S. and Carryer, E. (2004b). "Embedding Damage Detection Algorithms in a Wireless Sensing Unit for Operational Power Efficiency." Smart Materials and Structures 13(4): 800-810.

Lynch, J. P., Sundararajan, A., Law, K. H., Kiremidjian, A. S., Kenny, T. and Carryer, E. (2003). "Embedment of Structural Monitoring Algorithms in a Wireless Sensing Unit." Structural Engineering and Mechanics 15(3): 285-297.

Lynch, J. P., Wang, Y., Loh, K. J., Yi, J. H. and Yun, C. B. (2006). "Performance Monitoring of the Geumdang Bridge Using a Dense Network of High-Resolution Wireless Sensors." Smart Materials and Structures 15(6): 1561-1575.

Mascarenas, D., Flynn, E., Farrar, C. R., Park, G. and Todd, M. (2009). "A Mobile Host Approach for Wireless Powering and Interrogation of Structural Health Monitoring Sensor Networks." IEEE Sensors Journal 9(12): 1719-1726.

Mizuno, Y., Fujino, Y., Kataoka, K. and Matsumoto, Y. (2008). "Development of a Mobile Sensing Unit and Its Prototype Implementation." Tsinghua Science and Technology 13: 223-227.

Nagayama, T. and Spencer, B. F. (2007). Structural Health Monitoring Using Smart Sensors. NSEL Report Series. Urbana-Champaign, IL, University of Illinois at Urbana-Champaign.

NIST (2008). Advanced Sensing Technologies for the Infrastructure: Roads. Gaithersburg, MD, National Institute of Standards and Technology.

Oppenheim, I. J. (2003). "Two Demonstrations of Mems in Civil Engineering." Journal of Aerospace Engineering 16(3): 99-99.

Oppenhiem, A. V. and Schafer, R. W. (1999). Discrete-Time Signal Processing. Upper Saddle River, NJ, Prentice-Hall Inc.

Ozevin, D., Greve, D. W., Oppenheim, I. J. and Pessiki, S. P. (2006). "Resonant Capacitive MEMS Acoustic Emission Transducers." Smart Materials and Structures 15(6): 1863-1871.

Pakzad, S. N., Fenves, G. L., Kim, S. and Culler, D. E. (2008). "Design and Implementation of Scalable Wireless Sensor Network for Structural Monitoring." Journal of Infrastructure Systems 14(1): 89-101.

Park, G., Cudney, H. H. and Inman, D. J. (2000). "Impedance-Based Health Monitoring of Civil Structural Components." Journal of Infrastructure Systems, ASCE 6(4): 153-160.

Peeters, B. and Roeck, G. D. (1999). "Reference-Based Stochastic Subspace Identification for Output-Only Modal Analysis." Mechanical Systems and Signal Processing 13(6): 855-878.

Peeters, B. and Ventura, C. E. (2003). "Comparative Study of Modal Analysis Techniques for Bridge Dynamic Characteristics." Mechanical Systems and Signal Processing 17(5): 965-988.

Pesterev, A. V. and Bergman, L. A. (1997). "Response of Elastic Continuum Carrying Moving Linear Oscillator." ASCE Journal of Engineering Mechanics 123: 878-884.

Raghavendra, C. S., Sivalingam, K. M. and Znati, T. F. (2004). Wireless Sensor Networks. New York, NY, Springer.

Reynders, E., Pintelon, R. and De Roeck, G. (2008). "Uncertainty Bounds on Modal Parameters Obtained from Stochastic Subspace Identification." Mechanical Systems and Signal Processing 22: 948-969.

Rice, J. A., Mechitov, K. A., Spencer, B. F. and Agha, G. A. (2008). A Service-Oriented Architecture for Structural Health Monitoring Using Smart Sensors. 14th World Conference on Earthquake Engineering, Beijing, China.

Richart, F. E., Hall, J. R. and Wood, R. D. (1970). Vibrations of Soils and Foundations. Englewood Cliffs, NJ, Prentice Hall.

Ryu, J. (2004). State and Parameter Estimation for Vehicle Dynamics Control Using GPS. Department of Mechanical Engineering. Stanford, Stanford University. Ph.D.

Salas, K. I. and Cesnik, C. E. S. (2010). "Guided Wave Structural Health Monitoring Using Clover Transducers in Composite Materials." Smart Materials and Structures 19(1): 1-25.

Salawu, O. S. and Williams, C. (1995). "Review of Full-Scale Dynamic Testing of Bridge Structures." Engineering Structures 17(2): 113-121.

Shih, C. Y., Tsuei, Y. G., Allemang, R. J. and Brown, D. L. (1988). "Complex Mode Indication Function and Its Applications to Spatial Domain Parameter Estimation." Mechanical Systems and Signal Processing 2(4): 367-377.

Silicon Designs Inc. (2009). Model 2012 Analog Accelerometer Module. Issaquah, WA.

Sim, S. H., Carbonell-Márquez, J. F. and Spencer, B. F. (2008). Efficient Decentralized Data Aggregation in Wireless Smart Sensor Networks. Proceedings of SPIE: Sensing and Smart Structures Technologies of Civil, Mechanical and Aerospace Systems, San Diego, CA, SPIE.

Simon, D. (2006). Optimal State Estimation. Hoboken, New Jersey, John Wiley & Sons Inc.

Smyth, A. and Wu, M. (2007). "Multi-Rate Kalman Filtering for the Data Fusion of Displacement and Acceleration Response Measurements in Dynaminc System Monitoring." Mechanical Systems and Signal Processing 21: 706-723.

Sohn, H. and Farrar, C. R. (2001). "Damage Diagnosis Using Time Series Analysis of Vibration Signal." Smart Materials and Structures 10: 446 - 451.

Spencer, B. F., Ruiz-Sandoval, M. E. and Kurata, N. (2004). "Smart Sensing Technology: Opportunities and Challenges." Journal of Structural Control and Health Monitoring 11(4): 349-368.

Stengel, R. F. (1994). Optimal Control and Estimation. New York, NY, Dover Publications.

Straser, E. G. and Kiremidjian, A. S. (1998). A Modular, Wireless Damage Monitoring System for Structures. Stanford, CA, John A. Blume Earthquake Engineering Center,Stanford University.

Suzhen, L. and Zhishen, W. (2007). "Development of Distributed Long-Gage Fiber Optic Sensing System for Structural Health Monitoring." Structural Health Monitoring 6(2): 133-143.

Svinkin, M. R. (2008). Dynamic Effects of Impact Machine Foundations. Geotechnical Earthquake Engineering and Soil Dynamics IV Congress, Sacramento, CA.

Swartz, R. A. (2009). Collocation of Sensing, Computing, and Actuation in Low-Power Wireless Nodes for Smart Structure Applications in Civil and Mechanical Systems. Deptment of Civil and Environmental Engineering Ann Arbor, MI, University of Michigan. Ph.D. Thesis.

Swartz, R. A., Jung, D., Lynch, J. P., Wang, Y., Shi, D. and Flynn, M. P. (2005). Design of a Wireless Sensor for Scalable Distributed in-Network Computation in a Structural Health Monitoring System. 5th International Workshop on Structural Health Monitoring, Palo Alto, CA.

Swartz, R. A. and Lynch, J. P. (2009). "Strategic Network Utilization in a Wireless Structural Control System for Seismically Excited Structures." Journal of Structural Engineering, ASCE 135(5): 597-608.

Szary, P. and Maher, A. (2009). Implemetation of Weigh-in-Motion (WIM) Systems. Washington, D. C., Federal Highway Administration.

Tamura, K. (2001). Instrument Systems of Major Bridges in Japan. Instrumental Systems for Diagnostics of Seismic Response of Brdiges and Dams, Consortium of Organizations for Strong-motion Obervation Systems, Richmond, CA.

Texas Instruments Inc. (2003). ADS8341 16-Bit, 4-Channel Serial Output Sampling Analog-to-Digital Converter. Dallas, TX.

Texas Instruments Inc. (2008). CC2420 2.4 Ghz IEEE 802.15.4 / Zigbee-Ready RF Transceiver. Dallas, TX.

Timoshenko, S. P. (1922). "On the Forced Vibration of Bridges." Philosophical Magazine 6: 1018-1019.

Timoshenko, S. P., Young, D. H. and Weaver, W. (1974). Vibration Problems in Engineering. New York, NY, John Wiley & Sons.

USDOT (2009). State Transportation Statistics. Washington D.C., U.S. Department of Transportation.

Van Overschee, P. and De Moor, B. (1993). "Subspace Algorithm for the Stochastic Identification Problem." Automatica 29(3): 649-660.

Van Overschee, P. and De Moor, B. (1994). "N4SID: Subsapce Algorithms for the Identification of Combined Deterministic-Stochastic Systems." Automatica 30(1): 75-93.

Van Overschee, P. and De Moor, B. (1996). Subspace Identification for Linear Systems. Dordrecht, Netherlands, Kluwer Academic Publishers.

Van Pelt, T. H. and Bernstein, D. S. (1998). Least Squares Identification Using μ-Markov Parameterizations. 37th IEEE Conference on Decision & Control, Tampa, FL.

Verhaegen, M. (1994). "Identification of the Deterministic Part of MIMO State Space Models Given in Innovations Form from Input-Output Data." Automatica 30(1): 61-74.

Verhaegen, M. and Verdult, V. (2007). Filtering and System Identification: A Least Squares Approach. Cambridge, UK, Cambidge University Press.

Viberg, M. (1995). "Subspace-Based Methods for the Identification of Linear Time-Invariant Systems." Automatica 31(12): 1835-1851.

Viberg, M., Ottersten, B., Wahlberg, B. and Ljung, L. (1993). Performance of Subspace-Based System Identification Methods. IFAC Symposium on System Identification, Sydney, Austraila.

Wang, Y., Lynch, J. P. and Law, K. H. (2007). "A Wireless Structural Health Monitoring System with Multithreaded Sensing Devices: Design and Validation." Structural and Infrastructure Engineering 3(2): 103-120.

Weng, J. H. (2010). Application of Subspace Identification in System Identification and Structural Damage Detection. Department of Civil Engineering. Taipei, National Taiwan University. Ph.D. Thesis.

Weng, J. H., Loh, C. H., Lynch, J. P., Lu, K. C., Lin, P. Y. and Wang, Y. (2008). "Output-Only Modal Identification of a Cable-Stayed Bridge Using Wireless Monitoring Systems." Engineering Structures 30: 1820-1830.

Whelan, M. J. and Janoyan, K. D. (2009). "Design of a Robust, High-Rate Wireless Sensor Network for Static and Dynamic Structural Monitoring." Journal of Intelligent Material Systems and Structures 20(7): 849-863.

Wiss, J. F. (1981). "Construction Vibrations: State-of-the-Art." Journal of the Geotechnical Engineering Division, ASCE 107: 167-181.

Xiao, H., Bruhns, O. T., Waller, H. and Meyers, A. (2001). "An Input/Output-Based Procedure for Fully Evaluating and Monitoring Dynamic Properties of Structural Systems Via a Subspace Identification Method." Journal of Sound and Vibration 246(4): 601-623.

Yan, A. M. and Golinval, J. C. (2006). "Null Subspace-Based Damage Detection of Structures Using Vibration Measurements." Mechanical Systems and Signal Processing 20(3): 611-626.

Yan, G., Dyke, S. J. and Song, W. (2009). Structural Damage Localization with Tolerance to Large Time Synchronization Errors in Wsns. 2009 American Control Conference, St. Louis, MO.

Yang, Y. B., Lin, C. W. and Yau, J. D. (2004a). "Extracting Bridge Frequencies from the Dynamic Response of a Passing Vehicle." Journal of Sound and Vibration 272: 471-493.

Yang, Y. B., Yau, J. D. and Wu, Y. S. (2004b). Vehicle-Bridge Interaction Dynamics: With Applications to High-Speed Railways. Singapore, World Scientific Publishing Co.

Yi, J. H. and Yun, C. B. (2004). "Comparative Study on Modal Identification Methods Using Output-Only Information." Structural Engineering and Mechanics 17(3-4): 445-466.

Zarchan, P., Musoff, M. and Lu, F. K. (2009). Fundamentals of Kalman Filtering: A Practical Approach, American Institute of Aeronautics & Astronauts.

Zimmerman, A. T. (2010). Agent-Based Computational Architectures for Distributed Data Processing in Wireless Sensor Networks. Deptment of Civil and Environmental Engineering Ann Arbor, MI, University of Michigan. Ph.D. Thesis.

Zimmerman, A. T., Shiraishi, M., Swartz, R. A. and Lynch, J. P. (2008). "Automated Modal Parameter Estimation by Parallel Processing within Wireless Monitoring Systems." Journal of Infrastructure Systems, ASCE 14(1): 102-113.